Doctoral School **ED SMRE**

Unité de Catalyse et Chimie du Solide (UCCS)

University of Lille

Doctoral Thesis in Chemistry

Speciality **Molecules and Condensed Matter**

presented and defended by

Shreya Nandi

19th December 2019

Investigation of Perovskite-based Three-way Catalysts Using Surface Analysis Techniques and *in situ / operando* Spectroscopy

Thesis Supervisor: **Pr. Jean-François Paul, Professor, University of Lille**

Co-supervisors: **Dr. Anne-Sophie Mamede, Assistant Professor, ENSCL**
Dr. Elise Berrier, Researcher, CNRS

Jury

Pr. Moniek Tromp	Professor, University of Groningen, NL	Reviewer
Pr. Bruno Domenichini	Professor, University of Bourgogne, FR	Reviewer
Dr. Francisco Cadete Santos Aires	Researcher, CNRS IRCELYON, FR	Examiner
Pr. Antonella Glisenti	Professor, University of Padova, IT	Examiner
Pr. Pascal Granger(Jury president)	Professor, University of Lille, FR	Examiner

Ecole Doctorale **ED SMRE**

Unité de Catalyse et Chimie du Solide (UCCS)

Université de Lille

Docteur en Chimie

Spécialité **Molécules et Matière Condensée**

Présentée par

Shreya Nandi

19 Décembre 2019

Etude de catalyseurs à trois voies à base de pérovskites utilisant des techniques d'analyse de surface et la spectroscopie *in situ/operando*

Directeur de thèse : **Jean-François Paul, Professeur, Université de Lille**

Co-Encadrantes : **Anne-Sophie Mamede, Maître de conférences, ENSCL**
Elise Berrier, Chargé de Recherche, CNRS

Jury :

Pr. Moniek Tromp	Professeur, Université de Groningen, NL	Rapporteur
Pr. Bruno Domenichini	Professeur, Université de Bourgogne, FR	Rapporteur
Dr. Francisco Cadete Santos Aires	Chargé de Recherche, IRCELYON, FR	Examinateur
Pr. Antonella Glisenti	Professeur, Université de Padova	Examinateur
Pr. Pascal Granger (Président de jury)	Professeur, Université de Lille	Examinateur

To Mamma and Baba...

"You never fail untill you stop trying."
- Albert Einstein

"Everything comes to us that belongs to us,
if we create the capacity to receive it."
- Rabindranath Tagore

Acknowledgements

I feel pursuing PhD is not just about academic growth but a whole journey by itself, where you learn so much beyond academics. Today, I feel immense happiness writing this part of my thesis, because it allows me to personally thank each and everyone who helped me move forward through the ups and down of my PhD journey.

Firstly, I would like to thank all my supervisors - Dr. Elise Berrier, Dr. Anne-Sophie Mamede and Prof. Jean-François Paul for giving me this opportunity to work on this interesting and challenging topic, providing hands-on experience on using advanced surface/bulk techniques and perform experiments at the synchrotron facilities towards answering part of the scientific questions. I am grateful for their availability whenever I needed their advice or support, their office doors were always open for me. Each of them individually played a significant role on the advancement of this thesis work that is worth mentioning. I am thankful to Elise for helping me to get acquainted with the subject, introduce me to the know-hows of the sample preparation technique as well as the operando Raman setup and the fascinating discussions from time to time until today. She encouraged me to learn LaTeX for writing my thesis and helped me shaping the entire manuscript. Her kind and supportive nature was a big bonus. I am also grateful to Anne-Sophie for introducing me to the world of surface science, training me to become an independent user of LEIS and teaching me the casaXPS software patiently. She has been a huge support throughout, academically and personally. I will always cherish our discussions during the long drives to SOLEIL and the users meeting. Further, I would like to acknowledge Jean-François for several interesting discussions and our wonderful time during the NAP-XPS experiments at SOLEIL through midnight until sunrise. Overall, I am fortunate to have supervisors like them who inspired me to evolve as a researcher with constant support in every aspect of life.

Additionally, I would like to acknowledge all the jury members including Prof. Antonella Glisenti, Prof. Pascal Granger, Dr. Francisco Aires Cadete Santos and especially the reviewers, Prof.Moniek Tromp and Prof. Bruno Domenichini for evaluating my thesis work.

I am also thankful to the PARTIAL-PGMs EU Horizon 2020 project for financing this work. I would like to acknowledge the all partners of this consortium as well as the internal team at UCCS, including Prof. P. Granger, Dr. J-P Dacquin and Prof. C. Dujardin. I am utterly grateful to former PhD student Jianxiong Wu, now Dr. Wu, for providing me with the powder samples and for the useful discussions.

I would like to thank Dr. Asma Tougerti and Dr. Jean-Sébastien Girardon for helping me with the XAS experiments at SOLEIL synchrotron day in and day out. I am particularly grateful to Asma for teaching me about XAS from the scratch and taking out her valuable time to spend with me for the data processing. Working with her has been a brain-storming joyride. Some of the work would not have been possible without her. I will always remember how she calls my name with utter love every time.

I am also grateful to Dr. Nicolas Nuns for his help with all the ToF-SIMS experiments

and data-analysis. He taught me to not only use the spectrometer independently but also to handle the plethora of data that are generated. His kind and motivating nature made me feel more confident with this technique.

I would also like to extend my appreciation to the contributions of Dr. Pardis Simon and Ms. Martine Trentesaux for the numerous XPS analyses they helped me with at the lab as well as at the TEMPO beamline, SOLEIL. A big thanks to Pardis for useful discussions related to XPS results from time to time.

I am thankful to Dr. Emiliano Fonda from the SAMBA beamline (XAS) and Dr. Jean-Jacques Gallet (NAP-XPS) for helping us with their knowledge and expertise during the measurements at SOLEIL synchrotron.

I am also grateful to Dr. Ahmed Addad for all the microscopy analyses and the thorough discussions related to each result. Additionally, I am thankful to Dr. Pascal Roussel, Dr. Marie-Helene Chambrier and Mr. Olivier Gardoll for the XRD, AFM and TGA measurements, respectively.

I would like to thank the MATCAT team for permitting me to use their laboratory for all my sample preparations and providing such a friendly atmosphere to work in.

I am thankful to all my friends at the lab for keeping such a friendly and comfortable environment at the workplace - Alexandra, Guillaume, Tanushree, Shilpa, Paula, Hermann, Sara, Zhan, Bang, Maya, Carmen, Camilla, Melissa, Ayman, Betrand, Juliana and many more.

A special thanks to Debarun for everything, as well as all my friends outside the lab for always being there for me.

I would like to extend my deepest gratitude to my super-supportive family, my parents, Mamma and Baba, and my younger sister who believed in me throughout life and cheered me up every time I felt low. This thesis would not have been complete without their support. A big thanks to Baba also for proof-reading the manuscript and giving me valuable suggestions.

Finally, I am grateful to all those persons who I came across during my PhD studies in the last three years, whose names I might have forgotten to mention, each one of them have genuinely helped me in some way or the other.

Lastly, I am greatly thankful to the almighty for his blessings and for everything he has given me in life towards fulfilling my dreams.

Abstract/Résumé

The catalytic after-treatment of exhaust gases from gasoline engines requires simultaneous abatement of CO, NO and hydrocarbons and is commonly called three-way catalysis (TWC). Perovskites based materials like $LaFeO_3$, regarded as intelligent supports, are being considered as potential candidates as alternative TWC in context of reducing noble metal content. Such bulk catalysts often demonstrate variable surface compositions in comparison to the bulk. Since surface determines the catalytic performance in heterogeneous catalysis, deeper understanding of the surface characteristics especially under relevant reaction conditions becomes imperative. To this end, $LaFeO_3$ based model catalysts relevant to conventional catalysts have been investigated by combination of advanced suface analysis techniques like XPS, LEIS and ToF-SIMS to study the existing surface variations. In addition, catalysts behavior was studied under CO atmosphere by NAP-XPS and GI-XANES. This methodology allowed to reveal that inducing a La-deficiency in the structure helps to improve the catalytic performance due to an interfacial effect. In addition, the different catalytic operating modes of Cu or Mn substituted perovskite powders were determined by *in situ*/*operando* Raman spectroscopy.
Keywords: perovskites, surface analysis, three-way catalysts, *in situ*/*operando* spectroscopy

---

Le post-traitement catalytique des gaz d'échappement des moteurs à essence nécessite la conversion simultanée de CO, NO et des hydrocarbures. Ce procédé est connu sous le nom de catalyse trois voies (TWC). Les matériaux à base de perovskites comme $LaFeO_3$, décrits comme des supports "intelligents", sont considérés comme des candidats potentiels dans la recherche d'alternatives aux catalyseurs trois voies classiques, dans un contexte de réduction de leur teneur en métaux nobles. Ces catalyseurs massiques présentent en surface une composition souvent différente de leur formule chimique, qui caractérise ces matériaux dans leur volume. Etant donné que, en catalyse hétérogène, la surface est déterminante pour les performances catalytiques, il est impératif de mieux comprendre les caractéristiques de la surface, en particulier dans des conditions aux plus proches de celles de la réaction. Ainsi, des catalyseurs modèles plans à base de $LaFeO_3$, imitant les catalyseurs conventionnels sous forme de poudre, ont été étudiés en combinant des techniques avancées d'analyses de surface comme XPS, LEIS et ToF-SIMS pour étudier les variations de surface à différentes échelles de profondeur. De plus, le comportement des catalyseurs a été étudié sous atmosphère CO par NAP-XPS et GI-XANES. Cette méthodologie a permis de révéler qu'une composition déficitaire en La induit dans la structure permet d'améliorer les performances catalytiques grâce à un effet d'interface entre la perovskite et une phase minoritaire d'oxyde de fer. En outre, les différents modes de fonctionnement catalytiques de poudre de pérovskites substituées au Cu ou Mn ont été déterminés par spectroscopie Raman *in situ* et *operando*.
Mots-clefs : perovskites, analyses de surface, catalyseurs trois voies, spectroscopie *in situ* et *operando*

General Introduction

Exhaust gases from mobile sources are a major source of global air pollution. Indeed, internal combustion engines, whether using petrol or diesel as fuel, emit gases like carbon monoxide (CO), unburnt hydrocarbons (HC), nitrogen oxides (NO_x) as well as particulate matter. To regulate the level of such pollutants in the atmosphere, governments of different countries have laid strict emission standards that all automotive vehicles must abide with, such as, Euro 6 in the European Union, China V in China and Bharat Stage IV in India. The after-treatment of the released pollutants are performed by the catalytic converters located near the tailpipe of the automotive engines. It consists of a catalyst to eliminate CO, HC and NO_x simultaneously, and are thereby commonly known as Three-way catalysts (TWC). Such TWC are usually comprised of platinum group metals (PGMs) such as platinum, palladium and rhodium as the active-phases supported as nanoparticles over various oxides like ceria, zirconia, alumina etc. The usage of PGMs in this system makes it quite expensive owing to the imbalance in demand and supply arising from the social and environmental exploitation during mining. Moreover, commercial TWC currently used have been shown to undergo fast deactivation with time due to sintering of the noble metal nanoparticles under harsh operating conditions. This makes it imperative to decrease the PGMs content in TWC by at least partial replacement by other active materials, while maintaining the catalytic performances for longer duration. This objective is the keystone of the PARTIAL-PGMs project (2016-19), which received funding from the European Commission Horizon 2020 research and innovation program. The PARTIAL-PGMs project aims at developing integrated TWC-particulate filters systems based on nanomaterials with a reduction of more than 35% in PGMs and 20% in rare earth elements content by increasing catalytic performance and/or by tuning their properties by replacement with transition metals.

A potential material that can be utilized as TWC is a perovskite-type mixed oxide with general formula ABO_3, which has been investigated by several researchers since the last

decade owing to their high thermal stability, better resistance against sintering and composition versatility that allows tuning their properties by partial substitution at the lattice sites. However, such bulk materials have been observed to undergo composition variations at the surface compared to the bulk. Surface being the site of interest for heterogeneous catalysts, it must therefore be investigated in details for getting an *in depth* understanding of such active materials. Furthermore, the precise evaluation of the surface properties and its dynamics under operating conditions also makes it possible to fine-tune the catalyst composition towards improved catalytic performances. Therefore, the objective of this thesis work is to investigate a Fe-based, PGM-free perovskite oxide based on $LaFeO_3$, from both the surface and bulk properties point of views by means of a smart combination of advanced characterization techniques. More precisely, the effects of perturbing the $LaFeO_3$ stoichiometry by La deficiency at A site and substitution at B site are investigated in details in the present work.

The approach involves relevant surface models of $LaFeO_3$ in the form of thin films keeping their properties similar to that of conventional powder catalysts. This is carried out mainly by maintaining polycrystalline nature of the thin films. Such model catalysts provide better surface to bulk ratios, less charging issues with various analytical methods and act as discrete model materials with control of the film thickness in the desired range. The validation of the model catalysts is done by direct comparison to that of similarly synthesized powder catalysts. The surface and bulk of the relevant models are investigated by combination of surface techniques like XPS, LEIS and ToF-SIMS together with bulk techniques like Raman and XRD. The different $LaFeO_3$ based catalysts are further studied under TWC relevant reactive conditions in *in situ/operando* modes to understand the surface/bulk dynamics by using *in situ* GI-XANES, NAP-XPS and/or *in situ/operando* Raman spectroscopy. This work focuses on not only investigating surface properties and reactivity of such bulk catalysts by combination of complementary surface and bulk techniques, but also the scope of each technique to characterize perovskite-type materials.

Contents

1 Literature review **1**
1.1 Perovskites and automobile-exhaust pollution . . . 1
1.1.1 Context of three-way catalysis in automobile engines . . . 1
1.1.2 Perovskite type-oxide . . . 4
1.1.3 Perovskites as TWC catalysts . . . 7
1.1.4 Choice of perovskite: $LaFeO_3$ . . . 10
1.2 Physicochemical properties of perovskites . . . 11
1.2.1 Surface analysis techniques (XPS, LEIS, ToF-SIMS) . . . 12
1.2.2 Perosvskite structure by Raman and XANES . . . 20
1.3 Towards advanced characterization of catalysts . . . 23
1.3.1 Model catalysts . . . 23
1.3.2 Metal-oxide thin films . . . 27
1.4 Conclusions and thesis outline . . . 32
1.5 References . . . 34

2 Experimental approach and techniques **43**
2.1 Synthesis protocol . . . 44
2.1.1 Thin film . . . 44
2.1.2 Powders . . . 46
2.2 Physico-chemical analytical techniques . . . 46
2.2.1 Surface sensitive analyses . . . 46
2.2.2 Bulk and/or surface sensitive analyses . . . 58
2.2.3 Bulk sensitive analyses . . . 61
2.2.4 Microscopic techniques . . . 64
2.3 References . . . 66

3 Thins films as relevant model materials **69**
3.1 Characterization of Si(100) substrate . . . 70
3.2 Thickness optimization of thin films . . . 73
3.3 Characteristics of $LaFeO_3$-based thin films of intermediate thickness (LFO:Si-100) . . . 76
3.3.1 Morphology . . . 76
3.3.2 Structural properties . . . 77
3.3.3 Surface properties . . . 79
3.3.4 Towards ultra-thin film of perovskite (LFO:Si-10) . . . 87
3.4 Direct comparison with conventional powder catalysts . . . 93
3.4.1 GI-XANES analysis at Fe K-edge . . . 94
3.4.2 Quasi-*in situ* XPS analysis . . . 95
3.5 Conclusions . . . 97
3.6 References . . . 99

4 $LaFeO_3$ *vs.* $La_{0.7}FeO_3$ using advanced methods **101**
4.1 Ex-situ analysis of $La_{0.7}FeO_3$ and $LaFeO_3$ thin films . . . 102
4.1.1 XPS . . . 102
4.1.2 Raman spectroscopy . . . 103
4.1.3 X-Ray absorption near-edge structure at Fe K-edge . . . 104
4.1.4 Surface analyses by LEIS and ToF-SIMS . . . 107
4.1.5 Morphology of the $La_{0.7}FeO_3$ thin film . . . 114
4.2 *In situ* analysis of $LaFeO_3$ and $La_{0.7}FeO_3$ thin films under CO . . . 115
4.2.1 NAP-XPS investigation of $LaFeO_3$ vs. $La_{0.7}FeO_3$ thin films . . . 115
4.2.2 *In situ* GI-XANES analysis of $LaFeO_3$ vs. $La_{0.7}FeO_3$ thin films at Fe K-edge . . . 131
4.2.3 Discussion . . . 138
4.3 Conclusions . . . 144
4.4 References . . . 145

5 $La_{0.7}Fe_{0.8}Mn_{0.2}O_3$ and $La_{0.7}Fe_{0.8}Cu_{0.2}O_3$ **149**
5.1 B-site substituted $LaFeO_3$ by Cu ($La_{0.7}Fe_{0.8}Cu_{0.2}O_3$) . . . 150
5.1.1 Physicochemical characterization of $La_{0.7}Fe_{0.8}Cu_{0.2}O_3$ . . . 150
5.1.2 *In situ/operando* Raman analysis of $La_{0.7}Fe_{0.8}Cu_{0.2}O_3$ . . . 153
5.1.3 Quasi-*In situ* XPS analysis of $La_{0.7}Fe_{0.8}Cu_{0.2}O_3$ . . . 159
5.2 B-site substituted $LaFeO_3$ by Mn ($La_{0.7}Fe_{0.8}Mn_{0.2}O_3$) . . . 162
5.2.1 Physicochemical characterization of $La_{0.7}Fe_{0.8}Mn_{0.2}O_3$ . . . 162
5.2.2 *In situ/operando* Raman analysis of $La_{0.7}Fe_{0.8}Mn_{0.2}O_3$ . . . 165
5.2.3 Quasi-*in situ* XPS analysis of $La_{0.7}Fe_{0.8}Mn_{0.2}O_3$ . . . 171
5.3 Comparison of $La_{0.7}Fe_{0.8}Cu_{0.2}O_3$ and $La_{0.7}Fe_{0.8}Mn_{0.2}O_3$ with respect to their catalytic operating modes . . . 173
5.4 Conclusions . . . 177
5.5 References . . . 178

General Conclusions and Perspectives **181**

Chapter 1

Literature review

1.1 Perovskites and automobile-exhaust pollution

1.1.1 Context of three-way catalysis in automobile engines

With rising concerns about air pollution and the environment, stricter emission standards for automobile vehicles are being initiated worldwide to ameliorate the air quality. Likewise, European emission standards state strict limits for exhaust emissions that all new vehicles must abide with. Such legislation have come into action since 1992 with Euro 1 while Euro 6 was the previous stage introduced in September 2014 [1]. It is believed that more stringent limits are likely to be enforced for Euro 7 in 2020, particularly in terms of reduction in the CO_2 production. To this end, gasoline-based automobile vehicles have been installed with catalytic converters, developed and patented by the French chemical engineer Eugene Houdry in the United States. Since the 1970s, these have been installed at the engine tailpipes to remove the most hazardous gases produced in the automotive exhaust.

The chief pollutants formed by gasoline combustion engines are carbon monoxide (CO) and unburnt hydrocarbons (HC) caused by incomplete combustion of the fuel together with nitrogen oxides (NO_x) formed by the thermal fixation of nitrogen from air at very high temperatures during the course of the combustion process. Their release into the atmosphere is evaded by three way catalyst (TWC) installed within the catalytic converter, which plays the simultaneous role of oxidizing the CO and HC into carbon dioxide and water and reducing the NO_x into molecular nitrogen via a redox process. The major reactions taking place during three-way catalysis are presented below [2]:

Oxidation reactions:

$$2\,CO + O_2 \rightarrow 2\,CO_2 \tag{1.1}$$

$$C_nH_{2n} + \frac{3}{2}n\,O_2 \rightarrow n\,CO_2 + n\,H_2O \tag{1.2}$$

NO-reduction reactions:

$$2\,CO + 2\,NO \rightarrow 2\,CO_2 + N_2 \tag{1.3}$$

$$C_nH_{2n} + 3n\,NO \rightarrow n\,CO_2 + n\,H_2O + \frac{3}{2}n\,N_2 \tag{1.4}$$

$$2H_2 + 2NO \rightarrow 2H_2O + N_2 \tag{1.5}$$

In reaction 1.5, hydrogen is produced by side reactions like the water gas shift reaction between CO and H_2O and the steam reforming reaction of hydrocarbons and water to form H_2 and CO_2. The presence of hydrogen may assist in the reduction process, however, excess of it can result in undesirable ammonia production.

A heat engine undergoes combustion using fuel and oxygen from air and thereby their relative quantities play an important role in the distribution of exhaust gas composition. This is given by the air/fuel ratio (AFR) in a running engine defined as,

$$\text{AFR} = \frac{\text{mass of air}}{\text{mass of fuel}} \tag{1.6}$$

According to Fig.1.1, the maximum removal of the main pollutants is ensured at the stoichiometric AFR, marked by the dotted zone. For a gasoline and diesel powered engine, the stoichiometric AFR value is 14.7:1 and 14.5:1, respectively. Conversion above 95% is possible only within a narrow window of operation where the AFR is controlled accurately. However, there are always small fluctuations originating from the time required for the composition adjustments, making the air-fuel control system quite transient in nature [3].

In reality, automobile engines do not work exactly at the stoichiometric AFR. The ratio between the actual and the stoichiometric AFR is called lambda (λ) as given by,

$$\lambda = \frac{\text{actual AFR}}{\text{stoichiometric AFR}} \tag{1.7}$$

When the AFR is higher than this stoichiometric value, it is referred to as a lean mixture,

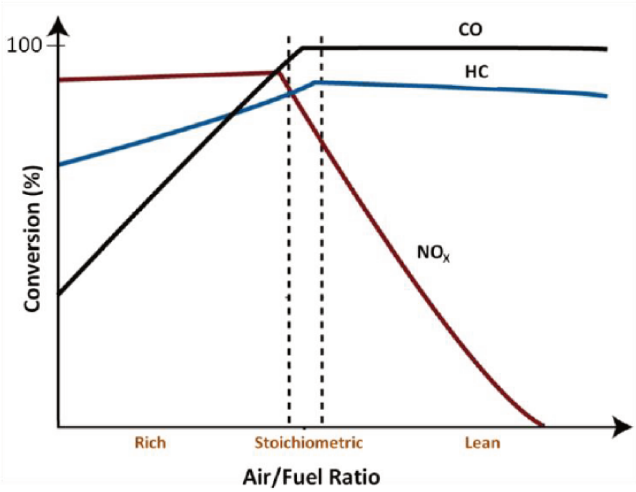

Figure 1.1: Variation of conversion of CO, HC and NO pollutants with the air/fuel ratio (AFR) in catalytic converters [4].

whereas when it is lower, it is called a rich mixture. Therefore, for a stoichiometric mixture λ=1, lean mixture λ <1 and for rich mixtures λ >1. This efficiency is controlled by utilizing a Lambda (λ) sensor at the inlet and outlet of the converter that measures the oxygen present in the exhaust and governs the fuel and air injection like a feedback-system [5]. A catalytic converter is shaped like a cylinder placed at the end of the engine enclosed in a stainless steel body comprising of three main components, the substrate, wash-coat and noble metals, as shown in Fig.1.2. The substrate acts as the internal structure, which is generally based on honeycomb-type ceramic monolith, foam or a metallic type substrate. The wash-coat, composed of high surface area oxides, is coated over the substrate while acting as a support for the active phase.

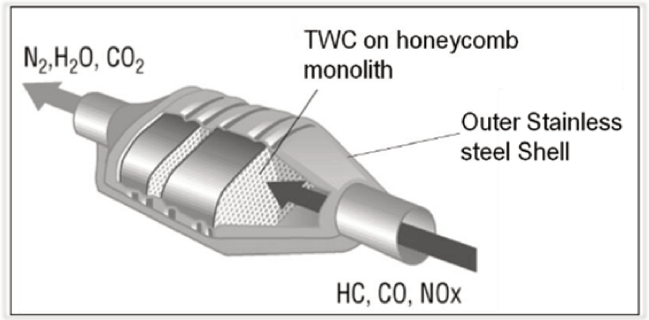

Figure 1.2: A scheme of a TWC catalytic converter [6].

The catalysts presently used for the TWC application are based on noble metals such as platinum, palladium and rhodium, often referred to as Platinum group metals or PGMs, supported over common oxide supports to increase their dispersion over high specific

surface area materials such as alumina, ceria, zirconia etc. Platinum and palladium are known to catalyze the oxidation reaction possessing intrinsic reactivity, robustness and thermal stability as necessary for automotive applications. On the other hand, rhodium is active for NOx reduction with an ability of reaching decent NOx conversions at stoichiometric and near-stoichiometric regimes while maintaining a lower selectivity towards ammonia formation [7]. The wide utilization of PGMs in the catalytic converters makes the entire system not only expensive but also one of the main industrial consumers of such critical raw materials. In fact, more than 50% of the world's platinum is required by the automobile industry [8]. Hence, it becomes imperative to reduce the amounts of PGMs, especially platinum, in order to bring down the cost and anticipate the potential scarcity of such precious metals.

Moreover, under working conditions the catalytic converter containing the TWC, which is placed close to the engine, can reach very high temperatures of up to 1000°C. Such harsh operating conditions make the catalyst vulnerable to sintering of the noble metal nanoparticles and/or their diffusion into the support as the catalyst ages, leading to its deactivation [9]. This leads to the necessity of scientific attention on not only reduction of the actual amount of PGMs used in such systems, but also enhance their catalytic lives by replacing, at least partially, with more enduring catalytic systems, such as a perovskite-type mixed oxide, with none or least amount of PGMs content.

1.1.2 Perovskite type-oxide

Perovskites are mixed oxides with a general formula of ABO_3, where the larger cation A is coordinated to 12 oxygen atoms and the smaller cation B takes the octahedral sites in the lattice framework, as shown in Fig.1.3. A mixed oxide can have a perovskite structure when the Goldschmidt tolerance factor (t) as given below, lies between 0.8 and 1 [10],

$$t = \frac{r_A + r_O}{\sqrt{2}(r_B + r_O)} \tag{1.8}$$

where the radii of A is r_A, B is r_B and that of the oxygen ion is r_O.

The archetipal perovskites have a cubic structure with t=1. On the other hand, lower t values lead to distorted structures with orthorhombic, rhombohedral or tetragonal symmetry. The A-cation is usually a rare earth, alkaline earth or alkali metal element like La, Sm, Pr, Ba, Ca, Sr, Na or K, while the B-site mostly comprises of a transition metal cation.

Hence, a perovskite can comprise of several elemental combinations at the A and B-sites by partial substitutions at each site, which permits to control the oxidation states of the cations and formation of ionic vacancies. This allows adjusting the surface composition as well as redox properties of the perovskite, ultimately determining their catalytic properties [11]. Thus, with the advantage of an easy-to-tune composition, perovskites embed an array of various catalytic as well as non-catalytic properties and are nowadays found in numerous applications (fuel cells, batteries, gas sensors, semiconductor industries etc.). Additionally, the formation of a perovskite structure helps to increase the thermal stability of the transition metal oxides [12].

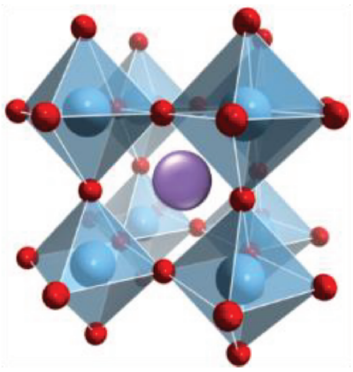

Figure 1.3: Structure of a perovskite: the A-site is represented by violet, B-site by blue and O atoms by red spheres [13].

Furthermore, the interest towards perovskites for their application in TWC rose immensely with the discovery of their self-regenerating property by Nishihata *et al* [14]. In their study on Pd-doped perovskite, $LaFe_{0.57}Co_{0.38}Pd_{0.05}O_3$, it was determined by X-ray diffraction and absorption spectroscopy that the palladium oscillated between the perovskite lattice under oxidative conditions, and out of the lattice as Pd^0 under reducing conditions throughout the redox fluctuations, typically existing in the exhaust gas as described in Fig.1.4.

This periodic reversible movement of the noble metals depending on the atmosphere encountered by the catalyst could prolong retention of the high dispersion of active phases over time, overcoming deactivation by sintering. Therefore, slowing down the progressive deactivation as the catalyst ages, unlike a conventional catalysts e.g. Pd/Al_2O_3, which tend to agglomerate much faster under the classic automotive environments [15], as presented in Fig.1.5. Thus, perovskite type-oxides came to be known as “intelligent” catalysts contributing to the process of self regeneration by forming a solid solution between the

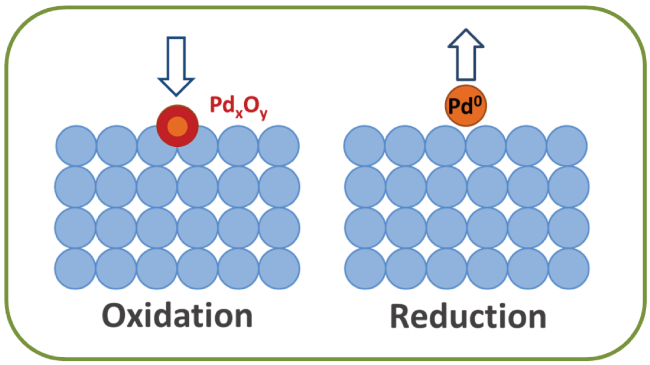

Figure 1.4: A scheme showing the self-regenerating phenomenon in $LaFe_{0.57}Co_{0.38}Pd_{0.05}O_3$ perovskite during redox cycling.

noble metals and the oxide with a much improved thermal resistance [15, 16].

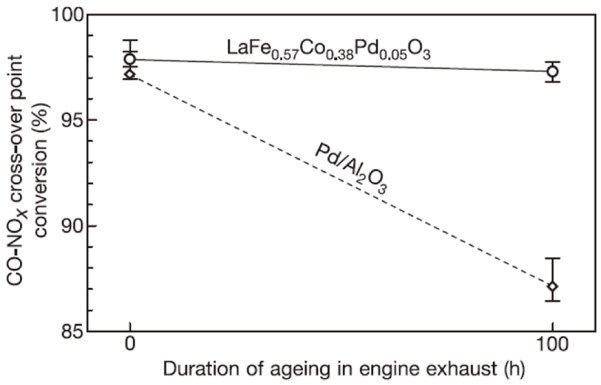

Figure 1.5: Change in activity of catalysts during aging for a perovskite (prolonged activity) compared to a conventional TWC catalyst (faster deactivation) [14].

Some researchers have begun to investigate the scope of this self-regenerative phenomenon further. As an example, microscopy techniques like STEM were employed to study epitaxially grown films of Pd-doped $LaFeO_3$ under redox conditions. The authors stated that the extent to which the Pd dissolution occurred was limited [17] and the reversible movement was evidenced mostly in the bulk of the perovskite and not available to the catalytic reaction at the surface to the same extent. However, they evidenced that the Pd particles strongly interacted with the lattice after the oxidation step.

In another study by the same group on Pt-doped $CaTiO_3$, they observed that after reduction, most of the Pt clusters on the surface tend to coarsen rather than precipitating back in the matrix during oxidation [18]. Even though these studies show that the novel phenomenon may occur only up to a small extent, but in all cases, a strong interaction between the noble metals at the surface and host lattice is evident, as can be seen in Fig.1.6

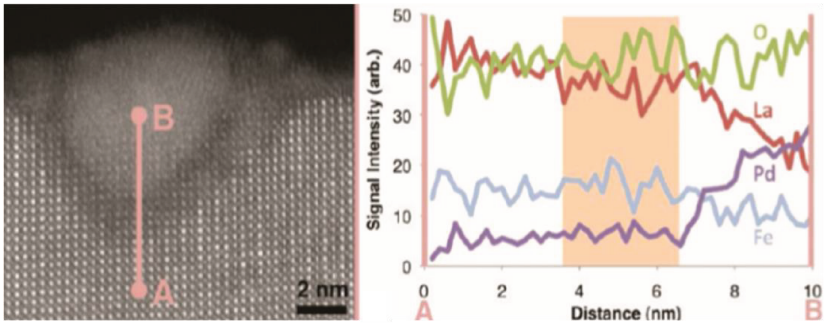

Figure 1.6: HAADF-STEM image of PdO nanoparticle strongly interacting with the host perovskite lattice (right) and an EELS line scan across AB (left) [17].

from the dark reaction zone from the HR-TEM image as well as the pink region (~2 nm) on the adjoining EELS image. This can help maintaining a steady catalytic activity by avoiding Pd agglomeration under realistic conditions. Interestingly, recently *in situ* STEM analysis of Rh-doped $CaTiO_3$ powder highlighted the self regeneration of Rh nanoparticles, which were rather clearly observed to appear on the surface under reducing conditions and revert to the as-received state under oxidizing atmosphere [19], as shown in Fig.1.7. Therefore, the extent of self-regeneration phenomenon may slightly differ from one perovskite to the other, but is overall beneficial as an intrinsic property of a perovskite oxide.

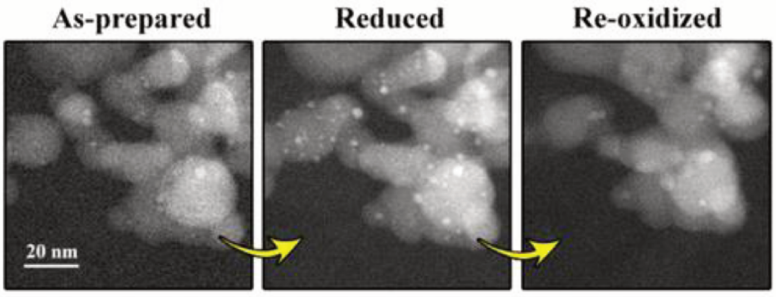

Figure 1.7: *In situ* STEM images of Rh-doped $CaTiO_3$ as-prepared, after reduction and after re-oxidation treatments at high temperature self explaining the self-regeneration process [19].

1.1.3 Perovskites as TWC catalysts

The intrinsic redox properties of perovskites make them suitable for application in catalysis. The nature of the B-site cations determines the key catalytic role of such bulk catalysts, while the A-site cation in a trivalent state plays almost no significant role as observed during CO and HC oxidation reactions shown in Fig.1.8 [20]. Likewise, in Fig.1.9 the La, Sm and Gd at A-site do not influence the rate of propane oxidation while change in the

B-site cation has a major influence, with Mn and Co being the most active [21]. Additionally, when the A cation is substituted by ions of a different valency, it can influence the catalytic activity by changing the valency of the B cation and/or the formation of oxygen vacancies [22]. For instance, a 20% substitution of La^{3+} by Sr^{2+} ions at the A-site in Lanthanum cobaltate increased the catalytic activity up to ten times, as shown in Fig.1.8.

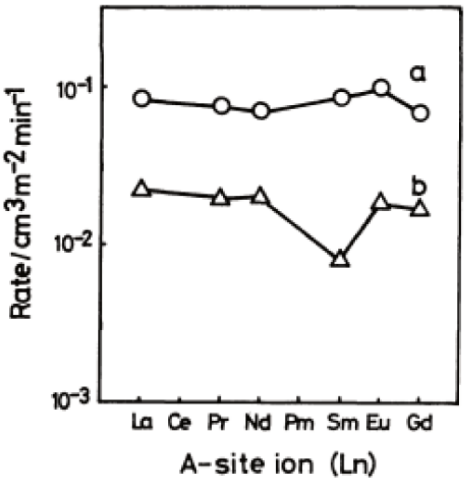

Figure 1.8: Catalytic activity of (a) Sr-substituted $Ln_{0.8}Sr_{0.2}CoO_3$ and (b) $LnCoO_3$ during propane oxidation reaction at 227°C, where Ln represents the A-site ion [20].

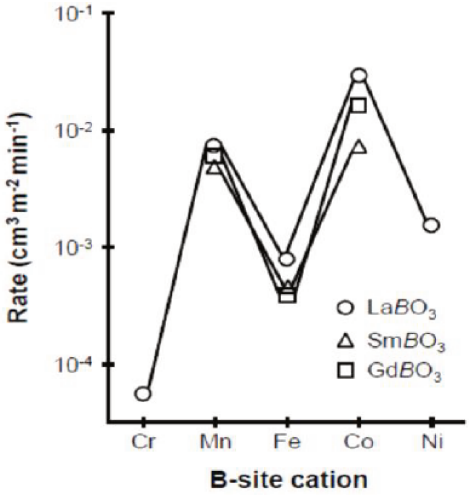

Figure 1.9: The effect of changing A and B-site cations of perovskites on propane oxidation reaction [22].

The conversion and selectivity are largely governed by the oxygen mobility and its storage capacity originating from the structural defects. Perovskites are known to adsorb large extent of oxygen and desorb two kinds of oxygen species namely, the α-oxygen and the β-oxygen [23]. The α-oxygen desorbs at lower temperature (<500°C), attributed

to the weakly bound O^-/O_2^- species formed during calcination on the transition metal sites of the perovskite surface. On the other hand, the β-oxygen desorption occurs at higher temperatures and originates from the bulk of the perovskite lattice. Their yield and desorption temperatures are dependent on the calcination temperature and are usually characterized by temperature-programmed desorption (TPD) experiments. They further result in two different redox mechanisms for the catalytic reactions. In the suprafacial mechanism involving the α-oxygen, the reactant molecules are activated by providing an appropriate adsorption site, while the intrafacial mechanism involves the consumption of the β-oxygen from the bulk, which later gets replenished by adsorption, dissociation and finally the incorporation of gas phase oxygen atoms. The type of mechanism is determined mainly by the reaction temperature, as in case of oxidation of methane that occurs suprafacially below 800°C and above that, intrafacially [24]. CO oxidation follows a suprafacial mechanistic route, which occurs by the adsorption of CO species followed by its interaction with the adsorbed dissociated oxygen species [25]. Additionally, NO reduction follows an intrafacial pathway. NO adsorbs dissociatively onto an oxygen vacancy, then two adsorbed N-species combine to form a nitrogen molecule [26]. The oxygen vacancies are replenished by the reducing gases in the feed such as CO.

In spite of several benefits of perovskites for TWC application, there are few issues that must be addressed to make them most relevant in real catalytic conditions. They usually have low surface areas (<5 m^2g^{-1}) due to the high calcination temperatures of up to 1000°C required during preparation of such oxide phases. However, this drawback is addressed to a large extent by suitable synthesis methods and as high as 100 m^2g^{-1} of specific surface area has been achieved, for instance, by nano-casting approaches by infiltrating perovskite precursor solution into pores of a host material like SiO_2 [27, 28]. Also, perovskites generally have low tolerance to sulfur-based poisons, which tend to improve with noble metal substitution in the structure [29, 30]. Moreover, the operative window of PGMs-free perovskites is narrower and they are intrinsically less active as compared to the ones with PGMs [31]. In spite of the few hitches to be tackled, it is possible to successfully bring down the PGMs concentration to a large extent and thereby the overall cost. Henceforth, the perovskites have already been commercialized as a constituent of TWC in Japan in 2002, thanks to their self-regeneration abilities [32].

1.1.4 Choice of perovskite: $LaFeO_3$

Since the B-site cation determines the chief catalytic role in the perovskite oxide, its choice is most imperative. Transition metal cations at the B-site such as Cr, Mn, Fe, Co and Ni can form the correct perovskite structure. However, the ones containing Cr, Co and Ni pose a threat to the environment since they are toxic and their usage must be avoided [32–34]. Although among the rest, Mn-based perovskites show best oxidation properties in CO and HC oxidation, the $LaFeO_3$ and other substituted ferrites are highly investigated due to their widespread availability and low cost of the iron precursors. Likewise, the $LaFeO_3$ has been chosen as the base perovskite by the PARTIAL-PGMs consortium as one of the materials of interest for further investigation. Thereby, lanthanum orthoferrite perovskite is the targeted material to be investigated for this thesis work.

Previous studies on $LaFeO_3$ by Schoen *et al* [35] have shown that the stoichiometric composition features a higher surface La/Fe ratio compared to the bulk ratio of 1, as evidenced by XPS analysis. This enrichment of lanthanum is often observed in Lanthanum based oxides due to their high reactivity under air to form surface lanthanum hydroxides and/or carbonates [35, 36]. On reducing the content of La in the non-stoichiometric form $La_{1-x}FeO_3$ (x=0, 0.1, 0.2, 0.33), the surface La/Fe ratio decreased to a value of 0.9 for x=0.33, as described in Table 1.1. The induced La-deficiency resulted in better catalytic activity not only in CO oxidation but also in NO reduction reactions, as presented by the decrease of the temperature of 50% conversion (T50) values in Table 1.2. The surface optimization by adjustment of the La/Fe ratio lead to higher accessibility of the active species of iron, thereby improving the CO as well as NO reactivity [35].

Table 1.1: Surface and bulk La/Fe ratios of $La_{1-y}FeO_3$ (y=0, 0.1, 0.2, 0.33) catalysts [35].

	La/Fe atomic ratio	
	XPS	ICP-AES
$LaFeO_3$	2.13	1.01
$La_{0.9}FeO_3$	1.64	n.a.
$La_{0.8}FeO_3$	1.31	n.a.
$La_{0.67}FeO_3$	0.88	0.66

The H_2-temperature programmed reduction (TPR) revealed the existence of additional hematite (Fe_2O_3) in strong interaction with the perovskite structure, formed as a result of the La-deficient composition. To ensure whether the enhancement in the activity was brought upon by this hematite phase, the $La_{1-x}FeO_3$ series were compared with that of a

Table 1.2: Temperatures of 50% conversion of the different gases in the exhaust feed for $La_{1-y}FeO_3$ catalysts (y=0, 0.1, 0.2, 0.33), hematite and a mechanical mixture of $LaFeO_3$ and hematite [35].

Condition	Stoichiometric				Rich
T_{50} (°C)	CO	C_3H_6	C_3H_8	H_2	NO
$LaFeO_3$	438	463	478	501	–
$La_{0.9}FeO_3$	386	443	467	439	510
$La_{0.8}FeO_3$	398	431	499	433	488
$La_{0.67}FeO_3$	384	420	497	471	479
Fe_2O_3	459	490	–	493	–
$Fe_2O_3 + LaFeO_3$	436	465	486	482	–

mechanical mixture of Fe_2O_3 and $LaFeO_3$ as well as the hematite alone. The CO conversion remained similar to that of the stoichiometric $LaFeO_3$ without any NO conversion in both cases (Table 2). Furthermore, an *in situ* Raman investigation on the stoichiometric ($LaFeO_3$) and La-deficient ferrite ($La_{0.7}FeO_3$) under cycles of air, moisture, CO and NO highlighted the reversible formation of an iron oxide nano-phase only at the surface of the La-deficient composition during treatment under oxidizing conditions [37]. This nano-phase strongly interacting with the perovskite was postulated to be the reason behind the improved catalytic activity in the La-deficient perovskite, in line with the study by Schoen *et al* [35].

Additionally, recent studies on $LaFeO_3$ based catalysts showed better activity in CO and propane oxidation on partial substitution of the La-deficient perovskite with Cu at the B-site [38]. Recent results also highlighted that part of the substituted copper existed as CuO, well dispersed on the perovskite surface [39]. Further, the NO reduction was enhanced by doping with Rh nanoparticles. This catalyst was compared to a commercial reference catalyst containing Pd and Rh, which resulted in higher NO conversion with lower ammonia production [40].

1.2 Physicochemical properties of perovskites

The scopes of characterizing the inherent properties of lanthanum ferrite and related perovskites by surface analysis techniques like LEIS, ToF-SIMS and XPS have been discussed in this section. The importance of applying these surface-sensitive techniques to such bulk catalysts has been highlighted through various examples. Finally, the aspects of bulk characterization techniques such as Raman and XANES have also been mentioned. More

details about the principles of each technique will be discussed later in Chapter 2.

1.2.1 Surface analysis techniques (XPS, LEIS, ToF-SIMS)

Low energy ion scattering spectroscopy (LEIS): It stands as a powerful tool when it comes to characterization of heterogeneous catalysts due to its extreme surface sensitivity to the very first atomic layer. Both bulk as well as supported catalysts have been studied using this technique. LEIS can be used to quantify the surface elemental composition as well as achieve information from sub-surface layers (<10 nm) relevant for dispersion of the active phase [41]. In addition, good quality spectra under static conditions (ionic dose less than 1% of a monolayer) can be recorded within short time periods (~60 s) with high sensitivity and specificity for different elements. This analytical method has been widely used to study perovskite-type materials to highlight some of their important features. In the field of fuel cell materials, it was observed by LEIS in a condensed pellet of $La_{0.6}Sr_{0.4}Fe_{0.8}Co_{0.2}O_3$ that the larger A-site cation (Sr) segregates and dominates the surface leaving a B-rich zone just beneath the surface as shown in Fig.1.10.

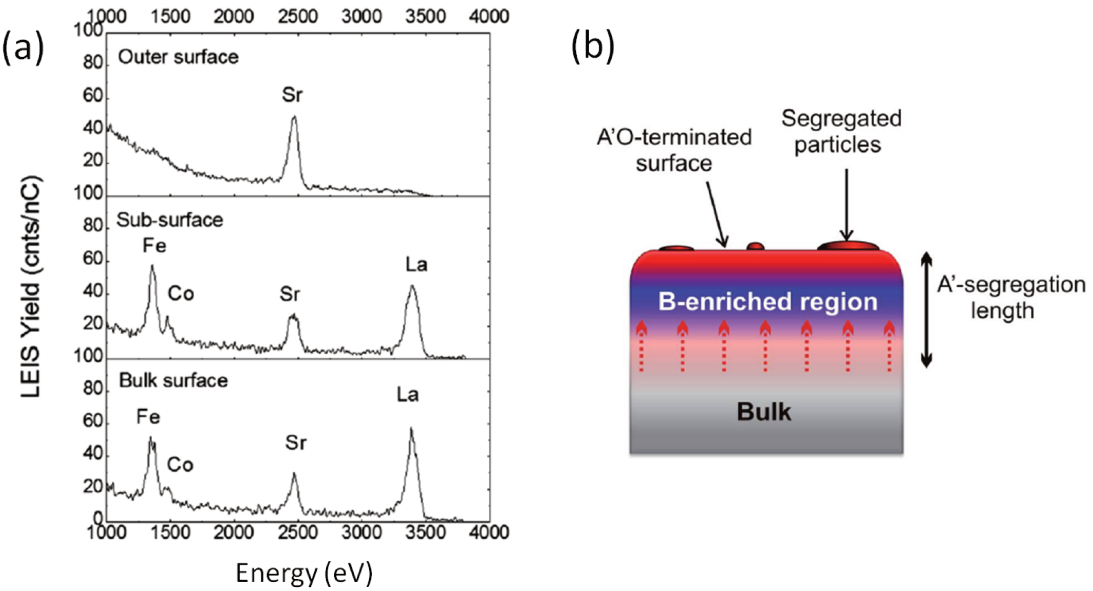

Figure 1.10: (a) LEIS $^{20}Ne^{+}$ spectra of $La_{0.6}Sr_{0.4}Fe_{0.8}Co_{0.2}O_3$ perovskite of its outermost surface, sub-surface and bulk composition, and (b) a scheme representing the variations in composition at the perovskite surface [42].

The perovskite presents an A-site (Sr) domination on the outermost surface with almost no signal from the transition metal cation (Fe). Such A-site segregation or enrichment has been observed for several perovskites, where the segregation is more enhanced

for a A substituent such as the Sr here. After light sputtering ($^{40}Ar^{+}$ at 500 eV), the sub-surface beneath was revealed with clear appearance of the B-site signal. Finally, with prolonged sputtering bulk composition is reached representing the bulk stoichiometry. The intensity of the Fe peak is slightly decreased in the bulk compared to the sub-surface [42]. This signifies a B-enriched region in the sub-surface of the perovskite. Such segregation in perovskites is considered to be caused by the existence of surface charges caused by charge mismatch of $A^{3+}O^{2-}$ and $B^{3+}O_2^{2-}$ planes in $A^{3+}B^{3+}O_3^{2-}$ perovskites in the form of secondary phases such as oxides, hydroxides or carbonates of A cation at the surface [43]. Further, Ding *et al.* and Lee *et al.* [44, 45] have also identified cation size mismatch causing strain in the lattice, as another driving force for the surface reconstruction. The A-enrichment further gives rise to the B-rich zone or in other words, an A-depleted region just underneath the outer surface. Such observations in perovskite oxides were also reported by other authors for $La_{0.65}Sr_{0.35}FeO_3$, $SrTiO_3$ and $BaTiO_3$ [46–48].

This surface segregation is also seen in related mixed oxide phases such as Ruddlesden-Popper (A_2BO_4) and double perovskite phases ($AA'B_2O_5$) and can be considered as a general trend of such materials [42]. It is therefore imperative to understand the occurrence and extent of such segregation or enrichment in a perovskite to predict if such surface phenomena may affect catalysis by, for instance, blocking the active sites.

Moreover, the actual reaction conditions under high temperature can cause the surface characteristics to change further. Blanck *et al.* [37] observed that the relative intensity of La and Fe LEIS signals for $La_{0.7}FeO_3$ catalysts strongly changed after successive exposures of CO followed by NO as shown in Fig.1.11, which was explained by the mobility of the segregated iron oxide species during the reaction at higher temperatures.

Time-of-flight secondary ion mass spectrometry (ToF-SIMS): It provides elemental and molecular information from ~1 nm of the top surface by mass spectrometric detection of the secondary ions generated from ion bombardment, with excellent detection limits (ppm-ppb) even for light elements. It can in addition provide spatial images (lateral resolution of ≃100 nm) as well as depth profiling information by combining a second sputter gun. ToF-SIMS is widely used in the field of electrochemistry, where perovskites are frequently used as materials for energy storage and conversion [49]. It is also gradually standing out as an effective method for surface sensitive analysis of catalysts [48, 50, 51]. Several perovskite-based materials have been studied by ToF-SIMS in

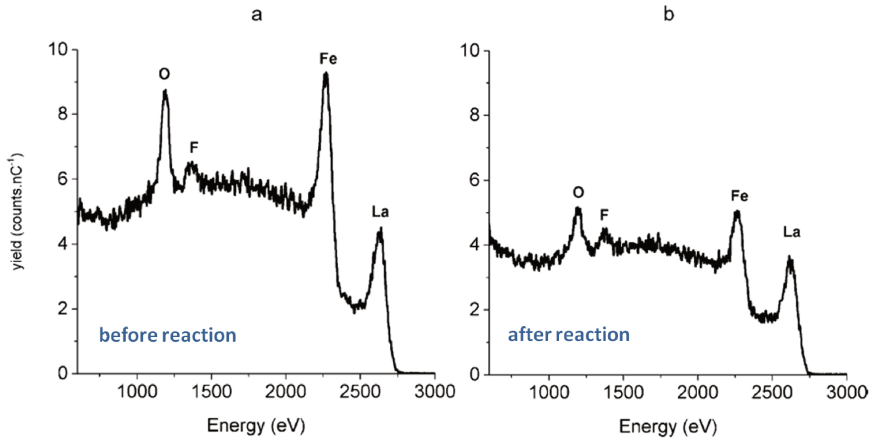

Figure 1.11: LEIS ($^4He^+$ at 3 keV) spectra of $La_{0.7}FeO_3$ catalyst (a) before and (b) after successive CO followed by NO exposures [37].

catalysis to examine surface reconstruction of the surface of a perovskite, study reaction-induced surface modifications as well as determine the poisoning effects in catalytic reactions [52–54]. Fe-substituted perovskites of the composition $LaCo_{1-x}Fe_xO_3$ were investigated by Wu *et al* [55] as N_2O decomposition catalysts. Mixed-oxide clusters were detected, *e.g.* $La_3CoFeO_6^+$, which confirmed the co-existence of the Fe and Co at the B-site of the perovskite lattice on the topmost surface of the catalyst. In another study, Kocemba *et al* [56] investigated that the catalytic activity of $Pt/BaSnO_3$ catalyst for CO + H_2 oxidation was determined by the strong chemical interaction between the Pt and the perovskite forming a bimetallic phase as revealed by ToF-SIMS analysis due to the presence of mixed oxide ionic fragments such as $BaPtO_3^+$ and $PtSnO^+$. In fact, the emitted positive or negative secondary ions are representative of the chemical composition of the surface of catalysts. Most reports indicate that the secondary ions detected by ToF-SIMS are generated from direct emission of ions with characteristic composition of the catalysts and not merely produced by a recombination process of the secondary ions [57–59].

Furthermore, depth profiling analysis by ToF-SIMS can elucidate surface anomalies such as surface segregation or enrichment on sample. Lee *et al.* [60] made depth profiling measurements on epitaxially grown thin films showing lower extent of Sr-segregation in $La_{0.6}Sr_{0.4}CoO_3$ film compared to polycrystalline thin films. The presense of grain boundaries were stated to facilitate transport of the segregating atoms thereby showing more extended surface segregation than single crystals [61, 62]. Such surface segregation can lead to lower catalytic activity for oxygen reduction in case of thin film-based electrodes [63]. The depth profile shown in Fig.1.12 displays the abundance of Sr^+ and Co^+ com-

pared to the bulk in $La_{0.6}Sr_{0.4}CoO_3$ perovskite.

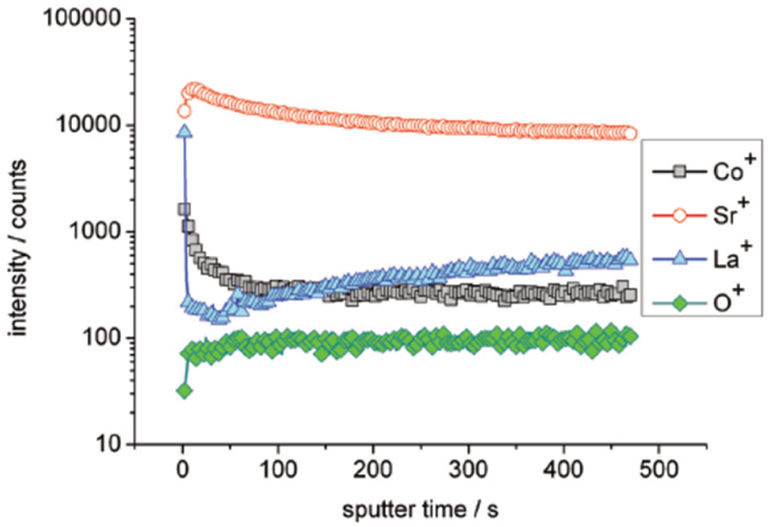

Figure 1.12: Depth profiling (0.5 keV, O_2^+) by ToF-SIMS in positive mode (25 keV, Bi_3^+) for $La_{0.6}Sr_{0.4}CoO_3$ perovskite [62].

Similarly, Co and La surface enrichment in $LaCoO_3$ cathode presented a detrimental effect on its performance [64]. The Co enrichment has been presented by ToF-SIMS mapping in Fig.1.13. In another study, B-site segregation as Co_3O_4 in $LaCo_{1-x}Fe_xO_3$ catalyst seemed to inhibit N_2O decomposition reaction [55, 64].

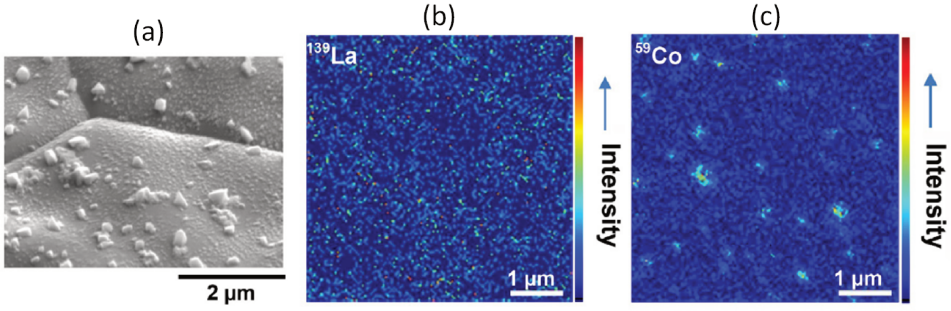

Figure 1.13: (a) Electron image, (b) La and (c) Co ToF-SIMS images of the $LaCoO_3$ cathode representing surface segregation of B-site Co species [64].

In addition, ToF-SIMS was used to examine the surface composition of fresh and aged commercial TWC catalyts, which highlighted the effect of poisoning elements like S, Ca and Pb originating from the fuel and lubricating oils within the automotive exhaust system, proportional the distance traveled [65]. The Ca and Pb containing ionic fragments have been shown in Fig.1.14. Thereby, ToF-SIMS analysis can provide a variety of surface oriented information regarding a catalyst with higher surface and elemental sensitivities, which could get blurred when analyzed by XPS with a higher analysis depth (~5-10 nm)

[66].

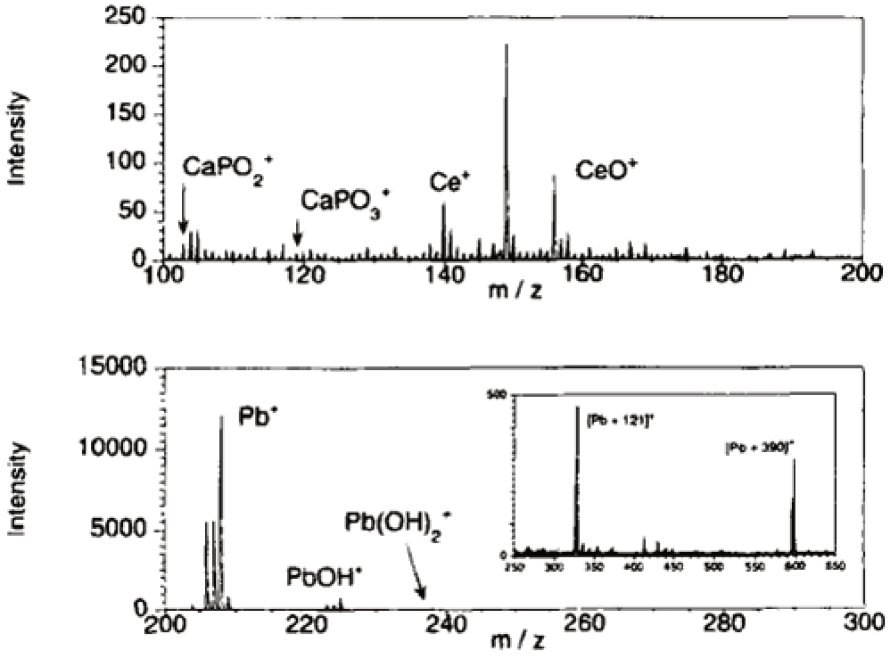

Figure 1.14: Positive ToF-SIMS mass spectra obtained from a vehicle-aged alumina-ceria based commercial TWC [65].

X-ray photoelectron spectroscopy (XPS): It is one of the most common techniques to characterize the surface chemistry of catalysts to measure the elemental composition, ratios as well as the chemical states from the top <10 nm of the material. Most studies relevant to perovskites use XPS to determine their surface composition and oxidation states of the constituent ions. In case of $LaFeO_3$ perovskite, both La and Fe exist in the 3+ oxidation state. The La is mostly studied using the La 3d orbital due to its higher photoemission cross section. The La 3d photopeak displays two visible components from spin-orbit coupling, $3d_{3/2}$ and $3d_{5/2}$, which further split due to multiplet splitting. The complex peak structure of the La spectrum is a result of charge transfer from the valence band of the ligand atom to the 4f orbital of the ionized core of La [67]. A typical example of a La 3d photopeak from $LaFeO_3$ is shown in Fig.1.15.

The binding energy of La 3d lies between 834.0-835.0 eV depending on the type of the La compounds. The magnitude as well as the intensity of the multiplet splitting components are dependent on the chemistry of the La-based compounds. As presented in Fig.1.16, La_2O_3, $La(OH)_3$ and $La_2(CO_3)_3$ have different magnitudes of the splitting as well as distinct shapes. However, the assignment of such chemistry is always ambiguous owing to the highly reactive nature of lanthanum-based compounds, which may hydrolyze

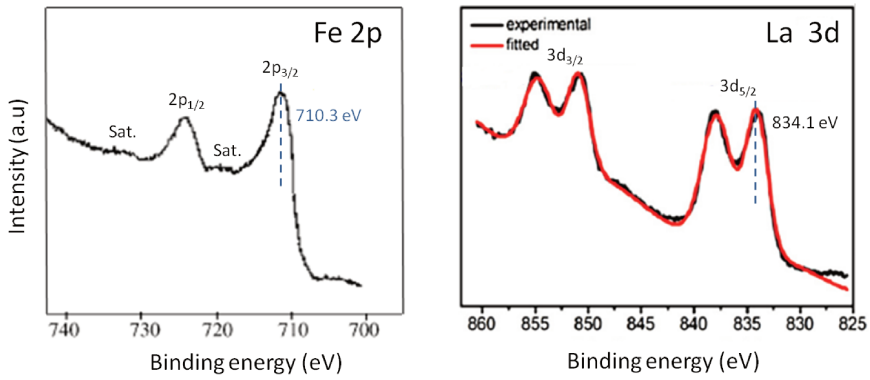

Figure 1.15: XPS spectra of $LaFeO_3$: Fe 2p and La 3d photopeaks featuring a 3+ oxidation state for both [68, 69].

to form $La(OH)_3$ or react with CO_2 to form surface carbonates. To this end, a reliable spectrum of lanthanum oxide for example, can be achieved by performing a high temperature oxidation treatment under *in situ* conditions to remove surface contaminants. However, the analysis of $La(OH)_3$ or even La-based mixed oxides without any pre-treatment can be tricky due to the inevitable presence of surface lanthanum carbonates. The La 3d photopeak overlaps with the La MNN Auger signal when Al Kα source is used, as displayed in Fig.1.17. This overlapping can be removed by subtraction of La MNN peak from La 3d or by only considering the half orbital (La $3d_{5/2}$), which has almost no interference with this Auger signal [67].

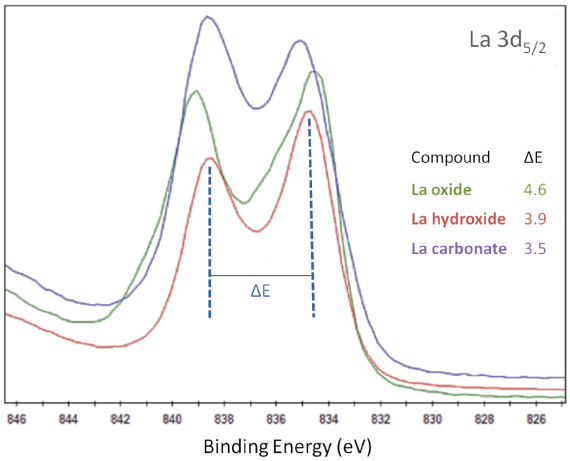

Figure 1.16: XPS La $3d_{5/2}$ spectra of different La compounds featuring differences in position, mutiplet splitting shape and magnitude [70].

In case of iron, the 2p orbital is the most commonly investigated orbital owing to its higher cross section. Fe 2p photopeak (Fig.1.15) presents a significant spin-orbit coupling with an energy separation of 13.1 eV. The binding energy of the Fe 2p orbital depends on

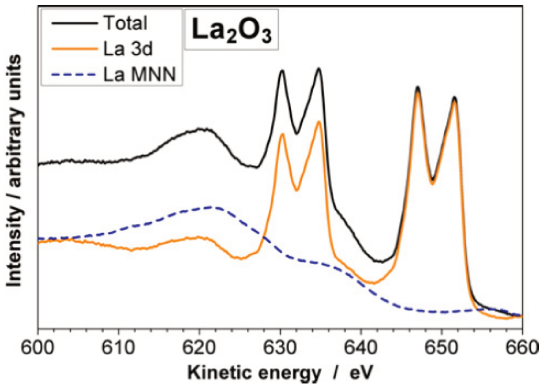

Figure 1.17: XPS La 3d spectrum with contribution from La MNN region for La_2O_3 [67].

the chemical state as well as the ligand nature. For instance, Fe 2p photopeak shows a binding energy of 709.6 eV in FeO and 710.4 eV in $FeCl_2$, both being Fe^{2+}. The different valence states and ligand nature are relatively easier to be predicted thanks to the shape and position of the satellite feature of Fe 2p. Fe^{3+} (Fe_2O_3) has a satellite feature around 8 eV higher, while Fe^{2+} (FeO) satellite feature is located 6 eV higher compared to the binding energy of the main Fe $2p_{3/2}$ peak [71]. Biesinger *et al.* [72] presents detailed multiplet splitting fitting parameters of reference Fe-based compounds.

The O 1s spectrum in case of perovskites is mostly composed of three components, as shown in Fig.1.18: the signal from the lattice oxygen (β-oxygen) lying between 529.4 and 530.1 eV, the thermodynamically stable O^-/O^{2-} surface oxygen species (α-oxygen), defects in oxides and hydroxides between 531.2 and 531.8 eV and other adsorbed surface contaminants like carbonates, organic oxygen or adsorbed water located at higher binding energies (>532 eV) [72–74]. The α-oxygen species, often called chemisorbed oxygen, may not always be seen directly as it may be hidden under the contribution from surface adsorbates such as the hydroxides. However, its contribution may be clearly seen on a pure perovskite surface for example after heating under oxidative conditions to remove the surface adsorbates.

The binding energy values of La 3d, Fe 2p and O 1s photopeaks for $LaFeO_3$ perovskite, as stated by several authors have been listed in Table 1.3 with their charge referencing values and synthesis methods.

The position of La 3d lies between 833.5 and 834.7 eV, while for Fe 2p between 709.8 and 710.6 eV. It is evident from these enlisted values that the binding energy of this mixed oxide phase is usually lower than that of the single oxide phase of Fe_2O_3 (Fe 2p at 710.9 eV) probably due to the difference in electron density around Fe in the mixed oxide phase

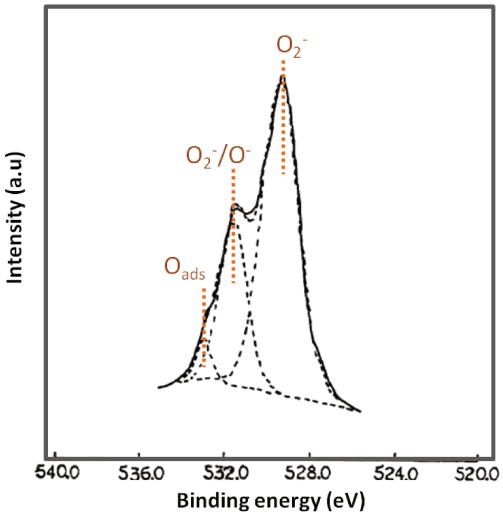

Figure 1.18: XPS O 1s spectrum of $LaFeO_3$ showing the different oxygen components [73, 74].

Table 1.3: Binding energy values of core level spectra for $LaFeO_3$ from literature with their synthesis methods and charge correction values [68, 75–83].

S.No.	Synthesis method	$LaFeO_3$			Charge correction with C 1s (eV)	Reference
		La $3d_{5/2}$ (eV)	Fe $2p_{3/2}$ (eV)	O 1s (eV)		
1	Citrate sol-gel	833.5	710.2	529.4	285.0	[74]
2	Electrospinning	834.7	709.8	528.8	284.5	[75]
3	Hydrothermal	834.3	710.2	528.3	284.6	[76]
4	Hydrothermal	834.4	710.6	530.0	284.6	[77]
5	Ultrasonic spray pyrolysis	834.1	710.5	529.3	284.8	[67]
6	Combustion	-	710.5	529.4	284.8	[78]
7	Polymerized complexation	833.5	709.9	529.1	-	[79]
8	Pecini	834.0	710.2	529.0	284.8	[80]
9	Self-combustion	833.8	710.1	529.1	285.0	[81]
10	Conventional Citrate	833.8	710.2	529.1	285.0	[82]

[71, 79]. Most articles related to $LaFeO_3$ present data related to the lattice oxygen only in its as-received state due to the feasibility and therefore only lattice oxygen values have been listed in the table.

The above example show the extent of different range of surface related information that can be obtained by XPS, LEIS and ToF-SIMS that can together provide a more complete picture of the surface characteristics of the bulk material. For deeper insights, the comparison of the general attributes of the three techniques have been enlisted in Ta-

ble 1.4 highlighting the type of possible data collection, resolution and detection limits of each [66, 84].

Table 1.4: Comparison of key properties and scope of the surface analysis techniques : XPS, LEIS and ToF-SIMS [66].

Properties	LEIS	ToF-SIMS	XPS
Surface sensitivity	Outermost atomic layer	A few atomic layers	*ca.* 10 nm
Static depth profiling	Inherent, *ca.* 10 nm	No	If multiple scans taken at multiple angles (angle resolved XPS), *ca.* 5 nm
Dynamic depth profiling	With sputter gun	With sputter gun	With sputter gun
Analysis time per spectrum	Typically minutes	Typically minutes	Somewhat longer
Detection limits	A few % of a monolayer for the lighter elements, up to 0.1–1% for the heavier elements	ppm	0.1–1% of a monolayer
Matrix effect	Essentially none	Strong	Essentially none
Quantitative results	Excellent	Relatively poor	Very good
Oxidation state information	None	Somewhat, through molecular fragments	Yes
Molecular information	None	Yes, through molecular fragments	Yes, through chemical shifts
Lateral resolution	*ca.* 100 microns	Submicron	*ca.* 10 microns

1.2.2 Perosvskite structure by Raman and XANES

Raman spectroscopy is an useful technique to investigate the structure, average lattice and phase transitions of a material. Owing to its high sensitivity towards structural distortion and oxygen motions, it can be used to determine the structure and phase of a multi-oxide system. Perovskite-based oxides have been moderately studied by Raman spectroscopy. The spectrum is highly sensitive to the type of B-site substitution that brings upon any structural distortions, as represented in Fig.1.19, where $LaFeO_3$, $LaMnO_3$ and $LaCoO_3$ have different Raman signatures with change of the B-site ion. The $LaMnO_3$ further undergoes Jahn Teller distortion due to the presence of Mn^{3+} ion, which presents a different Raman fingerprint compared to $LaFeO_3$ without such distortions [85].

$LaFeO_3$ has an orthorhombically distorted perovskite structure with 60 normal modes out of which, 24 are Raman active modes [86]. A better resolved Raman spectrum is shown in Fig.1.20, where bands below 200 cm^{-1} are attributed to La-vibrations (A modes) [76]. The line around 270 cm^{-1} comprises of 2 components at 263 and 289 cm^{-1} due to FeO_6 octahedral tilt (T modes). The oxygen octahedral bending vibration gives rise to the scattering around 400-500 cm^{-1} (B modes). The components above 600 cm^{-1} present the O-stretching vibrations (S modes) and the longitudinal optic phonons overlapping each other. A strong broad line at 1320 cm^{-1} is attributed to the second order scattering due to

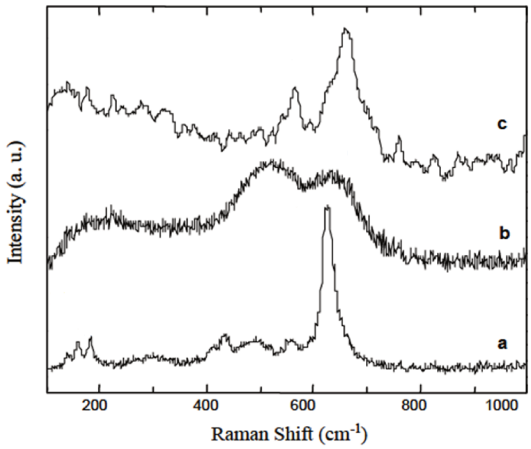

Figure 1.19: Raman spectra of (a) orthorhombic $LaFeO_3$, (b) rhombohedral $LaMnO_3$ and (c) rhombohedral $LaCoO_3$ collected using the 632.8 nm laser at 300K [86].

the combination of IR active LO phonons observed around 630 and 490 cm^{-1} [76, 87, 88]. The Raman bands related to $LaFeO_3$ have been enlisted in Table 1.5 [37].

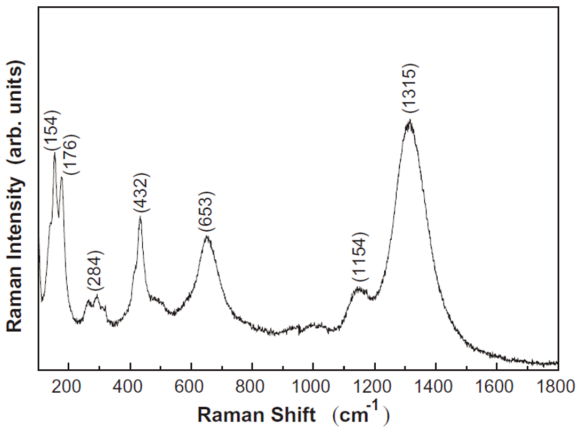

Figure 1.20: Raman spectrum of $LaFeO_3$ nanofibres calcined at 600°C [76].

Table 1.5: Wavenumbers of Raman bands with corresponding symmetry and atomic motions [37].

Wavenumber (cm^{-1})	Symmetry	Assignment
152	B_{2g}	displacement of La cations
175	A_g	displacement of La cations
263	A_g	tilt of FeO_6 octahedra
289	A_g	tilt of FeO_6 octahedra
330 (sh)		
400 (sh)	B_{2g}	FeO_6 out of phase bending
431	A_g	FeO_6 bending
500 (broad)		LO phonon mode
570	B_{3g}	FeO antisymmetric stretching
639 (broad)	A_g	FeO stretching and LO phonon mode

In addition, the effect of temperature on $LaFeO_3$ was studied by Coutinho *et al.* and Andreasson *et al.* [89, 90], the Raman peaks broadened and became less defined with

heating due to the increase in short-range disorder, besides a shift to lower wavenumbers due to increase in the lattice parameter with rising temperature.

X-ray absorption near-edge spectroscopy (XANES) is a powerful tool that provides information regarding the valence state, symmetry and the basic fingerprint of a sample. A sample containing a mixture of different crystalline phases can be detected by quantifying with a linear combination fitting of the reference spectra of known compounds. The typical Fe K-edge XANES spectra of $LaFeO_3$ has been shown in Fig.1.21 (orange line). It displays a weak pre-egde peak at ~7115 eV representing the 1s to 3d transition and the whiteline at ~7130 eV formed by the 1s to 4p transition [80, 91]. The absorption edge and the intensity of the whiteline can vary with substitutions within the perovskite lattice (Fig.1.21). In a study by Haas *et al.* [92], as the amount of Sr^{2+} increases at A-site in $La_{1-x}Sr_xFeO_3$, the intensity of the whiteline decreases together with a tiny shift in the edge value, probably due to the presence of segregated Sr-species on the surface and/or increasing amount of tetravalent iron in the lattice [93]. Therefore, XANES stands as a powerful technique to detect and quantify the occurrence of any surface/bulk anomalies that are common aspects observed in several perovskite-type mixed oxide systems.

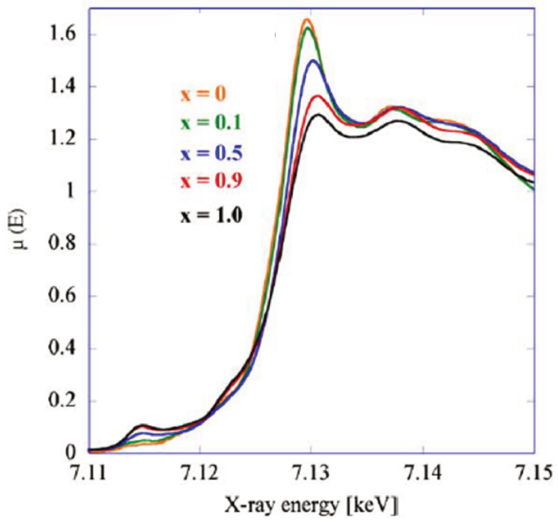

Figure 1.21: XANES region of normalized Fe K-edge X-ray absorption spectra of $La_{1-x}Sr_xFeO_3$ [92].

1.3 Towards advanced characterization of catalysts

1.3.1 Model catalysts

Looking at the catalyst before and after reaction only provides information regarding the surface composition, structural or morphological modifications of the catalyst and not the real picture during the catalytic process when it is performing its action. Most often a catalyst is only screened after optimization by trial and error method and therefore some scientists have even referred to catalytic research as magic rather than science [94]. Today many advances have been made to understand catalysis in more details by for example, studying model catalysts by *in situ* approaches. Deeper understanding towards the important aspects of catalysis can be studied by a systematic model approach, by variation in the complexity of the investigated materials in ambient condition, as proposed by Sauer *et al.* [95]. Fig.1.22 presents a pictorial representation of different type of model systems as a function of complexity that can enable to understand the essential features of a catalyst under working conditions in a step-by-step manner. Such an approach allows to receive the small pieces of relevant information unraveling more realistic picture of catalyst interaction to finally help with better fundamental understanding for designing a catalyst. Thus, in simple words, a model catalyst is inspired from real heterogeneous catalyst, which is prepared for understanding of a complex phenomenon by simplifying the system. The objective of studying such models is to gain information regarding a catalytic system such that it can allow us to understand and ameliorate current catalyst and not merely for exploring new catalysts for practical applications [96]. The strategy to prepare relevant model catalysts is to reduce the complexity of the system while compromising to the minimum on the features of the real catalyst [97]. Models catalysts can be in the form of metal single crystals representing the active phase, for e.g. Rh(100) for CO oxidation, or oxides supported metal clusters as thin films, *e.g.* Au on TiO_2 single crystal for CO oxidation reaction to study the metal-support interaction [98].

Material and pressure gap: Heterogeneous catalysis being a surface driven process makes it imperative to study effectively the surface properties of the model catalysts. Surface science-based technology to understand such model materials are not straightforward and come with challenges such as pressure and material gaps. The catalyst surface is analyzed mostly by ultra-high vacuum (UHV) based surface analytical techniques compared to the higher pressures in real catalytic conditions required by industrial appli-

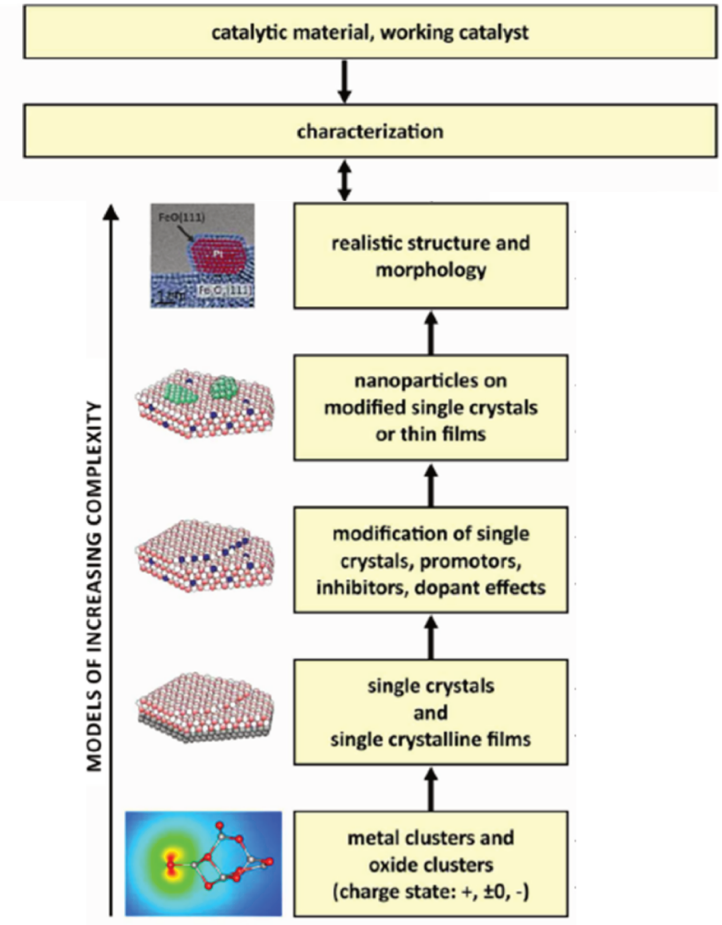

Figure 1.22: Schematic representation of different types of model systems as a function of increasing complexity [95].

cations, this difference is known as the pressure gap. Further, material gap refers to the discontinuity between model catalysts systems such as well-characterized single crystals and industrially relevant catalysts shaped as polycrystalline powder. Such gaps often lead to failed extrapolation of the results from the model to that of the real conditions. It could create a thermodynamic or kinetic barrier in viewing the catalytic system; new thermodynamically stable phases and/or kinetically dominated reaction pathways at higher temperature and pressure may remain unnoticed only under UHV conditions. In addition, catalysis is a dynamic process, such that structural defects may form during the reaction impacting the overall reaction performance that can determine the structure and chemistry of working catalysts, unlike the static conditions such as those used during surface techniques. This drives one towards the necessity of not only producing more suitable model materials depicting a catalytic system but also the requirement for *in situ/operando* experimental approaches, *i.e.* at elevated temperature and pressures such as those of real conditions, that can illustrate a catalyst surface directly under working conditions estab-

lishing a reliable structure-function relationship. Several efforts are being made by scientists since more than 40 years to look at atomic scale information while bridging these existing gaps [97]. To this end advances towards development of *in situ* and *operando* analytical experiments are on the rise to better understand the structure-activity correlations [99–101].

In situ/operando approach

As mentioned above, deeper mechanistic insights in a heterogeneous catalytic reaction can be acquired by combining advanced characterization techniques with *in situ/operando* characterizations. The recent development of optical, electronic and ionic spectroscopies as well as imaging techniques has opened the way to the depiction of active phases at the atomic and molecular scales. When the spectroscopic measurement is run under controlled conditions, it is termed as *in situ* spectroscopy. An *in situ* experiment involves the simultaneous functioning of a physico-chemical characterization technique with a combination of external constraints. In case of heterogeneous catalysis, such constraints can include the temperature, reactant feed, atmosphere and presence of an electric field or a light source. This approach has been developed in the 1950s for studying the structure of adsorbates originating from interaction of CO with silica-supported Pd, Ni, Pt and Cu materials using infrared spectroscopy [32]. There are by now numerous spectroscopic techniques available, which can provide a share of the required information regarding any catalytic system.

One step further was taken with the emergence of the *operando* concept, whose guiding principle is based on the simultaneous characterization of the catalyst and measurement of catalytic performances, thus building a direct structure-activity correlation. This approach has been introduced in 2002 by Perez *et al.* [102] by *operando* Raman investigation of Sb-V-O catalysts during propane ammoxidation with simultaneous recording of the catalytic yield, highlighting the presence of new phases which were not detected in the calcined samples.

Most techniques operating *in situ* are not directly surface-sensitive. Taking into account the fact that the catalytic processes take place at the outermost surface of the catalysts, a decent description may require additional efforts in the depiction of the exposed surface. Obtaining such fundamental information in bulk materials with intrinsically low surface areas is difficult since most techniques fail to discriminate between the surface

and the bulk containing the same elements and therefore spectroscopic data is rather only representing bulk signals [103]. However, precious insights can be achieved from a smart combination of experiments using probe-molecule reactions such as ambient-pressure XPS.

Thanks to *in situ* XAS study on $LaFe_{0.57}Co_{0.38}Pd_{0.05}O_3$ perovskite under cycles of oxidative and reductive atmospheres, the unique self regenaration properties of the perovskite were first discovered, as discussed previously. As shown in Fig.1.23, the Pd moves in and out of the perovskite lattice reversibly confirmed by the valence state of Pd. The Pd moves out of the lattice under reducing conditions in metallic state and again goes back into the lattice as PdO, given by the bond distances as well as the XANES spectra [14]. Such reversible structural changes have been further shown to be existing within the control frequency of an actual gasoline engine [104]. This property has been verified to some extent by *in situ* microscopy techniques as well [17, 19].

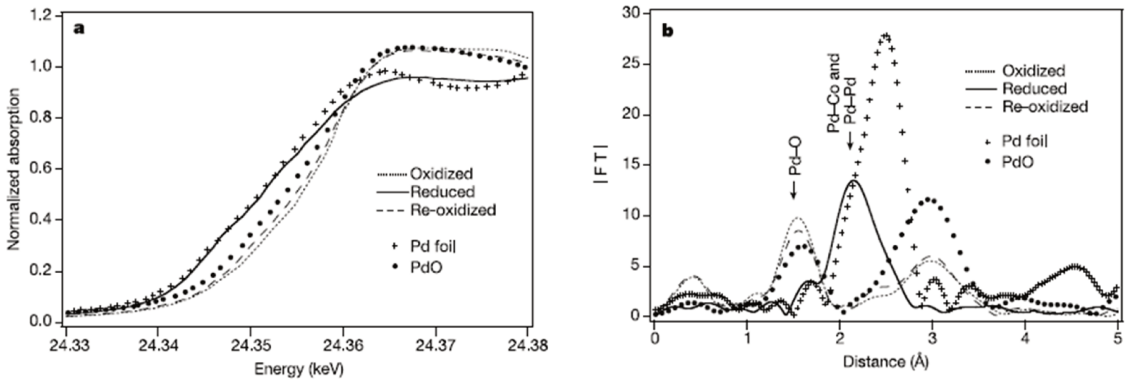

Figure 1.23: *In situ* XAS of $LaFe_{0.57}Co_{0.38}Pd_{0.05}O_3$ with PdO and Pd as reference materials: (a) XANES spectra at the Pd K-edge in transmission mode and (b) Radial distribution function showing local structure around Pd atom changing reversibly in a redox cycle [14].

Recently, lanthanum ferrite based perovskites were investigated by *in situ* Raman in stoichiometric ($LaFeO_3$) and non-stoichiometric ($La_{0.7}FeO_3$) compositions under O_2, H_2O, CO and NO environments as mentioned previously. A hematite-like nano-phase with a reversible character was evidenced only in case of $La_{0.7}FeO_3$, during reaction under oxygen and under hydrating conditions. This new phase was not observable under CO but re-surfaced under NO, highlighted by the Raman lines at 212 and 276 cm^{-1} (Fig.1.24). The appearance of this reversibly occuring phase was postulated to be assisting in better catalytic activity of $La_{0.7}FeO_3$ over $LaFeO_3$ by favoring formation of oxygen defects [37].

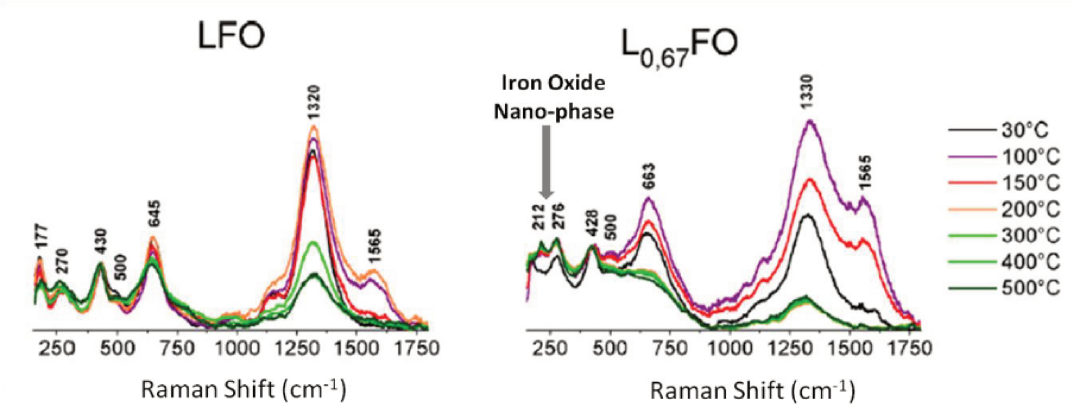

Figure 1.24: *In situ* Raman spectra of $LaFeO_3$ and $La_{0.7}FeO_3$ during the increase of calcination temperature under O_2 [37].

Some studies on $La_{0.6}Sr_{0.4}FeO_3$ based perovskite as thin film electrodes by *in situ* techniques such as NAP-XPS evidenced the occurrence of B-site iron exsolution as Fe^0. Opitz *et al* [105] observed formation of Fe^0 under cathodic polarization in electrochemical water splitting reaction, plausibly playing a positive role in the enhancement of the activity. In another study by the same authors, similar catalysts were investigated for electrochemical CO_2 reduction by NAP-XPS, which presented intermediate carbonate formation under reducing conditions with increase in oxygen vacancy concentration. Unlike in the case of water splitting reaction, the CO_2 kinetics were not affected by exsolved metallic Fe particles during reduction [106]. Further, Goetsch and co-authors inspected the Fe^0 formation of the same perovskite by heating under hydrogen up to 700°C with NAP-XPS. They observed the exsolution of ~18% Fe^0 on the extreme surface (1.8 nm) together with majority of Fe^{2+} formation (~78%) and small amount of Fe^{3+} remaining as shown in Fig.1.25 [107]. On changing the photon energy the analysis depth varied from 1.8 to 5 nm, presenting slightly different proportions of the respective ions. As expected, the so-called bulk spectrum contains higher contribution of Fe^{3+} compared to the sub-surface and the extreme surface.

1.3.2 Metal-oxide thin films

Thin film is a layer of a particular material such as a metal oxide supported onto a substrate, from monolayer to several microns in thickness. Single or mixed oxide thin films are commonly studied as model catalysts. The deposition of the thin film layer on the substrate is done by deposition techniques of chemical or physical origin. In case of chemical deposition, a liquid precursor is used, which transforms into the required material

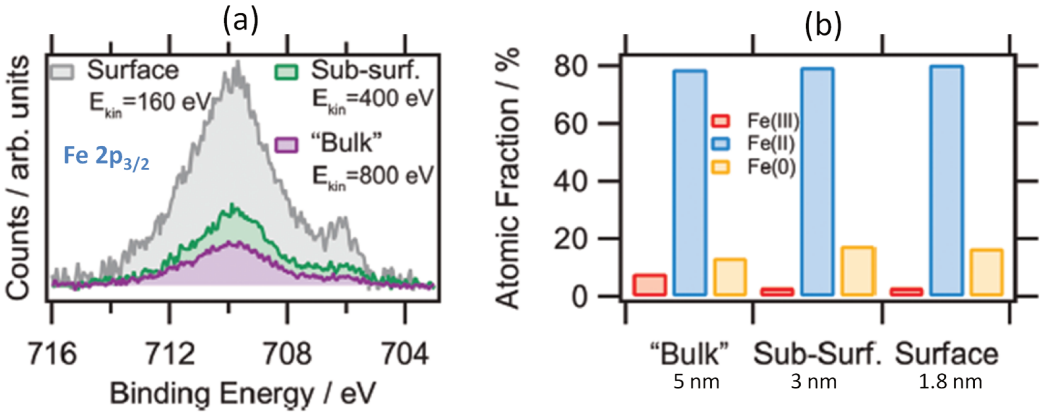

Figure 1.25: NAP-XPS of $La_{0.6}Sr_{0.4}FeO_3$ under H_2 at 700°C: (a) Fe $2p_{3/2}$ spectra with change of incident photon energy to vary the depth resolution and (b) atomic fraction of each Fe species at different surface depths [107].

by annealing leaving a solid layer behind, such as spin-coating, dip-coating, chemical vapor deposition and atomic layer deposition. While physical deposition techniques utilize mechanical, electro-mechanical or thermodynamic means to deposit a thin film like molecular beam epitaxy, magnetron sputtering, pulsed layer depositions etc.

The choice of the substrate for fabrication of a metal oxide thin film largely depends on the type of application. In case of studying model catalysts, an ideal substrate must have minimum interaction with the oxide film layers as well as high melting points due to usually high temperature and pressure conditions of the catalytic reaction. Silicon, alumina, aluminium nitride, glass, titanates, ferrites are often used as substrate materials. Silicon(100) single crystal is one of the commonly used substrates not only in the semiconductor industries but also as a substrate for model catalysts. Single oxides as well as mixed oxides like perovskites have been succesfully deposited on Si(100) wafers by several researchers [108–110]. Fig.1.26 presents the cross-sectional image of a perovskite thin film over Si(100) wafer with a thin amorphous layer of silica present between the film and the substrate, confirmed by angle-resolved XPS [111]. Thirumalairajan *et al* [112] successfully prepared $LaFeO_3$ thin films supported over silicon wafers as NO_2 gas sensor by magnetron sputtering .

Chemical methods involving deposition of a precursor solution to produce a thin film is one of the most simple and inexpensive routes to fabricate crystalline thin films with the required stoichiometries. The main steps with the corresponding structural evolution have been presented in Fig.1.27. Firstly, a precursor solution is prepared containing the metal cations according to the stoichimetric ratios. The precursor solution can

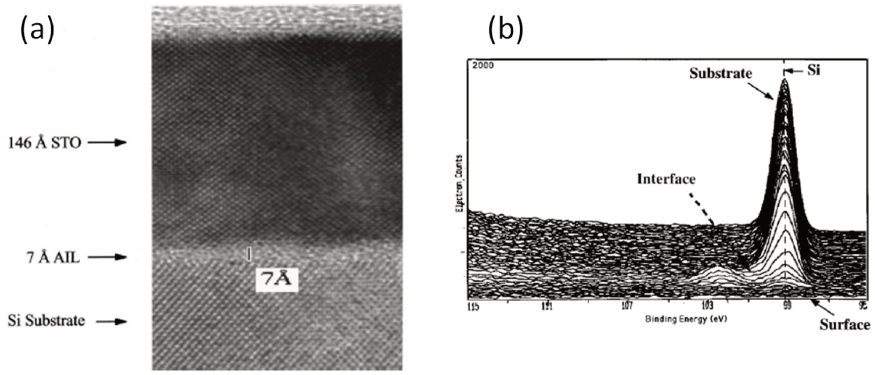

Figure 1.26: (a) HR-TEM of cross-section of $SrTiO_3$ thin film supported over Si(100) substrate (b) angle-resolved XPS highlighting the presence of SiO_2 between the perovskite film and the silicon substrate [110, 111].

be prepared in several methods such as sol-gel, citrate complexation, Pechini route, etc. [113, 114]. They allow good control of the stoichiometry of the film layer, however it can be accompanied by the formation of some cracks on the film surface [114].

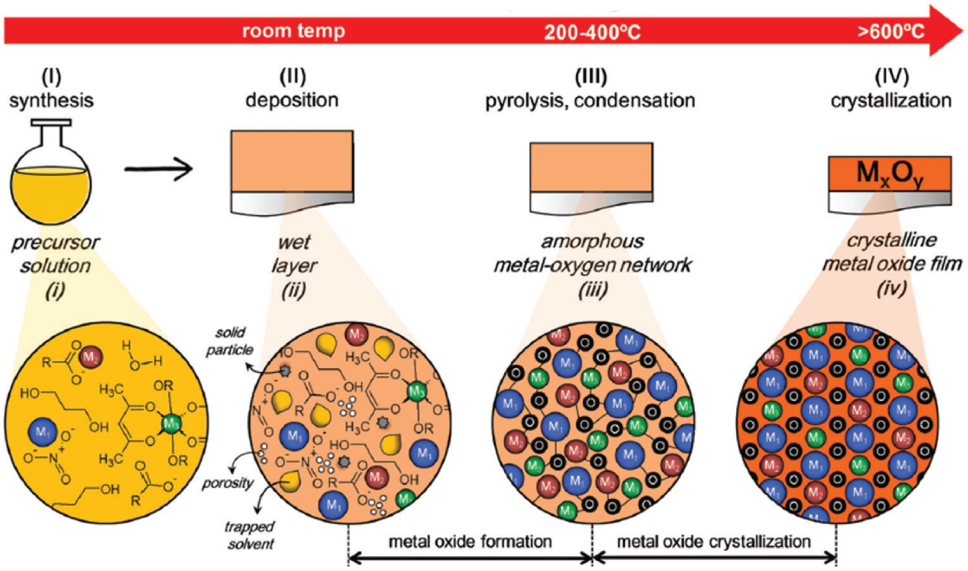

Figure 1.27: Steps of chemical solution deposition to produce thin films, with the corresponding stages from the initial precursor solution to final crystalline film [114].

Secondly, a thin wet layer of this solution is deposited on the substrate by a coating technique such as spin coating, dip coating, etc. Thirdly, this wet layer is then annealed to evaporate low boiling point compounds and decompose the metal precursors while promoting hydrolysis and condensation reactions towards an amorphous metal-oxygen network. Finally, further thermal treatment at higher temperature crystallizes the amorphous film to an ordered periodic arrangement. The formation of a crystalline film as-

sisted by the application of thermal energy, is governed by both kinetics and thermodynamics. The driving force of crystallization is given by the difference between the free energy of the crystalline and amorphous phases ($\Delta G = G_c - G_a$), which is inversely proportional to the temperature as shown in Fig.1.27(a). For thin films, this value can further depend on the interfacial energy contribution governed by the films bulk, top surface and the film-surface interface determining the crystallization process. Nucleation of the crystal phase drives the crystallization of the thin film either from the bulk of the existing amorphous phase or at the film interface (Fig.1.28(b)). The nucleation and growth process involved are dependent on the temperature, which governs the diffusion of the atoms in the film layer. Hence, it is possible to produce crystalline phases at comparatively low temperatures with longer annealing duration.

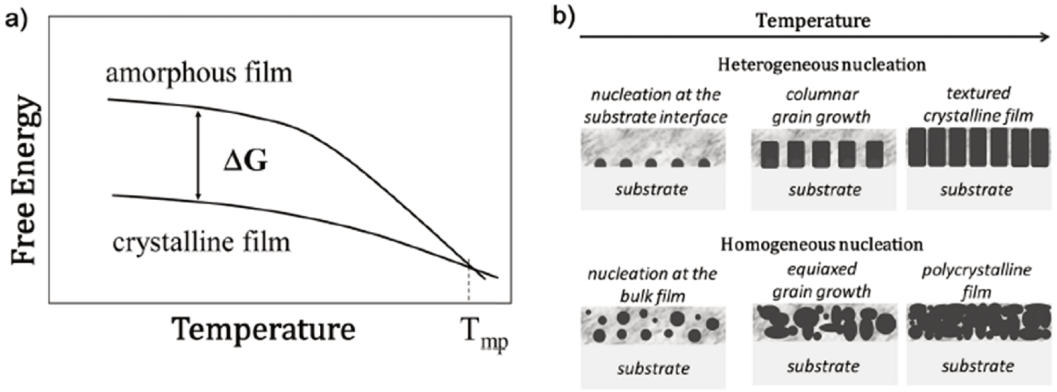

Figure 1.28: (a) Free energies for solution derived amorphous and crystalline thin film as a function of temperature, where ΔG is the driving force for crystallization and T_{mp} is melting point, (b) homogeneous and heterogeneous nucleation and growth of thin films [114].

The growth and nucleation of the thin film depends on the interaction between the adsorbates or the layer atoms (film) and the substrate surface, broadly classified into three growth mechanisms, as shown in Fig.1.29 [115]. According to the Volmer-Weber or island model, the adsorbate-adsorbate interactions are stronger than adsorbate-substrate interaction forming discrete 3-D nuclei on the substrate. A homogeneous layer can be eventually formed by nucleation and merging together of such island-like structures. In the Frank-van der Merve or layer model, the deposit grows first as a continuous mono layer followed by another layer on top. Here, interaction between the substrate and the layer atoms is stronger than the neighboring layer atoms. The Stranski-Krantanov or joint-islands model is a combination of both the above models. Here, growth occurs first in layer-by-layer mode, such that a mono layer is produced followed by formation of dis-

crete nuclei or islands over this layer.

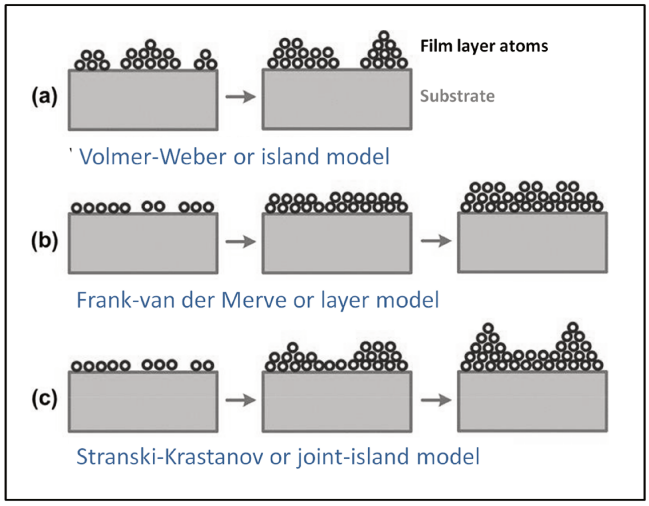

Figure 1.29: Representation of the different thin film growth models [115].

Spin coating

Spin coating is one of the popular chemical methods to fabricate uniform thin films since several decades. As presented in Fig.1.30, it involves depositing a thin film layer on the basis of centrifugal draining and evaporation consisting of four steps, namely, deposition, spin-up, spin-off and evaporation [116]. Firstly, excess of the precursor liquid is put on the substrate surface. Secondly, as the substrate starts to spin excess liquid is pushed away towards the edges due to the centrifugal forces. Thirdly, the liquid leaves the surface as small droplets. In the final step, the film becomes thinner and viscous as evaporation of solvent takes place. Often depending on the type of solvent, the evaporation can already begin at the spin-off stage. Spin coating often leads to uniformly thick thin films due to a balance between centrifugal force and the viscous force acting radially in opposite directions [117]. The film thickness can be controlled by varying the viscosity of the precursor solution and/or the time and speed of the spin coater, as has been verified by Extrand *et al* [118]. However, the film's quality can be greatly affected by the presence of dust particles on the substrate leading to voids or bubble-like structures on the final thin film. The substrates are therefore stored under distilled water to avoid any dust accumulation on the surface of the substrate prior to the deposition stage. Spin coating technique has been used to prepare $LaFeO_3$-based thin films by several authors with different thickness ranges from <10 nm to microns [119–122].

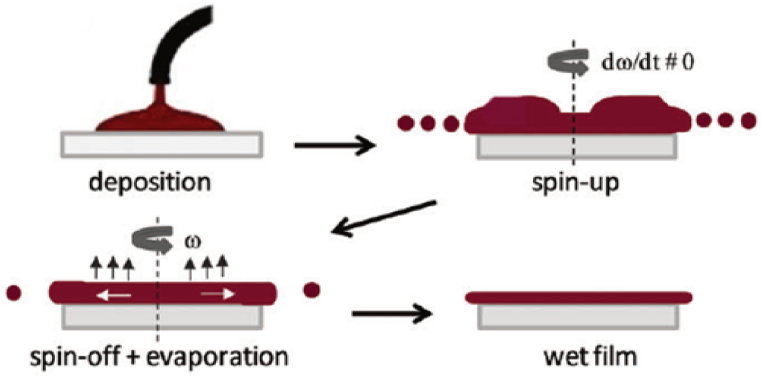

Figure 1.30: Stages of spin coating method for depositing thin films [114].

1.4 Conclusions and thesis outline

This chapter brings forward the necessity to find better alternatives for TWC catalysts with none or least amounts of PGMs while gaining deeper insights of the catalytic system by advanced characterization techniques. Having verified by several researchers the potential application of $LaFeO_3$-based catalysts as TWC, owing to its unique self-regenerating property, the importance of variable surface compositions are highlighted that directly control the catalytic activities. The application of a combination of different surface-sensitive techniques can reveal surface properties at different scales. The surface analysis of the perovskites is performed not only by applying surface-sensitive techniques but also preparing dedicated model materials shaped as thin films with high surface to bulk ratio to further enhance the detection of surface properties. The thin film can act as discrete models with tunable thickness. The choice of using silicon as the substrate reduces surface charging issues compared to insulating powders and such systems further allow more effective depth profiling studies revealing the presence of surface segregation, if any. Furthermore, one step further can be taken by application of *in situ/operando* surface and bulk techniques to unveil information that can be otherwise hard to detect by *ex situ* measurements.

Thereby, the goal of this thesis work is to investigate $LaFeO_3$-based bulk catalysts shaped as polycrystalline model thin films supported over Si(100) substrates prepared by spin coating by combination of surface and bulk techniques such as LEIS, ToF-SIMS, XPS, Raman and XANES. The polycrystalline nature of the model catalysts allows bridging the material gap to a large extent. The perovskites are further analyzed under *in situ/operando* modes by NAP-XPS, *in situ* GI-XANES and *in situ/operando* Raman spectroscopy to study

their behavior under more realistic catalytic conditions such as under CO at high temperatures, in direction of bridging the pressure gap. At most stages, the model catalysts are compared to powdered catalysts for verifying their relevance as suitable TWC models. This methodological approach enables to not only investigate the catalysts but also verify its reliability to be used as a general approach for studying bulk catalysts. To this end, the thesis is divided into the next four chapters as follows:

Chapter 2 presents the general principles and experimental conditions of all the experimental techniques used and the sample preparation methods.

Chapter 3 consists of a detailed description of the $LaFeO_3$-based thin films together with the substrate. The physico-chemical properties including the structural, morphological and the surface analyses are discussed. Finally, the model catalysts are directly compared to the conventional catalysts ($LaFeO_3$ powders) to compare its relevance as a TWC model.

Chapter 4 comprises of a systematic comparitive study of stoichiometric $LaFeO_3$ and more active La-deficient $La_{0.7}FeO_3$ by combination of different techniques including depth profiling by LEIS/TOF-SIMS. The thin films of both compositions are examined under CO atmosphere by NAP-XPS and GI-XANES analyses with an attempt to separate surface and bulk processes. The similarities or differences between the two stoichiometric compositions allows to understand the driving force of enhancement of catalytic activity of $La_{0.7}FeO_3$ over the stoichiometric catalyst composition.

Chapter 5 is devoted to studying the conventional catalyst powder after substitution at B-site by X ($La_{0.7}Fe_{0.8}X_{0.2}O_3$, X=Cu or Mn), short-listed by the Partial-PGMs consortium, by *in situ/operando* Raman spectroscopy. The driving force of the positive role of the B-site substitution is further investigated by XPS, ToF-SIMS and XANES.

Finally, cumulative results with respect to $LaFeO_3$-based catalysts are conclusively discussed together with future perspective of this work.

1.5 References

[1] N. Hooftman, M. Messagie, J. V. Mierlo, and T. Coosemans, *Renew. Sust. Energ. Rev.*, 2018, **86**, 1–21. 1

[2] M. V. Twigg, *Appl. Catal. B - Environ.*, 2007, **70**(1), 2 – 15. 1

[3] K. C. Taylor, in *Catalysis: Science and Technology Volume 5*, ed. J. R. Anderson and M. Boudart, Springer Berlin Heidelberg, 1984; pp. 119–170. 2

[4] T. Leroy, J. Chauvin, N. Petit, and G. Corde, *IFAC Proceedings Volumes*, 2007, **40**(10), 617 – 623. 3

[5] Jan Kašpar and Paolo Fornasiero and Neal Hickey, *Catal. Today*, 2003, **77**(4), 419 – 449. 3

[6] M. Laurenzi and R. Spigler, *Math. Indust.*, 2018, **9**(1), 1. 3

[7] H. Gandhi, G. Graham, and R. McCabe, *J. Catal.*, 2003, **216**(1), 433 – 442. 4

[8] E. Alonso, F. R. Field, and R. E. Kirchain In *IEEE International Symposium on Electronics and the Environment*, pp. 1–6, 2008. 4

[9] H. Yao, S. Japar, and M. Shelef, *J. Catal.*, 1977, **50**(3), 407– 418. 4

[10] V. M. Goldschmidt, *Naturwissenschaften*, 1926, **14**(21), 477–485. 4

[11] A. Weidenkaff, *Advanced Engineering Materials*, 2004, **6**(9), 709–714. 5

[12] H. Tanaka and M. Misono, *Curr. Opin. Solid St. M.*, 2001, **5**(5), 381–387. 5

[13] E. Olsson, X. Aparicio-Anglès, and N. H. de Leeuw, *J. Chem. Phys.*, 2016, **145**(1), 014703. 5

[14] Y. Nishihata, J. Mizuki, T. Akao, H. Tanaka, M. Uenishi, M. Kimura, T. Okamoto, and N. Hamada, *Nature*, 2002, **418**(6894), 164–167. 5, 6, 26

[15] H. Tanaka, M. Taniguchi, N. Kajita, M. Uenishi, I. Tan, N. Sato, K. Narita, and M. Kimura, *Top. Catal.*, 2004, **30**(1), 389–396. 5, 6

[16] J. Dacquin, C. Lancelot, C. Dujardin, C. Cordier-Robert, and P. Granger, *J. Phys. Chem. C*, 2011, **115**(5), 1911–1921. 6

[17] M. B. Katz, G. W. Graham, Y. Duan, H. Liu, C. Adamo, D. G. Schlom, and X. Pan, *J. Am. Chem. Soc.*, 2011, **133**(45), 18090–18093. 6, 7, 26

[18] M. B. Katz, S. Zhang, Y. Duan, H. Wang, M. Fang, K. Zhang, B. Li, G. W. Graham, and X. Pan, *J. Catal.*, 2012, **293**, 145–148. 6

[19] S. Dai, S. Zhang, M. B. Katz, G. W. Graham, and X. Pan, *ACS Catalysis*, 2017, **7**(3), 1579–1582. 7, 26

[20] N. M. Panich, G. N. Pirogova, R. I. Korosteleva, and Y. V. Voronin, *Russian Chemical Bulletin*, 1999, **48**(4), 694–697. 7, 8

[21] S. Royer and D. Duprez, *ChemCatChem*, 2011, **3**(1), 24 – 65. 8

[22] T. Nitadori, T. Ichiki, and M. Misono, *Bull. Chem. Soc. Jpn.*, 1988, **61**(3), 621–626. 8

[23] N. Yamazoe, Y. Teraoka, and T. Seiyama, *Chem. Lett.*, 1981, **10**(12), 1767–1770. 8

[24] H. Arai, T. Yamada, K. Eguchi, and T. Seiyama, *Appl. Catal.*, 1986, **26**, 265 – 276. 9

[25] R. J. H. Voorhoeve, J. P. Remeika, and L. E. Trimble, *Annals of the New York Academy of Sciences*, 1976, **272**(1), 3–21. 9

[26] L. Forni, C. Oliva, T. Barzetti, E. Selli, A. M. Ezerets, and A. V. Vishniakov, *Appl. Catal. B - Environ.*, 1997, **13**(1), 35 – 43. 9

[27] Y. Wang, X. Cui, Y. Li, Z. Shu, H. Chen, and J. Shi, *Microporous and Mesoporous Materials*, 2013, **176**, 8 – 15. 9

[28] Y. Wang, J. Ren, Y. Wang, F. Zhang, X. Liu, Y. Guo, and G. Lu, *J. Phys. Chem. C*, 2008, **112**(39), 15293–15298. 9

[29] D. Jovanovic, V. Dondur, A. Terlecki-Baricevic, and B. Grbic, *Stud. Surf. Sci. Catal.*, 1991, **71**, 371 – 379. 9

[30] P. Gallagher, D. Johnson, E. Vogel, and F. Schrey, *Mater. Res. Bull.*, 1975, **10**(7), 623 – 627. 9

[31] G. M. Rodríguez, K. Kelm, S. Heikens, W. Grünert, and B. Saruhan, *Catal. Today*, 2012, **184**(1), 184 – 191. 9

[32] H. Tanaka, *Catal. Surv. Asia*, 2005, **9**(2), 63–74. 9, 10, 25

[33] S. A. Bhalerao, A. S. Sharma, and A. C. Poojari, *Int. J. Pure Appl. Biosci.*, 2015, **3**(2), 345–355.

[34] F. Baruthio, *Biol. Trace Elem. Res.*, 1992, **32**(1), 145–153. 10

[35] A. Schön, C. Dujardin, J.-P. Dacquin, and P. Granger, *Catal. Today*, 2015, **258**, 543 – 548. 10, 11

[36] Y. Wu, X. Ni, A. Beaurain, C. Dujardin, and P. Granger, *Appl. Catal. B: Environ.*, 2012, **125**, 149 – 157. 10

[37] D. Blanck, A. Schön, A.-S. Mamede, C. Dujardin, J.-P. Dacquin, P. Granger, J.-F. Paul, and E. Berrier, *Catal. Today*, 2016. 11, 13, 14, 21, 26, 27

[38] A. Schön, J.-P. Dacquin, C. Dujardin, and P. Granger, *Top. Catal.*, 2017, **60**(3), 300–306. 11

[39] J. Wu *Development of novel catalytic materials with low content of precious metals for the after-treatment of automobile exhaust gas* PhD thesis, University of Lille, 2019. 11

[40] A. Schön, J.-P. Dacquin, P. Granger, and C. Dujardin, *Appl. Catal. B - Environ.*, 2018, **223**, 167 – 176. 11

[41] H. ter Veen, T. Kim, I. Wachs, and H. Brongersma, *Catal. Today*, 2009, **140**(3), 197 – 201. 12

[42] J. Druce, H. Tellez, M. Burriel, M. Sharp, L. Fawcett, S. Cook, D. McPhail, T. Ishihara, H. Brongersma, and J. Kilner, *Energy Environ. Sci.*, 2014, **7**, 3593–3599. 12, 13

[43] W. A. Harrison, *Phys. Rev. B*, 2011, **83**, 155437. 13

[44] H. Ding, A. V. Virkar, M. Liu, and F. Liu, *Phys. Chem. Chem. Phys.*, 2013, **15**, 489–496. 13

[45] W. Lee, J. W. Han, Y. Chen, Z. Cai, and B. Yildiz, *J. Am. Chem. Soc.*, 2013, **135**(21), 7909–7925. 13

[46] H. Dulli, P. A. Dowben, S.-H. Liou, and E. W. Plummer, *Phys. Rev. B*, 2000, **62**, 14629–14632. 13

[47] K. Szot and W. Speier, *Phys. Rev. B*, 1999, **60**, 5909–5926.

[48] K. Szot, C. Freiburg, and M. Pawełczyk, *Appl. Phys. A*, 1991, **53**(6), 563–567. 13

[49] Z. Feng, W. T. Hong, D. D. Fong, Y.-L. Lee, Y. Yacoby, D. Morgan, and Y. Shao-Horn, *Accounts Chem. Res.*, 2016, **49**(5), 966–973. 13

[50] L.-T. Weng, *Appl. Cata. A - General*, 2014, **474**, 203 – 210. 13

[51] Francesca Zurlo and Elisabetta Di Bartolomeo and Alessandra D'Epifanio and Valeria Felice and Isabella Natali Sora and Luca Tortora and Silvia Licoccia, *J. Power Sources*, 2014, **271**, 187 – 194. 13

[52] A. M. Vandenbroucke, M. N. Dinh, N. Nuns, J.-M. Giraudon, N. D. Geyter, C. Leys, J.-F. Lamonier, and R. Morent, *Chem. Eng. J.*, 2016, **283**, 668 – 675. 14

[53] D. Tripković, R. Küngas, M. B. Mogensen, and P. V. Hendriksen, *J. Mater. Chem. A*, 2019, **7**, 11782–11791.

[54] N. Nuns, A. Beaurain, M. N. Dinh, A. Vandenbroucke, N. D. Geyter, R. Morent, C. Leys, J.-M. Giraudon, and J.-F. Lamonier, *Appl. Surf. Sci.*, 2014, **320**, 154 – 160. 14

[55] Y. Wu, C. Cordier, E. Berrier, N. Nuns, C. Dujardin, and P. Granger, *Appl. Catal. B - Environ.*, 2013, **140-141**, 151 – 163. 14, 15

[56] I. Kocemba, J. Dlugolecka, M. Wrobel-Jedrzejewska, J. Rogowski, I. Dobrosz-Gomez, and J. Rynkowski, *React. Kinet. Mech. Cat.*, 2018, **123**(2), 659–677. 14

[57] F. Aubriet, C. Poleunis, and P. Bertrand, *J. Mass Spectrom.*, 2001, **36**(6), 641–651. 14

[58] L. Weng, P. Bertrand, O. Tirions, and M. Devillers, *Appl. Surf. Sci.*, 1996, **99**(3), 185 – 196.

[59] J. Grams, A. Ura, and W. Kwapiński, *Fuel*, 2014, **122**, 301–309. 14

[60] D. Lee, R. Jacobs, Y. Jee, A. Seo, C. Sohn, A. V. Ievlev, O. S. Ovchinnikova, K. Huang, D. Morgan, and H. N. Lee, *J. Phys. Chem. C*, 2017, **121**(46), 25651–25658. 14

[61] M. Kubicek, A. Limbeck, T. Frömling, H. Hutter, and J. Fleig, *ECS transactions*, 2011, **35**(1), 1975–1983. 14

[62] M. Kubicek, A. Limbeck, T. Frömling, H. Hutter, and J. Fleig, *J. Electromchem. Soc.*, 2011, **158**(6), B727–B734. 14, 15

[63] A.-K. Huber, M. Falk, M. Rohnke, B. Luerssen, M. Amati, L. Gregoratti, D. Hesse, and J. Janek, *J. Catal.*, 2012, **294**, 79 – 88. 14

[64] N. Ai, N. Li, W. D. A. Rickard, Y. Cheng, K. Chen, and S. P. Jiang, *ChemSusChem*, 2017, **10**(5), 993–1003. 15

[65] A. J. Oakes and J. C. Vickerman, *Surf. Interface Anal.*, 1996, **24**(10), 695–703. 15, 16

[66] C. V. Cushman, P. Brüner, J. Zakel, G. H. Major, B. M. Lunt, N. J. Smith, T. Grehl, and M. R. Linford, *Anal. Methods*, 2016, **8**, 3419–3439. 16, 20

[67] M. Sunding, K. Hadidi, S. Diplas, O. Løvvik, T. Norby, and A. Gunnæs, *J. Electron. Spectrosc.*, 2011, **184**(7), 399 – 409. 16, 17, 18

[68] Q. Zhang, Y. Huang, S. Peng, Y. Zhang, Z. Shen, J. ji Cao, W. Ho, S. C. Lee, and D. Y. Pui, *Appl. Catal. B - Environ.*, 2017, **204**, 346 – 357. 17, 19

[69] M. Goldwasser, M. E. Rivas, M. Lugo, E. Pietri, J. Perez-Zurita, M. Cubeiro, A. Griboval-Constant, and G. Leclercq, *Catal. Today*, 2005, **107-108**, 106–113. 17

[70] https://xpssimplified.com/elements/lanthanum.php, 2019. 17

[71] T. Yamashita and P. Hayes, *Appl. Surf. Sci.*, 2008, **254**(8), 2441 – 2449. 18, 19

[72] M. C. Biesinger, B. P. Payne, A. P. Grosvenor, L. W. Lau, A. R. Gerson, and R. S. Smart, *Appl. Surf. Sci.*, 2011, **257**(7), 2717 – 2730. 18

[73] X. Li, H. Zhang, X. Liu, S. Li, and M. Zhao, *Mater. Chem. Phys.*, 1994, **38**(4), 355 – 362. 19

[74] J. Fierro and L. G. Tejuca, *Appl. Surf. Sci.*, 1987, **27**(4), 453 – 457. 18, 19

[75] Y.-G. Cho, K.-H. Choi, Y.-R. Kim, J.-S. Jung, and S.-H. Lee, *B. Kor. Chem.Soc.*, 2009, **30**(6), 1368–1372. 19

[76] W.-Y. Lee, H. J. Yun, and J.-W. Yoon, *J. Alloy. Compd.*, 2014, **583**, 320 – 324. 20, 21

[77] S. Thirumalairajan, K. Girija, N. Y. Hebalkar, D. Mangalaraj, C. Viswanathan, and N. Ponpandian, *RSC Adv.*, 2013, **3**, 7549–7561.

[78] R. D. Kumar and R. Jayavel, *J. Mater. Sci. - Mater. El*, 2014, **25**(9), 3953–3961.

[79] Z.-X. Wei, Y.-Q. Xu, H.-Y. Liu, and C.-W. Hu, *J. Hazard. Mater.*, 2009, **165**(1), 1056 – 1061. 19

[80] S. Phokha, S. Pinitsoontorn, S. Maensiri, and S. Rujirawat, *J. Sol-Gel Sci. Techn.*, 2014, **71**(2), 333–341. 22

[81] O. P. Taran, A. B. Ayusheev, O. L. Ogorodnikova, I. P. Prosvirin, L. A. Isupova, and V. N. Parmon, *Appl. Catal. B - Environ.*, 2016, **180**, 86 – 93.

[82] Jérémy Faye and Alexandre Baylet and Martine Trentesaux and Sébastien Royer and Franck Dumeignil and Daniel Duprez and Sabine Valange and Jean-Michel Tatibouët, *Appl. Catal. B - Environ.*, 2012, **126**, 134–143.

[83] J. Wu, J. P. Dacquin, C. Cordier, C. Dujardin, and P. Granger, *Top. Catal.*, 2019, **62**(1), 368–375. 19

[84] H. Téllez, A. Aguadero, J. Druce, M. Burriel, S. Fearn, T. Ishihara, D. S. McPhail, and J. A. Kilner, *J. Anal. At. Spectrom.*, 2014, **29**, 1361–1370. 20

[85] M. Popa, J. Frantti, and M. Kakihana, *Solid State Ionics*, 2002, **154-155**, 437 – 445. 20

[86] M. Popa, L. V. Hong, and M. Kakihana, *Physica B*, 2003, **327**(2), 233 – 236. 20, 21

[87] M. Romero, R. Gómez, V. Marquina, J. Pérez-Mazariego, and R. Escamilla, *Physica B*, 2014, **443**, 90 – 94. 21

[88] B. P. Barbero, J. A. Gamboa, and L. E. Cadús, *Appl. Catal. B - Environ.*, 2006, **65**(1), 21 – 30. 21

[89] P. Coutinho, F. Cunha, and P. Barrozo, *Solid State Commun.*, 2017, **252**, 59 – 63. 21

[90] J. Andreasson, J. Holmlund, R. Rauer, M. Käll, L. Börjesson, C. S. Knee, A. K. Eriksson, S.-G. Eriksson, M. Rübhausen, and R. P. Chaudhury, *Phys. Rev. B*, 2008, **78**, 235103. 21

[91] S. Phokha, S. Pinitsoontorn, S. Rujirawat, and S. Maensiri, *Physica B*, 2015, **476**, 55 – 60. 22

[92] O. Haas, U. Vogt, C. Soltmann, A. Braun, W. S. Yoon, X. Q. Yang, and T. Graule, *Mater. Res. Bull.*, 2009, **44**. 22

[93] T. Uchiyama, M. Nishibori, H. Einaga, and Y. Teraoka, *J. Am. Ceram.Soc.*, 2015, **98**(4), 1047–1051. 22

[94] R. Schlögl, *Angew. Chem. Int. Ed.*, 1993, **32**(3), 381–383. 23

[95] J. Sauer and H.-J. Freund, *Catal. Lett.*, 2015, **145**(1), 109–125. 23, 24

[96] M. Boudart, *Top. Catal.*, 2000, **13**(1), 147. 23

[97] R. Imbihl, R. J. Behm, and R. Schlögl., *Phys. Chem. Chem. Phys.*, 2007, **9**, 3459–3459. 23, 25

[98] F. Gao and D. W. Goodman, *Annu. Rev. Phys. Chem.*, 2012, **63**(1), 265–286. 23

[99] D. Goodman, *J. Catal.*, 2003, **216**(1), 213 – 222. 25

[100] H.-J. Freund, H. Kuhlenbeck, J. Libuda, G. Rupprechter, M. Bäumer, and H. Hamann, *Top. Catal.*, 2001, **15**(2), 201–209.

[101] G. A. Somorjai, R. L. York, D. Butcher, and J. Y. Park, *Phys. Chem. Chem. Phys.*, 2007, **9**, 3500–3513. 25

[102] M. O. Guerrero-Pérez and M. A. Bañares, *Chem. Commun.*, 2002, pp. 1292–1293. 25

[103] I. E. Wachs and K. Routray, *ACS Catalysis*, 2012, **2**(6), 1235–1246. 26

[104] M. Uenishi, H. Tanaka, M. Taniguchi, I. Tan, Y. Nishihata, J. Mizuki, and T. Kobayashi, *Catalysis Commun.*, 2008, **9**(2), 311 – 314. 26

[105] A. K. Opitz, A. Nenning, C. Rameshan, R. Rameshan, R. Blume, M. Hövecker, A. Knop-Gericke, G. Rupprechter, J. Fleig, and B. Klötzer, *Angew. Chem. Int. Ed.*, 2015, **54**(9), 2628–2632. 27

[106] A. K. Opitz, A. Nenning, C. Rameshan, M. Kubicek, T. Götsch, R. Blume, M. Hävecker, A. Knop-Gericke, G. Rupprechter, B. Klötzer, and J. Fleig, *ACS Appl. Mater. Inter.*, 2017, **9**(41), 35847–35860. 27

[107] Götsch, Thomas and Köpfle, Norbert and Grünbacher, Matthias and Bernardi, Johannes and Carbonio, Emilia A. and Hävecker, Michael and Knop-Gericke, Axel and Bekheet, Maged F. and Schlicker, Lukas and Doran, Andrew and Gurlo, Aleksander and Franz, Alexandra and Klötzer, Bernhard and Penner, Simon, *Phys. Chem. Chem. Phys.*, 2019, **21**, 3781–3794. 27, 28

[108] W.-Y. Chung, G. Sakai, K. Shimanoe, N. Miura, D.-D. Lee, and N. Yamazoe, *Sensor. Actuat. B - Chem.*, 2000, **65**(1), 312 – 315. 28

[109] S. Matsubara, S. Miura, Y. Miyasaka, and N. Shohata, *J. Appl. Phys.*, 1989, **66**(12), 5826–5832.

[110] Z. Yu, J. Ramdani, J. A. Curless, J. M. Finder, C. D. Overgaard, R. Droopad, K. W. Eisenbeiser, J. A. Hallmark, W. J. Ooms, J. R. Conner, and V. S. Kaushik, *J. Vac. Sci. Technol. B*, 2000, **18**(3), 1653–1657. 28, 29

[111] Z. Yu, J. Ramdani, J. A. Curless, C. D. Overgaard, J. M. Finder, R. Droopad, K. W. Eisenbeiser, J. A. Hallmark, W. J. Ooms, and V. S. Kaushik, *J. Vac. Sci. Technol. B*, 2000, **18**(4), 2139–2145. 28, 29

[112] S. Thirumalairajan, K. Girija, V. R. Mastelaro, and N. Ponpandian, *ACS Appl. Mater. Inter.*, 2014, **6**(16), 13917–13927. 28

[113] X. Liu, H. Ji, Y. Gu, and M. Xu, *Mat. Sci. Eng. B*, 2006, **133**(1), 98 – 101. 29

[114] I. Bretos, R. Jiménez, J. Ricote, and M. L. Calzada, *Chem. Soc. Rev.*, 2018, **47**, 291–308. 29, 30, 32

[115] L. G. Benning and G. A. Waychunas, in *Kinetics of Water-Rock Interaction*, ed. S. L. Brantley, J. D. Kubicki, and A. F. White, Springer New York, New York, NY, 2008; pp. 259–333. 30, 31

[116] C. Brinker, A. Hurd, P. Schunk, G. Frye, and C. Ashley, *J. Non-Cryst. Solids*, 1992, **147-148**, 424–436. 31

[117] D. B. Hall, P. Underhill, and J. M. Torkelson, *Polym. Eng. Sci.*, 1998, **38**(12), 2039–2045. 31

[118] C. W. Extrand, *Polym. Eng. Sci.*, 1994, **34**(5), 390–394. 31

[119] T. Fang, Y. Guo, S. Cai, N. Zhang, Y. Hu, S. Zhang, Z. Li, and Z. Zou, *Nanotechnology*, 2017, **28**(39), 394003. 31

[120] G. P. Wheeler and K.-S. Choi, *ACS Energy Lett.*, 2017, **2**(10), 2378–2382.

[121] M. I. Díez-García and R. Gómez, *ChemSusChem*, 2017, **10**(11), 2457–2463.

[122] X. Chen, X. Bao, Y. Xiao, C. Zhang, L. Tang, L. Yao, G. Cui, and Y. Yang, *Appl. Surf. Sci.*, 2019, **466**, 989– 999. 31

Chapter 2

Experimental approach and techniques

This chapter includes the description of the experimental techniques along with the sample preparation protocols. Owing to the complementary nature of each analytical technique used, a combination of available surface-sensitive analysis techniques has been used to achieve an overall surface-viewpoint of the model catalysts besides the bulk sensitive techniques. It is aimed at distinguishing the surface/bulk regimes to understand the surface driven heterogeneous catalytic reactions like CO oxidation reaction, as well as the surface-modifications in the bulk catalysts like $LaFeO_3$ perovskites. To provide a quick view and summary of the advanced characterization techniques used in this work, a descriptive figure has been represented in Fig.2.1. XPS, GI-XANES and Raman spectroscopy have been used in *in situ/operando* mode for studying the surface/bulk dynamics.

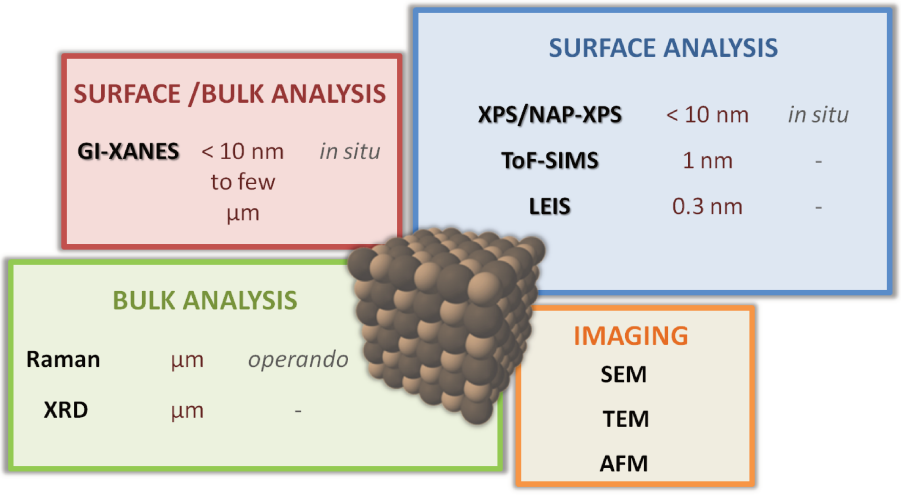

Figure 2.1: Descriptive summary of the characterization techniques used in this work with their scopes and depth resolutions.

2.1 Synthesis protocol

2.1.1 Thin film

Precursor solution

The preparation of the precursor solution for the thin films was based on the concept for preparing alumina supported $LaFeO_3$ thin films [1]. Required amounts of lanthanum nitrate hexahydrate (99.9%, Aldrich) and iron nitrate nonahydrate (99.9%, Aldrich) were diluted in millipore water (15.0 MΩcm at 17°C) for preparing 5 mL of bimetallic solution having an initial metal concentration of [Fe]=[La]=0.3 mol/L. Citric acid (99.5%, Sigma-Aldrich) was then added in order to reach a concentration of 0.6 mol/L, thus leading to a citric acid/(Fe+La) molar ratio of 1. Further, 250 µL of ethylene glycol (99.5%, Fluka) were added to facilitate the polymerization. The solution was then heated under reflux at 50°C overnight. Subsequently, the precursor solution was further heated at 60°C in air ranging between 20 minutes and 1 hour, depending on the required thickness and stoichiometry of the perovskite film as described in table 2.1, except for the ultra thin film (<10 nm) that was diluted in order to have a concentration of 0.03 mol/L. The heating step allows to control the viscosity (concentration) of the precursor solution, which governs the final thickness of the thin film [2].

Table 2.1: Duration of heating the precursor solution under air depending on thickness and/or composition.

S. No.	Perovskite stoichiometry	Thickness description	Thickness range	Heating in air (mins)
1	Stoichiometric	Intermediate	50-100 nm	20
2	La-deficient	Intermediate	50-100 nm	40
3	Stoichiometric	Thick	Upto few µm	45
4	La-deficient	Thick	Upto few µm	60
5	Stoichiometric	Very thin	< 10 nm	0 (dilution in water)

Silicon(100) substrate

Si(100) wafer (Prime CZ, Sil'Tronix) wafer was used as substrate for the thin films. Each circular wafer with a diameter of 7.6 cm was cut into small quadrilateral pieces (0.5 - 1

cm^2) using a diamond pen. They were then washed in acetone and isopropanol, successively, in an ultrasonic bath for 10 minutes each to remove the organic contaminants from the surface. Next after rinsing with millipore water, the samples were immersed into freshly prepared Piranha solution (1:1 vol.% H_2SO_4 and H_2O_2), a strong oxidising agent, for 20 minutes in order to remove any remaining residues. This improved the hydrophilicity of the surface by adding surface hydroxyl groups on the substrate supported by the formation of a thin layer of silica, as evidenced by XPS analysis (detailed later in chapter 3). Finally, the substrates were thoroughly rinsed multiple times with millipore water and stored in the same until just before deposition.

The effect of the oxidative cleaning procedure can be clearly observed in the wettability tests performed on Si-wafers in Fig.2.2 before and after this treatment procedure. On putting a drop of pure water on each substrate, the droplets spread according to the surface hydrophilicity. This is shown by the contact angle between the droplet and the Si-wafer. After the treatment, the contact angle was close to 0°, which ensures almost complete wetting of the substrate by the aqueous precursor solution.

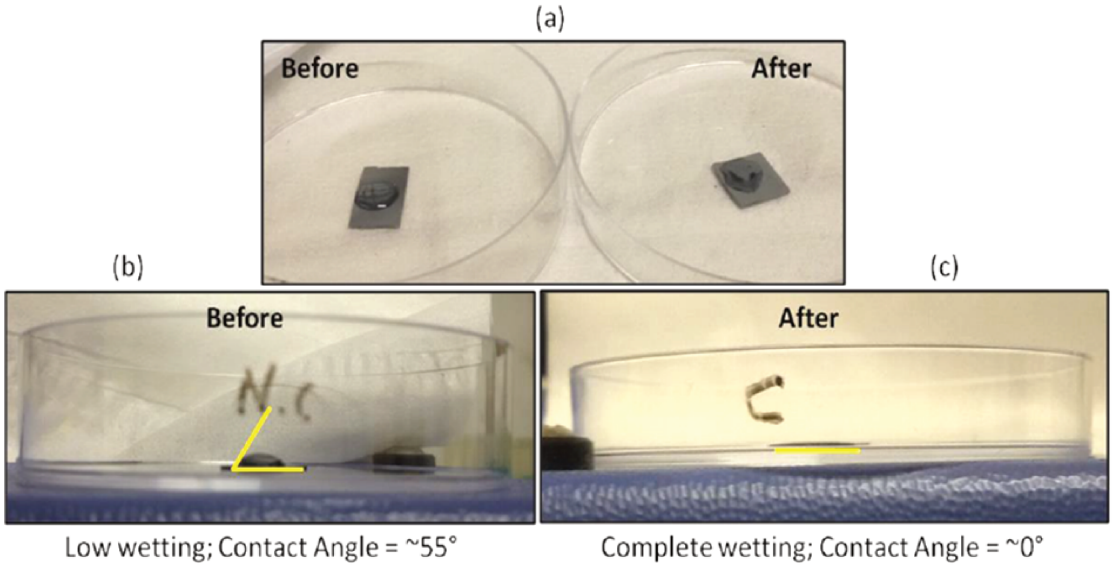

Figure 2.2: Wettability test of silicon substrates: (a) Top view, (b) and (c) side view displaying the contact angle between the water droplet and the substrate before and after the treatment, respectively.

Spin-coating and calcination

The passivated SiO_2/Si(100) substrates were dried under an air flow and immediately put on the spin-coater. About 60 µL of the required precursor solution were added to just cover this substrate well. The two-step spin-coater (SPS Spin 150) was then started at 500

rpm (rotations per minute) for 10 seconds followed by 2000 rpm for 150 seconds. The first step at lower speed ensures uniform spreading of the precursor solution, while the second step at higher speeed dries out the remaining solution by centrifugal forces. Under these spinning parameters, usually a homogeneous coating is formed over the silicon wafer, given the room humidity is below 50%. Every time prior to spin-coating the laboratory humidity was checked to ensure fine deposition.

The spin-coated films were then immediately transferred to a muffle furnace (Nabertherm P330) for calcination under air. The films were initially heated at 0.5°C min^{-1} until 150°C for 2 hours for decomposition of the nitrates from precursor salts. The slow heating ramp was maintained to ensure the formation of uniform thin films. This was followed by heating up to 650°C for $LaFeO_3$ and 800°C for all La-deficient perovskites for 2 hours. A higher calcination temperature was required for the La-deficient compositions to stabilize the perovskite phase in the structure as evidenced by GI-XANES analysis.

2.1.2 Powders

The synthesis of the catalyst powders were based on the conventional sol-gel method via the citrate route using nitrate salts of the metals. Solid precursors obtained after drying overnight at 80°C were calcined in air at 900°C for 8 hours. The preparation of all the powders analysed by advanced characterisation techniques during this work were done by fellow PhD student, Jianxiong Wu, as a part of the collaborative work under the framework of PARTIAL-PGMs project. Particularly, the powder based samples used were $LaFeO_3$, $La_{0.7}FeO_3$ and B-Site substituted ferrites $La_{0.7}Fe_{0.8}M_{0.2}O_3$ (M = Cu or Mn).

2.2 Physico-chemical analytical techniques

2.2.1 Surface sensitive analyses

The lab-based surface analysis techniques were used available at the combined surface analysis platform as shown in Fig.2.3, where XPS, LEIS and ToF-SIMS are connected to each other via a radial chamber allowing successive analysis without any air exposure. It is attached to an oxygen plasma cell to clean the sample surfaces prior to LEIS measurements and a catalysis treatment cell for a thermal pre-treatment of the investigated materials under gaseous feed.

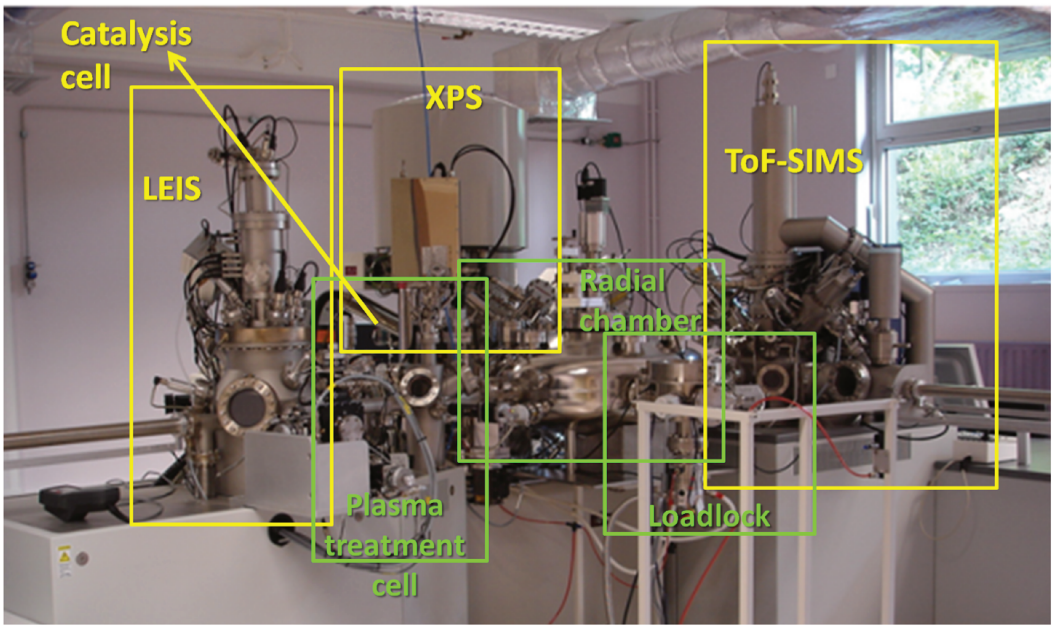

Figure 2.3: The surface analysis platform at UCCS, Univ. Lille.

X-ray photoelectron spectroscopy (XPS)

Principle: XPS is one of the most widely used surface analysis technique to characterize the surface composition, chemical and oxidation states of heterogeneous catalysts. Its use as an efficient analytical tool was ensured by the developments made by Kai Seigbahn in the 1960's, which won him a Nobel prize in 1981. It is a quantitative technique based on the principle of the photoelectric effect. Photoelectrons are ejected when an optimal amount of energy that is higher than the binding energy is used to excite electrons from the core levels of surface atoms of the investigated material. The kinetic energy (E_k) of the ejected photoelectrons are then measured by the analyzer. This phenomenon is described by the following equation:

$$h\nu = E_k + E_b + \phi \tag{2.1}$$

where, $h\nu$ is the energy of the incoming X-ray source. Most commonly used X-ray sources are Mg K_α and Al K_α with values of 1253.6 eV and 1486.6 eV, respectively. ϕ is the work function of the spectrometer. The binding energy (E_b) of the core level electron can thus be determined using this relation, which is the parameter of interest for elemental identification.

A photoemission spectrum can comprise of different features depending on the type of

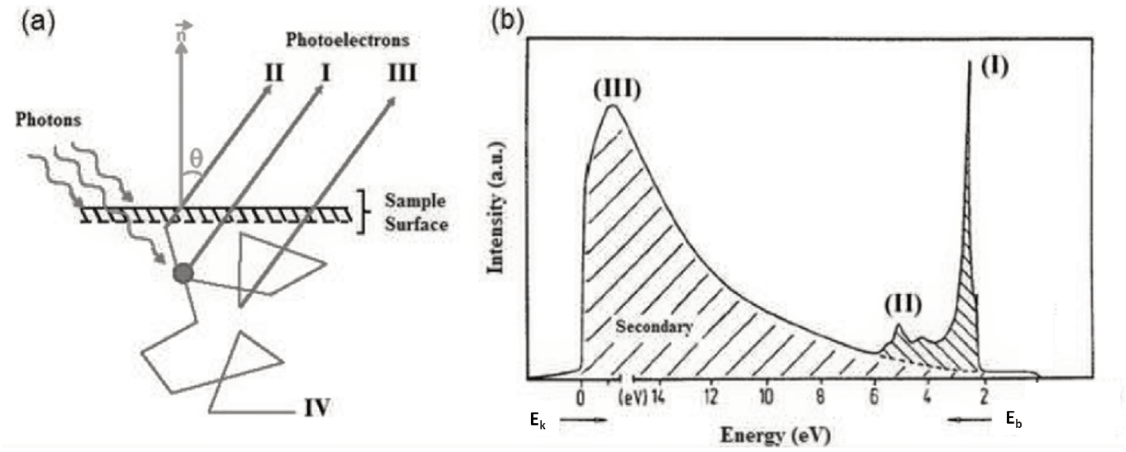

Figure 2.4: Photoelectron spectroscopy: (a) Possible interactions between the ejected photoelectrons with the sample near the surface after irradiation by X-rays and (b) scheme of a photoemission spectrum [3].

interaction of the photoelectron with the sample as shown in Fig.2.4 [3]. An XPS spectrum comprises of the main photopeak (I) formed by elastically scattered photoelectrons from the sample surface, which have suffered no loss in energy (Fig.2.4(b)). A photoemission peak is accompanied by energy loss peak caused by inelastic scattering of the electrons (II) that have lost small energies ranging from few eV up to 30 eV. The electrons undergoing multiple scattering with major loss in energy lead to secondary electrons (III), that contribute to the large background, commonly seen in the XPS survey spectrum. Also, some photoelectrons simply cannot escape from the surface and remain undetected due to large energy lost (IV).

The binding energy of an electron depends on the element, its orbital as well as its chemical environment. As the chemical bonding changes, the resulting E_b of the core electrons also vary depending on whether there is an withdrawal of valence electrons charge or not, which exhibits stronger electronic shielding effect to the core electrons. This is known as the chemical shift. For example, the C 1s photopeak of the C = O bond is at higher E_b than the C – C bond (taken as a E_b referenc) due to more shielded electrons in the carbonyls.

The fundamental differential equation of XPS considers the raw intensity dI from a slice of the solid sample of thickness dz, given by

$$dI_{X,nlj} = F\, n_X(z)\, (\frac{d\sigma_{X,nlj}\, \Delta\Omega}{d\Omega})\, T\, exp(\frac{-z}{\lambda\, sin\theta})\, dz \tag{2.2}$$

where, F is the photon flux from the X-ray source, $n_X(z)$ is the number of X atoms per unit

volume of the sample, $d\sigma_{X,nlj}/d\Omega$ is the differential cross-section of photo emission, $\Delta\Omega$ is the solid angle of the analyzer, θ is the angle between the direction in which the photoelectrons are emitted and the surface, T is the transmission factor of the spectrometer that includes geometric parameters and detector efficiency depending on the kinetic energy of the photoelectrons, λ is the inelastic mean free path of the photoelectrons emitted from the nlj orbital of the element X.

The depth of surface probed by XPS can vary from 2 to 10 nm depending on the inelastic mean free path (λ) of the photoelectron, which is related to the E_k of the electrons and the nature of the material probed. λ refers to the distance that an electron can travel before it faces any inelastic energy losses. The information depth is therefore given by $3\lambda\sin\theta$, corresponding to 95% of the ejected photoelectrons resulting in the XPS signal from this depth with a detection limit of around 1 atomic percent [3].

Near-ambient pressure XPS (NAP-XPS) : Conventional XPS system works under ultra high vacuum (UHV) conditions to avoid the interactions between the photoelectrons and the gas molecules. XPS measurements are therefore performed at 10^{-8} to 10^{-11} mbar to ensure maximum number of electrons reaching the analyzer. Today's technology has now permitted operating under higher working pressures (few mbar), called the near-ambient pressure XPS (NAP-XPS), allowing even analysis of liquids [4]. This has been made possible due to the presence of differential pumping system, which helps to separate the analysis chamber from the analyzer by lowering the pressure successively at each pumping stage while minimizing the rate of collisions, as presented in Fig.2.5. The electrons are focused into the aperture of each stage by electrostatic lenses ensuring collection of larger fraction of the photoelectrons through it. The pumping nozzle is therefore placed very close to the sample as shown in Fig.2.6, which also depends on the type of gas and the working pressure used.

In addition, X-rays originating from a synchrotron radiation source provides high photon flux leading to higher intensity of the emitted photoelectrons and maintain sufficient photon count for the signal in spite of the inelastic collisions from ambient gas molecules. The NAP-XPS system situated at the TEMPO beam line of synchrotron SOLEIL (France) has been utilised for *in situ* experiments in this work. The setup consists of five chambers namely, the loadlock, transfer, catalysis, preparation and the analysis chamber, as shown

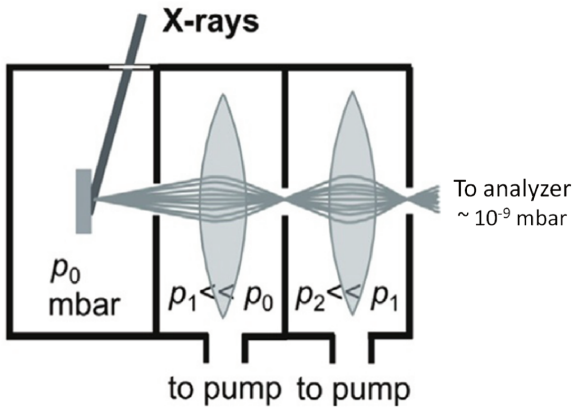

Figure 2.5: Schematic stages of differential pumping systems with electrostatic lenses for beam focusing [4].

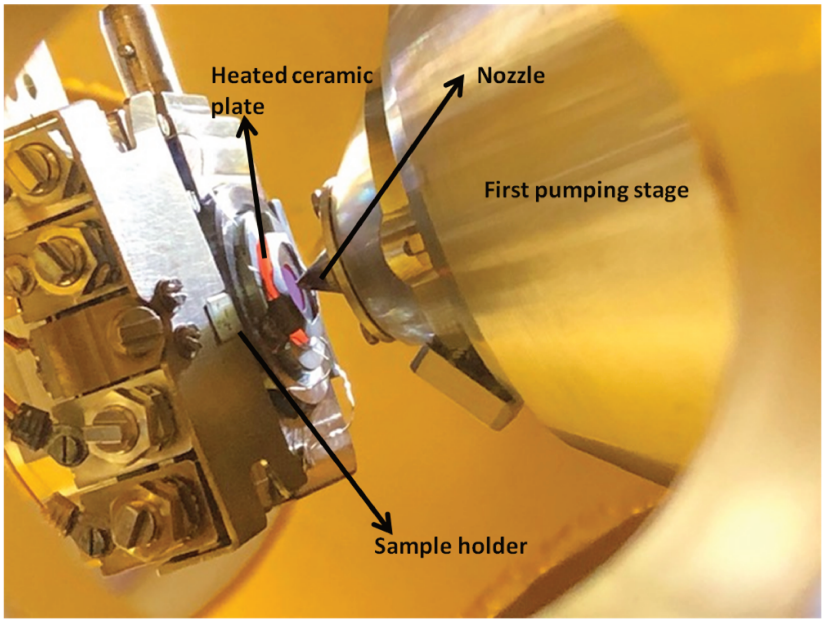

Figure 2.6: Sample holder and nozzle position during analysis of the sample in the analysis chamber.

in Fig.2.7. The loadlock allows the introduction of the samples at relatively higher vacuum pressure of 10^{-7} mbar while maintaining the isolation of rest of the setup at UHV before moving to the transfer chamber. The catalysis chamber is dedicated to any required thermal pre-treatment at high pressure (~bar) and the preparation chamber allows surface science based functions like ion sputtering, LEED, CVD etc. The sample can be directly transferred to the preparation chamber from the transfer chamber, if the catalysis chamber is not required. Finally, the analysis chamber allows heating of the sample using a ceramic plate on the sample holder (internal) or a laser heating device (external).

The photon energy for the incident photon beam can be tuned as per requirements between 50 to 1500 eV, which is one of the main advantages of using a synchrotron beam.

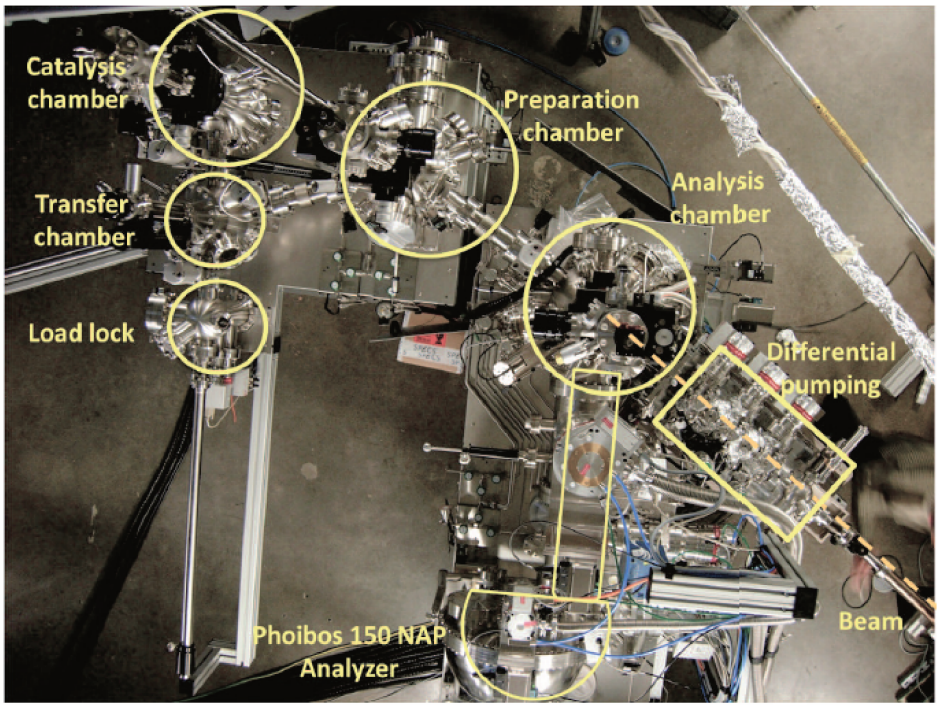

Figure 2.7: The NAP-XPS instrument at TEMPO beam line, SOLEIL Synchrotron (France).

Five windows with different ranges of energy are available across two hutches (HU44 and HU80) for this purpose as shown in Fig.2.8. This window is usually chosen based on the elemental orbital to be probed while keeping a decent photon flux.

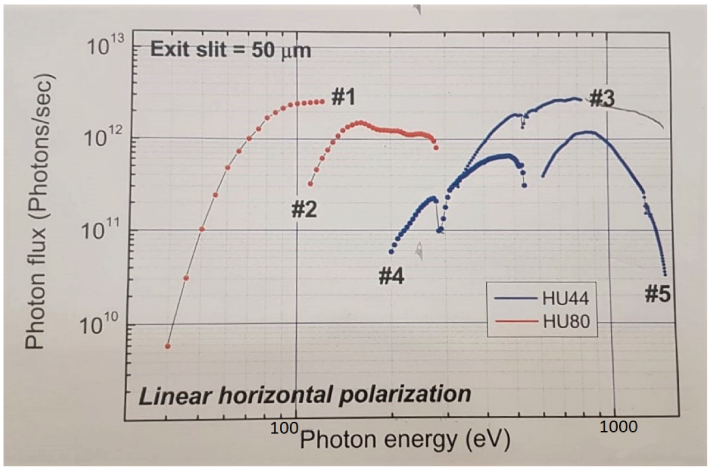

Figure 2.8: Variation of photon flux with photon energy across the different energy windows.

Experimental conditions: A Kratos Analytical Axis UltraDLD spectrometer was used for lab-based XPS analysis. A monochromatic aluminum Kα source at 1486.6 eV is used for the excitation. The pass energy was 20 eV for an analyzed surface area of 700 µm x 300 µm. Charge compensation was applied to neutralize any charging effects. The measurements were done at a pressure of 10^{-10} mbar in the analysis chamber. Quasi *in situ* measurements are made using the catalysis treatment cell, where the samples are ther-

mally pre-treated under gaseous reactant flow (50 mL/min) at 500°C for 1 hour under atmospheric pressure in a stainless steel sample holder at 5°C/min. The pre-treated sample is then transferred to the analysis chamber under UHV.

Additionally, the *in situ* experiments were performed at the TEMPO beamline of synchrotron SOLEIL [5]. NAP-XPS experiments were performed in an analysis chamber at 0.1 mbar of a reactive gas with a differentially pumped SPECS Phoibos 150-NAP electron analyzer. The analyzer aperture has a diameter of 0.3 mm at a distance of around 1 mm from the sample surface. The analyzer axis is normal to the sample surface and at 54° with respect to the beam entrance axis. No charge compensation is available for this setup. Overview spectra were recorded at 950 eV (maximum photon flux in $^{\#}3$) to allow comparison of the intensities of each element (La 3d, Fe 2p, O 1s, C 1s, and Si 2s) after every treatment step. This energy was experimentally chosen with respect to the highest binding energy of interest (La 3d >834.0 eV), maximum photon flux and correct background without Auger interference. Further, highly resolved spectra were collected while maintaining a E_k of 120 eV to probe similar depth for each orbital.

The C 1s from adventitious carbon contamination at 285.0 eV was used for referencing of all the XPS spectra. In case of absence of any carbon signal, the O 1s signal from the perovskite lattice was used as the reference (E_b ~530.0 eV). The spectral decomposition as well as the quantification were carried out using the CasaXPS software. The steps of the *in situ* treatment is shown in Fig.2.9 that involves firstly, activation of the catalyst under air followed by CO exposure for 1-2 hours (5°C/min). Return spectra at low temperature was recorded in each case to account for the thermal effects on the samples.

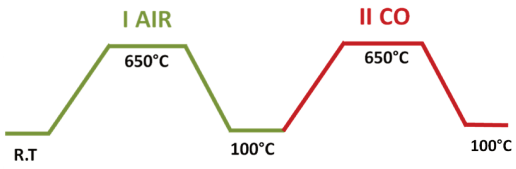

Figure 2.9: Steps of *in situ* treatment during NAP-XPS analyses.

Time of flight secondary ions mass spectrometry (ToF-SIMS)

Principle: ToF-SIMS is well-established surface analysis technique with high sensitivity in the ppm range (more sensitive than XPS) providing detailed elemental and molecular information about the surface with a depth resolution of ~1 nm. A general scheme of the

ToF-SIMS apparatus is given in Fig.2.10(a). It uses a pulsed beam (ns range) of primary ions (few keV range) to generate secondary ions and neutral species from the surface of the sample induced by a collision cascade as shown in Fig.2.10(b) originating from the uppermost one or two monolayers. The primary ions transfer their energy to the atoms of the targeted material during successive collisions and result in emission of molecular and atomic ionic species from the very surface. The positive or negative secondary ions emitted are then accelerated towards the time-of-flight analyzer by applying a potential (U), where the ions take different time (t) to travel through a fixed distance (L) according to their mass-to-charge ratio [6]. Measurement of the time-of-flight allows to determine the mass of all the secondary ions thus formed, given by the following equation:

$$\frac{m}{z} = \frac{2\mathrm{U}t^2}{\mathrm{L}^2} \tag{2.3}$$

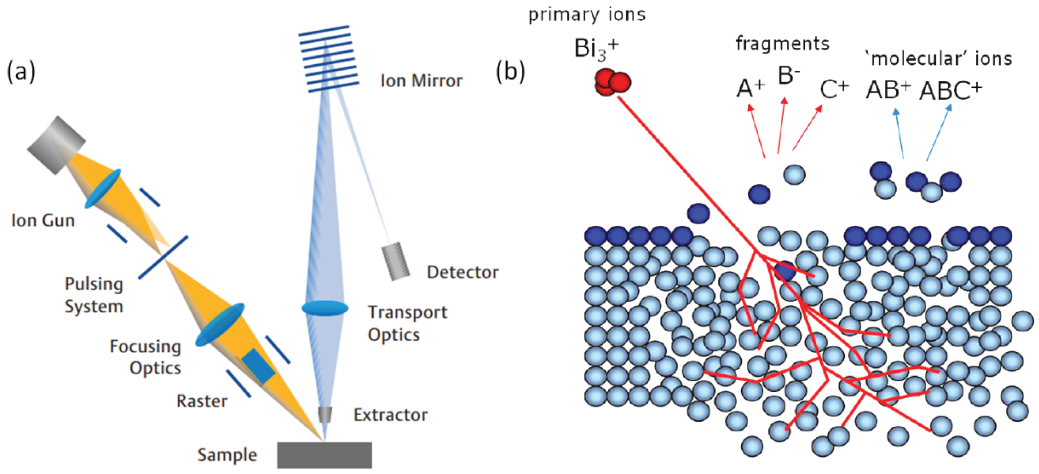

Figure 2.10: ToF-SIMS: (a) Scheme of experimental setup (source: ION TOF Gmbh) and (b) secondary ion emission by a collision cascade in ToF-SIMS [7].

An accurate surface analysis by ToF-SIMS is made under static conditions by keeping a low primary ion dose below 10^{13} cm^{-2}. This ensures sputtering less than 1% of a monolayer, such that the probability of the primary ion to interact with exactly the same region on the surface of the sample is almost negligible. When the ionic dose is higher leading to surface erosion, it is referred to as 'dynamic SIMS'. ToF-SIMS measurements can be done in three different modes [8] given as follows:

(1) Bunch mode for spectroscopic analysis - This static mode provides high mass resolution while compromising strongly with the lateral resolution (2-5µm).

(2) Burst/ burst alignment mode for imaging - The burst alignment mode allows to have

a good spatial resolution up to 200 nm under static conditions with poor mass resolution. The burst mode, however, permits both better mass and lateral resolution but with rather low signal intensities.
(3) Depth profiling mode - Depth profiling is made possible with a dual-beam configuration, where one primary ion beam is used for data collection and the other one is dedicated for sputtering of the material, sequentially. The analysed area is kept 2 to 3 times smaller than the sputtered one to avoid edge effects at the crater.

With this technique, all elements including hydrogen and their isotopes can be well identified chemically, both spatially and in depth. However, it does not allow easy quantification due to extensive matrix effects as the secondary ions yield vary with the change of the chemical nature of the surface.

Experimental conditions: The samples were analyzed on a ToF.SIMS 5 spectrometer (ION TOF GmbH, Germany) equipped with a pulsed bismuth liquid metal ion gun with the primary ion cluster of Bi_3^+ (25 keV, 1 pA current), as it has lower energy per atom, it causes less fragmention compared to Bi^+. The analyzed area was 500 µm x 500 µm for spectral analyses while maintaining static conditions, in both positive and negative polarity. For depth profiling measurements, Bi_3^+ was used for analysis and Cs^+ (1 keV, 90 pA) for sputtering as they enhance the yield of negative ions. The sputtered area was 400 µm x 400 µm while the analysis was done on an area of 100 µm x 100 µm. Charge compensation was used for all samples using low energy electrons (20 eV).

Low energy ion scattering spectroscopy (LEIS)

Principle: LEIS is an unique surface analytical technique that provides information on the elemental composition of the outer most atomic layer quantitatively. It is based on the principle of classical mechanics according to the law of energy and momentum conservation, where noble gas ions ($^4He^+$, $^{20}Ne^+$ etc.) with mass m_1 having a known energy E_i is aimed at the surface to collide with the surface atoms of mass m_2 and get backscattered as shown in Fig.2.11. The energy of these backscattered ions E_f is calculated by the following equation given in terms of the kinematic factor (K_m):

$$K_m = \frac{E_i}{E_f} = \left(\frac{cos\theta + \left(\left(\frac{M_2}{M_1}\right)^2\right) - sin^2\theta)^{1/2}}{1 + \frac{M_2}{M_1}}\right)^2 \tag{2.4}$$

where, θ is the backscattering angle fixed by the instrument geometry. Since E_i, m_1 and θ are already known, the E_f can be measured by the analyzer and therefore the mass of the surface atom can be calculated [9]. The detection of the elements is possible for atoms with mass greater than that of the incident ion. Typically, the analyzes are performed with $^4He^+$ at 3 keV energy, which show better resolution at lower masses (energy). To improve the resolution of the signals from heavier elements that are too close to each other, it is necessary to use primary ions of higher mass such as $^{20}Ne^+$ or $^{40}Ar^+$.

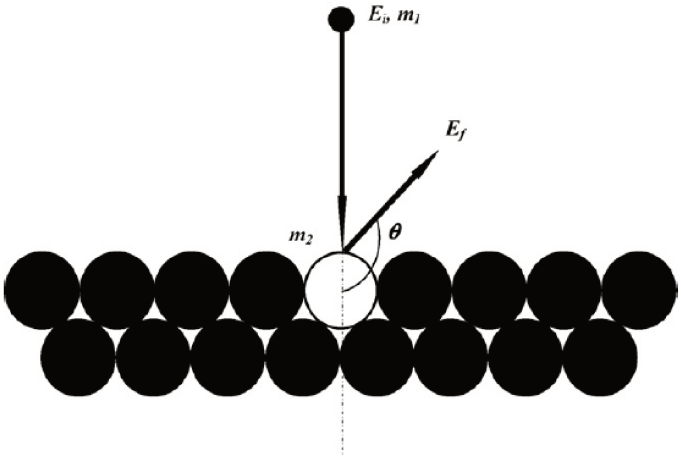

Figure 2.11: A scheme of low energy ion scattering process [10].

Typical LEIS signal of an element comprises of a surface peak and a preceding tail due to its presence in subsequent sub-atomic layers as shown in Fig.2.12 represented by a theoretical LEIS spectrim of a ZrO_2/Si thin film. Only Zr and O show a surface peak while Si only shows sub-surface signal given by the background. The LEIS spectrum can provide information about in-depth distribution non-destructively up to 10 nm. Here, only one in thousand He^+ ion is backscattered by the first atomic layer while others undergo neutralization by penetration into the solid and scattered by the sub-atomic layers or reionize when passing out of the solid giving rise to the background on the lower energy side. In addition, the intensity of the surface peak after background substraction is proportional to the surface coverage of the atom.

LEIS data can be quantified as they are known to have almost no matrix effects since the probablility of the scattered ions P_i^+ is not sensitive to the chemical state of the element, unlike in ToF-SIMS, as has been also experimentally observed in several kind of materials [11]. This means that the ionic yield of the element does not vary with the presence of another atom of any type. Thus, with this commonly accepted notion, it is possible to calculate the surface atomic concentrations using LEIS data. The yield of backscattered

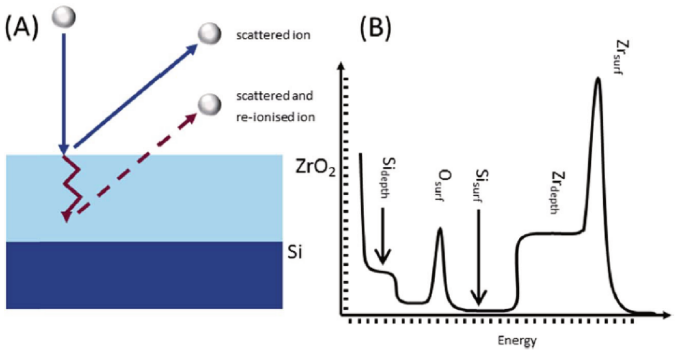

Figure 2.12: Typical LEIS signals with the surface elemental peak and a sub-surface tail dependent on distribution of sub-atomic layers [9].

ions S_i of element i is proportional to the atomic surface concentration N_i by the following relation:

$$S_i = \frac{I}{e} t \xi R n_i N_i \tag{2.5}$$

where, I is the current of primary ions, e refers to elementary charge, t is the time of acquisition, ξ is an instrumental factor depending on the analyzer transmission, detector efficiency and solid angle, R is the roughness factor (usually ~0.9 for oxides and ~0.6 for metals [12] and n_i is the elemental sensitivity factor given by:

$$n_i = P_i^+ \frac{d\sigma_i}{d\Omega} \tag{2.6}$$

where, P_i^+ is the ion fraction of projectiles after backscattering and $d\sigma_i/d\Omega$ is the differential cross-section of scattering. The factors I, t, ξ and $d\sigma_i/d\Omega$ are constants for analysis done with same instrumental parameters. Since neutralization is a complex process, the ion fraction is expected to be a fairly complex quantity, making the direct quantification of the surface composition using equation 2.5 a difficult task. Thus by calibration with a reference sample of known surface composition, the LEIS signals can be quantified according to:

$$N_i = \frac{S_i}{S_i^{ref}} N_i^{ref} \tag{2.7}$$

where, the atomic surface concentration N_i^{ref} for the reference sample can be calculated from their respective mass and density [13], according to the following relation:

$$(\rho^*)^{2/3} = \left(\frac{\rho N_A}{M}\right)^{2/3} \tag{2.8}$$

here, ρ is the bulk density and M is the molar mass of the reference sample, while N_A

refers to the Avogadro number equivalent to 6.02 x 10^{23} atoms/mol. For quantifying mixed oxides like a $LaFeO_3$ perovskite, lanthanum oxide (La_2O_3) and iron oxide (Fe_2O_3) can be used as the references by calculating their relative sensitivity factors, described in further details in chapter 3.

Furthermore, just like in ToF-SIMS, the 'static' conditions must be met, where less than 1% of the monolayer is eroded during analysis. The ionic dose (ions/cm^2) can be calculated according to the following equation:

$$I_d = \frac{ItS}{eA} \tag{2.9}$$

here, I is ionic current, t is the acquisition time (s), S is the ionic yield (depends on the type and energy of the primary ion and sample density), e refers to elementary charge (1.6 x 10^{-19} C) and A is the analyzed surface area (cm^2).

Experimental conditions: LEIS spectra were recorded with a Qtac100 spectrometer (ION TOF GmbH, Germany) with primary ion sources of $^4He^+$ at 3 keV (5 nA) and/or $^{20}Ne^+$ at 5 keV (1 nA). Special attention was given to the experimental parameters (analysed area and acquisition time) such that total ionic dose does not exceed 1-3% of a monolayer during the analysis. Prior to any LEIS measurements, the samples were subjected to the oxygen plasma source to remove the surface organic contaminants for 10 min at around 10^{-5} mbar partial pressure of oxygen before transfer to the main analysis chamber under UHV.

A depth profiling with LEIS was made using the primary gun for analysis and sputtering for qualitative information. $^4He^+$ at 3 keV (5 nA) was used for analysis with a acquisition time of 60 s on 300 µm x 300 µm with an ionic dose of 4.2x10^{14} ions/cm^2. The primary gun was then loaded with the $^{20}Ne^+$ at 5 keV (100 nA) and sputtered for 20 s at 2.2x10^{15} ions/cm^2 initially. The respective ions were loaded one by one for the consecutive measurement and sputtering cycles as the spectrometer is not equiped with a second dedicated sputter gun. The sputtering doses were gradually increased up to 1.8x10^{16} ions/cm^2. With these particular conditions, one depth profile took one day instead of less than 1 hour in case of ToF-SIMS depth profiling.

2.2.2 Bulk and/or surface sensitive analyses

Grazing incidence X-ray absorption near-edge spectroscopy (GI-XANES)

Principle: X-ray absorption spectroscopy (XAS) is also based on the principle of photo-electric effect similar to XPS. When the incident photon energy is more than the threshold energy, it can excite an electron from the core level into the continuum, leading to a sharp rise in the intensity of absorption called the absorption edge. The X-ray beam with intensity I_0 passes through a sample of thickness x, while being absorbed by the sample leading to the final beam intensity of I_t. The absorption cross-section $\mu(E)x$ is related to the attenuation of this X-ray beam, measured by ionization chambers and is given by:

$$ln\frac{I_0}{I_t} = \mu(E)x \tag{2.10}$$

The excited atom after photo ionization can relax through fluorescence as shown in Fig.2.13.

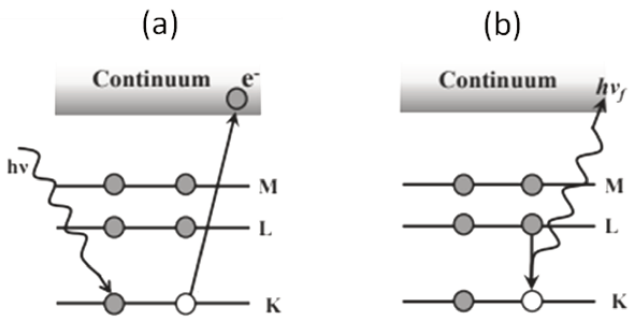

Figure 2.13: Schematic sketch of (a) X-ray photoionization process and its relaxation by (b) fluorescence.

A XAS experiment can be performed in the transmission mode or fluorescence mode. The former mode is used more commonly and allows to analyze the material, where the I and I_0 are measured by progressively stepping the monochromator across a range of wavelengths. In the latter case, a detector is placed close to the sample, perpendicular to the incident X-ray beam to detect larger fraction of the emitted fluorescence with the possibility of tuning the incident angle between the beam and the sample to adjust the penetration depth of the X-rays in grazing incidence. The absorption coefficient $\mu(E)$ in X-ray fluorescence is given by $\mu(E) \propto \frac{I_f}{I_0}$, where I_f is intensity of the fluorescence line associated with the absorption process.

This grazing incidence mode allows surface sensitive analysis of the sample under investigation with a depth resolution of 2 to 8 nm [14]. Grazing incidence XAS is useful for model systems with low amount of adsorbates on the surface of the sample and/or simultaneous surface and bulk measurements for a reactive system. Here, the flourescence yield is dependent on the angle, which allows to investigate the near surface of layered systems such as a thin film. Fig.2.15 shows the variation of flourescence with changing incidence angle for one of our samples ($LaFeO_3$ thin film). At the criticle angle, which is the smallest angle of incidence that results into total reflection, a standing wave is created due to incoming and reflected beams such that the intensity of the primary beam is largely enhanced (Fig.2.14). Hence, the signal of fluorescence sharply increases for the atoms located at the surface and then decreases as reflectivity is reduced towards the bulk. In this work, the investigated $LaFeO_3$ based perovskites have a theoretical critical angle of 0.34° (0.22° for Fe_2O_3). For our measurments the critical angle varies between 0.25° and 0.35° depending on the sample, which is in agreement with the theoretical ones calculated for the investigated materials.

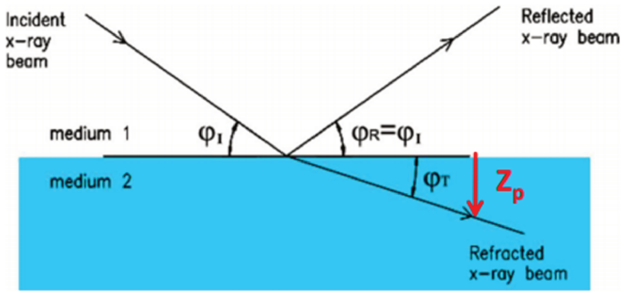

Figure 2.14: Scheme representing total refection of X-rays showing optical path of incident, reflected and transmitted beam at the interface of two media.

A typical X-ray absorption spectrum (Fig.2.16) comprises of the X-ray absorption near edge structure (XANES) and the extended X-ray absorption fine structure (EXAFS) corresponding to different kinds of physical processes. The XANES region constitutes the absorption edge with information regarding the oxidation state, symmetry and the electronic configuration of the excited atom corresponding to further excitation of the core electron towards the continuum, up to 50 eV above the absorption edge. In this work, phase composition determination is made using reference compounds by linear combination fits.

The EXAFS region, located 50 to 1000 eV above the edge energy corresponds to mainly single scattering processes. The photoelectron wave function is backscattered by the sur-

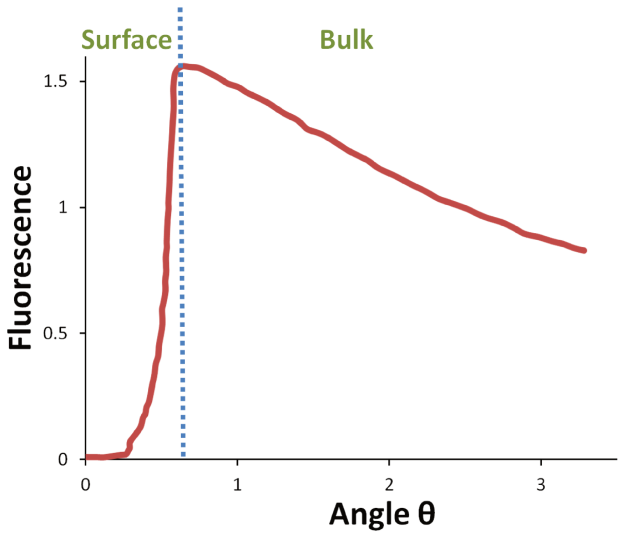

Figure 2.15: Variation of the fluorescence signal as a function of the incident angle for a $LaFeO_3$ thin film as recorded during our experiment.

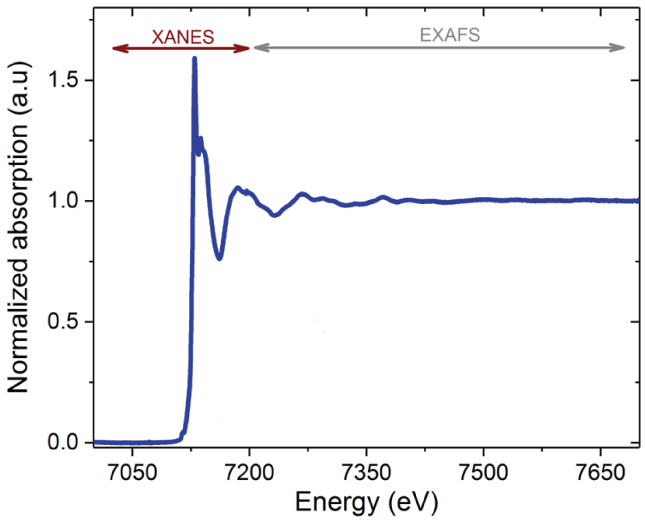

Figure 2.16: X-ray absorption spectrum of $LaFeO_3$ at the Fe K-edge showing the XANES and EXAFS regions.

rounding atoms resulting into an oscillatory nature of the absorption coefficient. This contains important structural information about the local environment like the inter atomic distances, coordination number and thermal disordering.

The investigation is mainly focused on the XANES region in this thesis work due its excellent ability to distinguish between phases. The EXAFS region had low signal-to-noise ratio due the low amount of matter on the thin film. Noise reduction could be made by longer acquisition time but was risky as long duration under high temperature could erode the film layers.

Experimental conditions: The GI-XANES measurements were made at the SAMBA

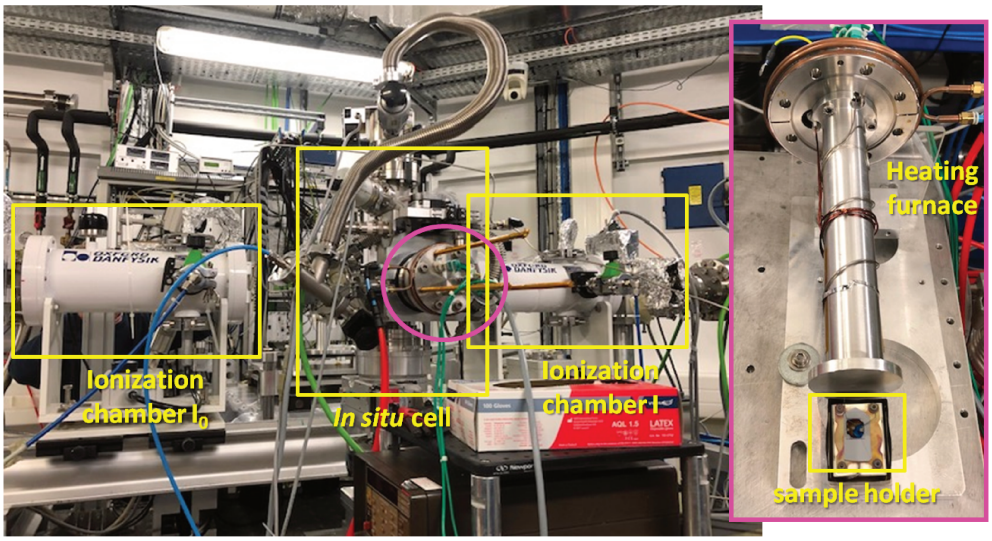

Figure 2.17: The GI-XANES experimental setup at SAMBA beamline, SOLEIL France.

beamline in SOLEIL synchrotron facility (France) [15, 16]. A picture of the beamline has been given in Fig.2.17. The beam size at the sample is 200 µm x 300 µm with a focusing monochromator between two bendable cylindrical mirrors with 6-35 keV energy range. Spectra were collected at the Fe K-edge in the fluorescence mode. The sample was loaded in an *in situ* chamber with a dynamic flow of either air or CO (5% CO in He) at 50-100 mbar. Reference powder compounds were recorded in the transmission mode by dilution in barium nitride. XANES data analysis was done using Athena software [17]. The *in situ* procedure has been already given in Fig.2.9 in section 2.1.1 (XPS part). It involves firstly, activation of the catalyst under air followed by CO treatment at 650°C for 1 hour. XANES spectra were recorded only at each temperature plateau, where several spectra could be averaged and not during the temperature ramp, since a single aquisition spectra was quite noisy owing to the low thickness of the thin film.

2.2.3 Bulk sensitive analyses

Raman spectroscopy

Principle: Raman spectroscopy is a popular technique used for chemical analysis of materials bulk providing information on the structure, crystallinity and phase of the investigated material. It is based on the principle of Raman scattering named after its discoverer Sir C.V. Raman, for which he won the nobel prize in 1930. When light interacts with a molecule, it gets scattered with and without change in energy of the incident light. Most of

the scattered light has the same energy as that of the source (ν_0), known as Rayleigh scattering, while only one in million photons are scattered inelastically by change in the polarizibility of the molecule. This can be caused by its interaction with the molecular vibrations and phonons of the scattering molecule with a loss in energy (ν_0-ν_m) called Stokes Raman or gain in energy (ν_0+ν_m), called the anti-stokes Raman scattering, as shown in Fig.4.2. Since, the transition rate from a more populated energy level to the virtual excited state is higher, therefore, Stokes lines are more intense in the Raman spectrum. The spectra are represented in terms of wavenumbers (cm $^{-1}$) to account for the energy shift caused by the scattering process. Each material has its own Raman fingerprint depending on the vibrational modes in the molecule.

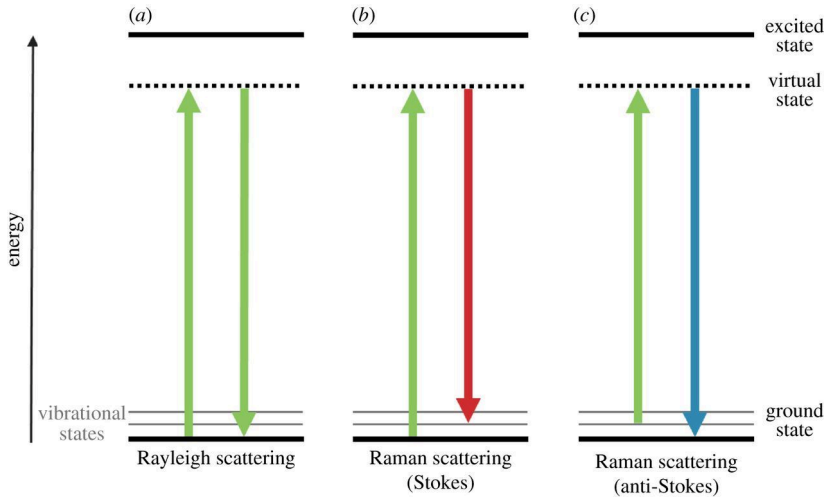

Figure 2.18: Energy diagram of Rayleigh and Raman scattered light.

Experimental conditions: An Ar^+ laser of 488 nm was used to record the Raman spectra installed with neutral density filters to adjust the laser power with a X100 microscope objective (N.A 0.9). The signals were collected through a confocal hole of 150 µm in backscattering mode with 1800 grooves grating having a resolution of around ~2 cm^{-1} and analyzed using a Peltier-cooled CCD from Horiba Labram HR. The spectrometer was calibrated using the most intense band of the Si(100) reference at 520.6 cm^{-1}.

***Operando* Raman:** The Raman spectrometer was extended for *operando* measurements as represented in Fig.2.19 with the detailed scheme in Fig.2.20 . An *in situ* Raman cell (Harrick) was used with its inlet connected to gas flow regulators and the outlet connected to a micro-GC to detect the gaseous products. A water saturator facility is also attached for providing a partial pressure of water by controlling the temperature (~940

Pa). The powder samples are directly put into the sample holder inside the cell while the thin films are put on a bed of well ground silicon carbide. For *in situ/operando* measurements, the sample was heated at 5°C/min and a spectrum was recorded at every 100°C. Every measurement was done on a fresh location on the sample to avoid any induced damage from the laser.

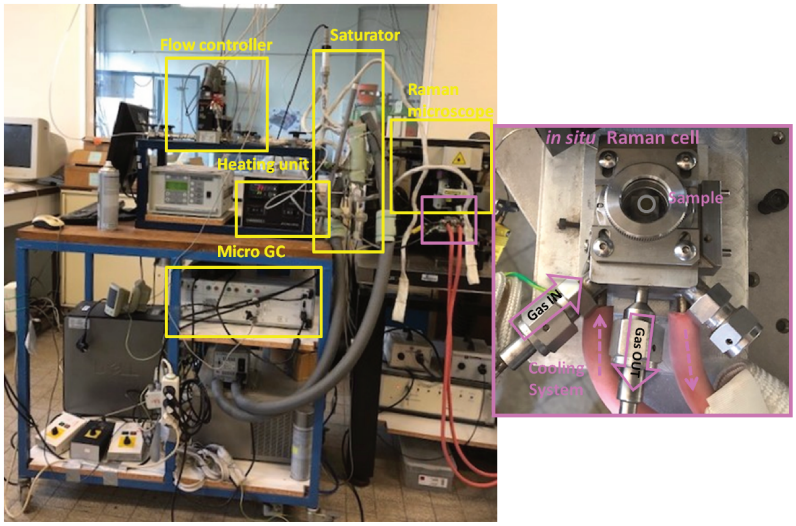

Figure 2.19: *Operando* Raman setup at UCCS, Univ. Lille.

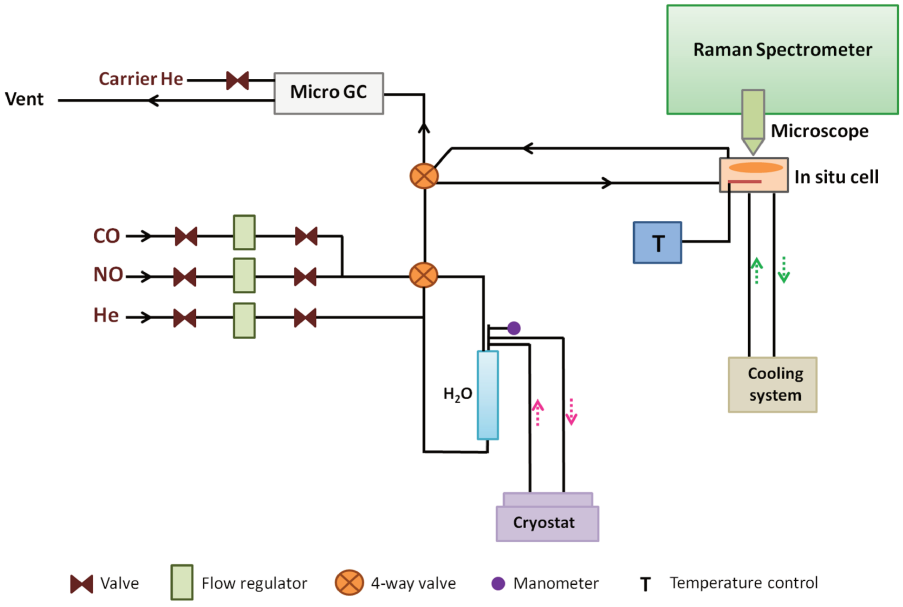

Figure 2.20: Experimental scheme of the *operando* Raman setup.

X-ray diffraction (XRD)

Principle: XRD is a widely used bulk technique to determine the phase and the lattice parameters of crystalline materials. A monochromatic X-ray light is directed to the sample where it creates constructive interference with the crystalline sample to satisfy the Braggs's law ($n\lambda=2d\sin\theta$), relating the incident wavelength to the lattice interplanar spacing d and the diffraction angle θ. The sample is scanned through a range of 2θ values giving rise to diffraction peaks that are converted into d-spacing values for identification of crystalline materials. It is non-destructive in nature with a limit of detection of 2% by volume and can detect nanoparticles above 5 nm in size.

Experimental conditions: The X-ray diffraction (XRD) structural characterization of the thin films were carried out using a 9-kW Rigaku Smartlab rotated anode X-ray diffractometer using Cu Kα (1.5418 Å), operated in Bragg-Brentano reflection geometry. To avoid any saturation of the detector due to the (004) peak of the oriented Si substrate, the sample was intentionally disoriented by 2°, once it was verified that the deposition was not epitaxial but polycrystalline.

2.2.4 Microscopic techniques

Scanning and transmission electron microscopy

Electron microscopy techniques use electrons possessing short wavelengths as a radiation source due to their ability to provide high resolution images. There are two main types: the transmission (TEM) and the scanning electron microscope (SEM). The SEM image is formed by scanning a focused beam of electrons in a raster pattern on the sample. The primary beam interacts with the surface atoms and emit particles at each raster point such as secondary and backscattered electrons (SEM imaging), diffracted backscattered electrons (EBSD for crystal structure determination) and X-rays (elemental analysis). Thus, providing quality data on sample's morphology, chemical composition and crystallinity. It has a lateral resolution of less than 20-40 nm. The TEM image is formed by transmission of the high voltage electron beam through a very thin sample (100 nm) carrying structural information of the analysed material. The image is then magnified by magnetic lenses and recorded on a photosensitive screen or detector. It allows to see atomic scale information within the sample. The resolution can be improved further by combination of the above two principles commonly called scanning transmission elec-

tron microscopy (STEM). It works similar to SEM but the beam is essentially scanned over a TEM sample. A CCD chip or a high angle annular dark field (HAADF) is used to detect the transmitted beam. In this thesis work, both SEM and TEM have been used for investigating the overall morphology of the thin film, its thickness, chemical and structural aspects. These analyses were done at the microscopy platform of UMET, University of Lille using Hitachi S4700 and FEI Tecnai G2-20 twin for SEM and TEM analysis, respectively.

Atomic force microscopy (AFM)

AFM is based on a tip (cantilever) assembly interacting with the sample in a raster scanning motion. A laser beam is used to detect the attractive/repulsive forces between the tip and the surface causing deflection of the cantilever. A position sensitive photo diode can track the changes in the cantilever deflection during lateral as well as vertical motion of the probe. An AFM setup commonly operates in three different modes depending in the nature of the motion of the tip: contact mode, tapping mode, and non-contact mode. The contact mode involves analysis when overall force is repulsive when in close contact with the surface with atomic resolution but prone to sample scraping. In the tapping mode the cantilever's oscillation amplitude changes according to the topography of the sample with high lateral resolution and least sample damage. The non-contact mode involves attractive forces between the cantilever and sample due to Van der Waals interactions, at higher tip-to-surface distances than the contact mode. The surface morphology of the thin films was locally investigated using a commercial AFM (MFP-3D, Asylum Research) at UCCS, University of Artois. It works in the tapping mode under ambient conditions using Si tips (Nanoworld Arrow-NC probes) with cantilever stiffness of 40 Nm^{-1}.

2.3 References

[1] X. Liu, H. Ji, Y. Gu, and M. Xu, *Mat. Sci. Eng. B*, 2006, **133**(1), 98 – 101. 44

[2] D. B. Hall, P. Underhill, and J. M. Torkelson, *Polym. Eng. Sci.*, 1998, **38**(12), 2039–2045. 44

[3] D. Briggs and J. T. Grant, *Surface analysis by Auger and X-ray photoelectron spectroscopy*, SurfaceSpectra, 2012. 48, 49

[4] A. R. Head and H. Bluhm, Elsevier, 2018; chapter Ambient Pressure X-Ray Photoelectron Spectroscopy. 49, 50

[5] M. G. Silly, T. Ferté, M. A. Tordeux, D. Pierucci, N. Beaulieu, C. Chauvet, F. Pressacco, F. Sirotti, H. Popescu, V. Lopez-Flores, M. Tortarolo, M. Sacchi, N. Jaouen, P. Hollander, J. P. Ricaud, N. Bergeard, C. Boeglin, B. Tudu, R. Delaunay, J. Luning, G. Malinowski, M. Hehn, C. Baumier, F. Fortuna, D. Krizmancic, L. Stebel, R. Sergo, and G. Cautero, *J. Sync. Rad.*, 2017, **24**(4), 886–897. 52

[6] A. Benninghoven, *Angew. Chem. Int. Ed.*, 1994, **33**(10), 1023–1043. 53

[7] V. Mazel and P. Richardin, in *Organic Mass Spectrometry in Art and Archaeology*, John Wiley & Sons, Ltd, 2009; chapter 15, pp. 433–457. 53

[8] R. N. S. Sodhi, *Analyst*, 2004, **129**, 483–487. 53

[9] C. V. Cushman, P. Brüner, J. Zakel, G. H. Major, B. M. Lunt, N. J. Smith, T. Grehl, and M. R. Linford, *Anal. Methods*, 2016, **8**, 3419–3439. 55, 56

[10] H. ter Veen, T. Kim, I. Wachs, and H. Brongersma, *Catal. Today*, 2009, **140**(3), 197 – 201. 55

[11] H. H. Brongersma, M. Draxler, M. de Ridder, and P. Bauer, *Surf. Sci. Reports*, 2007, **62**(3), 63 – 109. 55

[12] W. Jansen, A. Knoester, A. Maas, P. Schmit, A. Kytökivi, A. Denier vd Gon, and H. Brongersma, *Surf. Interface Anal.*, 2004, **36**(11), 1469–1478. 56

[13] L. C. A. van den Oetelaar, H. E. van Benthem, J. H. J. M. Helwegen, P. J. A. Stapel, and H. H. Brongersma, *Surf. Interface Anal.*, 1998, **26**(8), 537–548. 56

[14] U. Weisbrod, R. Gutschke, J. Knoth, and H. Schwenke, *Fresenius J. Anal. Chem*, 1991, **341**(1), 83 – 86. 59

[15] Briois, V., Fonda, E., Belin, S., Barthe, L., La Fontaine, C., Langlois, F., Ribbens, M., and Villain, F., *UVX 2010 - 10e Colloque sur les Sources Cohérentes et Incohérentes UV, VUV et X ; Applications et Développements Récents*, 2011, pp. 41–47. 61

[16] Camille La Fontaine and Laurent Barthe and Amélie Rochet and Valérie Briois, *Catalysis Today*, 2013, **205**, 148 – 158. 61

[17] B. Ravel and M. Newville, *J. Synchrotron Radiat.*, 2005, **12**(4), 537 – 541. 61

Chapter 3

Relevance of $LaFeO_3$ thin films as reliable models for surface investigation of TWC

To investigate and understand the surface properties of $LaFeO_3$-based bulk catalyst powders, which are commonly used for catalytic testing and optimization in the laboratory, it is ideal to constitute model catalysts shaped as thin films such that they closely mimic the conventional ones. The preparation of $LaFeO_3$ thin films deposited over silicon substrate allows to have a better surface representation with improved surface to bulk ratio while acting as discrete model materials with tunable thickness. They also help in minimizing the charging effects during surface analyses measurements and also allow efficient depth profiling measurements. The thin films are kept polycrystalline in order to mimic powder catalysts closely. Shaping as thin films is especially important for studying bulk catalysts by X-ray absorption spectroscopy in order to avoid losing relevant information in the bulk, unlike the supported catalysts. To this end, this chapter includes the in-depth investigation of the $LaFeO_3$-based model catalyst systems shaped as thin films, consisting of the perovskite layers over Si(100) substrate. Firstly, the substrate is characterized by XPS, ToF-SIMS and Raman spectroscopy to investigate its chemical state before deposition by spin coating. The film's thickness can be controlled by tuning the concentration of the precursor solution that is being deposited. The goal is to achieve a thin film of $LaFeO_3$ that is homogeneous in mm^2 range as well as can withstand high temperature experimental conditions. Thus, two types of $LaFeO_3$-based thin films are discussed, in sub-100 nm and sub-10 nm ranges. The morphology of each is analyzed using microscopy techniques followed by the structural characterization by Raman spectroscopy and XRD. The surface composition of these models is examined by combination of surface characteri-

zation techniques to achieve the overall surface-oriented view-point by LEIS, ToF-SIMS and XPS analyses. Finally, the two kinds of thin films are directly compared with the corresponding powder catalysts by the means of GI-XANES and quasi-*in situ* XPS analyses to establish the relevance of the $LaFeO_3$ thin films as relevant models for surface investigation of perovskite-based three-way catalysts.

3.1 Characterization of Si(100) substrate

The Si(100) substrate before deposition of the film layers was treated in order to remove impurities and improve its hydrophilicity by formation of a native oxide layer, as described in chapter 2. The post-treated substrate was analyzed by XPS to verify its surface composition. The silicon wafer is mainly composed of silicon and oxygen besides some adventitious carbon (14 at. %). The respective binding energy and atomic concentration of each has been shown in Table 3.1. In Fig.3.1, the Si 2p signal is shown with two components at 98.9 and 102.7 eV, representing elemental silicon (Si^0) and oxidized silicon (SiO_2), respectively. The Si $2p_{3/2}$ and $2p_{1/2}$ components are present in each photopeak, where the spin-orbit splitting is close to 1 eV, more clearly indicated by the asymmetric shape of the metallic signal of Si^0 [1]. The XPS analysis reveals the coverage of a passive layer of oxidized silicon over the substrate.

Table 3.1: Binding energy and atomic concentration of the elements present on Si(100) substrate as detected by XPS analysis.

Element	Binding energy (eV)	Atomic concentration (at. %)	Ratio SiO_2/Si^0
Si 2p (Si^0)	98.9	34.2	0.25
Si 2p (SiO_2)	102.7	8.6	
O 1s	532.3	42.9	
C 1s	285.0	14.3	

The thickness of this oxidized layer can be estimated using the fundamental XPS equation, described in chapter 2, by applying to a morphological model. According to this model, a continuous homogeneous layer of SiO_2 covering the Si(100) substrate is considered, as shown by the scheme in Fig.3.2 [2].

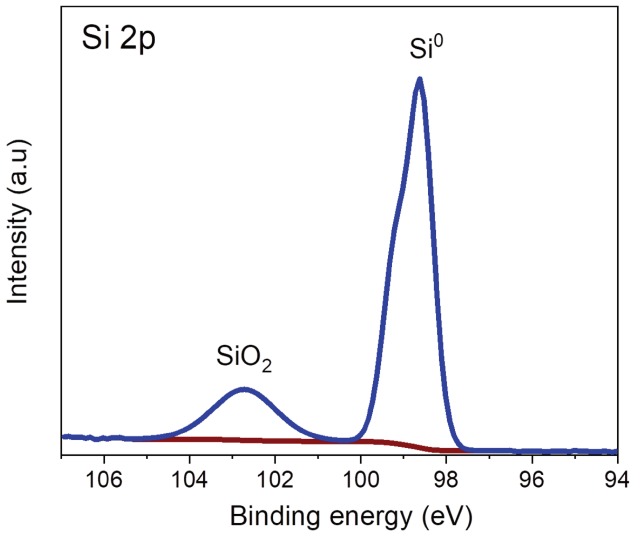

Figure 3.1: XPS Si 2p photopeak of the post-treated silicon substrate.

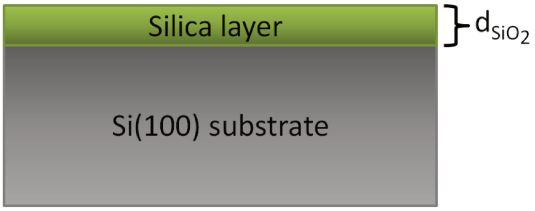

Figure 3.2: Scheme of morphological model of a continuous and homogeneous layer of silica on the silicon substrate.

Consequently, the integrated ratio of $I_{Si2p(SiO_2)}$ and $I_{Si2p(Si^0)}$ can be expressed by,

$$\frac{I_{Si2p(SiO_2)}}{I_{Si2p(Si^0)}} = \frac{n_{Si2p(SiO_2)}\,\lambda_{Si2p(SiO_2)\rightarrow SiO_2}\,(1-exp(-\frac{d_{SiO_2}}{\lambda_{Si2p(SiO_2)\rightarrow SiO_2}}))}{n_{Si2p(Si^0)}\,\lambda_{Si2p(Si^0)\rightarrow Si^0}\,exp(\frac{-d_{SiO_2}}{\lambda_{Si2p(Si^0)\rightarrow SiO_2}})} \tag{3.1}$$

as T is assumed to be constant within the small range of kinetic energy involved here and the cross section σ_{Si2p} equal to 0.33 is supplied by the manufacturer of the XPS spectrometer (Kratos Analytical Ltd). The mean free path λ is 3.08 nm for Si 2p/Si^0 and 3.75 nm for Si 2p/SiO_2, calculated from the formula proposed by Tanuma, Powell and Penn (TPP2M) [3]. Finally, the number of Si atoms per unit volume as calculated from the densities are found to be 4.9x10^{22} and 2.2x10^{22} atoms/cm^3 for SiO_2 and Si^0, respectively.

On applying this equation, the thickness of the SiO_2 layer over Si was calculated to be 1.4 nm, in agreement with the values from literature [1, 4]. The substrate can therefore be referred to as a SiO_2/Si(100) system.

The ToF-SIMS depth profile of the post-treated substrate has been shown in Fig.3.3,

which confirms the above model of a silica layer over the silicon. The depth profile presents the increase of the intensity of O_2^- and SiO_2^- fragments arising from the silica layer at the surface. With further sputtering, the intensity of these ionic fragments decreases while that of the Si_2^- ion increases since the silicon is situated beneath the silica layer. The depth of the silica layer was estimated at 20s to be close to 0.9 nm according to the experimental conditions.

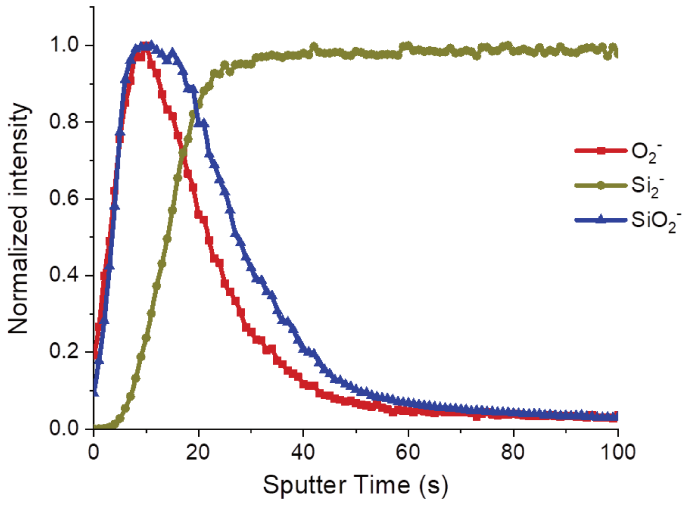

Figure 3.3: ToF-SIMS depth profile of SiO_2/Si(100) substrate in negative mode sputtered with 1 keV Cs^+ and analysed with 25 keV Bi^+.

The SiO_2/Si(100) wafer was also analyzed by Raman spectroscopy as shown in Fig.3.4. It is dominated by an intense characteristic Raman line at 520 cm^{-1} with broad lines of much lower intensity (inset) at 300 cm^{-1} and around 950 cm^{-1}. These Raman lines are characteristic of silicon vibrational modes [5].

The Raman signature of amorphous SiO_2 is composed of broad components, however, with a depth resolution of at least 1 µm in Raman spectroscopy, it remains insensitive to the 1.4 nm of the silica layer, as was evidenced by XPS analysis.

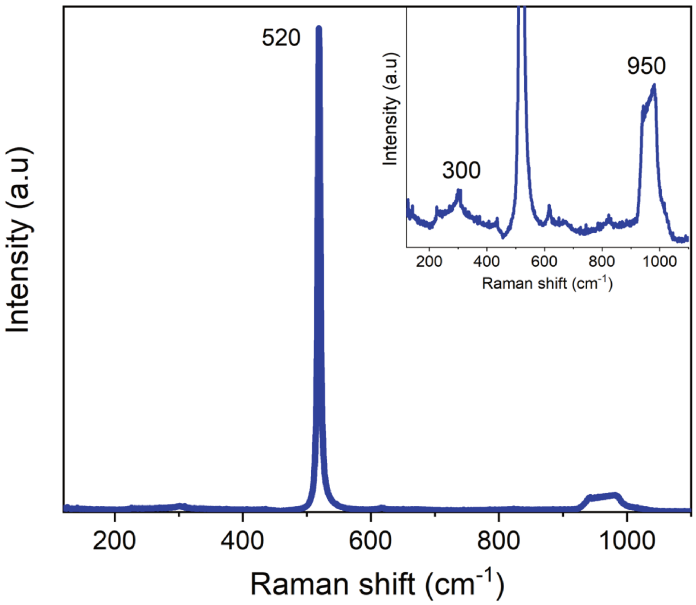

Figure 3.4: Raman spectrum of the SiO_2/Si(100) substrate.

3.2 Thickness optimization of thin films

The perovskite thin films were prepared by varying the concentration of the precursor solution while keeping rest of the spin-coating parameters constant, as described in chapter 2. The control of the concentration allowed to achieve desired thickness of these discrete model materials. Thin films synthesized by this technique are often susceptible to formation of voids or cracked zones as a result of the calcination treatment at high temperature. Hence, the ideal thin film to be achieved by this method must have rather homogeneous layer of the perovskite film in mm^2 range with minimum voids and an optimum thickness with the ability to withstand high temperature treatments under *in situ* conditions, discussed later in this chapter. To this end, thin films of $LaFeO_3$ were prepared in three different thickness ranges, namely, thick (few hundred nm to microns), intermediate (50-100 nm) and ultra-thin (<10 nm) films as shown in Fig.3.5(c), verified by electron microscopy measurements. The heating time or dilutions to prepare the thin films have been previously discussed in chapter 2.

Firstly, the thicker film ranging from a few hundreds of nanometers to microns in thickness consists of numerous cracks and a highly uneven surface. This film may be suitable for study by bulk analytical techniques such as Raman spectroscopy yielding lower interfering signal from the substrate. This film is however highly susceptible to damage due to very low adherence to the substrate and therefore will not be considered any fur-

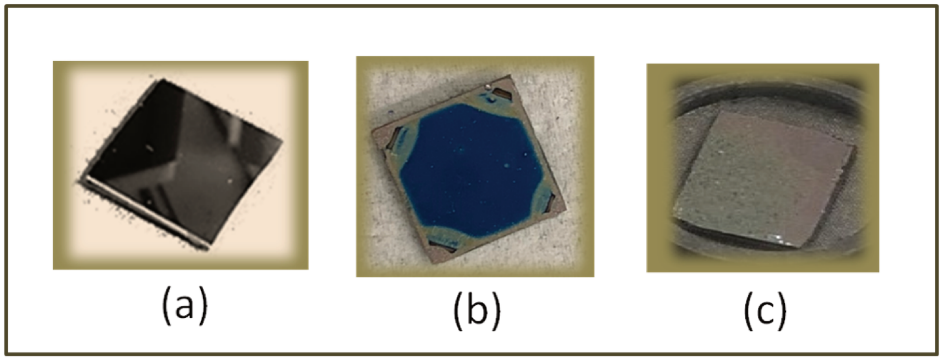

Figure 3.5: Images of (a) ultra-thin (<10 nm), (b) intermediate (50-100 nm) and (c) thick (few hundred nm to microns) thin films of $LaFeO_3$.

ther. This thick film retains the brownish orange color similar to that of a $LaFeO_3$ powder. Secondly, the thin film of intermediate thickness ranging between 50 and 100 nm (abbreviated as LFO:Si-100) shows homogeneous coverage of the film with negligible macroscopic voids (Fig.3.5(b)). This thin film possesses a bright blue color as a result of its nano-scaled dimensions. And thirdly, an ultra-thin film was prepared with a thickness of below 10 nm (referred to as LFO:Si-10). The film is invisible with the naked eyes as well as an optical microscope (100x) and simply looks like the surface of a bare Si substrate (Fig.3.5(a)). Although, this film provides a high surface to bulk ratio, it can only be characterized by highly surface and/or elemental sensitive techniques. Moreover, being so thin it is difficult to be treated for longer duration during *in situ* experiments at high temperature because of complete material volatilization. This matter loss can occur due to the phenomenon of melting point depression in nano-scaled materials [6].

The loss of matter (the film thickness evolution) evidenced on such thin films after treatment under oxygen at 900°C for 3 hours have been shown in Fig.3.6. It shows the decrease of the background caused by secondary electrons, which lose energy while arising from the deeper sample layers containing information related to the depth of the thin film. The loss in intensities of La 3d and Fe 2p occurs with increase of the Si 2p and Si 2s signals revealing the presence of the substrate. The intermediate thin film can withstand prolonged heating under relevant reaction conditions without complete loss of the film layer and therefore is more suitable for being studied by *in situ* techniques as a model catalyst. It must be noticed that the use of the treatment cell may induce contamination on the surface of the material, as it can be seen on the XPS survey spectrum (Fig.3.6) with the presence of Cu and Mo (<1 at. %).

More details have been described in the next section (section 3.3) together with the

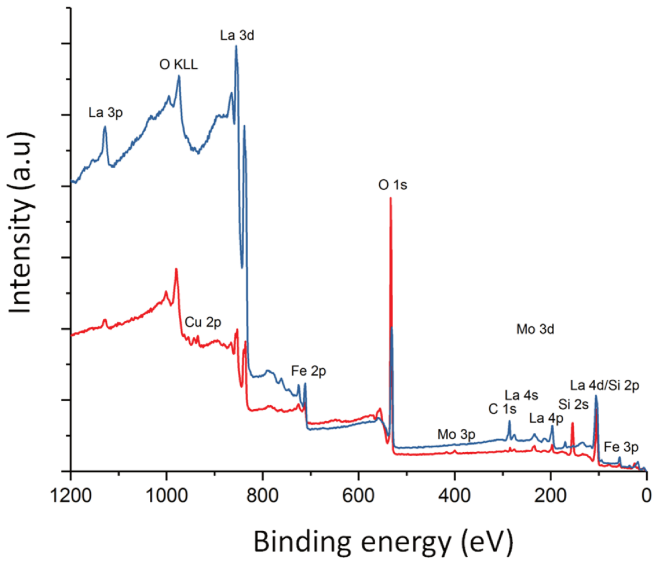

Figure 3.6: XPS survey spectra of the intermediate thin film of $LaFeO_3$ before (blue) and after (red) treatment under oxygen at 900°C for 3 hours.

ultra-thin film as an approach to investigate a more surface oriented perovskite sample (section 3.4). The surface investigation approach using discrete model catalysts has been described in Fig.3.7 in decreasing order of thickness from microns up to 1-10 nm. Such model catalysts allow not only to be more easily studied by surface sensitive techniques but also permit a highly sensitive bulk technique to become surface sensitive, driven by the low thickness of the sample itself. Thus, allowing surface analysis induced by the sample.

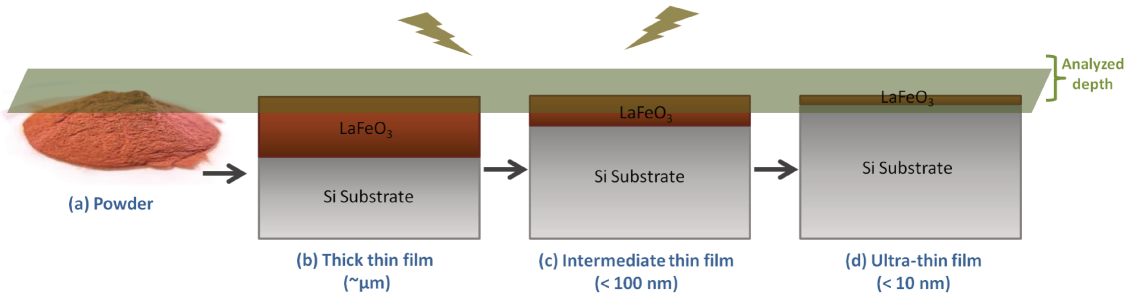

Figure 3.7: Description of the approach towards surface sensitive models.

3.3 Characteristics of $LaFeO_3$-based thin films of intermediate thickness (LFO:Si-100)

The $LaFeO_3$-based thin films of intermediate thickness (50-100 nm) have been characterized in depth for their morphological, structural and surface properties by combination of various analytical techniques.

3.3.1 Morphology

The top-view of the perovskite-based thin film (LFO:Si-100) has been shown by the SEM images in Fig.3.8(a). The coverage is quite homogeneous with very few regions consisting of any cracks or discontinuities exposing the substrate. Majority of the substrate is covered by layers of the deposited oxide. Fig.3.8(b) shows the atomic forced microscopy (AFM) images also confirming rather homogeneous coverage of the oxide film. The root mean squared roughness (R_q) defined by,

$$R_q = \sqrt{\frac{1}{n}\sum_{i=1}^{n} Y_i{}^2} \tag{3.2}$$

where Y_i is the i^{th} height of n data points, was found to reach about 1.4 nm.

The electron back-scattering diffraction (EBSD) images in Fig.3.9 further highlight the polycrystalline nature of the thin film represented by the multi-colored zones in each direction with different crystal orientations. The polycrystalline nature of this model catalyst mimics the crystalline nature of conventional catalysts shaped as powders. This bridges the material gap present between the commonly studied single crystal model catalysts and the conventional polycrystalline powder catalysts used at the laboratory.

The cross-sectional view of the thin film to determine the film thickness is made possible by the high-angle annular dark field scanning transmission electron microscopy (HAADF-STEM) imaging of its lamella prepared by focused ion beam (FIB). A protective layer of platinum is used to coat the sample before cutting the lamella, clearly seen in Fig.3.10(a) and (c). As shown in Fig.3.10(a), the thin film consists of a layer of around 70 nm with a mesoporous texture across depth. The pores are mostly located internally with rather flat surface on top. This layer also consists of a few open channels up to the substrate. The perovskite layer is followed by a very narrow dark zone of silica and then silicon in the substrate, also evidenced previously by XPS analysis. The periodic ordering

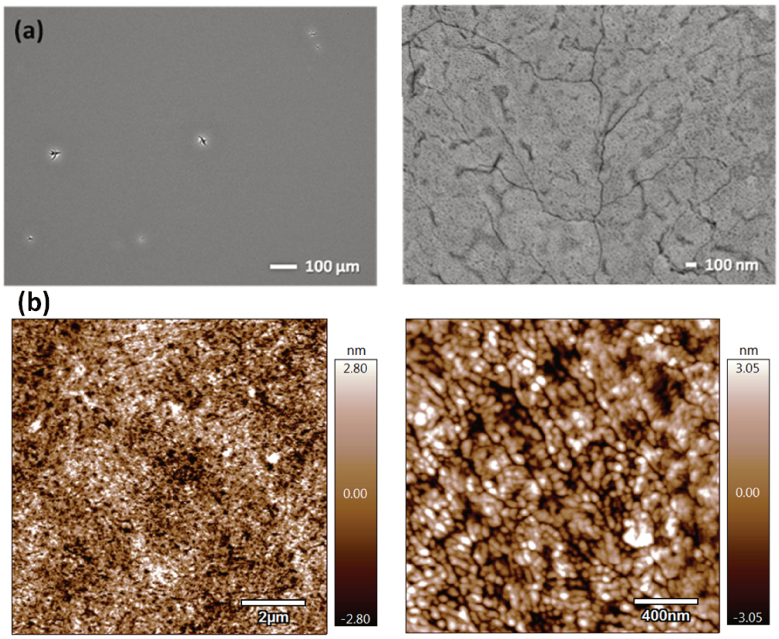

Figure 3.8: (a) SEM and (b) AFM images showing the top-view of $LaFeO_3$ thin film (LFO:Si-100).

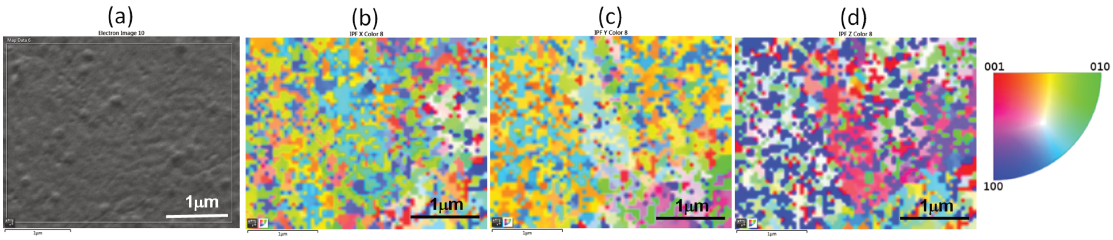

Figure 3.9: (a) Electron image and electron back-scattering diffraction (EBSD) images along (b) x, (c) y and (d) z directions of the $LaFeO_3$ thin film (LFO:Si-100), where each color represents an unique crystal orientation.

of the atoms are shown in Fig.3.10(b), highlighting the crystalline nature of the perovskite thin film. The elemental composition of the film's cross section is confirmed by energy dispersive X-ray spectroscopic (EDX) chemical mapping. The La, Fe and O were present uniformly throughout the perovskite layer with no evidence of any phase segregation or contamination.

3.3.2 Structural properties

X-ray diffraction The diffraction pattern of the oxide layer displayed in Fig.3.11 shows every reflection of the polycrystalline perovskite $LaFeO_3$ crystallized in orthorhombic lattice (PDF 74-2203) with lattice constants a = 5.553 Å, b = 5.563 Å and c = 7.867 Å (space group: Pbnm). No reflection of any other crystalline phases such as La_2O_3, $La(OH)_3$ or Fe_2O_3 are observed.

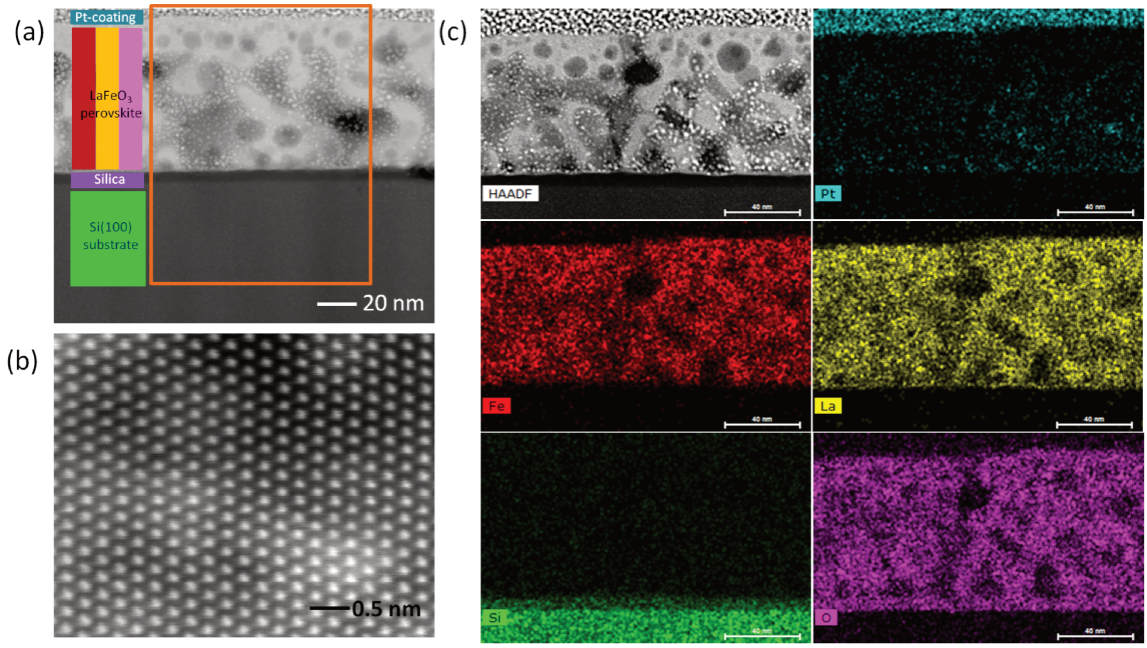

Figure 3.10: HAADF-STEM images of the cross sectional FIB-lamella of the $LaFeO_3$ thin film (LFO:Si-100): (a) cross-sectional image, (b) high resolution image of the crystalline perovskite layer and (c) EDX chemical mapping.

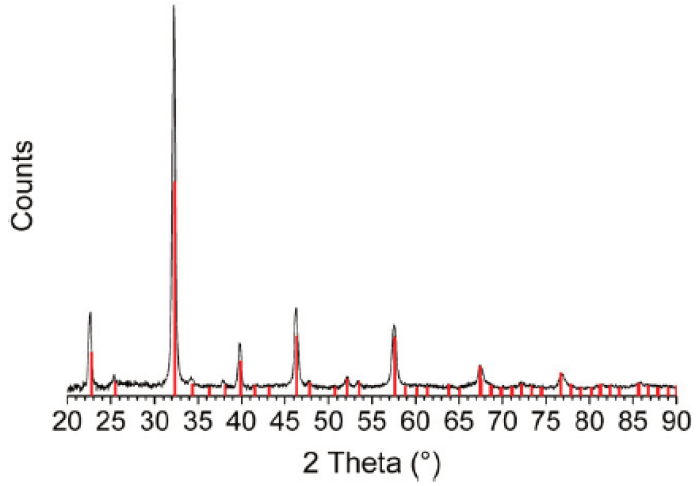

Figure 3.11: X-ray diffractogram of perovskite thin film (LFO:Si-100); red stick diagram: diffraction pattern of $LaFeO_3$ (PDF 74-2203).

Raman spectroscopy The typically analyzed sample depth by Raman spectroscopy is approximately 1 µm, which is one order of magnitude higher than the film's thickness. As a result, the Raman spectra recorded by focusing the laser beam at the surface of the film are largely dominated by the signature of crystalline silicon from the substrate, as can be seen in the Raman spectrum (black) presented in Fig.3.12. However, the signature of the polycrystalline lanthanum orthoferrite can be retrieved by subtracting the Raman spectrum of the bare Si substrate from that of the $LaFeO_3$ thin film, recorded under the same experimental conditions.

The difference spectrum shown at the bottom of Fig.3.12 is similar to the Raman signature of the same material shaped as powders [7]. The modes below 200 cm^{-1} are related to La motions, the doublet of lines observed at 269 and 298 cm^{-1} are oxygen octahedral tilt (T) modes while the line at 431 cm^{-1} is assigned to the bending vibration of FeO_6 octahedra. The band at 638 cm^{-1} is assigned to Fe–O and La–O stretch vibrations [8–10]. To sum up, in spite of the relatively low share of perovskite phase as compared to the volume probed by Raman spectroscopy, $LaFeO_3$ lines of high enough intensity are detected, which potentially paves the way to further *operando* Raman analyses.

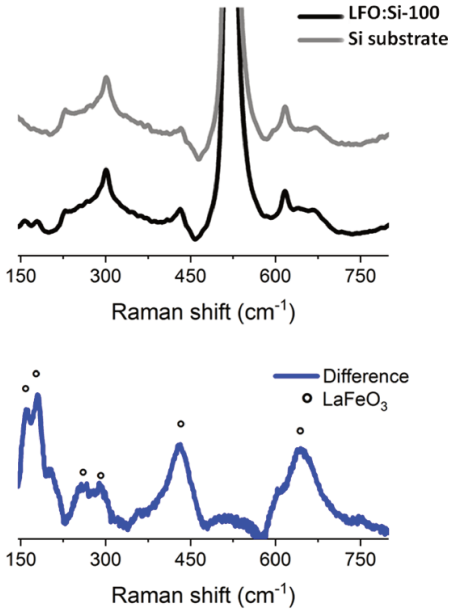

Figure 3.12: Top: Raman spectra at $\lambda_{exc.}$= 488 nm of bare SiO_2/Si(100) substrate (grey) and $LaFeO_3$ thin film (LFO:Si-100) (black), Bottom: Difference spectrum.

3.3.3 Surface properties

XPS analysis The XPS spectra of the $LaFeO_3$ thin film for C 1s, La 3d, Fe 2p, and O 1s are presented in Fig.3.13. The C 1s photopeak presents an aliphatic component (binding energy reference at 285.0 eV) together with weaker components at higher binding energy assigned to hydroxyl and carbonate surface contaminations. The peak at binding energy of 289.2 eV (with 16.2% of the total C 1s signal) is attributed to the adsorbed carbonate species at the surface of the $LaFeO_3$ film, as was previously also observed in the corresponding lanthanum-based powders [11]. The high-resolution spectrum of La 3d exhibits two peaks localized at 834.0 and 851.0 eV corresponding to the spin-orbit coupling of La

$3d_{5/2}$ and La $3d_{3/2}$ of La^{3+} ion in its oxide form [12–14]. Each of the spin-orbit peak is further split by multiplet splitting components. The multiplet structure associated to La $3d_{5/2}$ peak shows a magnitude of 4.3 eV. This value lies in between the one obtained from lanthanum oxide (4.6 eV) and lanthanum hydroxide (3.9 eV) phases [12]. Indeed, owing to the reactive nature of La compounds that react in ambient air with water and CO_2 to form La hydroxides and carbonates, it is possible that this La 3d component is consisting of contributions from surface lanthanum hydroxides and carbonates besides the mixed oxide. The binding energy of Fe $2p_{3/2}$ and Fe $2p_{1/2}$ are 710.3 and 724.1 eV, respectively, which is in line with the binding energy of Fe^{3+} ions in perovskite oxides [14]. This is further confirmed by the 9 eV binding energy separation between the main Fe $2p_{3/2}$ peak and its satellite (sat.), characteristic of Fe^{3+} [15]. La 3d and Fe 2p core-level spectra thus reveals that both La and Fe stand in +3 oxidation states and their respective areas allow to calculate an La/Fe atomic ratio of 1.8. Here, only the La $3d_{5/2}$ peak was considered for quantification keeping in mind the overlapping of La MNN Auger peak with the La $3d_{3/2}$ signal [12]. Compared to the nominal composition, the $LaFeO_3$ thin film exhibits an excess of lanthanum at the surface whose value is close to what has been already reported on the powdered samples [11].

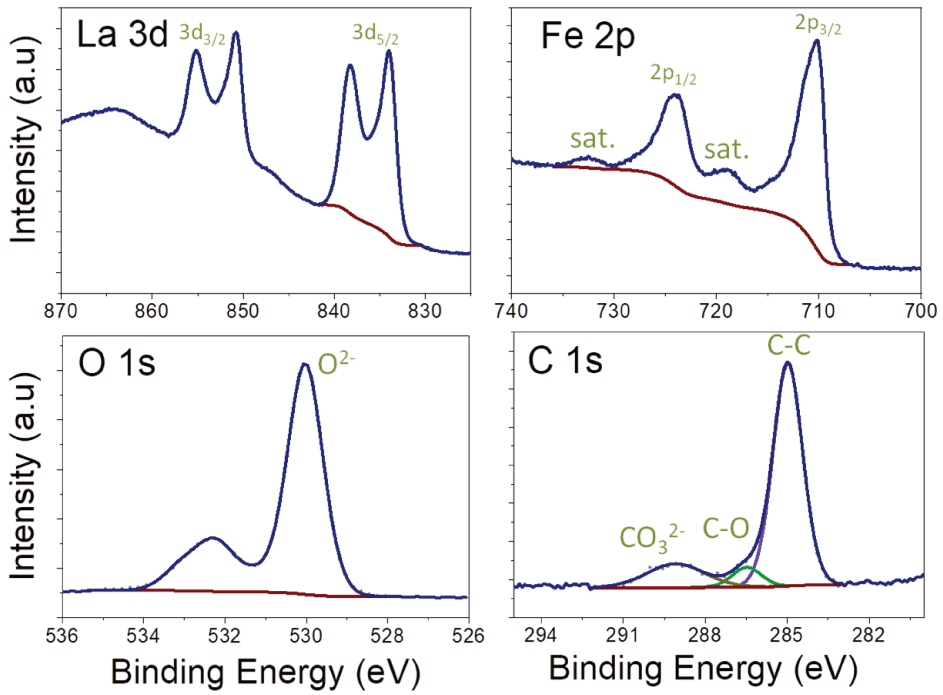

Figure 3.13: XPS La 3d, Fe 2p, O 1s and C 1s spectra of $LaFeO_3$ thin film (LFO:Si-100).

The high-resolution spectrum of O 1s of the perovskite film is dominated by two intense components at 529.4 and 531.7 eV. The first one is in line with previous studies with contribution from bulk lattice oxygen involved in lanthanum oxide and iron oxide groups [12, 14]. The broader second contribution centered at 531.7 eV is assigned to oxygen from adsorbed hydroxyl, O^-/O_2^- α-species and organic oxygen species. In case the analyzed area contains any voids exposing the SiO_2/Si substrate, the O 1s region will also show a contribution from silica at around 532.4 eV [16]. In this case, there is no silica signal detected meaning the XPS analysis was focused on a homogeneous void-free region of the thin film.

In addition, since the multiplet structure of La 3d is greatly modified according to the chemical environment of lanthanum. For example, in lanthanum carbonate the relative intensity of the higher binding energy multiplet peak is more intense unlike here, as confirmed by analyzing a commercial lanthanum carbonate powder (not shown). Hence, the multiplet structure relative intensity and shape vary with the amount of the different surface La species present on the surface. Thereby, the perovskite film is heated under oxygen up to a temperature of 900°C to remove completely the surface hydroxides and carbonates as shown in Fig.3.14. After heating, the amount of carbon decreased from 15% to 4% with complete removal of carbonates and hydroxide components, while the La/Fe ratio remained constant at 2.1. The multiplet structure of La 3d spectrum of $LaFeO_3$ after the oxygen treatment possessed a different shape (relative intensity and width of the main peak and multiplet feature) compared to that of La_2O_3 after similar treatment. Hence, revealing the shape of the La 3d photpeak of a clean surface of $LaFeO_3$. However, due to dramatic loss of film, SiO_2/Si(100) substrate is consequently revealed leading to an intense O 1s component from SiO_2, hiding the other eventual contributions.

LEIS analysis The LEIS spectrum of the $LaFeO_3$ thin film is presented in Fig.3.15. The spectrum indicates the elemental composition of the film's surface with respect to the first atomic layer only. Surface peaks from oxygen, iron and lanthanum are detected without presence of any other elements ensuring a clean thin film surface. The ratio of La/Fe raw peak intensity is 3.9 and 4.3 with $^4He^+$ and $^{20}Ne^+$ primary ion sources, respectively. Similar to the XPS quantification, the LEIS spectra also suggest higher concentration of lanthanum compared to iron on the outermost surface layer evident from the much higher intensity of La signal compared to Fe in the LEIS spectrum, qualitatively.

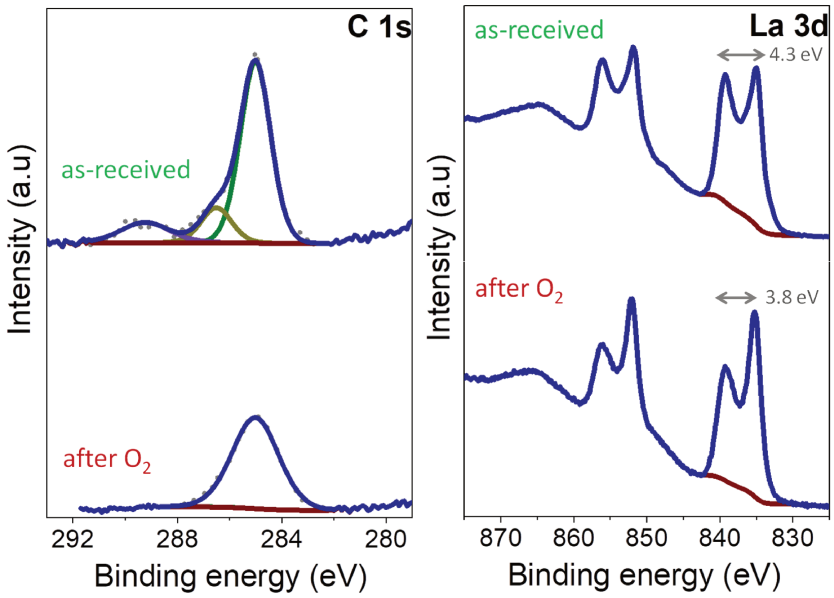

Figure 3.14: XPS C 1s and La 3d spectra of $LaFeO_3$ thin film: as-received and after heating under oxygen until 900°C.

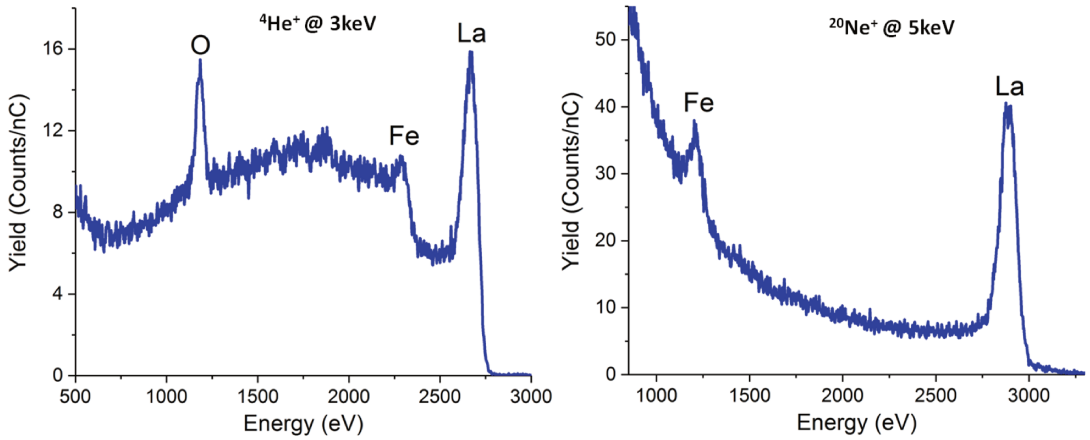

Figure 3.15: LEIS spectra of $LaFeO_3$ thin film (LFO:Si-100) using 3 keV $^4He^+$ (left) and 5 keV $^{20}Ne^+$ (right) as the primary ion sources, respectively.

In order to calculate the LEIS atomic ratios, reference oxides of La (La_2O_3) and Fe (Fe_2O_3) were analyzed as shown in Fig.3.16 and Fig.3.17. The references were sputtered with the primary ion source until the surface peak intensities were constant to avoid influence of any surface contamination. For quantification, the LEIS equation as previously discussed in chapter 2 (equation 2.5) has been used. Applying this equation, for La_2O_3

and Fe_2O_3, respectively, their ratio can be given by [17],

$$\frac{S_{La}^{ref}}{S_{Fe}^{ref}} = \frac{n_{La}}{n_{Fe}} \frac{N_{La}^{ref}}{N_{Fe}^{ref}} \tag{3.3}$$

where, $\frac{S_{La}^{ref}}{S_{Fe}^{ref}}$ is the ratio of raw areas of La and Fe in each of the reference oxides, $\frac{N_{La}^{ref}}{N_{Fe}^{ref}}$ is the ratio of the calculated atomic concentration of La and Fe in the reference oxides using equation 8 in chapter 2 and $\frac{n_{La}}{n_{Fe}}$ is the ratio of the elemental sensitivity factor that is to be calculated.

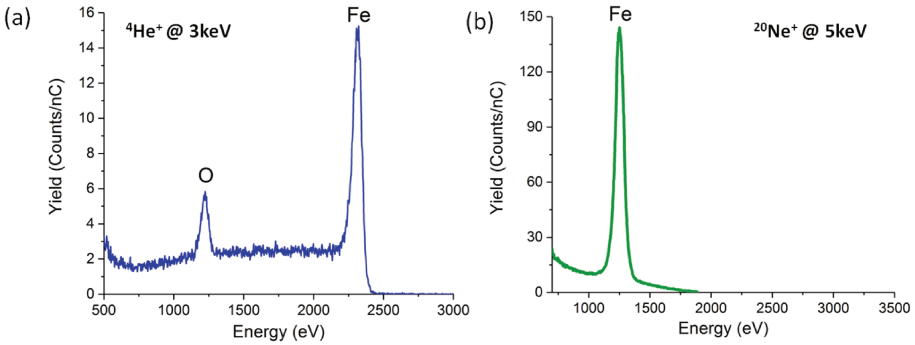

Figure 3.16: LEIS spectra of Fe_2O_3 reference oxide using 3 keV $^4He^+$ (left) and 5 keV $^{20}Ne^+$ (right) as primary ion sources, respectively.

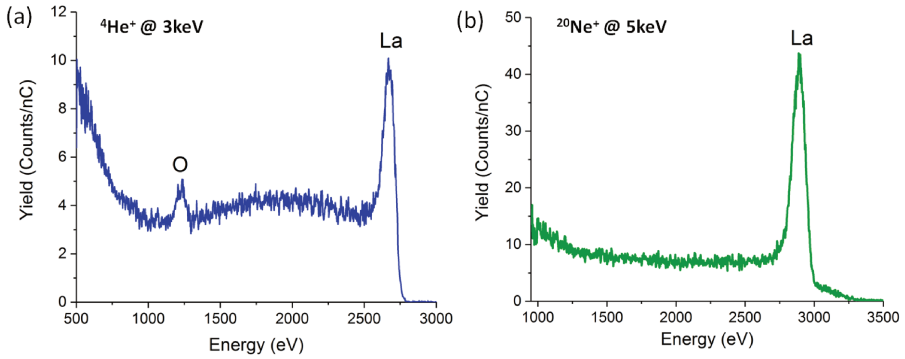

Figure 3.17: LEIS spectra of La_2O_3 reference oxide using 3 keV $^4He^+$ (left) and 5 keV $^{20}Ne^+$ (right) as primary ion sources, respectively.

The N_{La}^{ref} and N_{Fe}^{ref} take into account the density and the atomic size of the respective elements in the analyzed material. The sensitivity factor ratio can therefore be calculated using these known values from Table 3.2. The quantification was made with both $^4He^+$ and $^{20}Ne^+$ primary ions for comparison.

Using the above values, the sensitivity factor ratio was found to be 1.3 and 1.4 with

Table 3.2: LEIS intensities of reference oxide samples (Fe_2O_3 and La_2O_3), their ratios and calculated surface atomic concentration of La and Fe.

Reference oxide	Primary ion source	La or Fe raw peak area (S)	S_{La}/S_{Fe}	Surface concentration (N) (10^{15} atoms.cm^{-2})
Fe_2O_3	$^4He^+$	1077	0.96	0.73
La_2O_3	$^4He^+$	1029		0.52
Fe_2O_3	$^{20}Ne^+$	4684	1.01	0.73
La_2O_3	$^{20}Ne^+$	4738		0.52

$^4He^+$ and $^{20}Ne^+$ ion sources, respectively. The value of the sensitivity factor ratio is applied according to the following equation to calculate the atomic ratio of La/Fe,

$$\frac{N_{La}^{LFO}}{N_{Fe}^{LFO}} = \frac{S_{La}^{LFO}}{S_{Fe}^{LFO}} / \frac{n_{La}}{n_{Fe}} \tag{3.4}$$

where, $\frac{S_{La}^{LFO}}{S_{Fe}^{LFO}}$ is the ratio of the La and Fe intensities obtained from the LEIS spectrum of $LaFeO_3$ obtained after *in situ* O_2 plasma treatment to remove most of the carbon contamination, $\frac{n_{La}}{n_{Fe}}$ is the calculated sensitivity factor ratio and finally $\frac{N_{La}^{LFO}}{N_{Fe}^{LFO}}$ is the atomic ratio of La/Fe in the perovskite that can be determined. Thereby, the La/Fe atomic ratio is calculated to be 3.0 and 3.1 for the $^4He^+$ and $^{20}Ne^+$ primary ions, respectively.

This ratio is higher in the case of LEIS analysis as compared to that of XPS (La/Fe≈2). This difference in the value obtained by the two techniques can be explained by the depth probed in each case. This means that the La/Fe ratio in the first atomic layer probed by LEIS is 3, while in case of the ~5 nm probed by XPS, it is equivalent to 2. In both the cases, a surface enrichment of lanthanum is evident, which is commonly known to be caused by the reactive nature of La-based compounds forming La hydroxides or carbonate species on the extreme surface.

ToF-SIMS analysis The $LaFeO_3$ thin film was analysed by ToF-SIMS. The ionic fragments identified in the mass spectrum have been listed in Table 3.3 in both positive and negative modes. The La and Fe based fragments as well as the mixed oxide fragments originate from the perovskite film while the silicon based ions represent the SiO_2/Si substrate.

The lateral distribution of some selected ionic fragments has been displayed in Fig.3.18. It represents a uniform presence of the ionic fragments from the $LaFeO_3$ thin film through-

Table 3.3: Identified fragments in positive and negative modes generated by ToF-SIMS analysis of $LaFeO_3$ thin film.

Type of ions	Positive mode		Negative mode	
	Fragment	Mass (u)	Fragment	Mass (u)
La-based ions	La^+ LaH^+ LaO^+ $LaOH^+$ LaO_2^+	138.91 139.91 154.91 155.91 170.89	La^- LaO^- $LaOH^-$ LaO_2^- LaO_2H^- LaO_3^- $La_2O_4^-$	138.91 154.91 155.91 170.89 171.89 186.90 341.80
Fe-based ions	$^{54}Fe^+$ Fe^+ $^{54}FeO^+$ FeO^+	53.94 55.93 69.95 71.93	$^{54}Fe^-$ Fe^- $^{54}FeO^-$ FeO^- $^{54}FeO_2^-$ FeO_2^- FeO_3^- $Fe_2O_3^-$	53.94 55.93 69.95 71.93 85.94 87.93 103.93 159.87
Mixed oxide ions	$La^{54}FeO^+$ $LaFeO^+$ $LaFeOH^+$ $La^{54}FeO_2^+$ $LaFeO_2^+$ $LaFeO_2H^+$ $La_2{}^{54}FeO_4^+$ $La_2FeO_4^+$ $La_2FeO_4H^+$	208.98 210.85 211.86 224.84 226.83 227.84 395.73 397.72 398.73	Interference with substrate fragments	Interference with substrate fragments
Substrate-based ions	Si^+ $^{30}Si^+$ SiO^+ $^{30}SiO^+$ $^{30}SiO_2^+$	27.97 29.97 43.97 45.97 59.97	Si^- $^{30}Si^-$ SiO^- Si_2^- SiO_2^- SiO_3^-	27.97 29.97 43.97 55.97 59.99 75.97

out the surface, as previously seen by microscopy analysis. The lateral resolution of ToF-SIMS in our experimental conditions is at the best 200 nm and therefore any details below this limit may not be resolved and remain undetected. In general, oxides have higher intensity in the negative mode, especially for oxygen containing ions, compared to the positive mode. For example, the ions with only one oxygen can be observed in both polarities, however, the ions with more than one oxygen were not detected in the positive mode, such as FeO_2^+ and $Fe_2O_3^+$. The ToF-SIMS analyses were made in both polarities to analyze the $LaFeO_3$ surface.

The mixed oxide fragments, or in other words, the ions containing La, Fe and O together, have been shown in Fig.3.19, such as $LaFeO^+$, $LaFeOH^+$, $LaFeO_2^+$, $LaFeO_2^+H$, $La_2FeO_4^+$

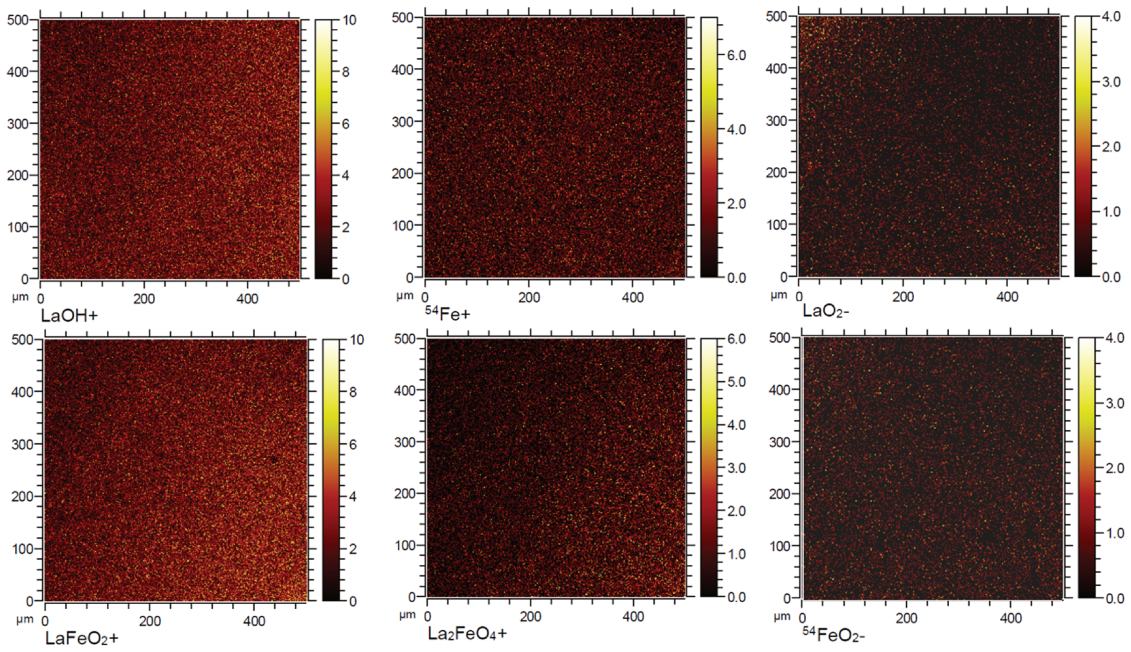

Figure 3.18: ToF-SIMS images of the surface of $LaFeO_3$ thin film (LFO:Si-100).

and $La_2FeO_4H^+$. Their presence was further confirmed by the existence of similar isotopic ions containing ^{54}Fe such as $La^{54}FeO^+$ (Fig.3.19). These mixed oxide ions can only be well identified in case of the positive mode without any overlapping contribution from the SiO_2/Si substrate as described in Fig.3.20. However, in case of the negative mode there are already intense peaks present originating from the substrate alone. For example, the $LaFeO^-$ fragment overlaps with the $Si_7CH_3^-$ ionic fragment, both having a mass of 210.85 u, thereby interfering with the mixed oxide fragments of interest. Hence, in order to follow the mixed oxide fragments that are indicative of the presence of mixed oxide phase of perovskite, it is necessary to analyze in the positive mode without any interference from larger ions arising from the Si wafer.

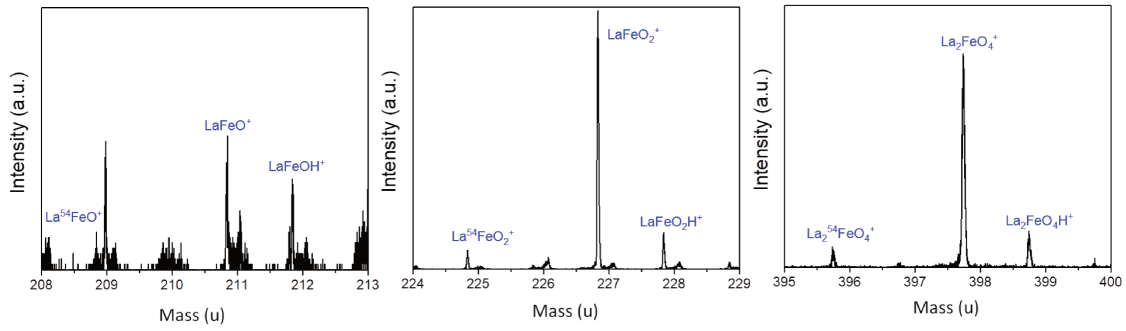

Figure 3.19: ToF-SIMS mass spectra of $LaFeO_3$ thin film (LFO:Si-100) showing the mixed oxide fragments containing La, Fe and O.

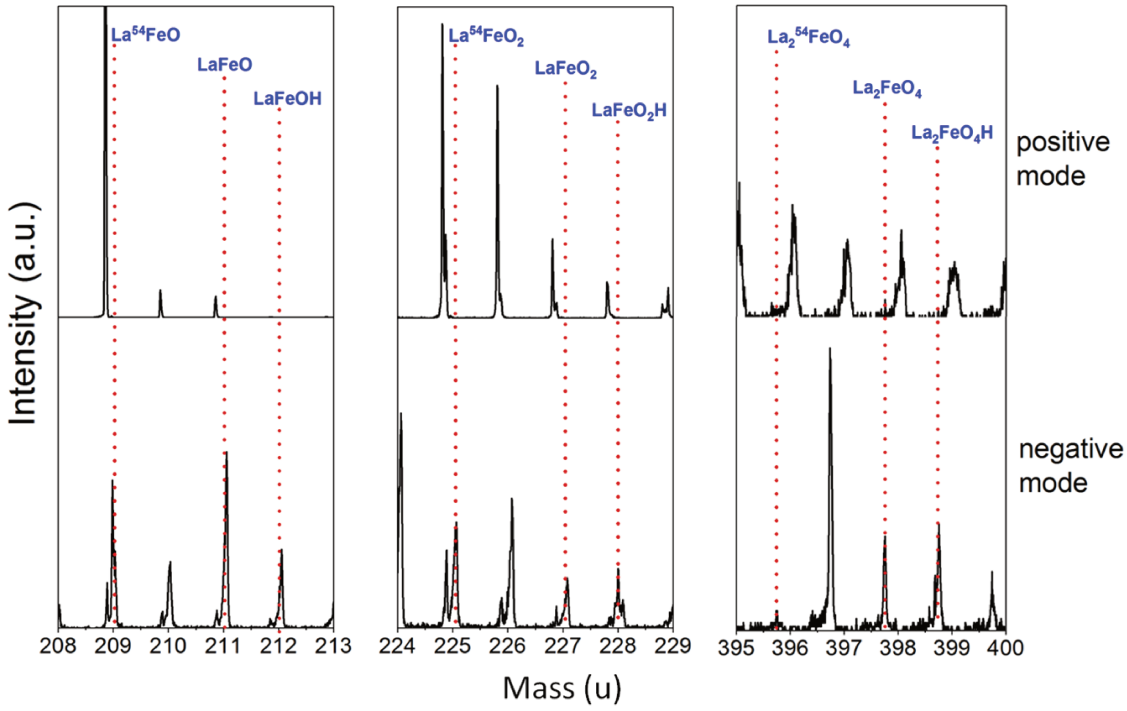

Figure 3.20: ToF-SIMS mass spectra of a bare SiO_2/Si(100) substrate measured in positive and negative modes at the m/z region expected from the mixed oxide fragments (dotted lines).

To ensure that the mixed oxide fragments are indeed originating from the surface of the perovskite layer and not merely as a result of recombination of the individual ions such as $La_xO_y^+$ and $Fe_xO_y^+$ from segregated phases of La or Fe oxides, a mechanical mixture of commercial powders of Fe_2O_3 and La_2O_3 was analyzed. This mixture was prepared by grinding together the two oxides to finally prepare a pellet. The mass spectrum of this mixture showed almost no signal in the region of a selection of the mixed oxide fragments of interest as shown in Fig.3.21. This confirms that detection of the mixed oxide ions is a direct indication of the presence of a perovskite phase only, and not an outcome of any recombination process. Several studies on different catalysts have shown that the secondary ions produced by ToF-SIMS are a result of the direct fragmentation of ions with compositions characteristic of the surface analyzed rather than any recombination process, as is the case here [18–21].

3.3.4 Towards ultra-thin film of perovskite (LFO:Si-10)

This section involves the LFO:Si-10 films prepared with the most dilute precursor solution yielding perovskite film in the ultra-thin range (<10 nm). The low thickness provides

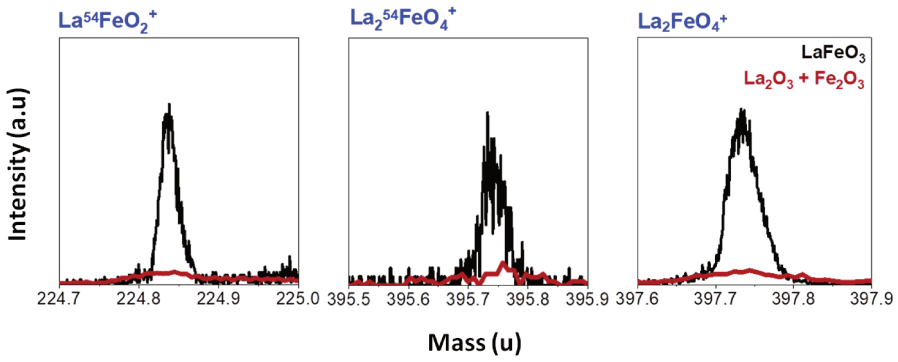

Figure 3.21: ToF-SIMS spectra of a mechanical mixture of La_2O_3 and Fe_2O_3 (red) and the $LaFeO_3$ thin film (LFO:Si-100) (black) in positive mode.

a higher surface to bulk ratio. Another advantage of such a sample is that it can act as a sample driven surface analysis even when highly sensitive bulk techniques are used. The main objective of studying this kind of ultra-thin film is to ensure the presence of the perovskite phase at such low thickness and also to correlate to the physico-chemical properties of the $LaFeO_3$ surface.

Morphology The surface of the as-prepared samples consists of regularly but randomly spaced round island-like zones as shown by the AFM image in Fig.3.22 with a mean diameter of 215 nm, which however fails to give a real depiction of the size distribution. By means of statistical analysis, the dimensions of the circular deposits show multi-modal distribution centered around 77 nm (21%), 124 nm (36%), 221 nm (20%) and 342 nm (23%). A line scan across a specific spot reveals the maximum height of the deposited perovskite to be around 3 nm with a diameter of around 250 nm (Fig.3.22). The beginning and the end of the line scan represent the surface roughness variation of the SiO_2/Si surface of the substrate.

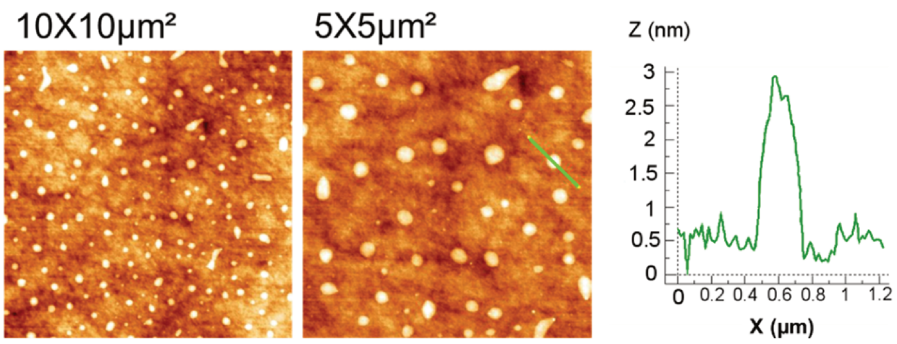

Figure 3.22: AFM images of the $LaFeO_3$ ultra-thin film (LFO:Si-10) and line-scan (green) across a spot.

The high resolution TEM analysis of the FIB-lamella of this thin film in Fig.3.23 also features a thickness close to 4 nm of the perovskite film. The FIB-lamella was cut across one of the spots to reveal the cross-sectional thickness. The deposited layer comprised of La and Fe across depth indicating presence of the mixed oxide. The image however does not clearly highlight the crystallinity of the deposited layer. On the regions without the circular deposits, no La or Fe signal were detected by EDX analysis. This confirms that only the island-like features are composed of the perovskite while the rest of the surface is non-coated substrate.

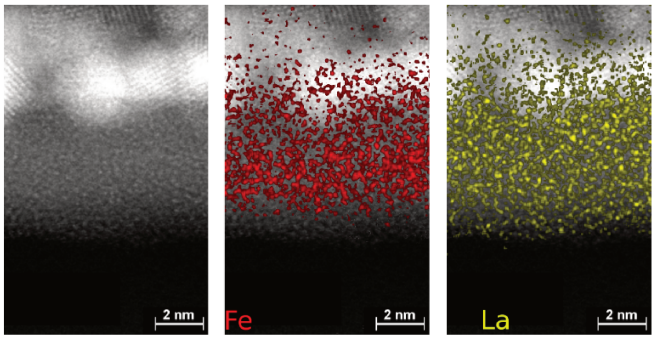

Figure 3.23: HR-TEM and EDX images of the cross-section of $LaFeO_3$ ultra-thin film (LFO:Si-10).

The morphology of the ultra-thin film is also indicative of the type of growth of the thin film. It follows a Volmer-Weber type growth model where the interface energy is large enough to slowdown the formation of a complete layer and instead discrete nuclei like structures are formed during the growth process [22]. This means the perovskite has a tendency to cluster as a result of weaker bonding with the substrate. According to this growth model, a homogeneous layer can be formed as the islands are nucleated and merge together. And with respect to this particular sample, due to the dilute precursor solution used, the merging together of the islands remains incomplete instead of formation of complete layers of the oxide. In any case, each of the island-like deposits can be considered to be representative of a $LaFeO_3$ perovskite thin film of ~3 nm.

XPS analysis The XPS spectra of the ultra-thin film in Fig.3.24 show similar characteristics as before (section 3.3) with some minor differences. The O 1s spectrum shows very small intensity from the lattice oxygen and majority of the signal arises from the silica layer of the substrate. Interestingly, the perovskite surface contains almost no carbonates, usually positioned around 289 eV in the C 1s signal. The lower amount of such adsorbed species on the surface is a result of the limited size and characteristic morphology

of the thin film. In this case, only surface hydroxides and aliphatic adventitious carbon are present summing to 9% of the total atomic concentration. The Fe 2p and La 3d photopeaks have a binding energy of 710.4 and 834.1 eV, respectively, indicating the oxidation of 3+ for both ions. The Fe^{3+} satellite feature is not so clearly resolved due to the low amounts of the deposited layer. However, the overall Fe 2p peak shape with the FWHM of 3.7 eV and the binding energy value signifies the valence state of 3+.

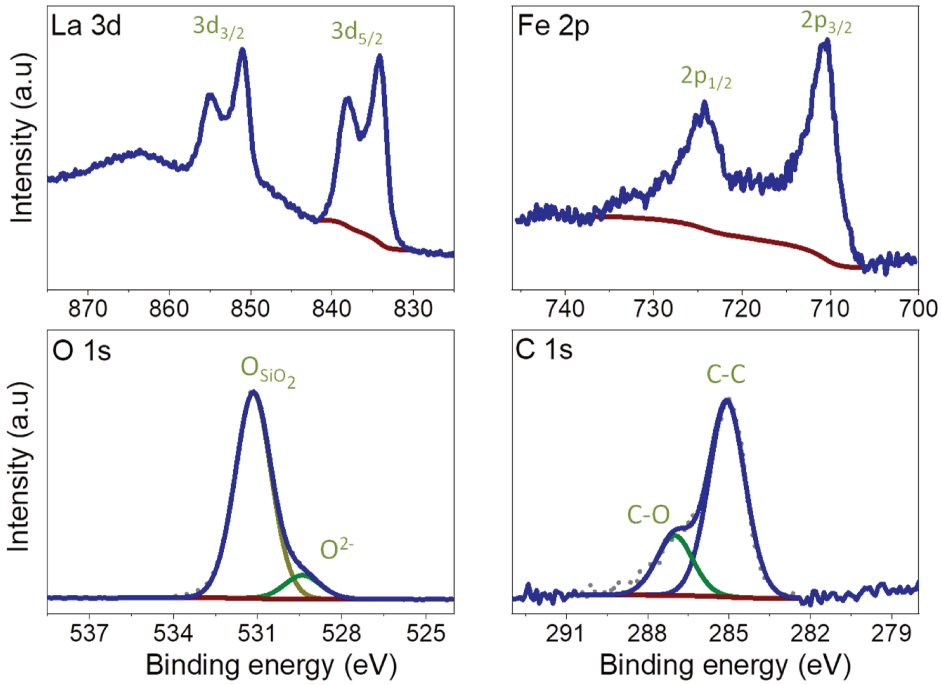

Figure 3.24: XPS La 3d, Fe 2p, O1s, and C 1s spectra of $LaFeO_3$ ultra-thin film (LFO:Si-10).

In case of the La $3d_{5/2}$ orbital, the component of the multiplet structure on the higher binding energy side is less intense than the other, with an energy separation of 3.8 *e*V. The multiplet structure intensity and shape in La 3d spectrum is in good agreement with that of a clean $LaFeO_3$ surface as evidenced by XPS La 3d spectrum of LFO:Si-100 after treatment at 900°C under oxygen (Fig.3.14). The LFO:Si-10 is therefore indicative majorly of the perovskite surface. Finally, the La/Fe atomic ratio for the ultra-thin film is 1.3, lower than in case of the intermediate thin film of 70 nm (close to 2) as previously discussed. This difference is caused by the low thickness and typical morphology of the thin film which responds differently by forming lower amount of surface lanthanum species, mostly hydroxides.

LEIS analysis The LEIS spectra of the ultra-thin film of $LaFeO_3$ is presented in Fig.3.25, analyzed at four different regions of 1000 x 1000 μm^2 on the sample surface. Each spec-

trum shows the elemental surface peaks of La, Fe, Si and O with similar intensities highlighting the homogeneous distribution of the perovskite deposit throughout the sample. The La and Fe signals from the perovskite layer show at lower energy side of surface peaks, low intensity sub-surface contribution (from deeper layers) owing to the low thickness of the $LaFeO_3$ layer. The relatively intense signal of silicon is caused by the low coverage of the perovskite on the substrate. The LEIS study confirms the presence of both La and Fe on the first atomic layer, or in other words, the perovskite layer on this ultra-thin film. The La/Fe atomic ratio was calculated to be 3.3, similar to the one obtained for LFO:Si-100.

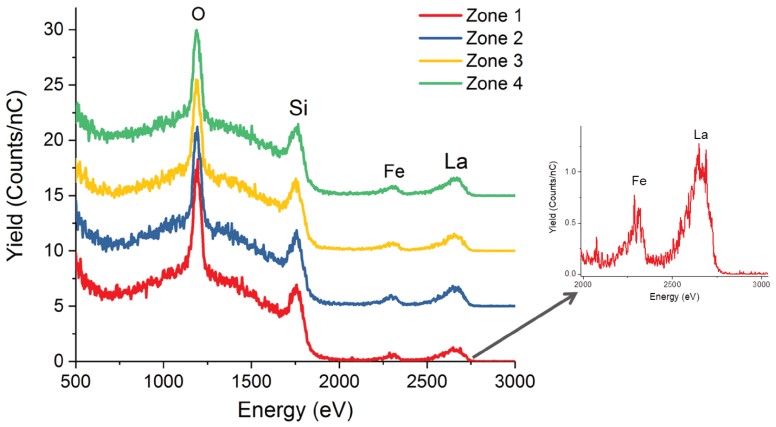

Figure 3.25: LEIS spectra of $LaFeO_3$ ultra-thin film (LFO:Si-10) using 3 keV $^4He^+$ on different analysis areas of 1000 x 1000 μm^2.

LEIS analysis was continued through several cycles of sputtering with 5keV $^{20}Ne^+$ in an attempt to depth profiling the thin deposited layer of perovskite. On sputtering gradually as shown in Fig.3.26, a sharp increase in the intensity of the silicon signal with decrease in the O signal occurs as the silica layer from the top was removed and the silicon was revealed. It must be noticed that during the sputtering process the $LaFeO_3$ film as well as the silica is removed at the same time although with different sputtering rates. The La and Fe signals are diminished as the sputtering progressed but were not completely removed after several cycles of sputtering (inset of Fig.3.26).

ToF-SIMS analysis The ToF-SIMS spectra consisting of the mixed oxide fragments similar to LFO:Si-100 have been shown in Fig.3.27. These mixed fragments are representative of the presence of the perovskite phase, since the occurrence of such fragments by recombination is almost negligible, as already discussed in section 3.3. The lateral distribution of some selected ions has been shown in Fig.3.28. Due to the limitation of lateral resolution in ToF-SIMS (100-200 nm), the specific spot-like feature of $LaFeO_3$ deposits

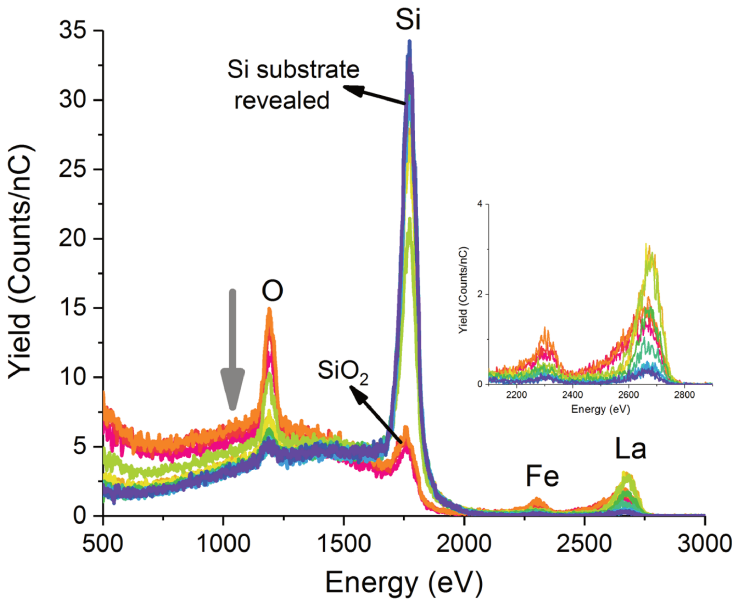

Figure 3.26: LEIS depth profile of $LaFeO_3$ ultra-thin film (LFO:Si-10) using 5 keV $^{20}Ne^+$ for sputtering and 3 keV $^4He^+$ for analysis.

are not visible. The images only represent the presence of the La, Fe and the mixed oxide fragments throughout the surface of the material.

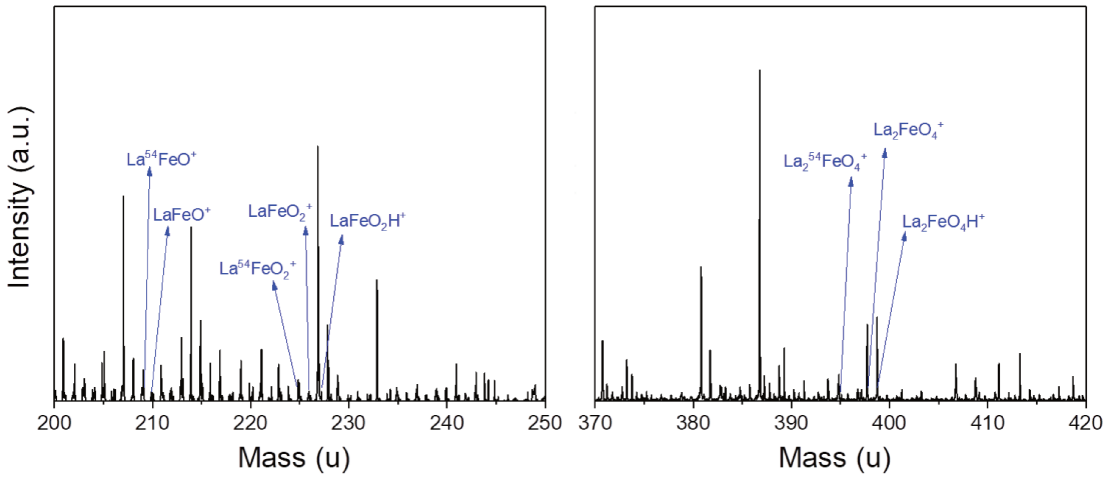

Figure 3.27: ToF-SIMS spectra of the ultra-thin film of $LaFeO_3$ (LFO:Si-10) of 500x500 μm^2 showing the mixed oxide fragments containing La, Fe and O.

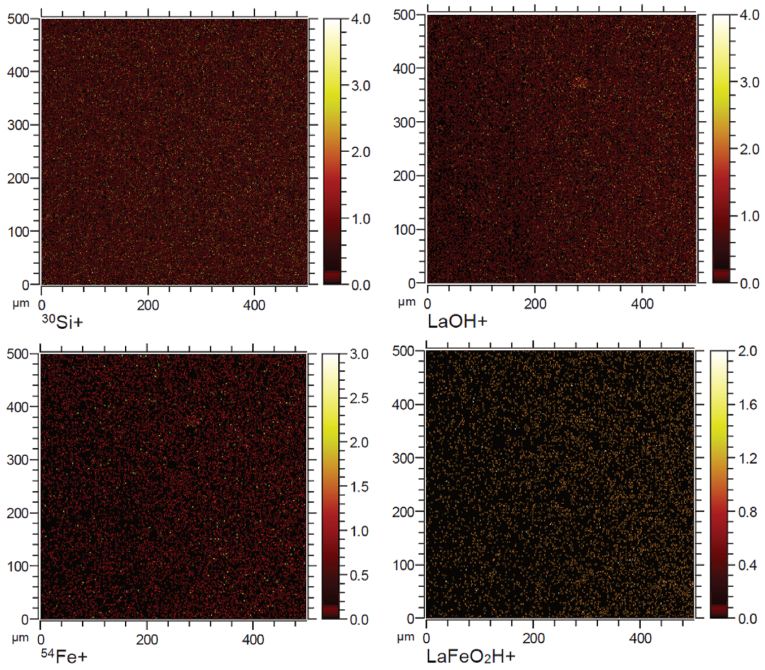

Figure 3.28: ToF-SIMS images of the surface of LFO:Si-10.

3.4 Direct comparison with conventional powder catalysts

In the previous sections, the thin films or model catalysts of $LaFeO_3$ were fully characterized by combination of different surface analytical techniques as well as bulk and microscopy techniques. It was confirmed that the film layer was indeed $LaFeO_3$ phase with sub-100 nm thickness. In this section, a comparative study between the $LaFeO_3$ thin film and the conventional powdered catalysts used at the lab scale has been made using a single technique. To this end, XANES has been used to study the similarities or differences between the two and thereby confirm their relevance as a suitable model catalyst for advanced characterization under operative conditions. XANES not only allows to obtain information on the coordination geometry and the oxidation states due to its sensitivity to local geometries and electronic structures, but can also provide valuable data on the sample's surface and bulk simultaneously when measured at grazing incidence (GI-XANES) in fluorescence mode.

In the second part, the LFO:Si-100 thin film and the corresponding powder were both analyzed by quasi-*in situ* XPS analysis using a coupled treatment cell, where the material was activated under oxygen up to 500°C followed by exposure under CO gas at the same temperature. After the *in situ* treatment, they were transferred to the XPS analysis chamber under UHV conditions without contact in air.

3.4.1 GI-XANES analysis at Fe K-edge

$LaFeO_3$ thin film of intermediate thickness The XANES spectrum of the $LaFeO_3$ powder has been shown in Fig.3.29, recorded in the transmission mode using a pellet. The perovskite powder shows a typical XANES fingerprint of $LaFeO_3$ with a pre-edge at the absorption edge of 7128.1 eV signifying the presence of Fe^{3+} [13, 23]. The pre-edge is formed due to the quadrupolar 1s→3d transitions and dipolar transitions due to mixing of p and d orbitals, while the intense edge region is caused by 1s→4p dipole-allowed transition [23].

Further, to study the surface as well as the bulk of the $LaFeO_3$ thin film by XANES, the measurement was done in the fluorescence mode at grazing incidence. The critical angle between the beam and the sample was adjusted such that measurement could be tuned from being surface sensitive to bulk sensitive as has been described in details in chapter 2. The surface and the bulk GI-XANES spectra are shown in Fig.3.29, both being similar to that of the $LaFeO_3$ powder in every respect. This indicates that the thin film has the same structure and chemical composition as that of the corresponding powders. Therefore they are well representative as a perovskite model material. In addition, similarity between the surface and the bulk XANES spectra of the thin film highlights the fact that the film is homogeneously composed of only $LaFeO_3$ throughout in depth. The surface spectrum does not show the presence of any phase segregation of iron oxide and hence can be considered as a good model to study the surface properties of such bulk catalysts by utilizing advanced techniques in *in situ* or *operando* modes.

$LaFeO_3$ ultra-thin film LFO:Si-10 was also analyzed by GI-XANES as shown in Fig.3.30 together with the XANES spectrum of $LaFeO_3$ powder. Interestingly, it is confirmed by this technique that the deposited film is indeed that of a perovskite without any additional phases of iron oxide, similar to the powdered catalyst as well as the intermediate film discussed above. Since this sample is already thin (~3 nm) in the range usually probed by the surface sensitive techniques (<10 nm), the surface and bulk spectra are in fact both representative of the surface. This sample generates quite noisy spectra due to the low coverage of the $LaFeO_3$ layer and its thickness. This study indicates that the ultra-thin film is also a good model of the bulk catalysts such as a perovskite. The disadvantage of this kind of sample is that it can only be probed by limited number of techniques since it falls under the limit of detection in most cases such as XRD, Raman and so on. Especially for this kind of a sample, GI-XANES is a very efficient technique, which can efficiently detect films of a few nanometers also, as is the case here.

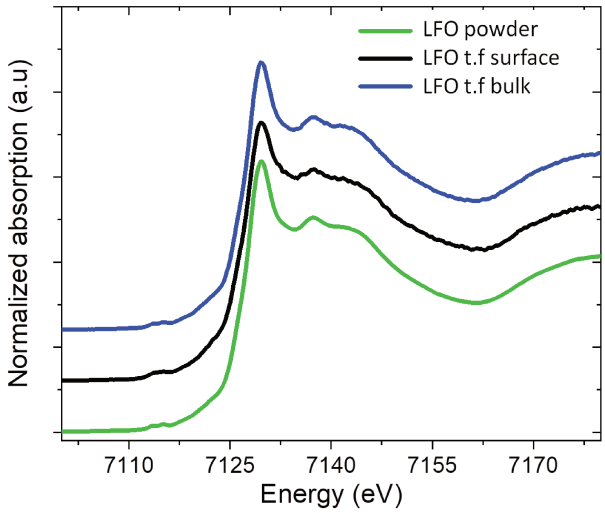

Figure 3.29: XANES spectra of $LaFeO_3$ powder (green) analyzed in transmission mode and surface (black) and bulk (blue) spectra of $LaFeO_3$ thin film (LFO:Si-100) analyzed in fluorescence mode in grazing incidence (GI-XANES).

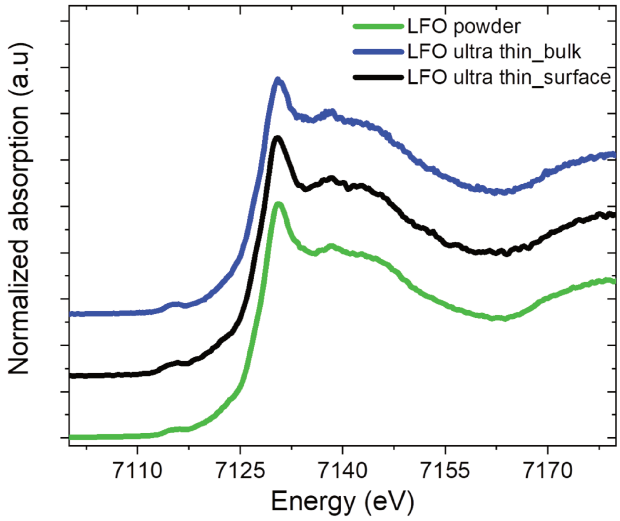

Figure 3.30: XANES spectra of $LaFeO_3$ powder (green) analyzed in transmission mode and surface (black) and bulk (blue) spectra of $LaFeO_3$ ultra-thin film (LFO:Si-10) analyzed in fluorescence mode in grazing incidence (GI-XANES).

3.4.2 Quasi-*in situ* XPS analysis

The $LaFeO_3$ thin film and the powder were also compared with respect to their XPS spectra in the as-received state prior to any treatment in the treatment cell under oxygen and CO gas. Table 3.4 shows the binding energy values of each orbital of interest together with the atomic concentration of the $LaFeO_3$ thin film and powder. The description of the $LaFeO_3$ thin film has been already made in the section 3.3 earlier. The binding energies show comparable values (±0.2 eV). The La/Fe atomic ratio is equivalent to 1.8 in both

cases. However, unlike the thin film, the powder is composed of slightly higher amount of adventitious carbon with 26% compared to only 17% in the thin film. The La 3d and Fe 2p photopeaks of both as-received samples are shown in Fig.3.31. La $3d_{5/2}$ signal at 834 eV has a more intense multiplet splitting component at higher binding energy in the powder, while the opposite is the case for the thin film. This shape is highly dependent on the amounts of lanthanum species on the surface due to the reactive nature of La based compounds. In case of the Fe 2p photopeak, both show similar features with a characteristic Fe^{3+} satellite feature at 719.1 eV with binding energy of 710.3 eV.

Table 3.4: Binding energies, atomic concentration and La/Fe atomic ratio of $LaFeO_3$ thin film (LFO:Si-100) and powder from XPS analysis.

Element	$LaFeO_3$ thin film			$LaFeO_3$ powder		
	Binding energy (eV)	Concentration (%)	La/Fe atomic ratio	Binding energy (eV)	Concentration (%)	La/Fe atomic ratio
La 3d	834.0	22.1	1.8	833.8	17.6	1.8
Fe 2p	710.2	12.7		710.0	10.3	
O 1s	529.4	48.0		529.2	46.4	
C 1s	285.0	17.1		285.0	25.7	
Si 2s	153.9	0.1		-	-	

The two $LaFeO_3$ materials were heated under oxygen up to 500°C, to remove majority of the surface contamination of carbon and obtain as clean surface as possible. After this activation step, less than 2% of the C was remaining on the surface. This allows to provide a clean surface of the perovskite for the succeeding treatment steps. As expected, the La 3d and Fe 2p signals remain in the +3 state after this activation treatment.

Finally, after CO exposure no significant evolution of the Fe 2p or La 3d is observed, evident from the unchanged binding energy value of the Fe 2p or La 3d as well as the Fe^{3+} satellite. This occurrence is shown by both the $LaFeO_3$ thin film as well as the powder indicating that both samples behave similarly under a specific condition, which is expected owing to similar physical and chemical properties of both. It has to be noticed that these XPS analyses were performed under UHV after the different treatments and do not allow to investigate the surface evolutions that may occur under reactive atmosphere. Certainly better information on the extent of CO reactivity on stoichiometric perovskite materials can be obtained if the analysis is done in *in situ* modes under operative conditions and temperatures (discussed in chapter 4).

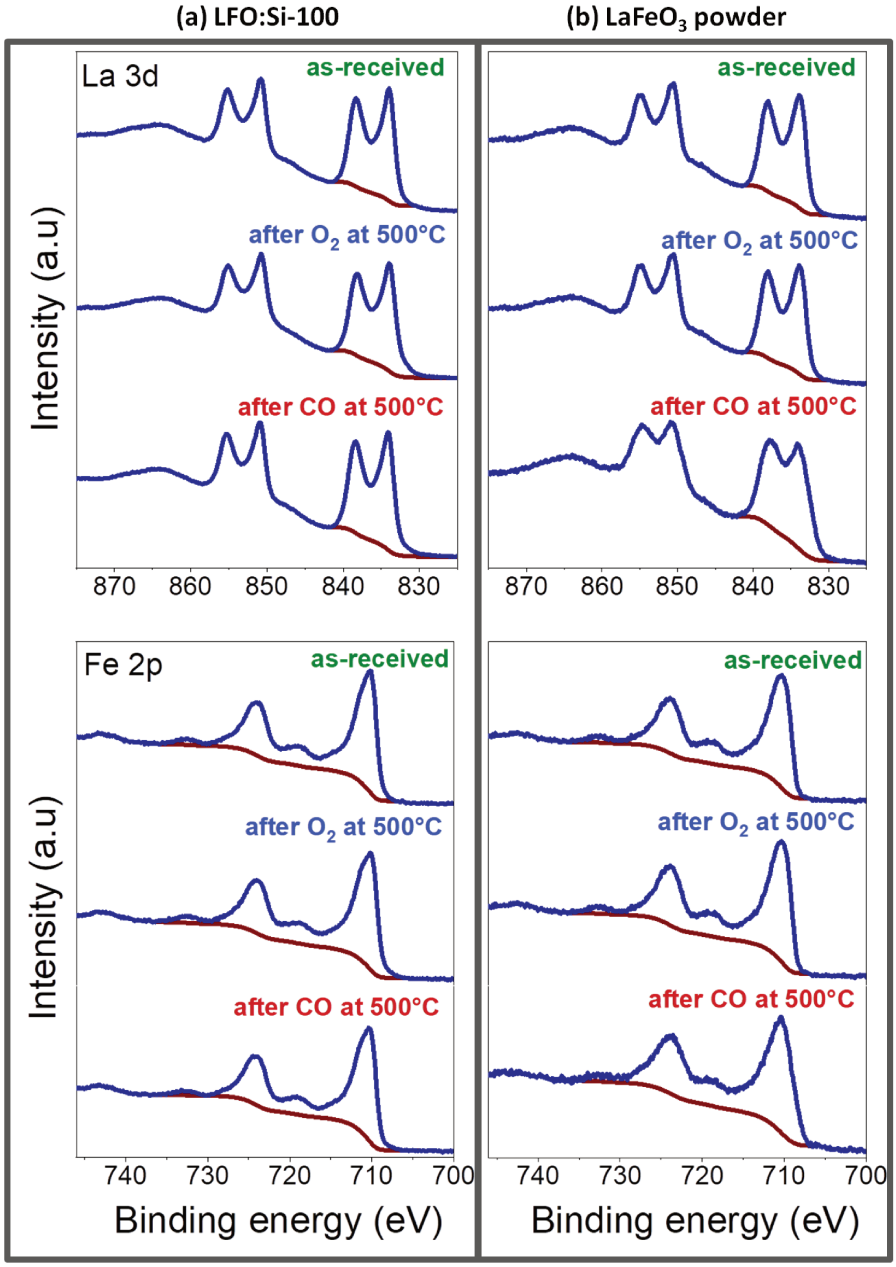

Figure 3.31: XPS La 3d and Fe 2p photopeaks of $LaFeO_3$ thin film (LFO:Si-100) and powder in the as-received state, after activation under oxygen and treatment under CO gas at 500°C.

3.5 Conclusions

The surface compositions, bulk structure and morphology of the $LaFeO_3$/Si based thin films were investigated. The Si substrate comprised of a 1.4 nm thick layer of amorphous silica over crystalline Si(100), revealed by XPS and ToF-SIMS. The thin films were prepared by adjusting the concentration of the precursor solution before deposition on the pre-treated SiO_2/Si(100) substrate. Two main thickness ranges were considered for inves-

tigation in this chapter, the sub-100 nm film of intermediate thickness (LFO:Si-100) and sub-10 nm ultra-thin film (LFO:Si-10) ranges as discrete models. Firstly, the LFO:Si-100 showed homogeneous layers of polycrystalline $LaFeO_3$ with minimum evidence of voids, with a thickness of ~70 nm. The $LaFeO_3$ was crystallized in orthorhombic lattice with a La-enriched surface indicated by the respective surface atomic ratios by XPS and LEIS as mentioned in Table 3.5. ToF-SIMS further highlighted presence of the perovskite phase given by the mixed oxide fragments, an useful way to determine mixed oxide phase when present under detection limits of other techniques. Similarly, the ultra-thin film (LFO:Si-10) also indicated the presence of $LaFeO_3$, although it features incomplete film coverage with a thickness of below 5 nm. It featured lower contamination from carbonates and thereby less enrichment of La on the surface, presented in Table 3.5. This kind of models having a thickness in the range usually analyzed by surface analysis techniques allows to provide surface sensitive data using bulk techniques with excellent sensitivities. Finally, the two kinds of thin films were compared to conventional powder catalysts, thanks to GI-XANES analysis. Both LFO:Si-100 and LFO:Si-10 thin films featured the same XANES fingerprint as that of the powder at the surface as well as the bulk. The reactivity of the thin film and the powder after CO exposure was analyzed highlighting identical behavior. Thereby, such thin films have been demonstrated to be relevant model catalysts that can be reliably used for surface investigations of TWCs. Therefore, having confirmed the relevance of the model catalysts, such models will be further investigated under *in situ* conditions to reveal difference in catalytic performances induced by changing the stoichiometric compositions of lanthanum ferrite, namely, $LaFeO_3$ and $La_{0.7}FeO_3$.

Table 3.5: Summary of the surface atomic ratios of $LaFeO_3$ thin films of intermediate (LFO:Si-100) and ultra-thin thickness (LFO:Si-10).

Sample	Structure	Thickness (nm)	La/Fe (XPS)	O/(La+Fe) (XPS)	Carbonates C1s % (XPS)	La/Fe (LEIS)
LFO:Si-100	$LaFeO_3$ orthorhombic	70	1.8	1.4	16.2	3.1
LFO:Si-10	$LaFeO_3$ orthorhombic	5	1.3	1.3	-	3.3

3.6 References

[1] X.-R. Yu and H. Hantsche, *Surf. Interface Anal.*, 1993, **20**(7), 555–558. 70, 71

[2] J. Grimblot, *L'analyse de surface des solides par spectroscopies électroniques et ioniques, avec problèmes résolus*, Elsevier Masson, 1995. 70

[3] C. J. Powell and A. Jablonski, *Journal of Vacuum Science & Technology A*, 1999, **17**(4), 1122–1126. 71

[4] M. Morita, T. Ohmi, E. Hasegawa, M. Kawakami, and M. Ohwada, *J. Appl. Phys.*, 1990, **68**(3), 1272–1281. 71

[5] J. H. Parker, D. W. Feldman, and M. Ashkin, *Phys. Rev.*, 1967, **155**, 712–714. 72

[6] J. Lee, J. Lee, T. Tanaka, and H. Mori, *Nanotechnology*, 2009, **20**(47), 475706. 74

[7] D. Blanck, A. Schön, A.-S. Mamede, C. Dujardin, J.-P. Dacquin, P. Granger, J.-F. Paul, and E. Berrier, *Catal. Today*, 2016. 79

[8] Andreasson, Jakob and Holmlund, Joakim and Rauer, Ralf and Käll, Mikael and Börjesson, Lars and Knee, Christopher S. and Eriksson, Annika K. and Eriksson, Sten-G. and Rubhausen, Michael and Chaudhury, Rajit P., *Phys. Rev. B*, 2008, **78**, 235103. 79

[9] A. Dubroka, J. Humlíček, M. Abrashev, Z. Popović, F. Sapina, and A. Cantarero, *Phys. Rev. B*, 2006, **73**, 224401.

[10] M. Popa, J. Frantti, and M. Kakihana, *Solid State Ionics*, 2002, **154-155**, 437 – 445. 79

[11] A. Schön, C. Dujardin, J.-P. Dacquin, and P. Granger, *Catal. Today*, 2015, **258**, 543 – 548. 79, 80

[12] M. Sunding, K. Hadidi, S. Diplas, O. Løvvik, T. Norby, and A. Gunnæs, *J. Electron. Spectrosc.*, 2011, **184**(7), 399 – 409. 80, 81

[13] S. Phokha, S. Pinitsoontorn, S. Maensiri, and S. Rujirawat, *J. Sol-Gel Sci. Techn.*, 2014, **71**(2), 333–341. 94

[14] S. Thirumalairajan, K. Girija, V. R. Mastelaro, and N. Ponpandian, *ACS Appl. Mater. Inter.*, 2014, **6**(16), 13917–13927. 80, 81

[15] M. C. Biesinger, B. P. Payne, A. P. Grosvenor, L. W. Lau, A. R. Gerson, and R. S. Smart, *Appl. Surf. Sci.*, 2011, **257**(7), 2717 – 2730. 80

[16] M. L. Miller and R. W. Linton, *Anal. Chem.*, 1985, **57**(12), 2314–2319. 81

[17] H. H. Brongersma, M. Draxler, M. de Ridder, and P. Bauer, *Surf. Sci. Reports*, 2007, **62**(3), 63 – 109. 83

[18] F. Aubriet, C. Poleunis, and P. Bertrand, *J. Mass Spectrom.*, 2001, **36**(6), 641–651. 87

[19] L. Weng, P. Bertrand, O. Tirions, and M. Devillers, *Appl. Surf. Sci.*, 1996, **99**(3), 185 – 196.

[20] L.-T. Weng, *Appl. Cata. A - General*, 2014, **474**, 203 – 210.

[21] J. Grams, A. Ura, and W. Kwapiński, *Fuel*, 2014, **122**, 301–309. 87

[22] L. G. Benning and G. A. Waychunas, in *Kinetics of Water-Rock Interaction*, ed. S. L. Brantley, J. D. Kubicki, and A. F. White, Springer New York, New York, NY, 2008; pp. 259–333. 89

[23] O. Haas, U. Vogt, C. Soltmann, A. Braun, W. S. Yoon, X. Q. Yang, and T. Graule, *Mater. Res. Bull.*, 2009, **44**. 94

Chapter 4

Comparing $LaFeO_3$ and $La_{0.7}FeO_3$ based model catalysts by combination of advanced characterization techniques

Having verified in the previous chapter, the surface and structural relevance of $LaFeO_3$ perovskite-based thin films as suitable model catalysts, such materials are thereby used to investigate the differences in the catalytic behaviours of stoichiometric $LaFeO_3$ and La-deficient $La_{0.7}FeO_3$. As it is already observed in previous studies discussed in chapter 1, inducing an A-site deficiency reduces the extent of La-enrichment on the surface of the perovskite catalyst. This permits better catalytic performance for CO oxidation as well as NO reduction of $La_{0.7}FeO_3$ as compared to $LaFeO_3$. In order to further investigate this improved activity, the models of the two respective compositions are systematically studied in this chapter. Initially, *ex situ* techniques are employed to determine and compare the physico-chemical properties of the as-received samples by XPS, LEIS, ToF-SIMS and Raman analyses. In addition, depth profiling by ToF-SIMS and LEIS is performed to highlight any surface variations on each composition, a common aspect in perovskites. Finally, the two compositions are compared by employing *in situ* analyses under a TWC-relevant gas such as CO, to study the surface reactivity during CO exposure at high temperature by NAP-XPS and *in situ* GI-XANES investigations. The NAP-XPS analysis allows to track the different behaviors of the two stoichiometries under CO environment to provide a reliable methodology to describe the trends under reactive conditions by analyzing the changes in the overall oxidation states of the extreme surface (~2 nm). Furthermore, a detailed study under similar conditions is performed by *in situ* GI-XANES to reveal the

structural information at the surface (~2-8 nm) and the bulk simultaneously. Finally, the XANES spectra are fitted by linear combination of Fe-based reference materials to quantitatively examine the phase composition at each step. The ameliorating role of the induced La-deficiency in the perovskite is thereby explained by a predicted model. In the light of all experimental results, a schematic conclusion will be proposed to describe the promoting role of La-deficient perovskite.

4.1 Ex-situ analysis of $La_{0.7}FeO_3$ and $LaFeO_3$ thin films

4.1.1 XPS

The XPS spectra of $La_{0.7}FeO_3$ thin film are given in Fig.4.1 and those of $LaFeO_3$ have been previously presented in chapter 3 (section 3.3.3). Both feature La in +3 oxidation state characterized by the position of La $3d_{5/2}$ at 834.1 and 834.3 eV, respectively. They show an energy separation of 4.2 eV in the multiplet splitting component of the La $3d_{5/2}$, corresponding to oxides of lanthanum [1]. The Fe $2p_{3/2}$ photopeak is located at a binding energy of 710.4 eV for $LaFeO_3$ and 710.7 eV for $La_{0.7}FeO_3$ confirming iron in the +3 oxidation state, given by the characteristic satellite feature, 8.8 eV higher than the $2p_{3/2}$ photo peak [2]. The stoichiometric perovskite $LaFeO_3$ shows a high La/Fe ratio of 1.8 (instead of 1) due to the formation of surface La carbonates, supported by the presence of 16% of the total carbon as carbonates. While the $La_{0.7}FeO_3$ has a La/Fe ratio of close to 1 by limiting the formation of the surface La species confirmed by the lower amount of only 4% carbonates in the C 1s spectra, similar to the powders of same composition as discussed by Schöen *et al* [3]. Further, $La_{0.7}FeO_3$ presents O 1s orbital with a main components around 529.8 eV attributed to the lattice oxygen (O^{2-}) and another contribution centred at 531.3 eV representing the surface O_2^-/O^- species, adsorbed hydroxyls, carbonates and/or organic oxygen species. Additionally, the O/(La+Fe) ratio for $LaFeO_3$ and $La_{0.7}FeO_3$ is 1.4 and 1.7, close to the empirically expected value of 1.5 and 1.8, respectively. The oxygen excess in the La-deficient $La_{0.7}FeO_3$ is known to be usually caused by A/B site vacancies with their partial elimination as the respective oxide phases [4].

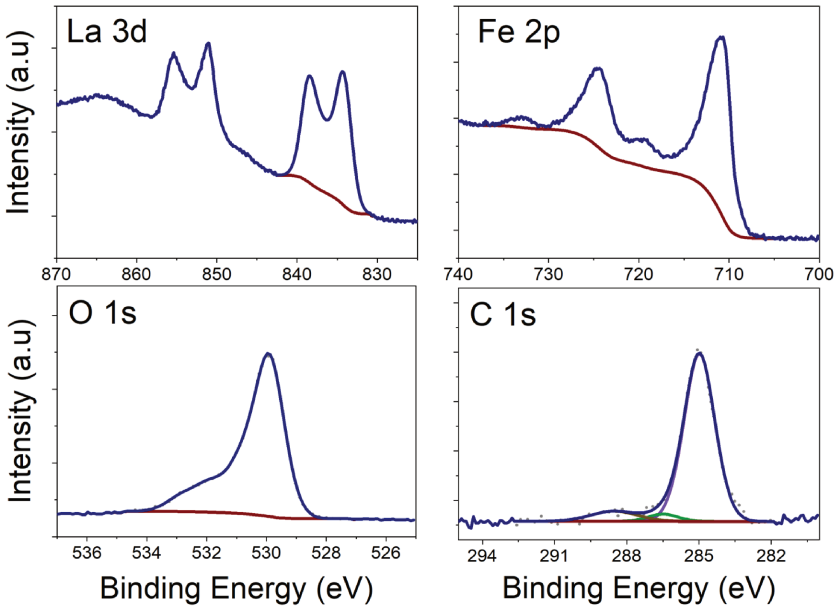

Figure 4.1: XPS La 3d, Fe 2p, O 1s and C 1s spectra of $La_{0.7}FeO_3$ thin films under UHV conditions.

4.1.2 Raman spectroscopy

Owing to the low thickness of the thin film, the Raman spectra are dominated largely by the signal of silicon from the Si(100) substrate. Subtracting the Si signal from the spectrum of the film revealed the signature of the $LaFeO_3$ perovskite phase. The assignment of these lines has been previously detailed in previous chapters and [5]. All the expected bands from $LaFeO_3$ are present at 160, 180, 269, 298, 231 and 638 cm^{-1} as shown in Fig.4.2(a). Similarly, the La-deficient perovskite shows not only all the lines of $LaFeO_3$ perovskite and but also some additional lines from the α-Fe_2O_3 or hematite phase. The prominent lines at 223, 295, 410 and 620 cm^{-1} display the Raman fingerprint of well crystallized hematite phase [6, 7]. Further, the presence of some γ-Fe_2O_3 or maghemite phase cannot be ruled out due to the very broad nature of its signal at around 650 cm^{-1}. The other maghemite bands present around 350 and 500 cm^{-1} are not easy to detect due to overlapping lines. The Raman analysis therefore highlights that the non-stoichiometric perovskite is composed of perovskite as well as the most stable phase of Fe_2O_3 formed as a result of the La-deficient composition. In contrast, the stoichiometric $LaFeO_3$ film only indicates the perovskite phase without any addditional phase of iron oxide(s).

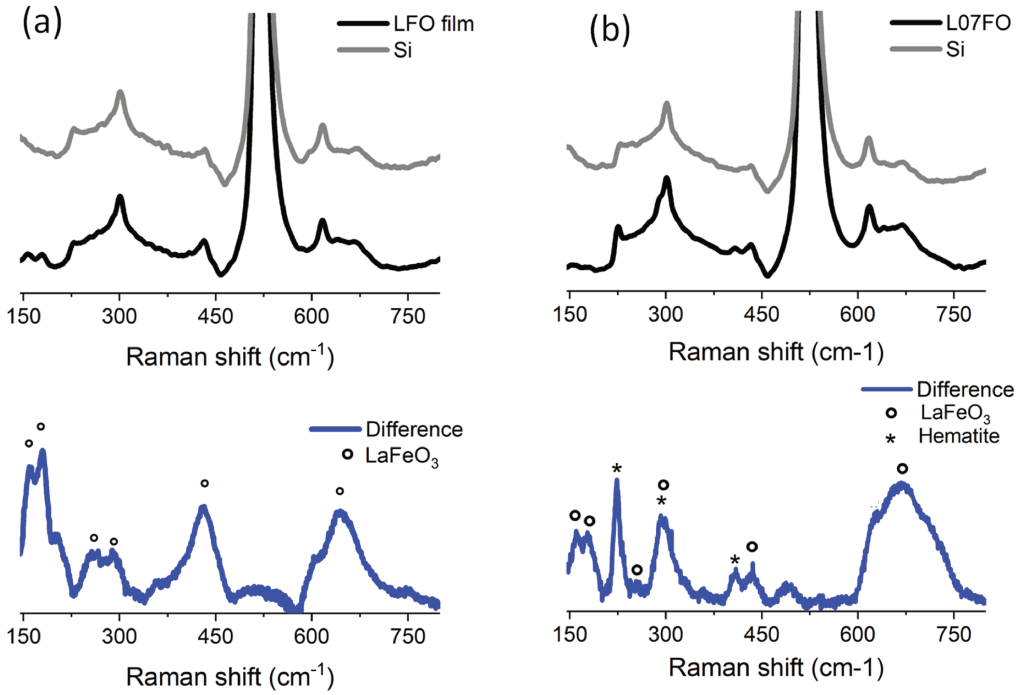

Figure 4.2: Raman difference spectra of (a) $LaFeO_3$ and (b) $La_{0.7}FeO_3$ thin films obtained by subtracting the spectrum of the Si substrate from that of the thin film.

4.1.3 X-Ray absorption near-edge structure at Fe K-edge

Stoichiometric perovskite $LaFeO_3$: The normalized XANES spectra of the surface and bulk of the stoichiometric perovskite thin film have been shown in Fig.4.3. The experimental details of this technique have been provided in chapter 2. Both show identical fingerprint of the $LaFeO_3$ phase with the position of the absorption edge at 7128.3 eV, as discussed previously in chapter 3. The composition of the thin film is the same for the surface and the bulk, except slightly lower signal-to-noise of the surface spectrum, confirming the in-depth homogeneity of the perovskite across this model catalyst.

La-deficient perovskite $La_{0.7}FeO_3$: Fig.4.4 presents the surface and bulk spectra of $La_{0.7}FeO_3$ thin film, with an absorption egde at 7127.6 eV, slightly lower than the stoichiometric one. The XANES spectra of this La-deficient composition are different in shape compared to that of the stoichiometric one, especially the whiteline structure. Both surface and bulk spectra however feature similar shape at the pre-edge with a small variation in the intensity of the whiteline, lower in case of $La_{0.7}FeO_3$ bulk spectrum. Higher intensity of the whiteline likely signifies higher contribution from the perovskite in the XANES spectrum, as is the case in Fig.4.3. To highlight these differences more precisely, each

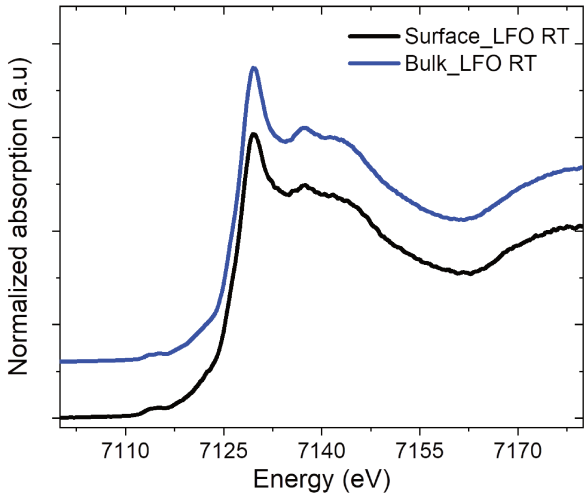

Figure 4.3: Fe K-edge surface (black) and bulk (blue) XANES spectra of $LaFeO_3$ thin film at room temperature measured in fluorescence mode.

spectrum is compared to the XANES spectra of typical iron oxide references, as shown in Fig.4.5, such as the hematite (α-Fe_2O_3), maghemite (γ-Fe_2O_3), magnetite (Fe_3O_4), wüstite (FeO), Fe metal and $LaFeO_3$ powders with absorption edge of 7126.7, 7126.7, 7124.3, 7119.4, 7112.0 and 7128.1 eV, respectively. The edge energy is dependent on the oxidation state of the iron in the material. These reference spectra are used for performing linear combination fitting (LCF) of all the experimentally obtained XANES spectra.

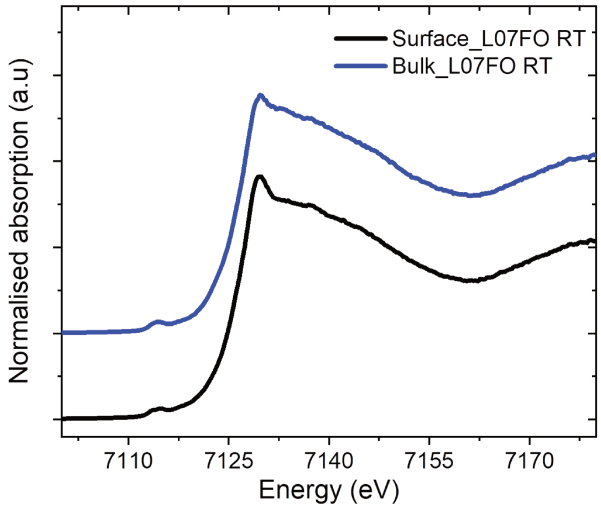

Figure 4.4: Fe K-edge surface and bulk XANES spectra of $La_{0.7}FeO_3$ thin film at room temperature measured in fluorescence mode.

Comparison between $LaFeO_3$ and $La_{0.7}FeO_3$ surface/bulk: As evident from Fig.4.3

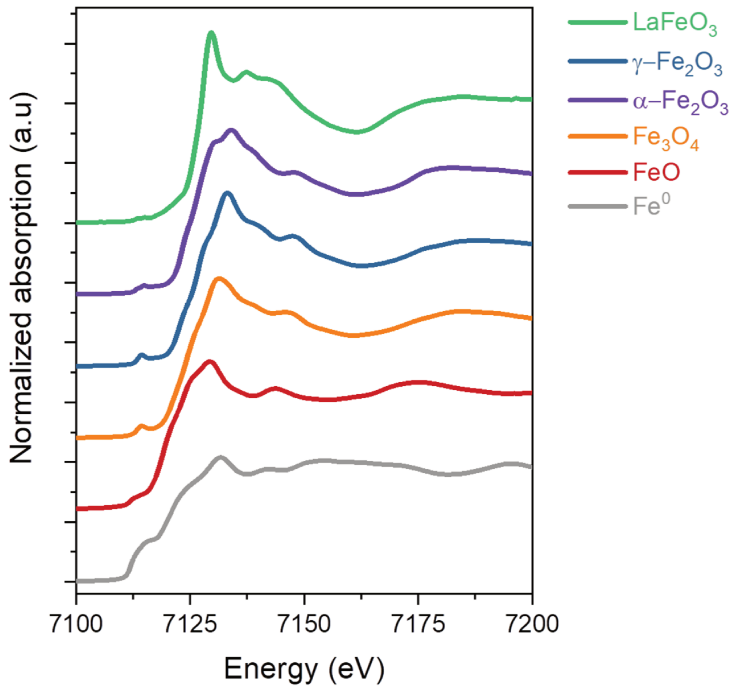

Figure 4.5: Fe K-edge XANES spectra of different Fe-based references measured in transmission mode.

and 4.4 the XANES spectra of $La_{0.7}FeO_3$ thin film display a different shape compared to those of $LaFeO_3$ film, indicating variation in their respective compositions. The differences in the two stoichiometries can be explained by the LCF analysis of the respective XANES spectra. No precipitation of any additional phase is detected in stoichiometric perovskite as the spectra are similar to the one of $LaFeO_3$ powder at the surface and bulk (described in chapter 3). Thus, the $LaFeO_3$ thin film essentially consists of a single perovskite phase. While the non-stoichiometric composition $La_{0.7}FeO_3$ is composed of not only the perovskite phase but also additional iron oxide phase(s) as evident from Fig.4.6. The film's surface is composed of 60% perovskite and 40% hematite phase. While the bulk consists of 50% perovskite, 35% hematite and 15% of maghemite phase. The presence of hematite is also confirmed by Raman analysis previously, offering a different starting point for $La_{0.7}FeO_3$. These observations suggest that the induced La-deficiency does not form a single phase of non-stoichiometric perovskite but yields a mixture of the stoichiometric perovskite and the iron oxide phases, particularly α-Fe_2O_3. This occurrence is assisted by the presence of excess of iron in the composition of $La_{0.7}FeO_3$, indicating that the perovskite has a higher tendency to remain in the stoichiometric formulation, instead of forming a single structure with A-site (La) vacancies.

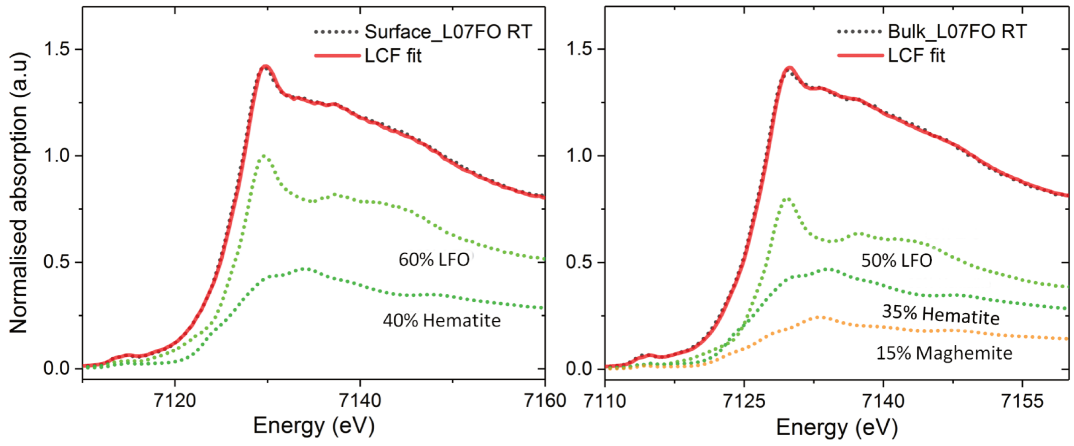

Figure 4.6: LCF analysis of surface (left) and bulk (right) XANES spectra of $La_{0.7}FeO_3$ thin film.

4.1.4 Surface analyses by LEIS and ToF-SIMS

The LEIS spectra of stoichiometric $LaFeO_3$ and non-stoichiometric $La_{0.7}FeO_3$ have been presented in Fig.4.7. The LEIS spectra in both cases probing the first atomic layer, present the expected surface elemental peaks of La, Fe and O indicating a rather clean surface. The $LaFeO_3$ spectrum presents a much higher intensity of La signal compared to Fe signal due to La-enrichment caused by the formation of surface La-species such as oxides, hydroxides or carbonates. This trend is reversed on inducing the La-deficiency in the structure in $La_{0.7}FeO_3$ with higher coverage of Fe than La. The La/Fe atomic ratios calculated from the LEIS spectra were determined to be 3.1 and 0.7 for $LaFeO_3$ and $La_{0.7}FeO_3$, respectively, using our elemental sensitivity factors, as has been previously discussed in chapter 3. The LEIS atomic ratios are slightly different to those obtained by XPS analysis (1.8 for $LaFeO_3$, 1 for $LaFeO_3$), owing to the extreme surface sensitivity to the first atomic layer compared to 5-10 nm probed by XPS. Both LEIS as well as XPS show similar trends within the same order of magnitude. It highlights majority of La atoms on $LaFeO_3$ while that of Fe on $La_{0.7}FeO_3$ at the surface of each composition.

Depth profiling by ToF-SIMS on stoichiometric $LaFeO_3$ thin film has been displayed in Fig.4.8. The depth profile highlights three distinct zones, the SiO_2/Si(100) substrate, the perovskite bulk and the surface with higher concentration of $^{54}FeO^-$ and O_2^- ions. The $^{54}Fe^-$, $LaO^-$and La^- fragments evolve similarly during the depth profiling from surface towards the bulk, with interfacial variations due to matrix effects as the substrate is approached. The higher intensity of $^{54}FeO^-$ (and O_2^-) is indicative of the presence of iron-enriched region near the surface. This is quite an unexpected outcome since any

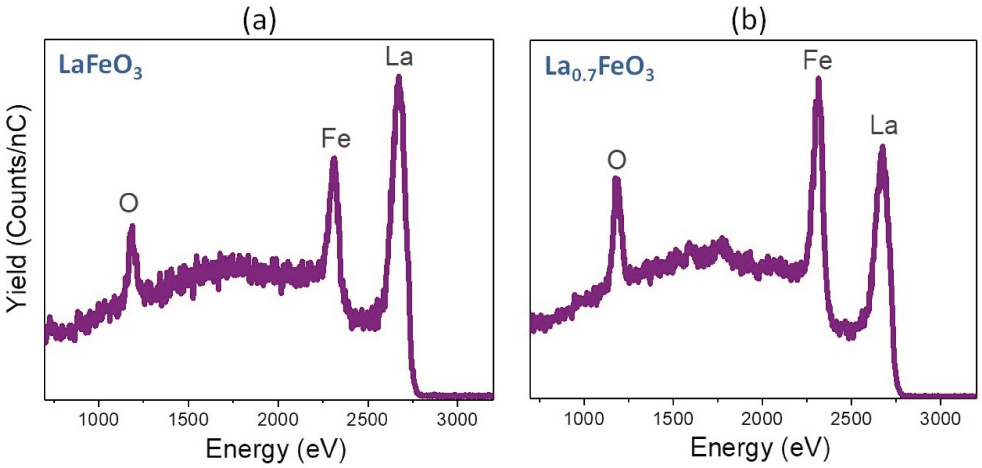

Figure 4.7: LEIS spectra of (a) $LaFeO_3$ and (b) $La_{0.7}FeO_3$ thin films analyzed using $^4He^+$ at 3 keV.

other additional phases have not been detected by other techniques like Raman, XRD and XANES analysis of the stoichiometric composition ($LaFeO_3$).

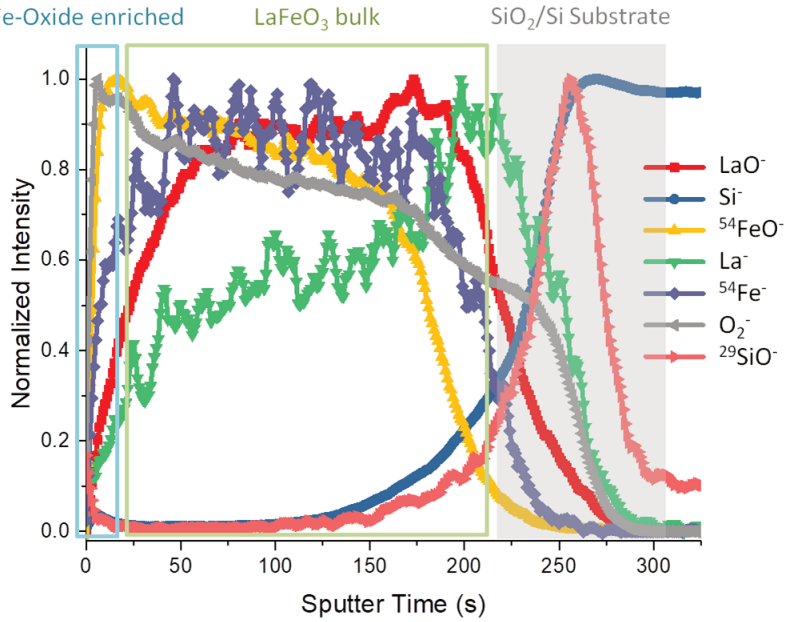

Figure 4.8: ToF-SIMS depth profile of $LaFeO_3$ thin film obtained by sputtering with 1 keV Cs^+ (90 nA, 400x400µm^2).

In case of $La_{0.7}FeO_3$, the depth profile presented in Fig.4.9 also features an enrichment of the O_2^- ions near the outer surface arising from the surface adsorbates as well as that of $^{54}FeO^-$ fragments due to presence of any segregated iron oxide phase, already observed by Raman and GI-XANES. A distinct difference here is with respect to the LaO^- fragments, which evolve differently to that of the $LaFeO_3$ profile. The $^{54}Fe^-$ and La^- emerge similarly throughout the profile. Here, four zones according to depth can be distinguished, namely,

the SiO_2/Si(100) substrate, the film's bulk, LaO^- enriched zone near the sub-surface and the $^{54}FeO^-$ enriched zone at the outermost surface. The depth profiling therefore highlights the segregation of the Fe_2O_3 as is already confirmed by complementary methods and possibly some La_2O_3, as discussed later in this chapter. The depth profiles for each thin film were repeated at three different analysis areas (100x100µm^2), where each profile gave similar results as shown here.

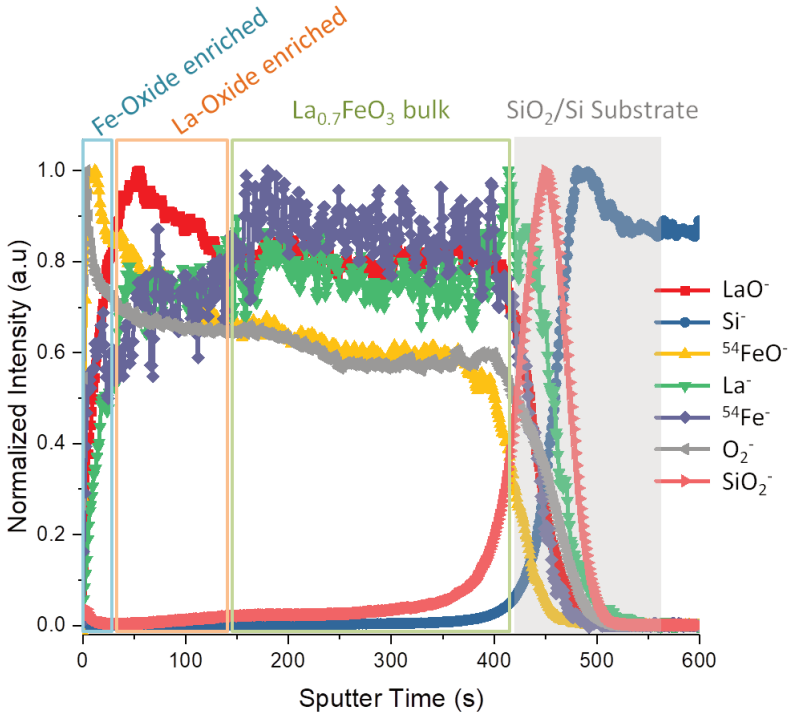

Figure 4.9: ToF-SIMS depth profile of $La_{0.7}FeO_3$ thin film obtained by sputtering with 1 keV Cs^+ (90 nA, 400x400µm^2).

The obvious question that arises at this point is whether the different behavior of $^{54}FeO^-$ and $^{54}Fe^-$ ions is an intrinsic property of the ionic fragmentation or does it really signify any phase segregation/enrichment phenomenon. In order to elucidate this, a thin film of pure phase of Fe_2O_3 was prepared using the citrate-complexation method and its synthesis was confirmed by Raman spectroscopy (not shown here). The evolution of the $^{54}FeO^-$ and $^{54}Fe^-$ ions were determined for this iron oxide thin film as shown in Fig.4.10. Interestingly, Fe_2O_3 presents similar fragmentation and depth profile for both $^{54}FeO^-$ and $^{54}Fe^-$ ions throughout the oxide layer. This reveals that $^{54}FeO^-$ and $^{54}Fe^-$ (and O_2^-) are expected to display similar profiles when originating from the same phase with similar chemical envirnment. Hence, the dominating presence of $^{54}FeO^-$ ions at the surface of $LaFeO_3$ and $La_{0.7}FeO_3$ indeed represents a surface enrichment or segre-

gation phenomenon. The widely known La-enrichment caused by the reactive nature of La-based compounds was not distinctly detected in the ToF-SIMS depth profiles for either of the thin films.

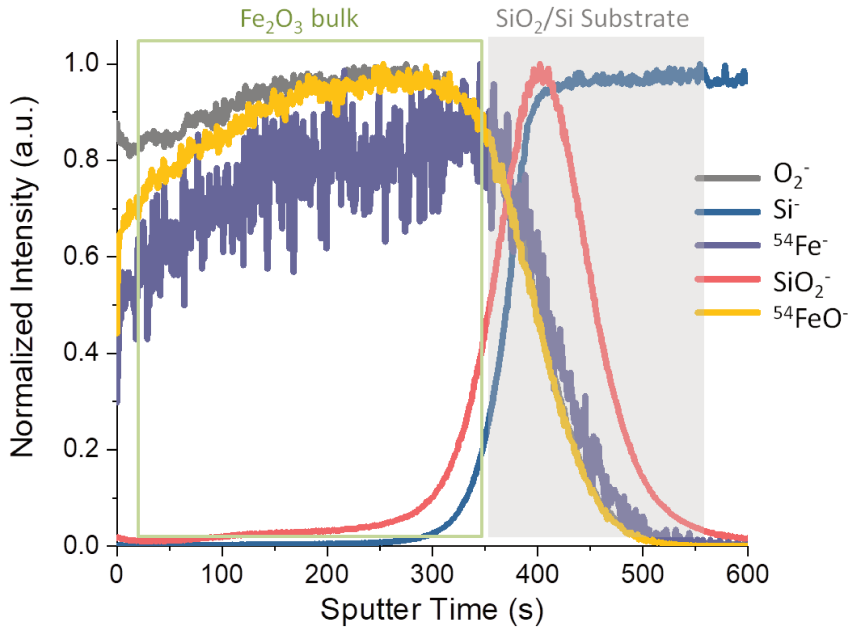

Figure 4.10: ToF-SIMS depth profile of Fe_2O_3 thin film obtained by sputtering with 1 keV Cs^+ (90 nA, 400x400µm^2).

The intensities of the mixed oxide fragments ($La_xFe_yO_2^+$) in the secondary ions mass spectra were compared for each composition by normalizing with respect to the intensity of $La^{54}FeO_2^+$. The relative intensity of each mixed oxide fragment has been shown in Fig.4.11. In case of $LaFeO_3$, it generally presents more intense mixed oxide fragments compared to $La_{0.7}FeO_3$, signifying the presence of higher concentration of mixed oxide phase such as the perovskite in the stoichiometric composition as compared to the La-deficient composition. This semi-quantitative approach indicates that the extent of surface segregation for $La_{0.7}FeO_3$ is certainly higher than that of the stoichiometric $LaFeO_3$.

Furthermore, the $LaFeO_3$ thin film was subjected to prolonged cycles of LEIS sputtering using 5 keV $^{20}Ne^+$ ions and analyzed with 3 keV $^4He^+$. The sputtering has been carried out with the primary ion gun as the spectrometer is not equipped with a dedicated sputter gun. The variation of the intensity of each elemental peak with increasing sputtering cycles is shown in Fig.4.12. The intensity of the iron peaks varies significantly while the intensity of lanthanum peaks remain almost constant. Near the surface, it presents a higher Fe coverage as compared to the end of the sputtering cycles, indicating surface enrichment of B-site ions, similar to the observations made by ToF-SIMS depth profil-

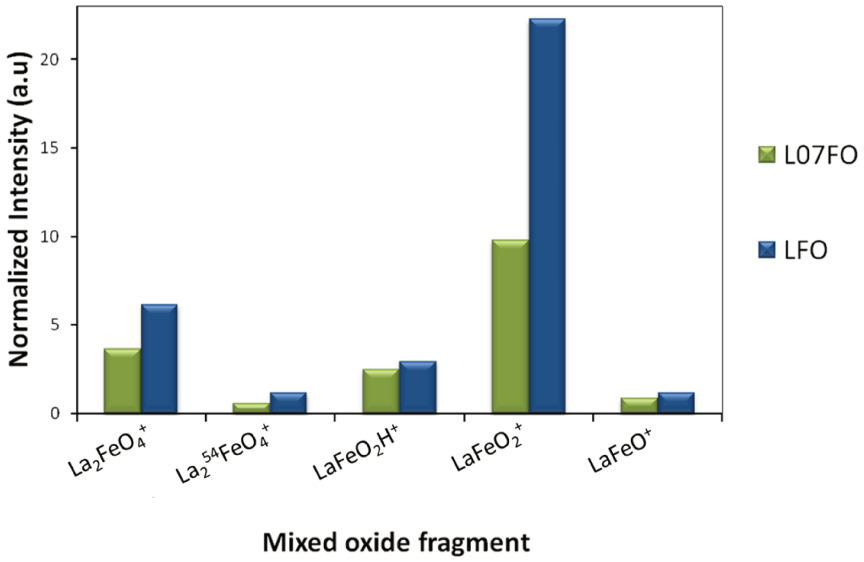

Figure 4.11: Comparison of intensities of the mixed oxide fragments in ToF-SIMS mass spectra of $LaFeO_3$ (LFO) and $La_{0.7}FeO_3$ (L07FO) thin films, normalized with respect to the $La^{54}FeO_2^+$ fragment.

ing. This is also clearly evidenced from respective LEIS spectra at the outermost surface, which shows lower concentration of iron compared to the sub-surface, that is reached upon soft sputtering. Finally, by performing prolonged sputtering of the material the bulk is reached, revealing lower intensity of Fe signal compared to the sub-surface. This verifies once again a B-site enrichment of Fe in the sub-surface region. The higher relative concentration of La on the extreme surface is due to the A-site La-enrichment due to the reactive nature of the La-based oxide materials. Higher intensity of La compared to Fe is however maintained throughout the sputtering cycles.

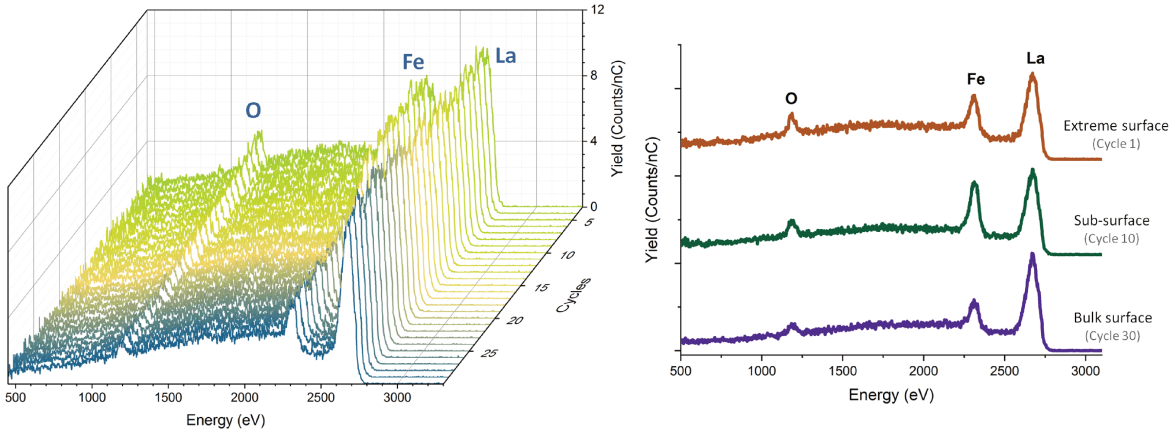

Figure 4.12: Cycles of LEIS sputtering with 5 keV $^{20}Ne^+$ ions and analysis by 3 keV $^4He^+$ on the $LaFeO_3$ thin film.

In case of the $La_{0.7}FeO_3$ perovskite, the changes upon LEIS sputtering and analysis

cycles have been presented in Fig.4.13. Unlike $LaFeO_3$, the intensity of both Fe and La signals varies as the material is progressively sputtered. The Fe shows higher intensity near the surface and then continuously keeps decreasing. On the other hand, the La signal shows a continuously changing intensity in depth. Fig.4.13(b) further highlights more intense signal of Fe in the sub-surface compared to the outermost layers, similar to $LaFeO_3$. Towards the final sputtering cycles, the La becomes more intense than Fe like the stoichiometric composition. The variable intensity of both La and Fe LEIS signals indicates non-homogeneous distribution of La as well as Fe segregated species as lanthanum oxide and iron oxide, as is also indicated by ToF-SIMS depth profiling. Both thin films do not feature any silicon signal, indicating that these analyses were made at an area without any cracks and the cycles of sputtering did not reveal the substrate, unlike ToF-SIMS. These LEIS depth profiling analyses verify higher overall content of La in $LaFeO_3$ and Fe in $La_{0.7}FeO_3$, as is expected according to the empirical stoichiometry of each.

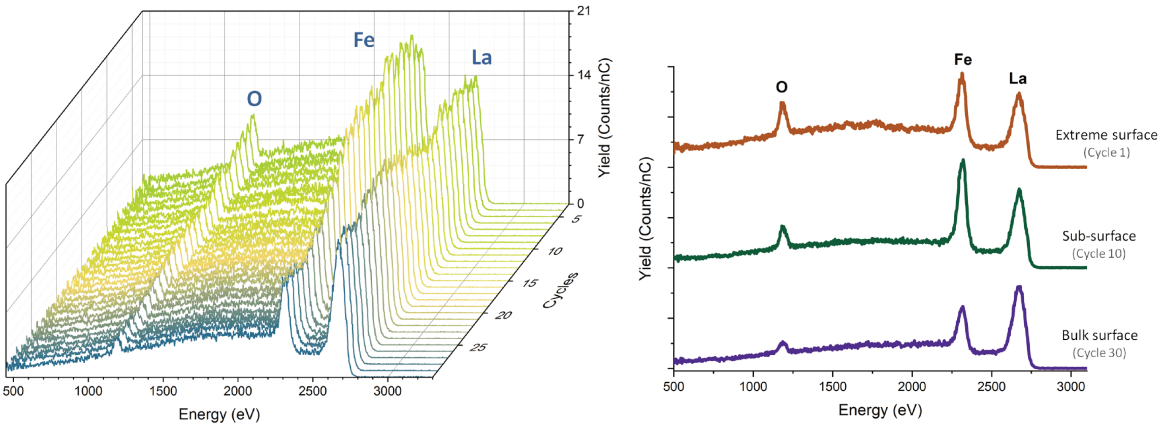

Figure 4.13: Cycles of LEIS sputtering with 5 keV $^{20}Ne^+$ ions and analysis with 3 keV $^4He^+$ on the $La_{0.7}FeO_3$ thin film.

LEIS as well as ToF-SIMS depth profiles suggest the presence of Fe-rich surface and sub-surface in $La_{0.7}FeO_3$. Only the La-deficient perovskite indicates likely presence of lanthanum oxides phases also, formed as a result of the formation of Fe_2O_3 phase after inducing La-deficiency. In addition, relatively lower amount of the perovskite phase is present in $La_{0.7}FeO_3$ compared to $LaFeO_3$ as verified by the semi-quantitative comparison of the perovskite-related fragments from ToF-SIMS mass spectra. It is worth mentioning that the analyzed depth with LEIS and ToF-SIMS are not in the same range, we assume that the bulk surface defined by LEIS could only correspond to the enriched zones above the bulk defined by ToF-SIMS.

Origin of surface segregation in $LaFeO_3$ and $La_{0.7}FeO_3$: Surface analyses by LEIS and ToF-SIMS highlighted detailed surface characteristics of the two compositions, $LaFeO_3$ and $La_{0.7}FeO_3$. LEIS of $LaFeO_3$ featured higher coverage of La in the depth profiling analysis. This A-site enrichment of La is a widely known property of lanthanum-based perovskites, mostly evidenced by XPS analysis [8–10]. The stoichiometric composition shows significant La-enrichment due to higher content of La in the structure, driving the rapid formation of La-based surface species. Interestingly, LEIS analysis also points out that although La-enrichment is a dominant surface characteristic, it does not mask the B-site Fe ions completely, which are considered the active sites for a catalytic reaction. Perovskite oxides of the form $A^{3+}B^{3+}O_3$ comprises of $A^{3+}O^{2-}$ and $B^{3+}O_2^{2-}$ planes leading to an overall charge mismatch driving the segregation of secondary phases such as oxides, hydroxides or carbonates of A-cation at the surface. The lattice strain caused by the cation size mismatch is another possible driving force for such observations as suggested by Ding *et al* [11] and Lee *et al* [12]. Depth profiling analysis further signifies the presence of Fe-rich zone near the surface in contrast to the bulk. Indeed, the A-site enrichment leaves behind a B-rich zone as a result of the A-depletion just underneath the outer surface and is a likely cause of the B-site enriched zone in stoichiometric $LaFeO_3$ [8]. Such surface reconstruction has also been observed in other perovskites like $La_{0.65}Sr_{0.35}FeO_3$, $SrTiO_3$ and $BaTiO_3$ [13–15]. The enhanced signal of $^{54}FeO^-$ is not attributed to any iron oxide phase as no such segregated phase was evidenced by combination of techniques previously mentioned, with an uncertainty of ~5%. Thus, these observations using LEIS and ToF-SIMS allow to sketch a model of the stoichiometric ferrite as shown in Fig.4.14(a). It represents the La enrichment on the outer surface without covering all the Fe species, which further generates a Fe-enriched zone in the sub-surface region finally followed by the bulk.

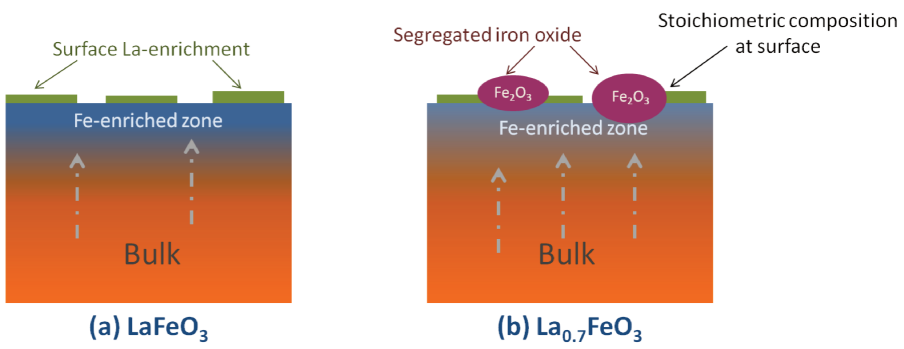

Figure 4.14: Schematic representation of the surface of $LaFeO_3$ and $La_{0.7}FeO_3$ thin films

In case of $La_{0.7}FeO_3$, on inducing the La-deficiency the A-site enrichment is abated to

some extent by the presence of the segregated iron oxide, also evidenced by GI-XANES and Raman analyses. This rather large extent of phase segregation of Fe_2O_3 in $La_{0.7}FeO_3$ results in the accumulation of the segregated surface particles. The enhanced presence of the $^{54}FeO^-$ fragments near the surface is a result of a mixture of perovskite and iron oxide phases, unlike $LaFeO_3$ where Fe-enrichment near the surface is more likely driven by the La-enrichment on the outermost surface that leaves behind an La-depleted or Fe-rich sub-surface. This enhances the Fe signal in the LEIS spectrum of the non-stoichiometric perovskite. It also makes available more Fe species on the surface supporting an enhancement in the catalytic performance. In general, surface segregation in perovskites is more pronounced on polycrystalline thin films compared to the epitaxially grown single crystals, due to the presence of grain boundaries that enables easier transport of the segregating atoms [16, 17]. Therefore, LEIS and ToF-SIMS observations direct towards a schematic representation of the surface of $La_{0.7}FeO_3$ (Fig.4.14(b)). It represents the Fe_2O_3 particles on the outer surface supported on the $LaFeO_3$ film. The La-enrichment and any Fe-rich sub-surface might also be present but to a much smaller extent than the stoichiometric perovskite thin film. Therefore, the different behavior of the $^{54}FeO^-$ fragments in the ToF-SIMS depth profiles indicating the surface reconstructions can be considered to be caused by different origins for the thin films of both stoichiometries, *i.e.*, in case of $LaFeO_3$, it is driven by the surface La-enrichment while for $La_{0.7}FeO_3$, it is an outcome of mainly the segregation of iron oxide particles on the surface/sub-surface regions.

4.1.5 Morphology of the $La_{0.7}FeO_3$ thin film

The morphology of the La-deficient perovskite is finally elucidated by SEM and AFM imaging as shown in Fig.4.15. The top-view by SEM and AFM images indicate the presence of segregated crystalline particles on the surface over the thin film bed. The morphology of these particles is further displayed in Fig.4.15(b) bottom, with a height reaching up to 5 nm. The root mean squared roughness determined by AFM analysis is around 3 nm, compared to 1 nm in case of $LaFeO_3$, as was presented in chapter 3. The presence of these segregated particles increases the surface roughness of the film. Chemical analysis by SEM-EDX further confirms the presence of these segregates as iron oxide particles shown by higher intensity of Fe and O located in similar regions. This corroborates to the estimated scheme previously shown on the basis of LEIS, ToF-SIMS and GI-XANES analyses. The Fe_2O_3 particles are rather large ranging around ~100 x 200 nm^2 laterally with a height

of ~5 nm. Further, the brown region is representative of the $LaFeO_3$ layer over which the Fe_2O_3 crystallites are embedded.

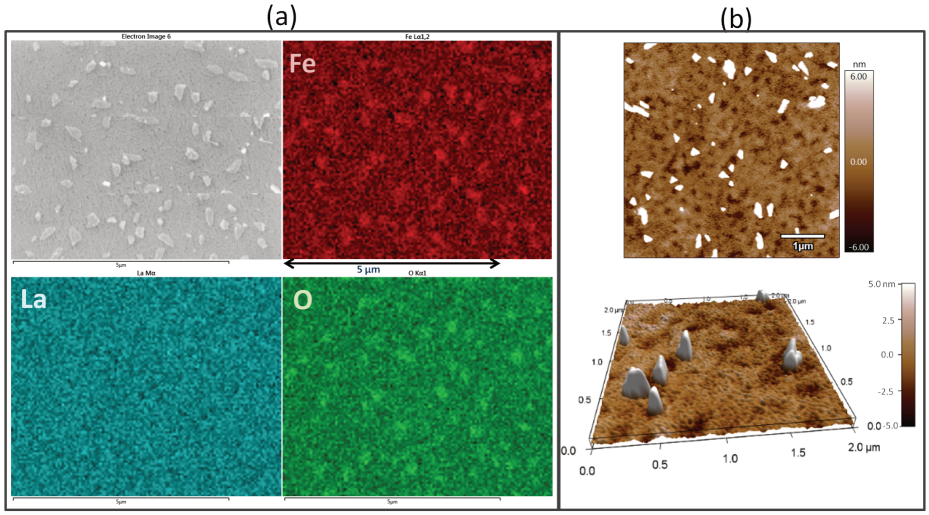

Figure 4.15: (a) SEM-EDX and (b) AFM images of $La_{0.7}FeO_3$ thin film.

4.2 *In situ* analysis of $LaFeO_3$ and $La_{0.7}FeO_3$ thin films under CO

4.2.1 NAP-XPS investigation of $LaFeO_3$ vs. $La_{0.7}FeO_3$ thin films

The surface reactivity of the La-deficient perovskite $La_{0.7}FeO_3$ has been compared with respect to that of the stoichiometric perovskite $LaFeO_3$ by means of NAP-XPS (TEMPO beamline at SOLEIL synchrotron) in the presence of CO at around 10^{-1} mbar to highlight the promoting role of the induced non-stoichiometry in the catalyst composition.

Overview and surface sensitivity with NAP-XPS

The XPS spectra based on the synchrotron source were first collected at an incident energy of 950 eV for all the orbitals of interest. These spectra allowed the comparison of the raw intensities of the elements to provide a quantitative outlook, since some physical properties such as inelastic mean free path of photoelectrons that depend on the gas and pressure as well as the transmission function of the equipment are not available for quantification of atomic concentrations. In addition, a second set of analysis was performed for obtaining information from the same depth of the material for each element by keeping the same kinetic energy around 120 eV by tuning the energy of the incoming X-rays,

thanks to the synchrotron facility. The XPS spectra for each element have been shown in Fig.4.16 for a general comparison between the two incident energies considered. In Table 4.1, the orbitals with their respective incidence energy, binding energy, kinetic energy, inelastic mean free path λ (TPP2M formula) and the probed depth have been listed [18]. The La 3d photopeak at 950 eV, Fe 2p at 850 eV, O 1s at 650 eV, C 1s at 400 eV have been analyzed probing 1.5 nm depth of the material. These conditions provide a higher surface sensitive information including chemical environment under relevant working conditions.

Table 4.1: XPS signals collected with values of binding energy, kinetic energy, inelastic mean free path λ and the probed depth.

E_{source} (eV)	Orbital	$E_{binding}$ (eV)	$E_{kinetic}$ (eV)	λ (nm)	Depth (nm)
950	La 3d	834.7	115.3	0.5	1.50
950	Fe 2p	710.9	239.1	0.7	2.01
950	O 1s	530.1	419.9	1.0	2.88
950	C 1s	285.0	665.0	1.3	3.90
950	Si 2s	153.9	796.1	1.5	4.50
850	Fe 2p	711.0	139.0	0.5	1.59
650	O 1s	530.2	119.8	0.5	1.50
400	C 1s	285.0	115.0	0.5	1.50
400	Si 2s	154.3	245.7	0.7	2.07

The survey spectra at each incident energy have also been shown in Fig.4.16 along with the respective elemental spectra of the $La_{0.7}FeO_3$ thin film. The La $3d_{5/2}$ photopeak is present at 834.7 eV indicative of the La^{3+} oxidized state [1]. The Fe 2p photopeaks at the two different energies present similar features with respect to the binding energy and oxidation state, given by the position and spectral shape, respectively. The Fe $2p_{3/2}$ photopeak has a binding energy of 711.0 ± 0.1 eV with the characteristic satellite feature of Fe^{3+} at around 719.6 eV [2]. Interestingly, this thin film shows no contamination from carbonates or hydroxides as evident from the C 1s spectra at both energies. Only contribution from C-C is observed at 950 and 400 eV, respectively. The O 1s features three components, lattice oxygen (O^{2-}), defects in oxides and adsorbed species and oxygen from mainly silica, respectively. The O 1s shows slightly different ratios of the respective components. More signal from the silica and the surface oxygen species at 532.6 and 531.2 eV, respectively are seen with an incident energy of 650 eV, being more sensitive to the surface. In contrast, higher contribution of the lattice oxygen at 530.1 eV from the per-

ovskite is present at 950 eV incident energy [19, 20]. In the successive sections, the spectra recorded at lower energies for similar probed depths have been used to present the XPS spectra at each *in situ* treatment step.

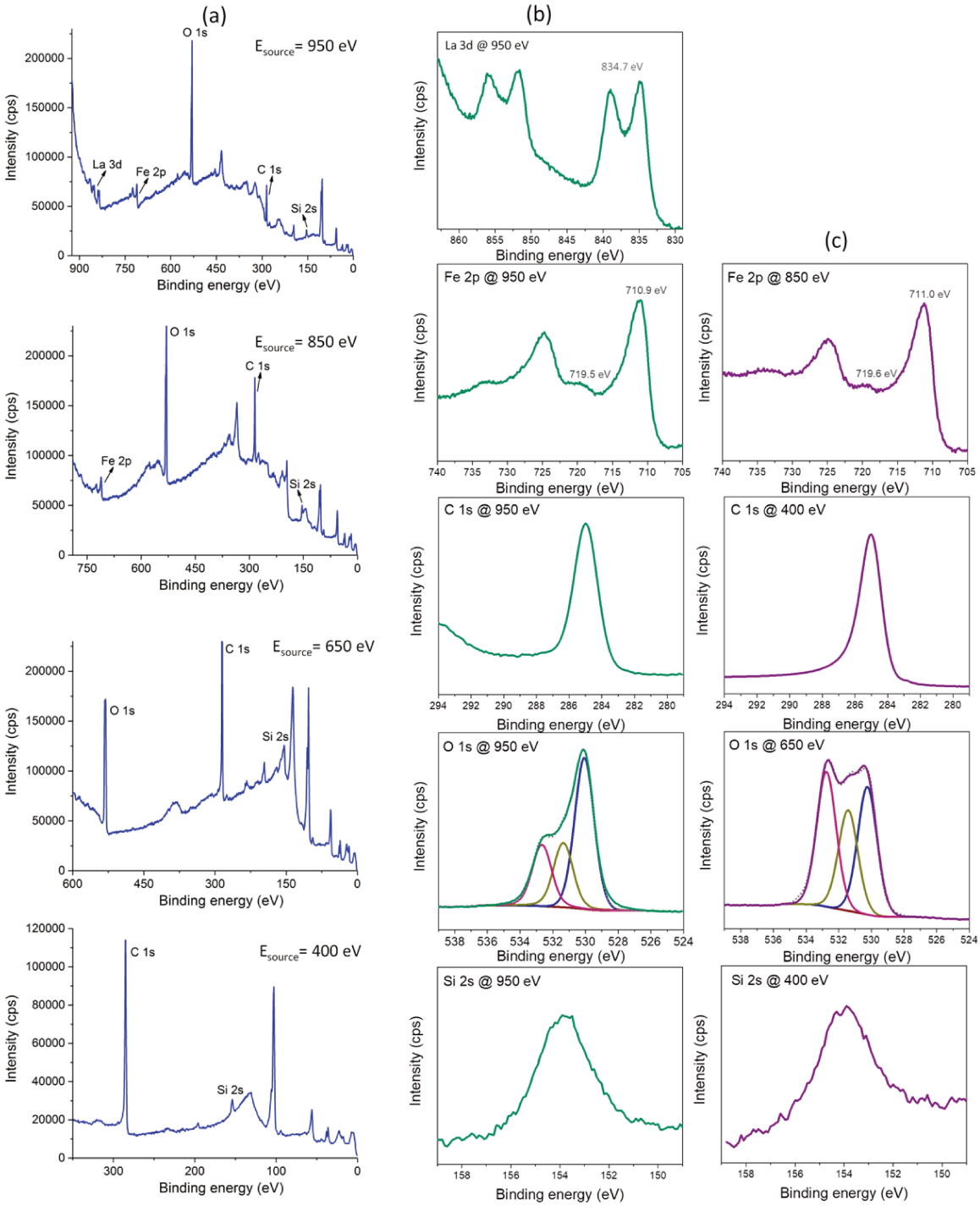

Figure 4.16: XPS spectra of $La_{0.7}FeO_3$ thin film as collected at synchrotron SOLEIL: (a) Survey spectra at different incident energies, (b) La 3d, Fe 2p, C 1s, O 1s and Si 2s at 950 eV and (c) Fe 2p at 850 eV, O 1s at 650 eV, C 1s and Si 2s at 400 eV at room temperature under UHV.

NAP-XPS during activation under oxygen

$La_{0.7}FeO_3$: The thin film is treated at high temperature under oxygen to remove the surface contamination such as the adventitious carbon to have a clean surface. The material was gradually heated until the C 1s signal was completely removed. Carbon started to disappear around 427°C and was completely removed at 442°C as shown in Fig.4.17 during heating under oxygen at 10^{-1} mbar.

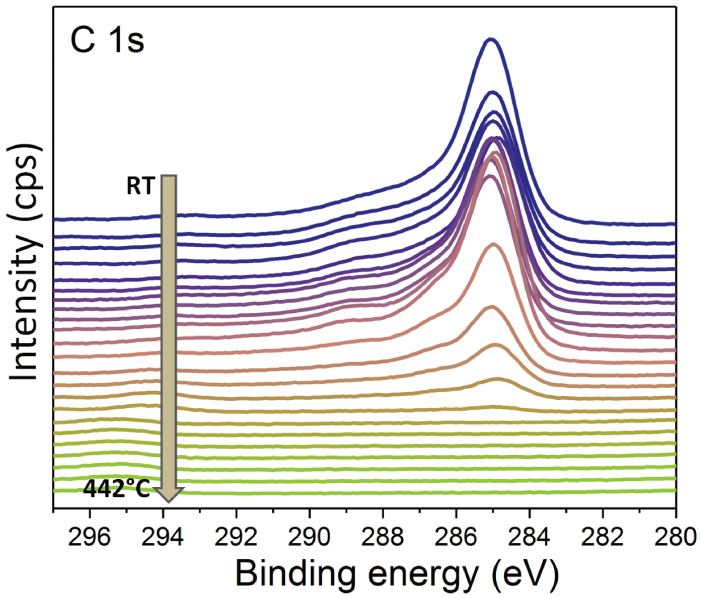

Figure 4.17: NAP-XPS C 1s spectra of $La_{0.7}FeO_3$ thin film during heating under 0.1 mbar oxygen up to 442°C.

The sequence of all orbitals of interest was collected at the temperature of 442°C and again after cooling down to room temperature under UHV condition to detect any temperature specific changes. The La $3d_{5/2}$ is always present at 834.7 eV, representing a 3+ oxidation state. The higher binding energy multiplet splitting component of La $3d_{5/2}$ shows a lower intensity, usually seen after the removal of the La hydroxides and/or carbonates based surface contaminants, typically observed for clean perovskite surfaces. Similarly, the Fe 2p also remains in 3+ state marked by the constant peak position with a FWHM of 3.4 eV and presence of the satellite feature at 719.6 eV. The O 1s spectra show the presence of mainly three components throughout the heating procedure while the C 1s signal disappears at high temperature under oxygen as the surface carbonaceous species are desorbed or react with activated O_2. However, as the material is cooled down to room temperature under O_2 and then under UHV, the C 1s signal reappears although less intense, implying the same status of the surface before and after the activation step with

respect to the adventitious carbon. This can be caused by the low dynamic conditions during high pressure experiments at 10^{-1} mbar due to large volume (35 L) of the analysis chamber as well as low pumping capacity for very small atoms from the analysis chamber, such that they are not easily removed and therefore settle down on the surface as the temperature is decreased.

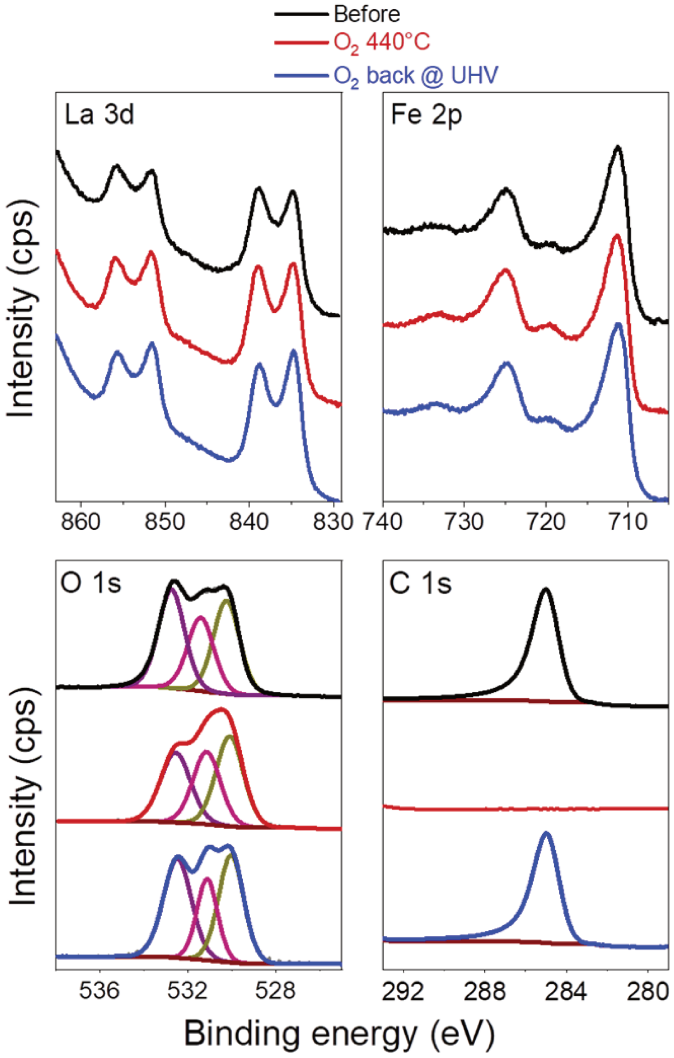

Figure 4.18: NAP-XPS La 3d, Fe 2p, O 1s and C 1s XPS spectra of $La_{0.7}FeO_3$ thin film before in UHV (blue), under 0.1 mbar O_2 at 440°C (black) and after coming back to room temperature under O_2 and then UHV conditions (red).

$LaFeO_3$: Due to the reappearance of the carbon species after the oxidation treatment, it was chosen not to heat the stoichiometric $LaFeO_3$ thin film under oxygen. The XPS spectra are shown in Fig.4.19 measured under UHV at room temperature. In this case, the La $3d_{5/2}$ peak is positioned at 834.9 eV with the typical shape for perovskites with 3+ charge. The Fe $2p_{3/2}$ signal also shows a binding energy of 710.6 eV with Fe^{3+} satel-

lite featuring at 719.4 eV having a FWHM of 3.2 eV. Here, the C 1s spectrum analyzed at 400 eV shows the typical distribution of adventitious carbon with hydroxyl and carbonate species. However, with incident energy of 950 eV it only shows a single peak from C-H and C-C aliphatic bonds (inset of Fig.4.19), indicating that the amount of the C-O/CO_3^{2-} contamination are located at the surface in low amounts. Therefore, the O 1s photopeak must also feature part of the signal arising from these carbon surface adsorbates.

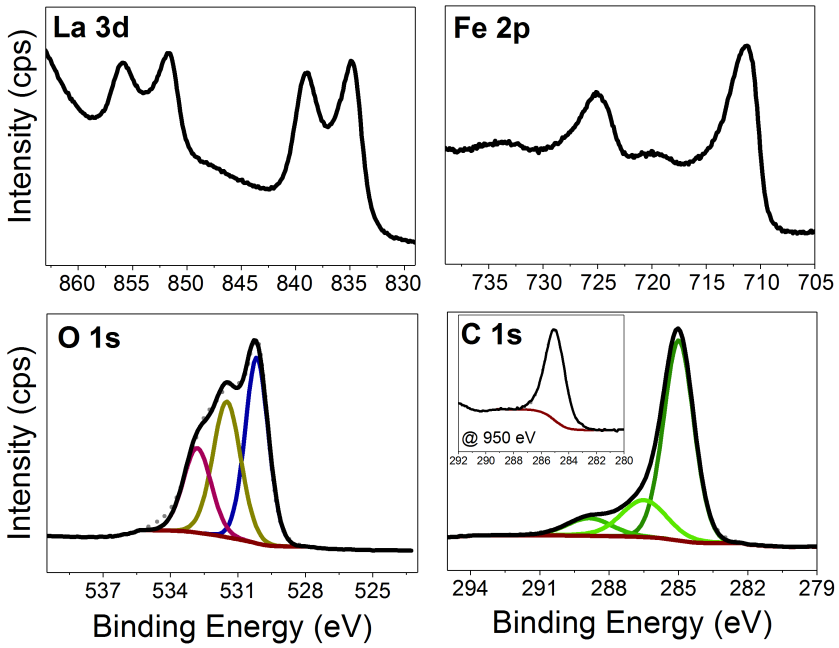

Figure 4.19: NAP-XPS La 3d, Fe 2p, O 1s and C 1s spectra of $LaFeO_3$ thin film under UHV at room temperature.

Both $LaFeO_3$ and $La_{0.7}FeO_3$ films feature similar properties of La and Fe in 3+ oxidation states with similar binding energies and peak shapes. Here, it has to be reminded that the contribution of the Fe signal originates from both the perovskite as well as the iron oxide present in $La_{0.7}FeO_3$, as observed previously. XPS of Fe 2p spectrum does not allow to differentiate the two phases with the same chemical environment (+3 oxidation state and O^{2-} oxide ligand) in $La_{0.7}FeO_3$. The thin films are comparatively clean with almost no significant evidence of surface hydroxides and carbonates for the deficient perovskite. In general, as seen previously the stoichiometric perovskite possesses more surface contaminants compared to $La_{0.7}FeO_3$.

NAP-XPS analysis during CO exposure at 0.1 mbar

$La_{0.7}FeO_3$: The $La_{0.7}FeO_3$ thin film was heated under CO gas up to 550°C and then cooled down to 100°C in presence of CO and then finally CO gas was evacuated until reaching UHV conditions. The spectral changes of C 1s and Fe 2p regions are followed while heating the sample under CO gas in Fig.4.20. Throughout heating, the C 1s spectra show only a single contribution from C-C/C-H carbon bonds. At 477°C, all the carbon is completely removed due to the desorption or reaction of the carbon species at higher temperature. In case of the Fe 2p signal collected at every 100°C and calibrated with respect to the lattice O 1s obtained at the same energy at 530.1 eV. The Fe $2p_{3/2}$ peak shows a shift in the binding energy towards lower energy together with a loss of the characteristic Fe^{3+} satellite feature during heating 500°C onward. Near 600°C, the iron reduces further to Fe^0 (metal) and Fe^{2+} as evident by development of a component at 706.6 eV and the characteristic satellite feature at 714.8 eV, respectively [2]. The formation of iron carbide although likely, is ruled out due to absence of any signal in the C 1s region at this temperature. At 550°C

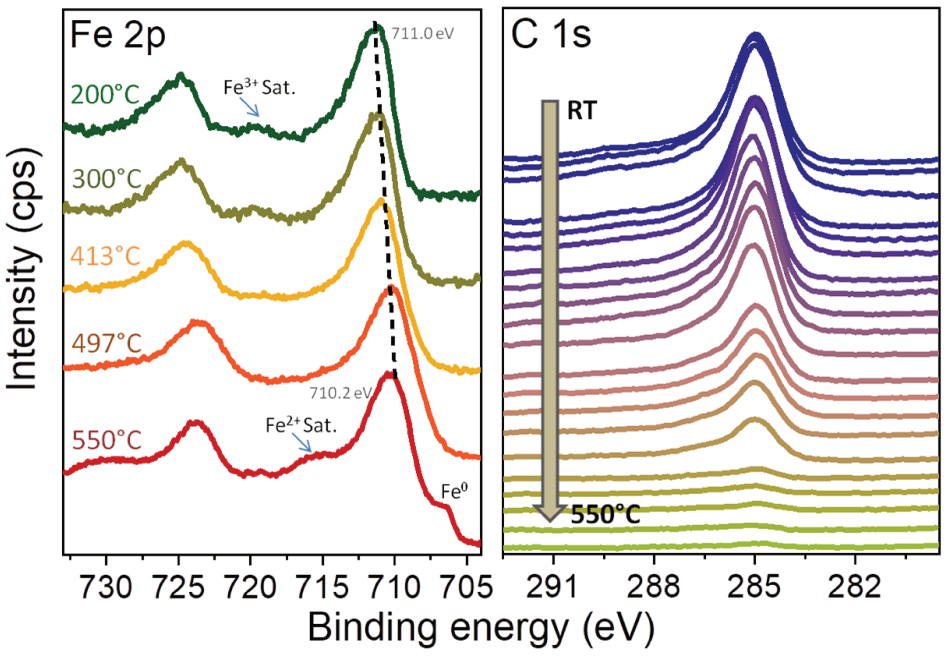

Figure 4.20: Evolution of NAP-XPS Fe 2p and C 1s photopeak of $La_{0.7}FeO_3$ thin film during heating under CO at 0.1 mbar.

under CO in Fig.4.21, the La 3d photopeak retains the same shape and binding energy as previously under UHV, confirming that La^{3+} is not involved in CO adsorption and/or reactivity. In contrast, the Fe $2p_{3/2}$ signal shows a major reduction from Fe^{3+} to Fe^{2+} and

Fe^0 with a shift of binding energy to 710.2 eV from around 711.0 eV. This is accompanied by an increase in the FWHM value from 3.5 eV at room temperature to 4.2 eV at 550°C, suggesting the appearance of Fe^{2+} fingerprint (asymmetric main peak $2p_{3/2}$ with satellite feature). The FWHM of the Fe $2p_{3/2}$ peak of $La_{0.7}FeO_3$ after O_2 treatment is around 3.2 eV. The width increases due to the appearance of the additional component from Fe^{2+} as CO reactivity with La-deficient perovskite induces reduction of Fe^{3+}. The Fe 2p peak

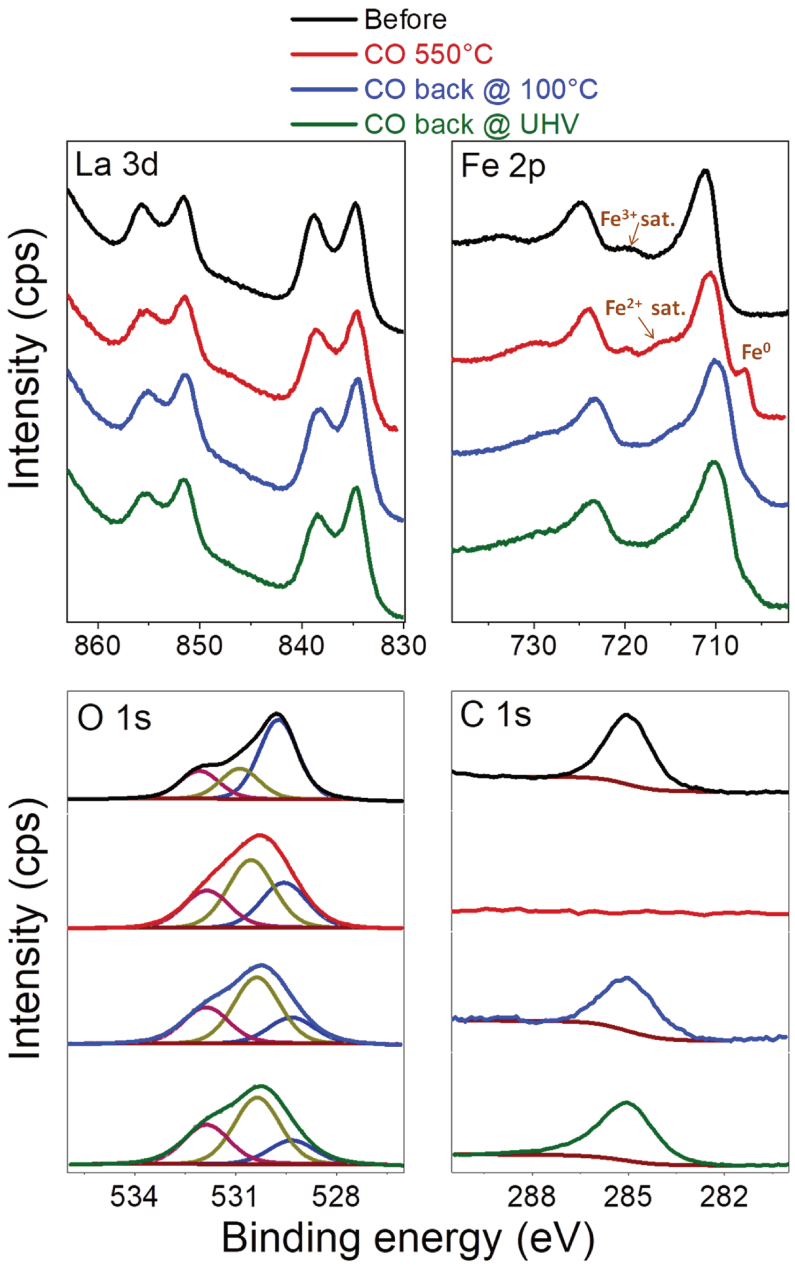

Figure 4.21: NAP-XPS La 3d, Fe 2p, O 1s and C 1s spectra of $La_{0.7}FeO_3$ thin film under UHV (blue), under CO 0.1 mbar at 550°C (black), under CO 0.1 mbar back at 100°C (red) and back under UHV (green).

decomposition to estimate the distribution of Fe species regarding their oxidation state

is done using the reference spectra of Fe^{3+} with the lineshape from $La_{0.7}FeO_3$ after returning to UHV after oxygen treatment. By comparing the Fe 2p spectrum recorded at 440°C under O_2 to the one after cooling down to UHV conditions, we estimate spectral lineshape difference of ~10% induced by temperature, whereas the Fe 2p spectra of the as-received material and after O_2 treatment in UHV are similar (Fig.4.22(a)). The reduced Fe species fingerprint spectrum is obtained by applying the vectorial method, generally applied to spectroscopic data involving a data set that is evolving featuring a mixture of different chemical species [21, 22]. This method helps in avoiding the necessity to fit complex spectra with multiple synthetic components, as in the case for Fe 2p. Instead, the experimental spectra can be reduced to basic spectral shapes that are difficult to be measured experimentally and thereby a possible peak model can be constructed. According to this approach, mathematical vectors with a physical meaning are extracted through their linear combinations, which together can reproduce the whole data set. This method is applied to the Fe 2p spectrum after O_2 treatment under UHV (initial spectrum S_i in which we assume that only Fe^{3+} is present) and the one under CO at 550°C (final spectrum S_f in which we assume a mixture of Fe^{3+} and reduced Fe species), according to the equation,

$X_j=(1-C_j)S_i-C_jS_f$

where, C_j is varying between 0 and 1 by a step scan of F/100, where F is the chosen factor taken as 0.5 in our case. Two vectors have to be then identified from the 200 vectors generated to account for the evolution of the set of spectra. Here unfortunately, it was not possible to consider as initial and final spectra, the two spectra recorded at high temperature (440°C under O_2/ 550°C under CO) as the acquisition ranges were not comparable. Following the generation of the vectors, the first vector is easily identified as it corresponds to Fe^{3+} from $La_{0.7}FeO_3$ (S_i, initial spectrum). The second one should present coherent spectroscopic features (only positive and existing peaks) corresponding to reduced Fe species, respecting the theoretical intensity ratio $I(2p_{1/2})/ I(2p_{1/2}) = 1/2$ for each doublet. Indeed, the reduced species spectral form appears as the spectral form of a mixture of Fe^{2+} and Fe^0. In order to refine this extracted spectral form, the vectorial method was used iteratively to it, firstly with the initial spectrum and secondly with the final spectrum, respectively. The two selected spectral forms extracted from vectorial method can be combined to reproduce the original spectra using a linear least square approximation (4.22(b)). Finally, the decomposition of the spectral form of reduced iron species leads to 20% Fe^0 at binding energy of 706.6 eV given by an asymmetric lineshape LA(1.2,4.8,3) [2]

and 80% Fe^{2+} given by the same asymmetric lineshape to model the multiplet structure (709.8 eV) and a symmetric one GL(30) for the satellite at 716.1 eV, shown in Fig.4.22(c).

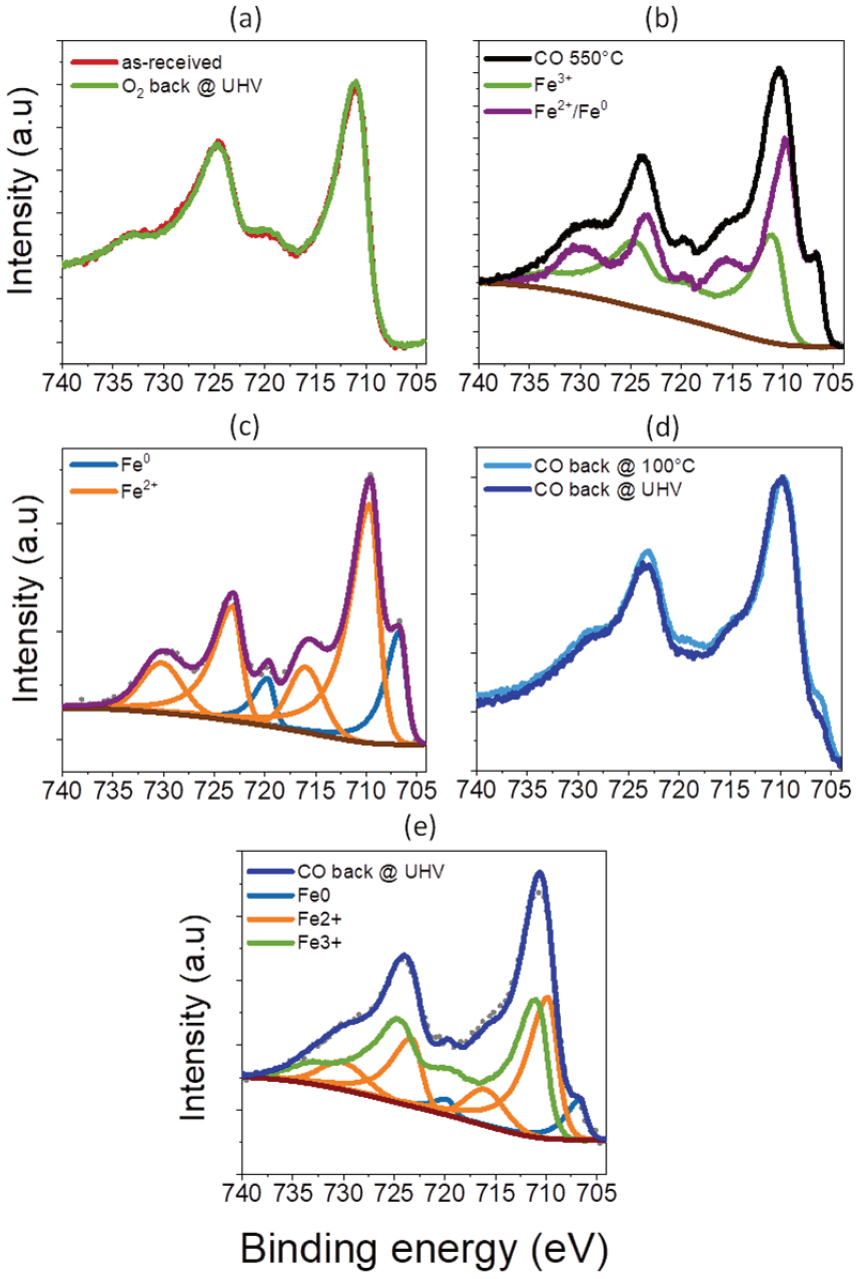

Figure 4.22: NAP-XPS Fe 2p spectra of $La_{0.7}FeO_3$ thin film: (a) before and after O_2 treatment under UHV, (b) linear least square approximation with the two selected vectors to spectrum under CO at 550°C spectrum, (c) components of extracted spectrum of reduced Fe species (d) back under CO at 100°C and then under UHV, and (e) spectral decomposition of the spectrum back at UHV conditions.

Thus, the Fe 2p spectrum under CO at 550°C features 50% of Fe^{2+}, 37% of Fe^{3+} and 13% of metallic iron, according to Fig.4.22(b) and (c). Here, the majority of the Fe^{3+} in $La_{0.7}FeO_3$ present as perovskite and Fe_2O_3 phase has been reduced into Fe^{2+} and Fe^0.

In the case of O 1s signal, it always presents three contributions, where the O 1s component from the lattice oxygen at 530.1 eV decreases during the CO treatment, signifying a reduction of the perovskite lattice along with an increase in the second component attributed to O_2^-/O^- species, defects in oxides and/or single oxide phases under CO on $La_{0.7}FeO_3$ surface.

As the sample is cooled down under CO at 0.1 mbar as shown in Fig.4.23, the signal from the metallic iron gradually decreases along with a slight increase of the FWHM of Fe $2p_{3/2}$. These changes indicate the evolution of the surface ratios of Fe species during the cooling step.

After cooling down to 100°C under CO, the Fe^0 signal is decreased with only a tiny shoulder visible besides the decrease in the Fe^{2+} satellite feature. Since the temperature was not constant at 100°C, spectral decomposition presents higher uncertainty at this temperature. Nonetheless, this spectrum remains comparable to the one after return to UHV conditions (Fig.4.22(d)). According to the spectral decomposition presented in Fig.4.22(e), the amount of the remaining Fe^0 is close to 6% with an increase in the ratio of Fe^{3+} from 37% to 50% and the rest remains as Fe^{2+}, with an increased FWHM of 4.9 eV. The distribution of Fe species evolves between the cooling step under CO and its evacuation. Indeed, at lower temperature (below 400-300°C), CO is no more activated or reactive, and so there is a re-arrangement of surface iron species. The O 1s signal from the perovskite lattice at 530.1 eV remains similar after cooling down, while the C 1s peak re-emerges similar to the activation step.

$LaFeO_3$: The $LaFeO_3$ thin film was heated under CO gas up to 567°C and then cooled down to room temperature in presence of CO and analyzed again after CO evacuation. During the temperature ramp presented in Fig.4.24, the C 1s signal decreases with complete removal of the carbonates and hydroxides components. Here, the C 1s is not completely removed even at 567°C, unlike in case of $La_{0.7}FeO_3$. The Fe 2p spectra evolves under CO as the material is heated with loss of the satellite feature of Fe^{3+} along with an increase in the FWHM of Fe $2p_{3/2}$ signal indicating appearance of the Fe^{2+} contribution, as also previously observed for $La_{0.7}FeO_3$. At 567°C under CO as shown in Fig.4.25, the La 3d undergoes no changes as observed earlier while the Fe 2p signal slightly shifts to lower

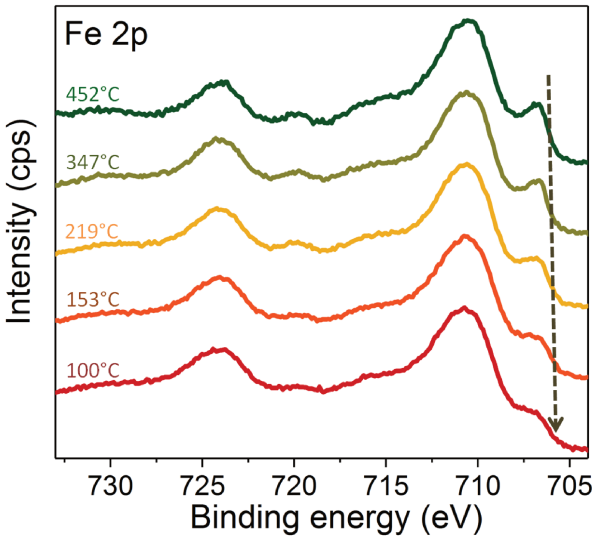

Figure 4.23: Fe 2p spectra of $La_{0.7}FeO_3$ thin film during cooling down from 550 to 100°C under CO.

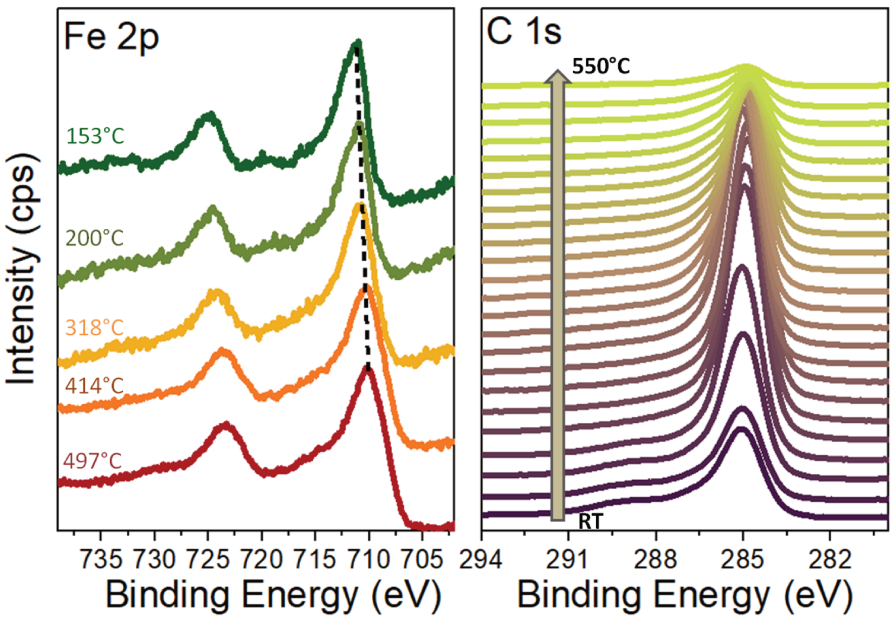

Figure 4.24: Evolution of Fe 2p and C 1s photopeak of $LaFeO_3$ thin film during heating under CO.

energy from 710.6 to 710.2 eV with loss of the Fe^{3+} satellite feature. No evident satellite structure of Fe^{2+} is detected here. The FWHM of Fe $2p_{3/2}$ peak also increases from 3.2 to 4.2 eV. In this case, no contribution from metallic Fe is observed, unlike the La-deficient perovskite. However, spectral quality of Fe 2p after heating is not optimum for using the vectorial method, as it leads to incoherent vectors. In any case, the Fe 2p spectrum under CO at high temperature can accomodate up to 65% of Fe^{3+} using Fe 2p lineshape of the as-received $LaFeO_3$. This attempt only allows to have an approximate evaluation of the reduction of the Fe^{3+} species after CO reaction. Nevertheless, by simple comparison of

the spectral features with that of the $La_{0.7}FeO_3$ thin film, Fe 2p spectrum of $LaFeO_3$ under CO at 567°C shows no clear evidence of Fe^{2+} satellite feature, its presence is however indicated by the loss of the Fe^{3+} satellite feature. Moreover, it undergoes a smaller shift in the binding energy (0.4 eV) compared to that of $La_{0.7}FeO_3$ (0.8 eV). This indicates lower extent of reduction in the stoichiometric perovskite after reacting under CO. The C 1s signal

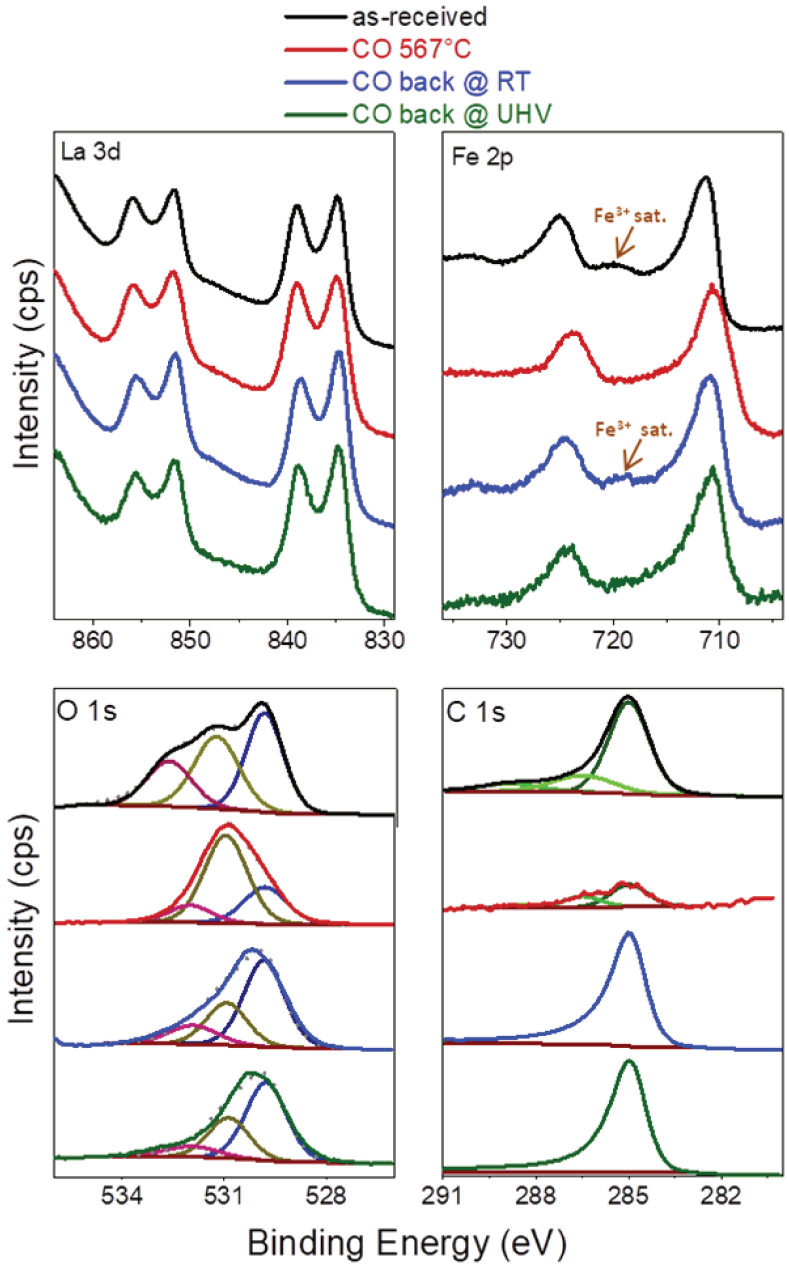

Figure 4.25: NAP-XPS La 3d, Fe 2p, O 1s and C 1s spectra of $LaFeO_3$ thin film under UHV (blue), under 0.1 mbar CO at 567°C (black), under CO 0.1 mbar back at room temperature (red) and under UHV conditions (green).

decreases in intensity after heating under CO while the O 1s spectrum shows complete removal of the contribution from the surface adsorbates as well as decrease in the O^{2-}

from lattice oxygen of the perovskite as it gets reduced.

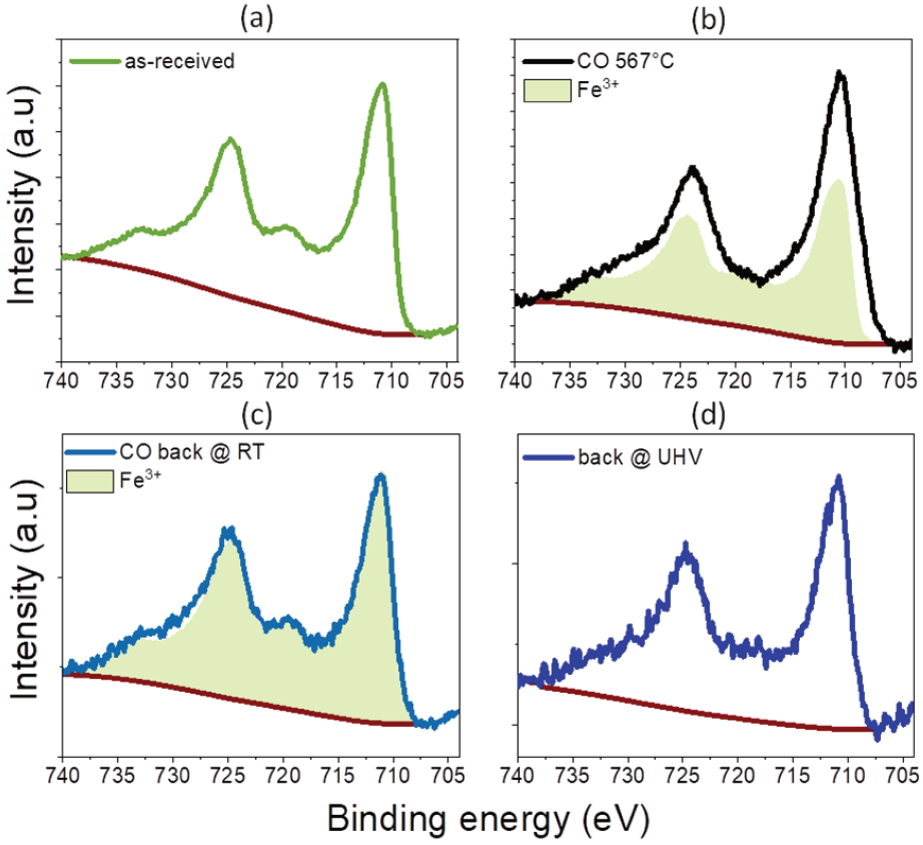

Figure 4.26: Spectral decomposition of Fe 2p XPS spectra of $LaFeO_3$ thin film: (a) before under UHV, (b) under CO at 567°C, (c) back under CO at room temperature and (d) back at UHV conditions.

While cooling down to room temperature under CO, the FWHM of the Fe 2p signal decreases together with re-emergence of the Fe^{3+} satellite feature with a similar trend as $La_{0.7}FeO_3$. On reaching room temperature, the binding energy of the Fe $2p_{3/2}$ increases by 0.2 eV. The Fe 2p spectrum at RT under CO features up to ~90% of Fe^{3+} contribution. The component from the perovskite lattice oxygen increases as the temperature is reduced to room temperature in line with the re-appearance of Fe^{3+}. The C 1s spectrum shows a rise in the intensity with return of the signal from hydroxide and carbonates after return to room temperature. As UHV conditions are achieved again, the Fe 2p signal appears quite noisy with the loss of spectral information. Here, the satellite structure is not clearly visible.

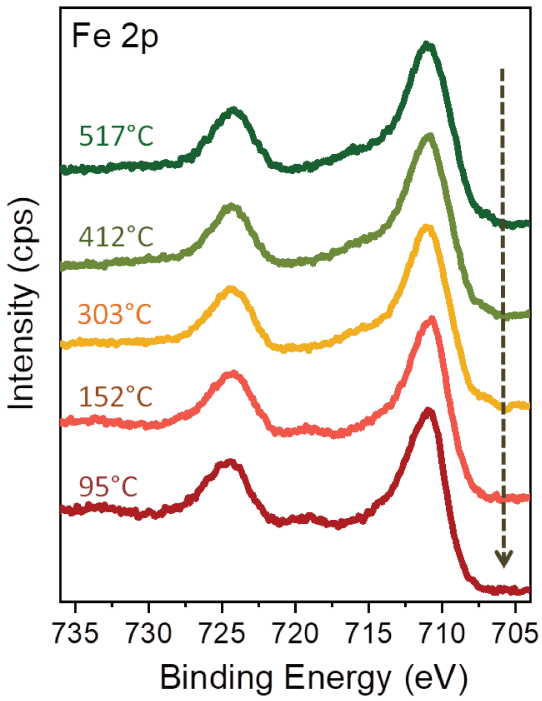

Figure 4.27: Fe 2p spectra of $LaFeO_3$ thin film during cooling down from 567°C to room temperature under CO.

Distinguishing surface behavior of $La_{0.7}FeO_3$ from $LaFeO_3$: insights from NAP-XPS

As seen previously, the surface of the stoichiometric $LaFeO_3$ contains a single phase of perovskite while the La-deficient $La_{0.7}FeO_3$ contains two phases, namely the perovskite and the iron oxide ($\alpha - Fe_2O_3$), possessing different starting points with respect to their compositions. At room temperature the two materials give rise to similar XPS spectra for La, Fe and O. Only $LaFeO_3$ contains carbonates and hydroxides as surface contamination, evident from the C 1s spectra, while both stoichiometry show C-C/C-H type adsorbates. From the XPS point of view, both samples portray similar oxidation states and chemical environment in the as-received state as well as after oxygen treatment.

As both the samples are treated under CO around 550°C, most of the iron in $La_{0.7}FeO_3$ present as Fe^{3+} reduces to 50% Fe^{2+} and 13% Fe^0. The $La_{0.7}FeO_3$ undergoes extensive reduction with 63% of the initial Fe^{3+} reducing to Fe^{2+}/Fe^0 species. Here, indeed both the perovskite and the iron oxide can react.

On the other hand, the $LaFeO_3$ in stoichiometric composition undergoes reduction to Fe^{2+} to a much lower extent (estimated to ~35%) than the La-deficient composition without any metallic Fe, given by smaller chemical shift in binding energy. Further, since the $LaFeO_3$ forms no metallic species, it can be inferred that the Fe^0 may originate from the

iron oxide phase present in $La_{0.7}FeO_3$. Owing to the experimental results from this NAP-XPS investigation, it can be concluded that the La-deficient perovskite shows a higher CO reactivity compared to the stoichiometric $LaFeO_3$. This higher reducibility under CO for $La_{0.7}FeO_3$ highlights the promoting role of the additional phase of the Fe_2O_3 during CO reaction.

Additionally, on cooling down both the materials to lower temperature, the contribution from Fe^{3+} increases while that of the reduced species decreases. In case of $La_{0.7}FeO_3$, the concentration of Fe^{3+} increases from 37% to 50% with decrease in the Fe^{2+}/Fe^0 concentration, while for $LaFeO_3$ the Fe^{3+} rises approximately from ~65% to ~90%. The re-appearance of Fe^{3+} seems to occur more readily for $LaFeO_3$ than $La_{0.7}FeO_3$ due to the different surface compositions of the respective stoichiometries. Since this occurs while the analysis chamber is still under CO gas, it is very unlikely that some external oxygen molecules might have entered the analysis chamber especially in an UHV based instrument. As the temperature decreases and CO is no more activated, the surface could undergo re-distribution of the surface species. In addition, bulk diffusion of oxygen cannot be ruled out owing to the low activation energy of 0.7 eV [23]. These processes can assist in regenerating the Fe^{3+} on the surface of the perovskite, which can be an attractive property of a redox material especially for its application in three way catalysis. Although, NAP-XPS helps to evidence significant differences in the reactivity of $LaFeO_3$ and $La_{0.7}FeO_3$ during CO reaction, the absolute structural information is not available. For instance, the Fe^{2+} contribution can arise from the presence of reduced Fe oxides such as Fe_3O_4 and/or FeO. In addition, the spectral decomposition has a rather high error margin of 10-20% owing to the parameters of XPS decomposition of transition metals and their multiplet structures. To avail more detailed information, the next section is dedicated to *in situ* GI-XANES analysis of the two stoichiometries under similar conditions, which will not only allow to identify the possible phase transformations at the surface, but also provide a simultaneous comparison to the bulk.

Remark

In our experimental conditions with NAP-XPS equipment at SOLEIL, gaseous reactants and products were not significantly detected at the near surface of the materials. This could be due to the partial pressure of CO (0.1 mbar) since when it is increased to few mbar, gas phase CO signal was detected at higher binding energy of the carbonaceous

compounds of the material, however with a significant loss of intensity of signals.

4.2.2 *In situ* GI-XANES analysis of $LaFeO_3$ vs. $La_{0.7}FeO_3$ thin films at Fe K-edge

Activation under air

The sample is heated to high temperature to remove the presence of carbonaceous surface contamination, similar to the NAP-XPS. This ensures a clean surface for the forthcoming steps as well as a common starting point for all surfaces under investigation.

Stoichiometric perovskite $LaFeO_3$: The spectrum at room temperature evolves after heating under air at 650°C as shown in Fig.4.28. The intensity of the white line decreases while the edge position remains the same and the first EXAFS oscillation located around 7180 eV changes owing to the Debye Waller factor. Interestingly, this change is completely reversible in nature with decrease of temperature as shown by the return spectrum at 100°C. This thermal influence in the XANES spectra could be due to the non-linear lattice expansion across the antiferromagnetic to paramagnetic transition in $LaFeO_3$ around 460°C as the sample is heated [24].

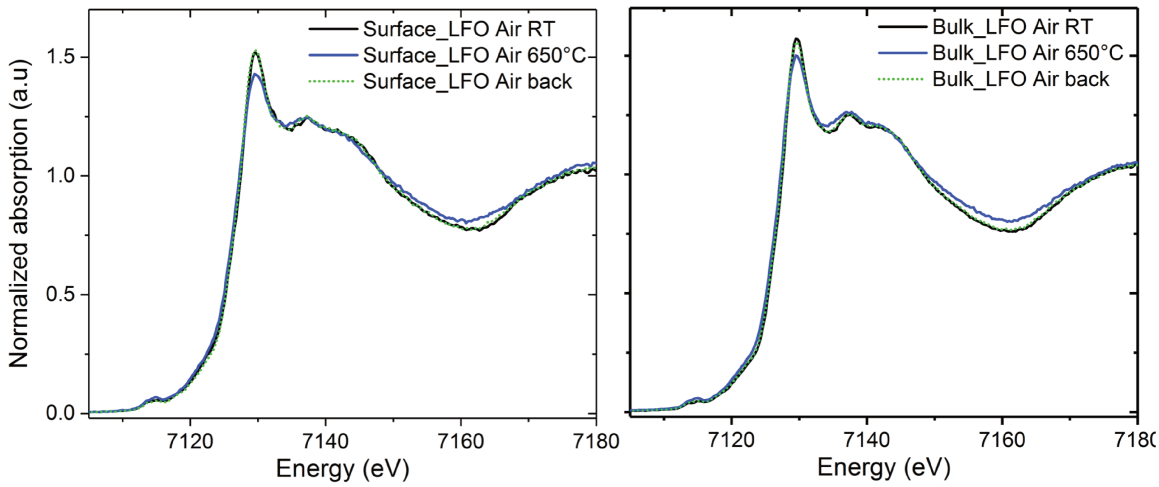

Figure 4.28: Surface and bulk XANES spectra of $LaFeO_3$ thin film at room temperature (black), 650°C under air (blue) and back at 100°C under air (dotted green).

La-deficient perovskite $La_{0.7}FeO_3$: Fig.4.29 presents the surface and bulk spectra after heating under air. Both the surface as well as bulk spectra undergo changes at 650°C and retain them even on reducing the temperature back to 100°C. Unlike the stoichiometric composition, the $La_{0.7}FeO_3$ undergoes irreversible spectral changes under oxidiz-

ing atmosphere. This spectral modification arises from the formation of the maghemite or γ-Fe_2O_3 phase as presented by the LCF analysis in Fig.4.30. Interestingly, the fitting results indicate that the ratio of the perovskite phase is maintained same as the starting point at around 60% and 50% at the surface and the bulk respectively, while only part of the hematite goes into the maghemite phase. In general, the two phases of Fe_2O_3 could co-exist in equilibrium around 650°C as been observed by Ketteler *et al* during annealing of magnetite under oxygen [25]. Also, similar effect can be induced by a partial structural transformation at similar temperature range as studied by Genezio *et al* [26]. This could also be accompanied by re-distribution of the maghemite from the bulk to the surface after heating. The occurrence of the hematite phase has also been observed in a previous *in situ* study by Raman spectroscopy at room temperature and up to 500°C under air in the powdered form. The maghemite phase was not easily observed perhaps due to lower operative temperature unlike this case [5]. Similarly, the maghemite was also not detected by ex situ Raman analysis in the previous section.

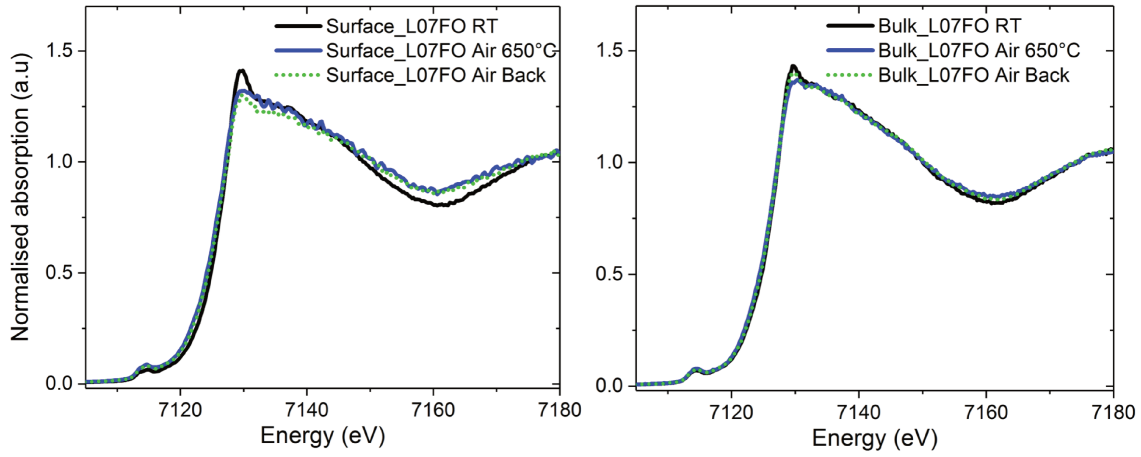

Figure 4.29: Surface and bulk XANES spectra of $La_{0.7}FeO_3$ thin film at room temperature (black), 650°C under air (blue) and back at 100°C under air (dotted green).

CO reaction

Stoichiometric perovskite $LaFeO_3$ The XANES spectra after treatment under CO at 650°C have been shown in Fig.4.31. The surface spectrum presents a shift in the absorption edge towards lower energy (inset) compared to the one at room temperature, indicating reduction of the surface $LaFeO_3$. The LCF analysis presented in Fig.4.32 further highlights 13% reduction of $LaFeO_3$ to the FeO phase. Similarly, the bulk also shows minor reduction given by the smaller shift in the edge with only around 6% of FeO content. The fits

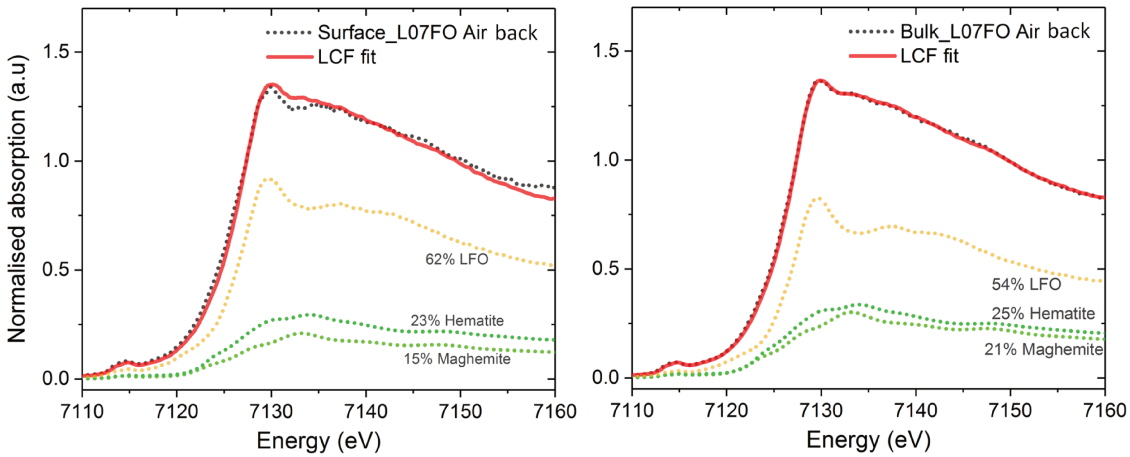

Figure 4.30: LCF analysis of surface (left) and bulk (right) XANES spectra of $La_{0.7}FeO_3$ thin film after treatment in air.

are done with the $LaFeO_3$ recorded under 650°C to take into account the slight changes induced by temperature observed earlier. The perovskite undergoes reduction under CO and directly leads to the formation of FeO without forming any intermediate species such as magnetite. On reducing the temperature back to 100°C under CO, the perovskite still remains partially reduced in the return spectrum both at the surface and the bulk as seen in the respective insets of Fig.4.31. According to the fits, the direct reduction of the stoichiometric formulation under CO can be represented by the following reaction.

$$2\,LaFeO_3 + CO \longrightarrow 2\,FeO + La_2O_3 + CO_2 \tag{4.1}$$

The reduction rate is in line with H_2-TPR studies made previously on powder catalyst of the same composition, which shows almost none or little reduction of $LaFeO_3$ up to 700°C [3].

La deficient perovskite $La_{0.7}FeO_3$:

Bulk: The spectral changes of $La_{0.7}FeO_3$ bulk under CO at 650°C is shown in Fig.4.33. In presence of CO, the bulk of the non-stoichiometric perovskite indicates shift of the edge energy in addition to slight changes in the spectral shape. It highlights not only reduction of the bulk but also more distinct change in the phase composition to some reduced species. The LCF analysis displayed in Fig.4.35(right) allows to reveal 43% $LaFeO_3$, 32% magnetite, 14% hematite and 11% FeO under CO. The starting point of this catalyst contained a 50-50 mixture of $LaFeO_3$ and Fe_2O_3 in the bulk. According to the LCF analysis, most of the Fe_2O_3 initially present gets reduced to magnetite and FeO. But the perovskite

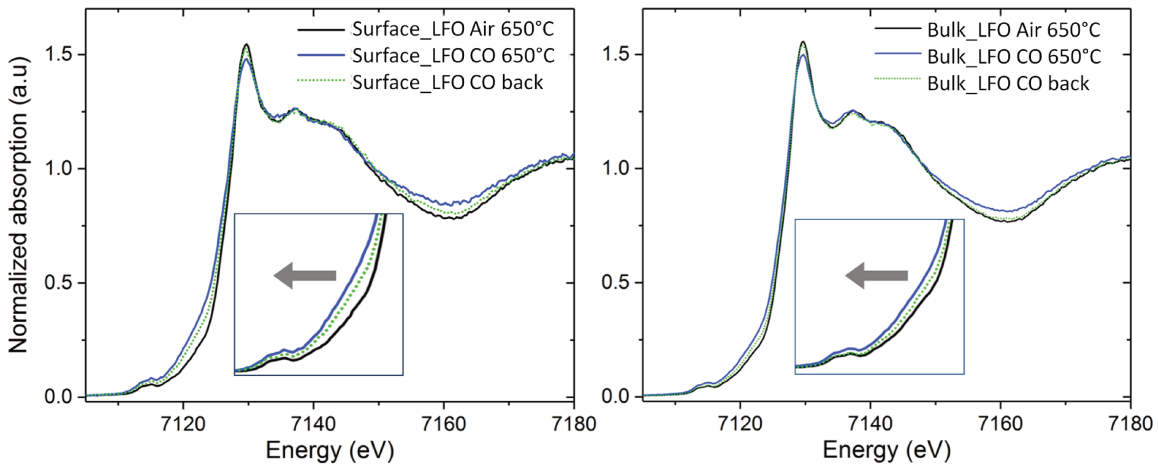

Figure 4.31: Surface and bulk XANES spectra of $LaFeO_3$ thin film under air (black) at 650°C, under CO (blue) at 650°C and back at 100°C under CO (dotted green).

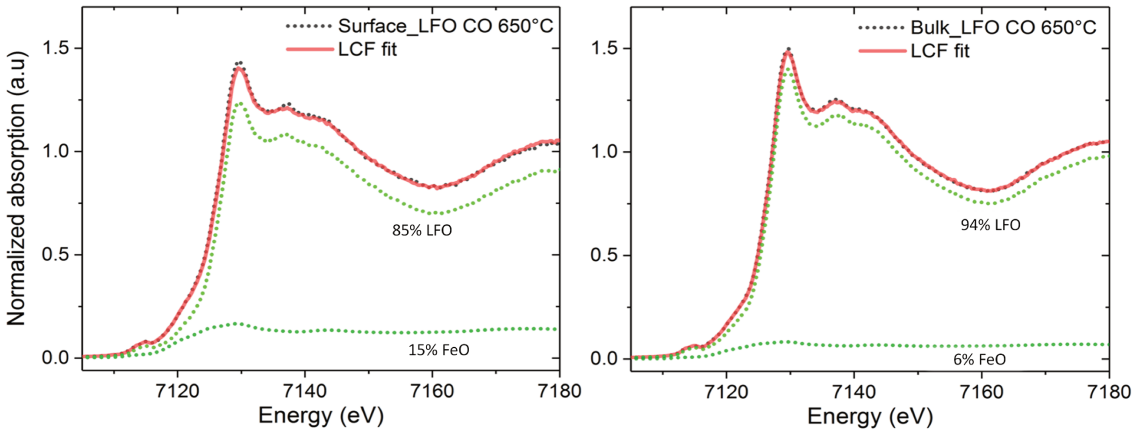

Figure 4.32: LCF analysis of surface (left) and bulk (right) XANES spectra of $LaFeO_3$ thin film at 650°C under CO.

remains only negligibly reduced at 43% at the bulk compared to 50% after activation in air. It is likely that this small amount of $LaFeO_3$ might have reduced to FeO while major reduction only takes place for the iron oxides phases. At this point 2 simultaneous reactions can be considered to be taking place, firstly the reduction of $LaFeO_3$ under CO (equation 4.1) and secondly, for the iron oxides given by the following reaction.

$$2\,Fe_2O_3 + CO \longrightarrow FeO + Fe_3O_4 + CO_2 \tag{4.2}$$

Surface: The $La_{0.7}FeO_3$ surface undergoes strong spectral changes under CO at 650°C compared to the bulk as evident from Fig.4.33. It features a higher shift in the edge position and drastic change in the shape of the whiteline. The XANES spectra of $LaFeO_3$ and $La_{0.7}FeO_3$ under CO have been compared in Fig. 4.34 (left), where the spectral signature

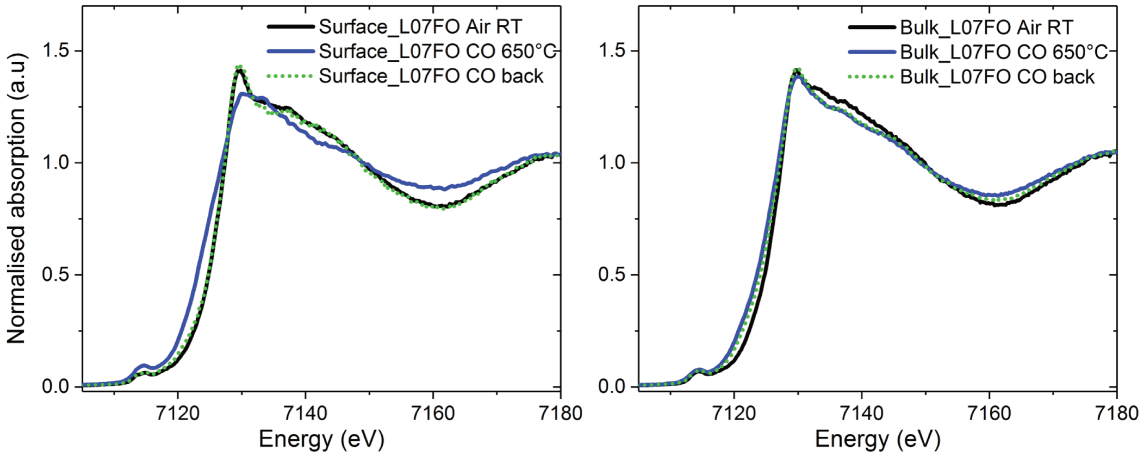

Figure 4.33: Surface and bulk XANES spectra of $La_{0.7}FeO_3$ thin film under air at room temperature (black), under CO at 650°C (blue) and back at 100°C under CO (dotted green).

of $La_{0.7}FeO_3$ under CO features striking similarity to that of the magnetite reference, signifying a major presence of this phase (right). The LCF analysis in Fig.4.35 further confirms this, with 69% magnetite, 8% FeO and 23% $LaFeO_3$. Rather large amount of the surface $La_{0.7}FeO_3$ has reduced primarily to magnetite. Additionally, the iron oxide at the surface have also been completely reduced at this stage. In contrast, the bulk only undergoes 10% reduction of the perovskite with some remaining unreduced Fe_2O_3.

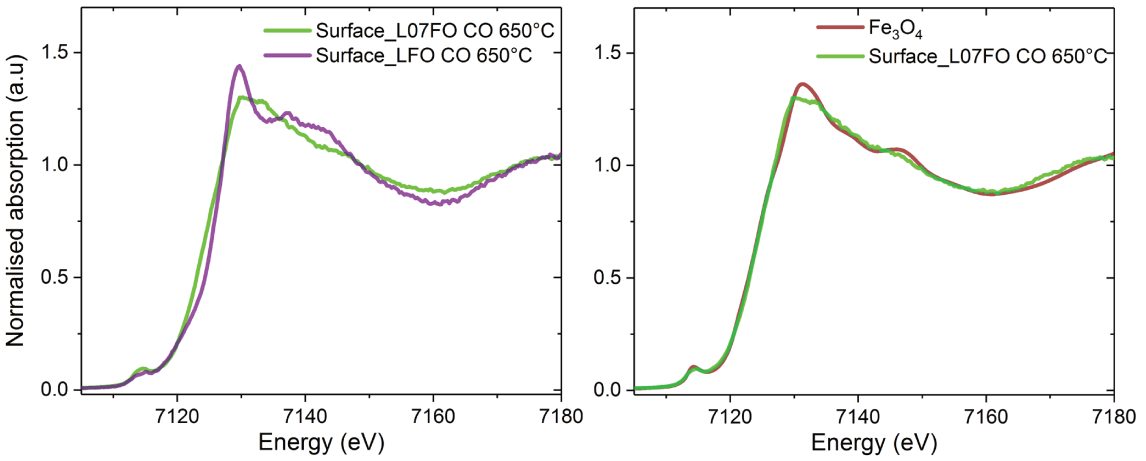

Figure 4.34: Comparison of surface XANES spectra of $La_{0.7}FeO_3$ at 650°C under CO with (a) $LaFeO_3$ thin film under similar conditions, (b) magnetite (Fe_3O_4) reference.

Origin of different surface/bulk behaviors under CO: As previously discussed, the stoichiometric $LaFeO_3$ thin film is composed of only the perovskite phase while the non-stoichiometric perovskite consists of 40% and 50% of Fe_2O_3 at the surface and bulk respectively, besides the perovskite phase. Thereby, both materials possess different starting points for any reaction. On reacting with CO, one can expect the following possible

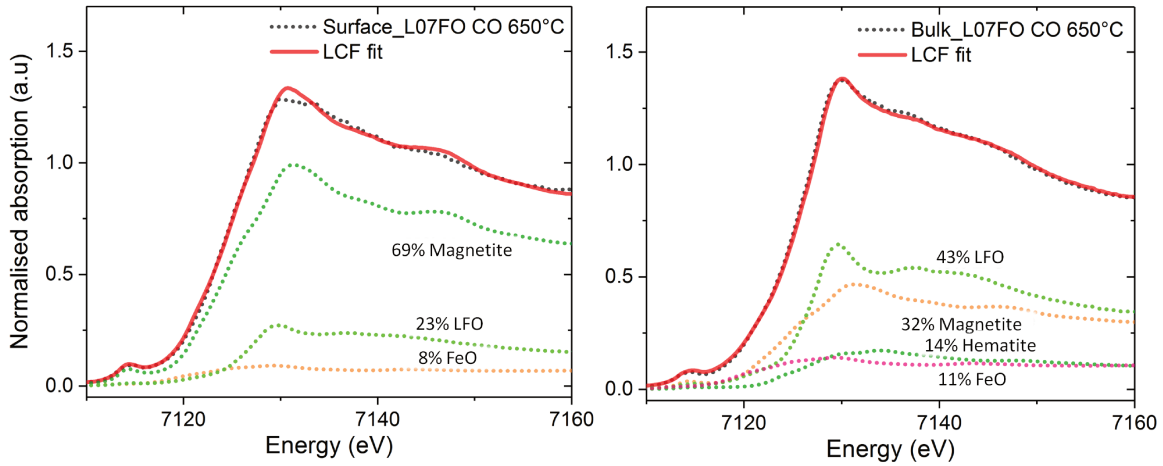

Figure 4.35: LCF analysis of surface (left) and bulk (right) XANES spectra of $La_{0.7}FeO_3$ thin film at 650°C under CO.

reactions to occur,

$$3\,Fe_2O_3 + CO \longrightarrow 2\,Fe_3O_4 + CO_2 \tag{4.3}$$

$$Fe_2O_3 + CO \longrightarrow 2\,FeO + CO_2 \tag{4.4}$$

$$6\,LaFeO_3 + CO \longrightarrow 2\,Fe_3O_4 + 3\,La_2O_3 + CO_2 \tag{4.5}$$

$$2\,LaFeO_3 + CO \longrightarrow 2\,FeO + La_2O_3 + CO_2 \tag{4.6}$$

The LCF results of each treatment for the surface and bulk spectra are summarized in table 4.2.

Table 4.2: Summary of the surface/bulk GI-XANES analyses of $LaFeO_3$ and $La_{0.7}FeO_3$.

Sample/ Conditions	As-received		Air 650°C		CO 650°C	
	Surface	Bulk	Surface	Bulk	Surface	Bulk
$LaFeO_3$	100% $LaFeO_3$	100% $LaFeO_3$	100% $LaFeO_3$	100% $LaFeO_3$	85% $LaFeO_3$ 15% FeO	94% $LaFeO_3$ 6% FeO
$La_{0.7}FeO_3$	60% $LaFeO_3$ 40% α-Fe_2O_3	50% $LaFeO_3$ 50% α-Fe_2O_3	62% $LaFeO_3$ 23% α-Fe_2O_3 15% ϒ-Fe_2O_3	54% $LaFeO_3$ 25% α-Fe_2O_3 15% ϒ-Fe_2O_3	23% $LaFeO_3$ 69% Fe_3O_4 8% FeO	43% $LaFeO_3$ 14% α-Fe_2O_3 32% Fe_3O_4 11% FeO

According to the LCF results, for the stoichiometric composition 15% of $LaFeO_3$ seems to reduce only to the FeO phase under CO at 650°C (reaction 4.6). Formation of any magnetite was not evident. In case of the La-deficient $La_{0.7}FeO_3$ under similar conditions, however, CO reaction results into 69% magnetite in addition to 23% of $LaFeO_3$ and 8% FeO at the surface. Since the $La_{0.7}FeO_3$ consists of both Fe_2O_3 and $LaFeO_3$, it can be considered that the Fe_3O_4 formed after CO reaction is due to the reduction of Fe_2O_3 only. However, if it was the case one would expect that the amount of $LaFeO_3$ will remain constant which is not the case as indicated in table 4.2 (62% before reaction, 23% after reaction). Furthermore, the amount of Fe_3O_4 after reaction exceeds the amount of Fe_2O_3 initially present on the surface (40%). This indicates the 69% of Fe_3O_4 is coming from the reduction of both Fe_2O_3 and $LaFeO_3$ phases. The LCF shows that the non-stoichiometric perovkite is basically a mixture of the stoichiometric perovskite $LaFeO_3$ and Fe_2O_3 phases. Additionally, no Fe_3O_4 was formed and only reaction 4.6 was observed for the reduction reaction of the stoichiometric perovskite (15% FeO) after CO reaction (table 4.2). One can conclude that for $La_{0.7}FeO_3$, reaction 4.5 does not occur. In fact, the origin of the presence of high amount of Fe_3O_4 seems to be due to reactions other than reaction 4.3 and 4.6. One possible reaction could be as follows:

$$Fe_2O_3 + FeO \longrightarrow Fe_3O_4 \tag{4.7}$$

In the above reaction, the FeO formed from the stoichiometric $LaFeO_3$ could react with some unreacted Fe_2O_3 phase to finally produce the magnetite phase. Reaction 4.7 could be supported by the presence of a strong interaction or an interface between Fe_2O_3 and $LaFeO_3$ phases in $La_{0.7}FeO_3$. According to this assumption based on the LCF results, as the $LaFeO_3$ reduces to FeO under CO, the FeO finds Fe_2O_3 in close vicinity at the interface to react and form Fe_3O_4 leading to the decrease in the initial amount of the perovskite. This reaction is in line with the observations made by Kettler *et al* who evidenced the formation of an intermediate FeO phase at the phase boundary during reduction of Fe_2O_3 to Fe_3O_4 [25]. Therefore in $La_{0.7}FeO_3$, the perovskite seems to be acting like a reservoir of iron that continues to reduce to FeO as it keeps getting consumed by the Fe_2O_3 at the interface forming majority of the magnetite phase. Interestingly, this predicted chemical behavior is also in line with the catalytic performances studied previously [3]. It was observed that the CO conversion improved only in case of La-deficient $La_{0.7}FeO_3$ perovskite

composition and not for a mechanical mixture of Fe_2O_3 and $LaFeO_3$ phases, which remained comparable to the stoichiometric $LaFeO_3$.

Back spectra under CO: As the temperature is reduced back to 100°C under CO, the spectral signature of the surface tends to go back to the starting point as presented in Fig.4.33. LCF analysis of the surface spectrum shows presence of 70% $LaFeO_3$, 24% hematite and 6% FeO in Fig.4.36. The surface is thereby seems to have returned to the starting point of the $La_{0.7}FeO_3$ perovskite. The magnetite species observed under CO at high temperature could also be re-oxidized to perovskite as the CO molecule is no longer activated at low temperature. In fact, the surface may be easily re-oxidized according to equation 4.8.

$$4Fe_3O_4 + 3La_2O_3 + O_2 \rightarrow 6LaFeO_3 + 3Fe_2O_3 \tag{4.8}$$

As suggested by this equation, with only one O_2 molecule required to form 6 molecules of $LaFeO_3$, it is quite simple to form surface $LaFeO_3$ again.

In contrast, the bulk still remains reduced on decreasing the temperature to 100°C while retaining the magnetite phase to a similar extent as under CO at higher temperature constituting 43% perovskite, 40% magnetite, 3% FeO and 14% hematite.

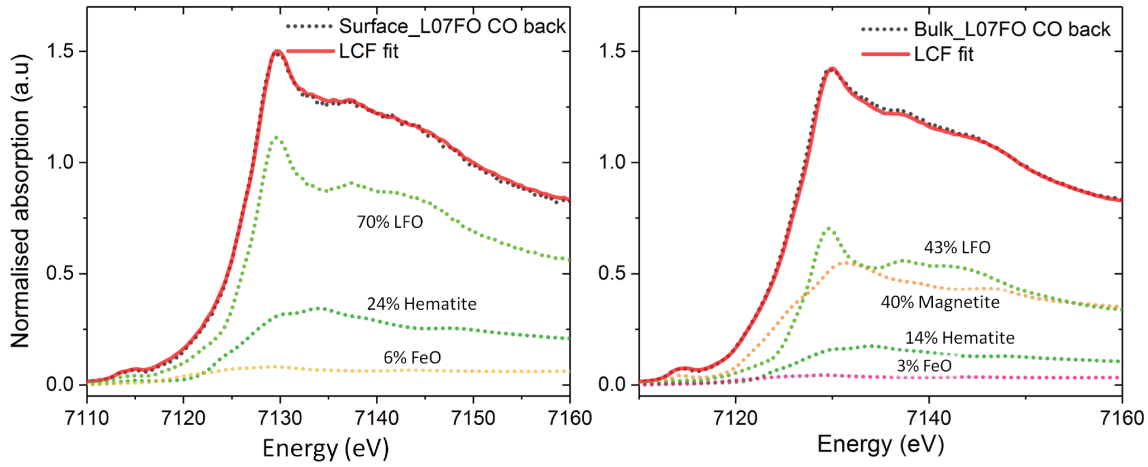

Figure 4.36: LCF analysis of surface (left) and bulk (right) XANES spectra of $La_{0.7}FeO_3$ thin film at 100°C under CO.

4.2.3 Discussion

Chemical behavior of stoichiometric and non-stoichiometric perovskites: The surface of the non-stoichiometric $La_{0.7}FeO_3$ thin film in comparison to stoichiometric $LaFeO_3$ has been analyzed in *in situ* mode under CO at 550-567°C. The NAP-XPS investigation with

a depth resolution of 1.5 nm highlighted the overall reactivity of the two compositions. The La-deficient perovskite presented an intense Fe^{2+} satellite and a metallic component, which remained absent in stoichiometric $LaFeO_3$ with only loss of the initial Fe^{3+} satellite feature.

During CO reaction, around 35% of the Fe^{3+} in $LaFeO_3$ is transformed to reduced Fe species, meaning around one third of the perovskite is undergoing reduction. In contrast, $La_{0.7}FeO_3$ presents 50% Fe^{2+}, 13% Fe^0 and 37% Fe^{3+} during reduction under CO. The absence of Fe^0 in $LaFeO_3$ in contrast to $La_{0.7}FeO_3$ under CO at ~550°C, suggests that Fe^0 is arising from the more easily reducible iron oxide phase present in $La_{0.7}FeO_3$, since the $LaFeO_3$ thin film contains no such segregated phases [3]. This also rules out the likelihood of any exolution of Fe metallic species from the perovskite under CO. However, NAP-XPS allowed to investigate only the oxidation states of Fe species under reactive conditions without information regarding the phase compositions from which the Fe^{3+} and Fe^{2+} signals arise.

These differences have been further investigated by GI-XANES, which allows the determination of the phase compositions at each step of the experiment. The application of GI-XANES allowed to not only study the surface of the thin film (2-8 nm) but also the bulk composition simultaneously by adjusting the incidence angle between the incident X-ray beam and the sample. The surface spectrum of $La_{0.7}FeO_3$ reveals the presence of 60% $LaFeO_3$ and 40% hematite, while the bulk consists of 50% $LaFeO_3$, 35% hematite and 15% maghemite (γ-Fe_2O_3), according to the LCF results. Hence, the $La_{0.7}FeO_3$ perovskite thin film is composed of 50-60% of the perovskite phase across depth and the rest remains as iron oxide, also observed earlier by Raman analysis. On the other hand, the $LaFeO_3$ thin film is entirely composed of the perovskite phase throughout. Under CO at 650°C, the stoichiometric perovskite undergoes slight reduction of the surface to FeO (15%) without forming any other phases like magnetite. This indicates that only FeO is formed from the stoichiometric $LaFeO_3$ under CO. In case of $La_{0.7}FeO_3$, the surface mostly reduces to 69% magnetite and 8% FeO while 23% remains unreacted. However in the bulk, the perovskite shows slight reduction with mainly reduction of the iron oxides occurring. This highlights once again the enhanced reduction of the perovskite surface in $La_{0.7}FeO_3$ compared to the stoichiometric composition. Interestingly, the LCF results also show that the perovskite is mainly reducing to the magnetite phase directly, as the maximum amount of magnetite must not exceed 40% if it was only arising from the hematite phase. Of course,

at this point both reduction processes including the reduction of $LaFeO_3$ to FeO as well as reduction of Fe_2O_3 to Fe_3O_4 and FeO must be occurring. Although, these alone cannot explain why the $La_{0.7}FeO_3$ perovskite reduces to magnetite, unlike the case of stoichiometric $LaFeO_3$. The most plausible explanation behind this observation in $La_{0.7}FeO_3$ may be given by a two-step process: (i) the perovskite ($LaFeO_3$) reduces to FeO under CO at high temperature, and (ii) as FeO is formed, it finds Fe_2O_3 in its close vicinity at the interface and reacts with it to form magnetite. The presence of such an interface between the perovskite and the segregated Fe_2O_3 particles allows the perovskite to show enhanced reduction to the magnetite phase and thereby help in improving the overall reducibility of $La_{0.7}FeO_3$ catalyst during CO reaction. The beneficial role of the interface is also predicted by the catalytic performances when compared to a mechanical mixture of $LaFeO_3$ and Fe_2O_3, which shows similar catalytic performance as that of the stoichiometric composition during CO/NO reaction [3]. This indicates that a strong interaction between the two phases in $La_{0.7}FeO_3$ is required for this enhancement of the catalytic activity. Any signal from metallic iron was not detected by GI-XANES throughout the *in situ* measurements under CO at 650°C.

Combining the observations from NAP-XPS and *in situ* GI-XANES together, in line with SEM and AFM images, a scheme has been proposed to illustrate the predicted chemical behavior of the two perovskites, as shown in Fig.4.37. In case of $LaFeO_3$ thin film under CO at high temperature, the surface reduces to FeO only, since there is no other species for FeO to react with (Fig.4.37(a)). On the contrary for $La_{0.7}FeO_3$, the perovskite reduces to FeO and then further reacts with the Fe_2O_3 present close to it to form magnetite, which is the major phase formed under these conditions. Thus, the perovskite acts like a reservoir of Fe^{2+} species that allows this reaction to occur continuously to form Fe_3O_4. Indeed, Fe_2O_3 must also simultaneously reduce to magnetite followed by FeO and Fe^0 as widely known in literature [27]. Since every process can be considered to occur via formation of a gradient, one can consider that the reduced species (Fe^0, FeO, Fe_3O_4) will be arranged according to their valence states with the most reduced species *i.e.* Fe^0, being towards the extreme surface as described in Fig.4.37(b). This further helps in establishing an oxygen-gradient from the surface towards the bulk, which can also assist in oxygen mobility as well as its redox capabilities. The metallic iron formed can further contribute to augment

the reduction of $LaFeO_3$ and Fe_2O_3 given by the following reactions,

$$2\,Fe_2O_3 + Fe \longrightarrow 2\,FeO + Fe_3O_4 \tag{4.9}$$

$$2\,LaFeO_3 + Fe \longrightarrow 3\,FeO + La_2O_3 \tag{4.10}$$

Neverthless, the presence of metallic iron cannot justify the reduction of the perovskite to magnetite and thereby cannot be considered the active species of this process. In any case, if Fe^0 is present depending on the reaction temperature, it appears to promote the reduction process under CO.

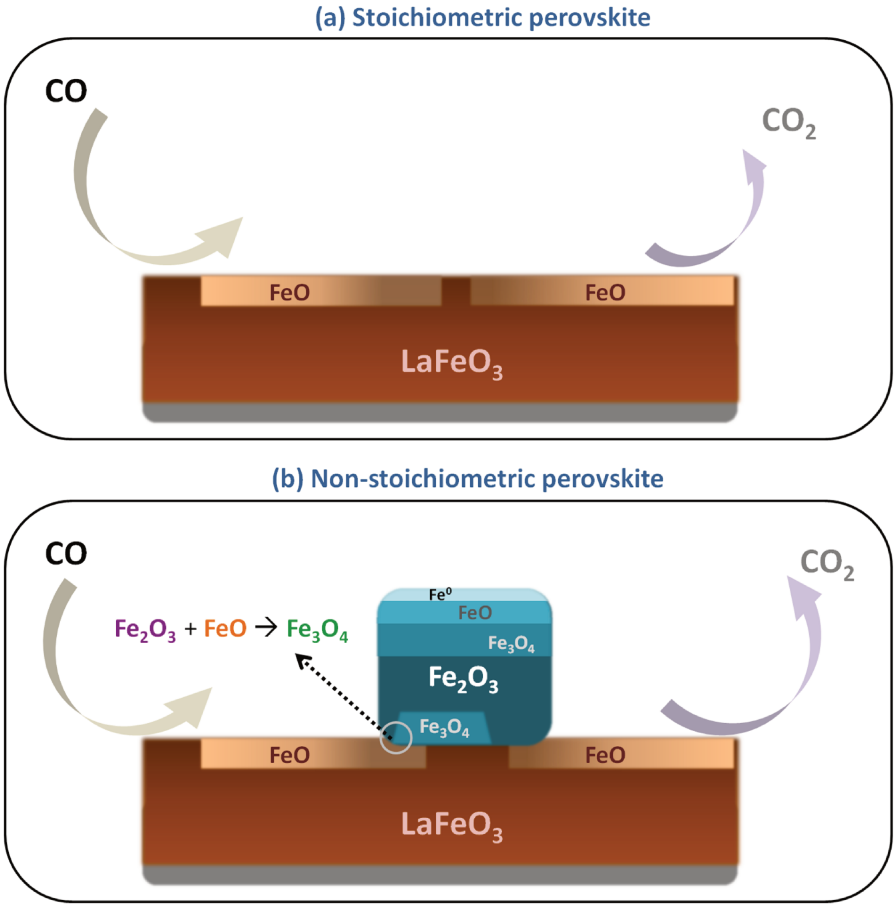

Figure 4.37: Scheme representing the chemical behavior of (a) $La_{0.7}FeO_3$ and (b) $LaFeO_3$ under CO at high temperature.

Finally, the $La_{0.7}FeO_3$ model catalyst must be compared to conventional powders of the same composition by GI-XANES. The LCF for the $La_{0.7}FeO_3$ powder shown in Fig.4.38 presents 65% perovskite with 20% hematite and 15% maghemite, which contains 35% residing as segregated phases. The LCF results are in line with surface and bulk analysis of $La_{0.7}FeO_3$ thin film confirming the presence of the iron oxide segregates. This vali-

dates the model of $La_{0.7}FeO_3$ perovskite indicating that the findings made on this thin film can be extended to catalysts shaped as powders. The extent of the iron oxide segregation is probably more enhanced in the thin film due to its typical shape and dimension (~70 nm), still acting as a reliable model of the non-stoichiometric perovskite. The non-stoichiometric $La_{0.7}FeO_3$ could be considered like a supported catalyst with Fe_2O_3 particles in strong interaction with $LaFeO_3$ forming an interface between the two, as predicted from the NAP-XPS and GI-XANES results.

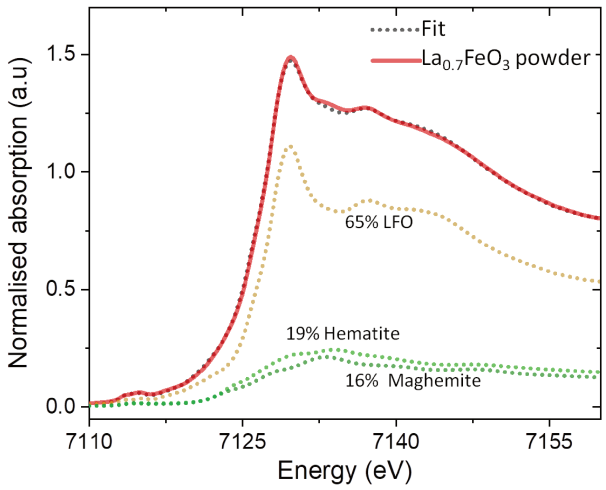

Figure 4.38: XANES of $La_{0.7}FeO_3$ powder catalyst and its LCF analysis.

Comparing NAP-XPS and GI-XANES analyses: Even though both techniques highlight similar trends that is the higher reducibility of the perovskite in $La_{0.7}FeO_3$ compared to $LaFeO_3$ thin film. However, some differences exists, which must be discussed here in order to understand their possible origins. No metallic iron is observed in case of *in situ* GI-XANES analysis, unlike NAP-XPS. This can be explained by the different detection limits from the depth resolutions of the two techniques, 1.5 nm in NAP-XPS and ~2-8 nm in GI-XANES [28]. For instance, a 12% Fe^0 in 1.5 nm is equivalent to close to ~2% in 8 nm, assuming a linear gradient of the species on the thin film. In addition, the absolute experimental conditions are likely to be different such as the sample temperature, pressure, flow rate (more dynamic conditions in XANES), reactor design etc. Any variation of the absolute temperature of the experiment even with a difference of around 50°C can result in very different extent of reduction to different ratios of reduced species as has been depicted by Jozwiak *et al* [27]. For example, the amount of Fe^0 can increase by double on increasing the temperature by 50°C during reduction of FeO under hydrogen. This shows

that even a small difference in experimental temperature, as is the case here, can yield different quantitative results. Moreover, the analysis areas of the sample during acquisition for each technique are distinct as depicted in Fig.4.39. On one hand, XPS probes 1.5 nm of the surface with almost no influence of the sample roughness, being a material specific technique. On the other hand, GI-XANES probes 2-8 nm of the surface and is dependent on the surface roughness since the depth resolution changes with the sample-beam geometry. Therefore, it is more cautious to consider the qualitative aspects of each technique without direct quantitative comparisons.

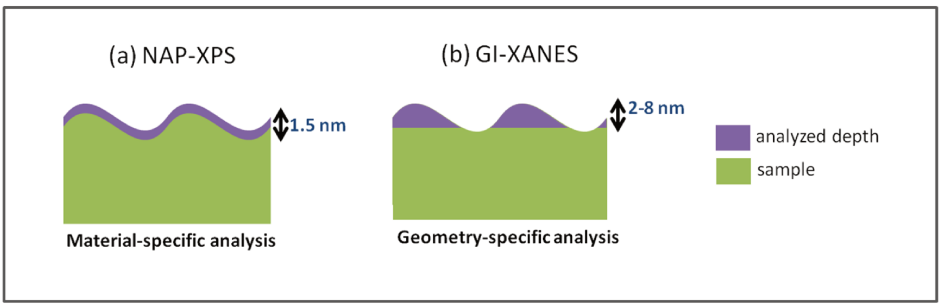

Figure 4.39: Comparison of XPS and GI-XANES analysis.

4.3 Conclusions

This chapter deals with systematic comparison of the stoichiometric $LaFeO_3$ and non-stoichiometric $La_{0.7}FeO_3$ thin film compositions. XPS and LEIS analyses confirmed the decrease of the commonly known La-enrichment given by the surface atomic La/Fe ratio by inducing the La-deficiency in the structure ($La_{0.7}FeO_3$). Raman spectroscopy highlighted the presence of segregated Fe_2O_3 phase in $La_{0.7}FeO_3$, given by the additional hematite lines besides the one from perovskite. Likewise, the segregation of the iron oxide in the surface as well as bulk could be quantified with GI-XANES analysis ranging from 40-50%. In contrast, the stoichiometric $LaFeO_3$ comprised of 100% perovskite phase. Depth profile of the respective thin film composition further indicated an enrichment of Fe (FeO^- fragments) in the perovskites of both stoichiometries. Although the Fe-enrichment was expected for $La_{0.7}FeO_3$ owing to the extent of iron oxide segregation, its appearance in $LaFeO_3$ was a surprising outcome. Since no additional phases besides the perovskite were determined in $LaFeO_3$ thin film from the other complementary techniques, the existence of any other phase segregation was unlikely. In fact, the existing surface La-enrichment promoted the resulting Fe-rich zone underneath it, as evidenced in ToF-SIMS profile. Such surface reconstruction has been widely evidenced by other researchers also. The two films were then exposed to CO molecules and their surface reactivity was studied by NAP-XPS and *in situ* GI-XANES measurements around 550-650°C. The La-deficient composition resulted in higher reducibility of perovskite compared to $LaFeO_3$ shown by more prominent Fe^{2+} satellite as well as binding energy shift in $La_{0.7}FeO_3$. Finally, to elucidate the proportion of each phase, LCF of GI-XANES spectra was employed. Under CO the $LaFeO_3$ mildly reduced to only FeO, while $La_{0.7}FeO_3$ reduced to a mixture with majority of magnetite besides some FeO. The extensive reduction of the $La_{0.7}FeO_3$ perovskite was predicted by the presence of an interface between the segregated Fe_2O_3 particles and the perovskite itself, where the perovskite acted like a Fe^{2+} reservoir assisting in a continuous reduction process. This lead to enhancement in the reactivity of $La_{0.7}FeO_3$ during CO oxidation reaction. The model catalyts were finally compared to conventional catalysts and their catalytic performances to validate this hypothesis.

4.4 References

[1] M. Sunding, K. Hadidi, S. Diplas, O. Løvvik, T. Norby, and A. Gunnæs, *J. Electron. Spectrosc.*, 2011, **184**(7), 399 – 409. 102, 116

[2] M. C. Biesinger, B. P. Payne, A. P. Grosvenor, L. W. Lau, A. R. Gerson, and R. S. Smart, *Appl. Surf. Sci.*, 2011, **257**(7), 2717 – 2730. 102, 116, 121, 123

[3] A. Schön, C. Dujardin, J.-P. Dacquin, and P. Granger, *Catal. Today*, 2015, **258**, 543 – 548. 102, 133, 137, 139, 140

[4] B. Tofield and W. Scott, *J. Solid St. Chem.*, 1974, **10**(3), 183–194. 102

[5] D. Blanck, A. Schön, A.-S. Mamede, C. Dujardin, J.-P. Dacquin, P. Granger, J.-F. Paul, and E. Berrier, *Catal. Today*, 2016. 103, 132

[6] I. Chamritski and G. Burns, *J. Phys. Chem. B*, 2005, **109**(11), 4965–4968. 103

[7] D. L. A. de Faria, S. Venàncio Silva, and M. T. de Oliveira, *J. Raman Spectrosc.*, 1997, **28**(11), 873–878. 103

[8] J. Druce, H. Tellez, M. Burriel, M. Sharp, L. Fawcett, S. Cook, D. McPhail, T. Ishihara, H. Brongersma, and J. Kilner, *Energy Environ. Sci.*, 2014, **7**, 3593–3599. 113

[9] Y. Wu, C. Cordier, E. Berrier, N. Nuns, C. Dujardin, and P. Granger, *Appl. Catal. B - Environ.*, 2013, **140-141**, 151 – 163.

[10] A. Schön, J.-P. Dacquin, C. Dujardin, and P. Granger, *Top. Catal.*, 2017, **60**(3), 300–306. 113

[11] H. Ding, A. V. Virkar, M. Liu, and F. Liu, *Phys. Chem. Chem. Phys.*, 2013, **15**, 489–496. 113

[12] W. Lee, J. W. Han, Y. Chen, Z. Cai, and B. Yildiz, *J. Am. Chem. Soc.*, 2013, **135**(21), 7909–7925. 113

[13] H. Dulli, P. A. Dowben, S.-H. Liou, and E. W. Plummer, *Phys. Rev. B*, 2000, **62**, 14629–14632. 113

[14] K. Szot, C. Freiburg, and M. Pawełczyk, *Appl. Phys. A*, 1991, **53**(6), 563–567.

[15] K. Szot and W. Speier, *Phys. Rev. B*, 1999, **60**, 5909–5926. 113

[16] M. Kubicek, A. Limbeck, T. Frömling, H. Hutter, and J. Fleig, *ECS transactions*, 2011, **35**(1), 1975–1983. 114

[17] M. Kubicek, A. Limbeck, T. Frömling, H. Hutter, and J. Fleig, *J. Electromchem. Soc.*, 2011, **158**(6), B727–B734. 114

[18] C. J. Powell and A. Jablonski, *Journal of Vacuum Science & Technology A*, 1999, **17**(4), 1122–1126. 116

[19] Sébastien Royer and Daniel Duprez and Fabien Can and Xavier Courtois and Catherine Batiot-Dupeyrat and Said Laassiri and Houshang Alamdari, *Chem. Rev.*, 2014, **114**(20), 10292–10368. 117

[20] M. L. Miller and R. W. Linton, *Anal. Chem.*, 1985, **57**(12), 2314–2319. 117

[21] S. Béchu, B. Humbert, V. Fernandez, N. Fairley, and M. Richard-Plouet, *Appl. Surf. Sci.*, 2018, **447**, 528 – 534. 123

[22] V. Fernandez, D. Kiani, N. Fairley, F.-X. Felpin, and J. Baltrusaitis, *Appl. Surf. Sci.*, 2019, p. 143841. 123

[23] T. Ishigaki, S. Yamauchi, J. Mizusaki, K. Fueki, H. Naito, and T. Adachi, *J. Solid St. Chem.*, 1984, **55**(1), 50 – 53. 130

[24] S. M. Selbach, J. R. Tolchard, A. Fossdal, and T. Grande, *J. Solid St. Chem.*, 2012, **196**, 249 – 254. 131

[25] G. Ketteler, W. Weiss, W. Ranke, and R. Schlögl, *Phys. Chem. Chem. Phys.*, 2001, **3**, 1114–1122. 132, 137

[26] F. Genuzio, A. Sala, T. Schmidt, D. Menzel, and H.-J. Freund, *Surf. Sci.*, 2016, **648**, 177–187. 132

[27] W. Jozwiak, E. Kaczmarek, T. Maniecki, W. Ignaczak, and W. Maniukiewicz, *Appl. Cata. A - General*, 2007, **326**(1), 17 – 27. 140, 142

[28] Götsch, Thomas and Köpfle, Norbert and Grünbacher, Matthias and Bernardi, Johannes and Carbonio, Emilia A. and Hävecker, Michael and Knop-Gericke, Axel and

Bekheet, Maged F. and Schlicker, Lukas and Doran, Andrew and Gurlo, Aleksander and Franz, Alexandra and Klötzer, Bernhard and Penner, Simon, *Phys. Chem. Chem. Phys.*, 2019, **21**, 3781–3794. 142

Chapter 5

Mn or Cu substituted $LaFeO_3$ TWCs: Highlighting different catalytic operating modes of $La_{0.7}Fe_{0.8}M_{0.2}O_3$

A/B-site substitution in perovskites can effectively tune the catalytic properties by controlling the valency of constituent ions and lattice defect vacancies, as discussed in chapter 1 [1]. The combined presence of two different ions at the B-site can bring about synergistic effects and can be effective in enhancement of the reducibility [2]. In this chapter, the aspect of B-site substitution in $LaFeO_3$ perovskite catalysts by Cu or Mn, particularly, $La_{0.7}Fe_{0.8}Cu_{0.2}O_3$ and $La_{0.7}Fe_{0.8}Mn_{0.2}O_3$ will be studied by the means of *in situ* / *operando* Raman spectroscopy. These two perovskite compositions were chosen by the Partial-PGMs consortium based on catalytic performance screening and theoretical calculations [3]. Catalytic tests of the substituted as well as the non-substituted perovskites have shown that besides inducing a La-deficiency in the composition ($La_{0.7}FeO_3$), the addition of Cu or Mn further improves the catalytic activity in CO oxidation reaction. Their temperature of 50% conversion (T_{50}) for CO oxidation to CO_2 have been shown in Table 5.1. B-site substitution by Mn improves the T_{50} value by 45°C, while the Cu substitution improves it by 125°C. Although, the operating feed consists of a complex mixture of gases including CO, NO, hydrocarbons, O_2, H_2, H_2O etc., the first approach is to study the catalysts under simplified conditions with only one or two gaseous environments. Therefore, to understand the promoting role of each substituted element, the two catalysts will be comparatively studied under *in situ* conditions under oxidative (O_2/He) and reductive (H_2/He) environment as well as under partial pressure of water.

Table 5.1: Temperature of 50% CO conversion (T_{50}) to CO_2 for the investigated perovskites (0.1% NO, 0.7% CO, 0.045% C_3H_6, 0.022% C_3H_8, 0.23% H_2, 0.73% O_2, 15% CO_2, 10% H_2O, balance He; Gas hourly space velocity 60000 mL. $h^{-1}.g^{-1}$)

Catalyst	T_{50} (°C)
$LaFeO_3$	470
$La_{0.7}FeO_3$	385
$La_{0.7}Fe_{0.8}Mn_{0.2}O_3$	340
$La_{0.7}Fe_{0.8}Cu_{0.2}O_3$	260

In addition, their behavior will be studied during CO reaction while online monitoring of its conversion to carbon monoxide, i.e. in the *operando* mode. The catalysts will be analyzed in the conventional powder form to have decent data regarding the activity, which is quite challenging in thin films due to very low amount of matter and surface area. Also, the efficiency of the *in situ/operando* Raman technique to study the structure-activity correlations will be evaluated in context of such catalytic systems. Finally, each catalyst will be investigated by quasi *in situ* XPS to attribute the chemical environment of exiting species. The combined observations will allow to interpret the nature and the operating modes of each catalyst under model reactive conditions.

5.1 B-site substituted $LaFeO_3$ by Cu ($La_{0.7}Fe_{0.8}Cu_{0.2}O_3$)

5.1.1 Physicochemical characterization of $La_{0.7}Fe_{0.8}Cu_{0.2}O_3$

XRD analysis

The XRD pattern of $La_{0.7}Fe_{0.8}Cu_{0.2}O_3$ perovskite is presented in Fig.5.1. The diffractogram shows the characteristic reflections of an orthorhombic crystal structure with Pbnm space group (JCPDS PDF 37-1493). The lattice constants are a=5.545 Å, b=7.857 Å and c=5.550 Å. In addition, the diffraction pattern shows weak reflections at 35.6° and 38.7°, corresponding to the (111) and (-111) reflections of some segregated CuO phase.

XPS analysis

The XPS La 3d, Fe 2p, Cu 2p, O 1s and C 1s photopeaks of $La_{0.7}Fe_{0.8}Cu_{0.2}O_3$ have been shown in Fig.5.2. The O 1s contribution from the lattice oxygen is located at 529.2 eV, while the one from hydroxides, defects in oxides and/or organic species is present at

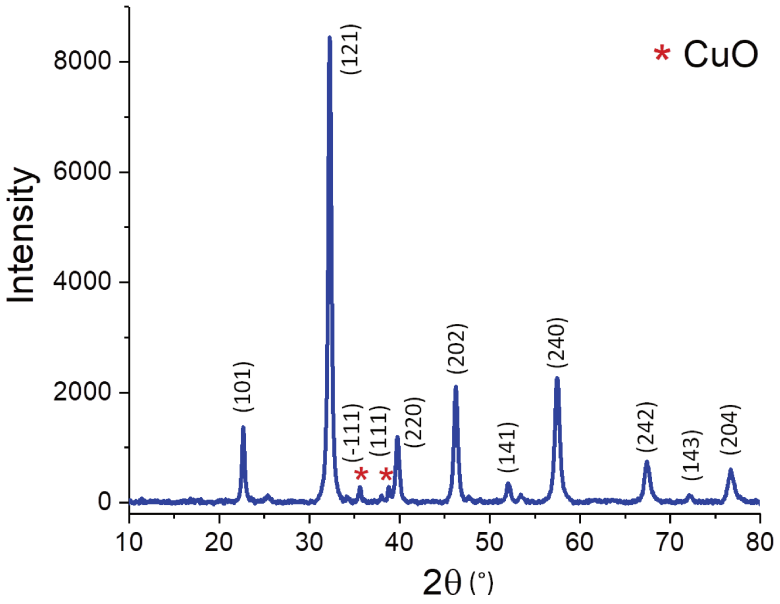

Figure 5.1: X-ray diffraction pattern of Cu-substituted perovskite powder, $La_{0.7}Fe_{0.8}Cu_{0.2}O_3$ and assignment of reflections of $LaFeO_3$ crystallised the Pbnm space group (PDF 37-1493).

531.7 eV. The C 1s signal originates from the adventitious carbon constituting 28% of the total atomic concentration. This amount and distribution of carbon contamination were also previously observed for $LaFeO_3$ powder in chapter 3. The La $3d_{5/2}$ photopeak shows a binding energy of 833.7 eV with 3.9 eV separation of the multiplet splitting component, corresponding to the La^{3+} oxidation state [4]. The Fe 2p signal at 710.2 eV displays the Fe^{3+} shake-up satellite feature at 718.8 eV [5]. The Cu $2p_{3/2}$ photopeak with the binding energy of 933.5 eV shows a broad and intense satellite feature centered at 943 eV, characteristic of the presence of Cu^{2+} ions. On comparing the Cu 2p spectrum after oxygen treatment (presented later), a lower binding energy and broader peak is revealed indicating the presence of reduced Cu^0/Cu^+ species besides majority of Cu^{2+} species, as already observed by Wu *et al.* on the same material [6].

The La/(Fe+Cu) atomic ratio is estimated to 0.68, similar to that of the theoretical bulk composition. The atomic ratio of the B-site cations, Cu/Fe, is 0.33 instead of 0.25 as per the empirical formula. This indicates an excess of copper on the surface of the Cu-substituted perovskite catalyst.

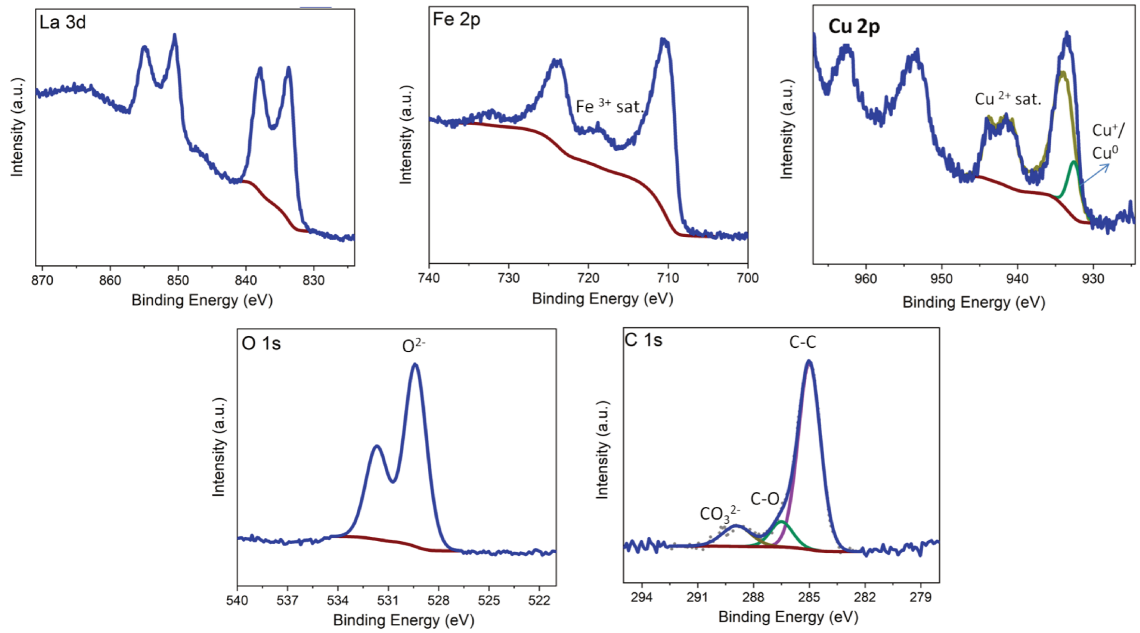

Figure 5.2: XPS La 3d, Fe 2p, Cu 2p, O 1s and C 1s spectra of Cu-substituted perovskite powder, $La_{0.7}Fe_{0.8}Cu_{0.2}O_3$.

Raman analysis

The *ex situ* Raman spectrum of $La_{0.7}Fe_{0.8}Cu_{0.2}O_3$ has been shown in Fig.5.3, together with that of the parent $La_{0.7}FeO_3$ perovksite. It is to be noted that all the Raman lines expected from lanthanum orthoferrite perovskite are present at around 180, 270, 300, 430 and 640 cm^{-1} as shown by the black line in Fig.5.3. The attribution details of each band has already been discussed in chapter 3 (section 3.3.2). Here, the doublet at 270 and 300 cm^{-1} are not well resolved and give a single broad line around 300 cm^{-1}. Additionally, the spectrum shows no clear evidence of any iron oxide phase. On simple comparison between the Raman spectra of $La_{0.7}FeO_3$ and $La_{0.7}Fe_{0.8}Cu_{0.2}O_3$ in Fig.5.3, the region around 150 and 635 cm^{-1} are more intense, the contribution around 300 cm^{-1} is broader and an additional line is noticed at 475 cm^{-1} in case of the Cu-substituted perovskite.

The Raman difference spectrum (dotted blue) obtained by subtracting the Raman spectrum of $La_{0.7}FeO_3$ from that of $La_{0.7}Fe_{0.8}Cu_{0.2}O_3$ has also been shown in Fig.5.3. This difference spectrum reveals the presence of additional Raman lines around 300-340, 475 and 635 cm^{-1}. The Raman signature of CuO is generally observed at ~290, ~340 and ~625 cm^{-1}, while that of $Cu(OH)_2$ are observed at ~292 and ~488 cm^{-1} [7, 8]. By taking into account the observations from XPS and XRD analyses regarding the presence of the segregated copper oxide species, an attribution of the Raman bands becomes possible. The

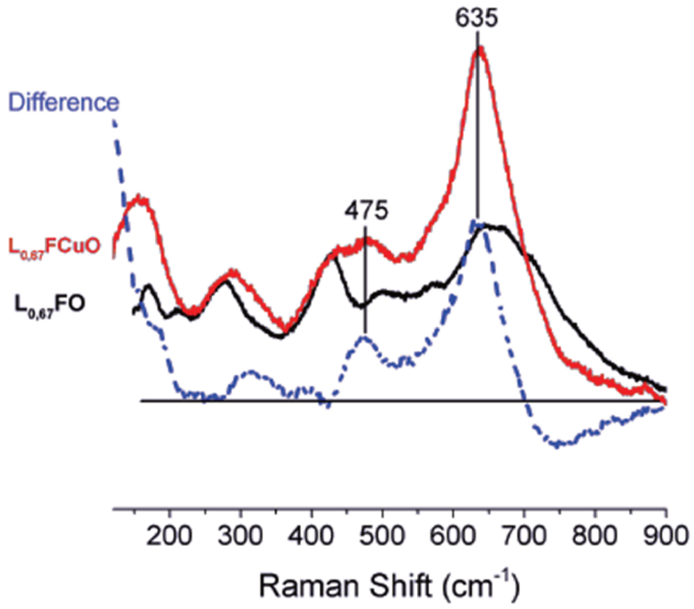

Figure 5.3: Raman spectra of $La_{0.7}Fe_{0.8}Cu_{0.2}O_3$ (red) and $La_{0.7}FeO_3$ (black) powders and their difference spectrum (dotted blue); $\lambda_{exc.}$=488 nm.

new broad feature between 300-340 cm^{-1} may originate from a summed contribution from ~290 and 340 cm^{-1} lines of the CuO phase, while the new peak at 475 cm^{-1} could be attributed to the presence of the $Cu(OH)_2$ phase. However, this line is susceptible to overlap with optical phonon modes present around 500 cm^{-1}, as previously observed by Blanck *et al.* [9]. The scattering line at 635 cm^{-1} is representative of both the perovskite and CuO phases. The attributions from the Raman spectrum alone could be quite risky owing to its complex nature possessing several spectral components, nevertheless with additional data from complementary techniques, the attribution becomes more reliable. For simplification, the characteristic Raman lines of the copper oxide with least interferences from the parent perovskite would be at ~340 cm^{-1}. It is to be noted that, owing to their low signal to noise ratio all the Raman spectra have been smoothed after baseline correction.

5.1.2 *In situ/operando* Raman analysis of $La_{0.7}Fe_{0.8}Cu_{0.2}O_3$

The $La_{0.7}Fe_{0.8}Cu_{0.2}O_3$ perovskite is investigated during heating under relevant conditions to observe its chemical behaviour. In the first step, the catalyst is exposed under an oxidative atmosphere up to 400°C to activate the surface and determine any temperature induced structural changes. Secondly, the sample was treated under the partial pressure

of water to study the effect of moisture on its structure. Thirdly, the perovskite was observed under reducing conditions using hydrogen gas followed by a re-oxidation under oxygen to obtain the initial oxidized state. Finally, the material was subjected to CO flux, where the spectral changes were recorded simultaneously while monitoring the CO conversion in *operando* mode.

In situ activation treatment under O_2/He

The $La_{0.7}Fe_{0.8}Cu_{0.2}O_3$ perovskite was heated under atmosphere of 20% O_2 in He, where a Raman spectrum was recorded at each 100°C as shown in Fig.5.4. As the $La_{0.7}Fe_{0.8}Cu_{0.2}O_3$ is heated from room temperature, the relative intensities of the lines change, for example, the component at 635 cm^{-1} decreases with increasing temperature, in agreement with the trends observed by Andreasson *et al.* on perovskites [10]. During this activation step, the structure of the stretching modes are better resolved, with visible shoulders at 592, 623 and 663 cm^{-1}, which already started to appear 200°C onward. Similarly, the intensities of the tilt modes from the perovskites at 290 cm^{-1} also decreased with temperature. Also, the relative intensity of the component at 421 cm^{-1} increases and the one at 480 cm^{-1} decreases as the heating progresses, as previously observed [9]. Although, the intensity of the line at 480 cm^{-1} is indicative of copper hydroxide at room temperature, it is difficult to follow it during heating due to the above-mentioned interferences. In addition, the hydroxide will begin to decompose above 200°C. A contribution from CuO only becomes clearly visible at around 340 cm^{-1} at 300°C. As the temperature reaches 400°C, it is not possible to clearly detect any Cu species and the spectrum resembles that of the parent perovskite at high temperature [9]. Most spectral changes occurring while heating the perovskite are temperature-induced being reversible in nature. This is verified by the return spectrum at 100°C, recorded after the activation step, which is quite similar to the one recorded at the same temperature at the beginning of the treatment.

In situ treatment under partial pressure of water

The $La_{0.7}Fe_{0.8}Cu_{0.2}O_3$ perovskite was subjected to partial pressure of water (~940 Pa) and heated up to 400°C as shown in Fig.5.5. The Raman spectrum at 100°C presents the lines for CuO besides the perovskite fingerprint. As the temperature reaches 200°C, the intensity of the Raman line remains intense at 490 cm^{-1} indicating the likely presence of $Cu(OH)_2$, enhanced in the presence of moisture. Above 300°C, the intensity at 490 cm^{-1}

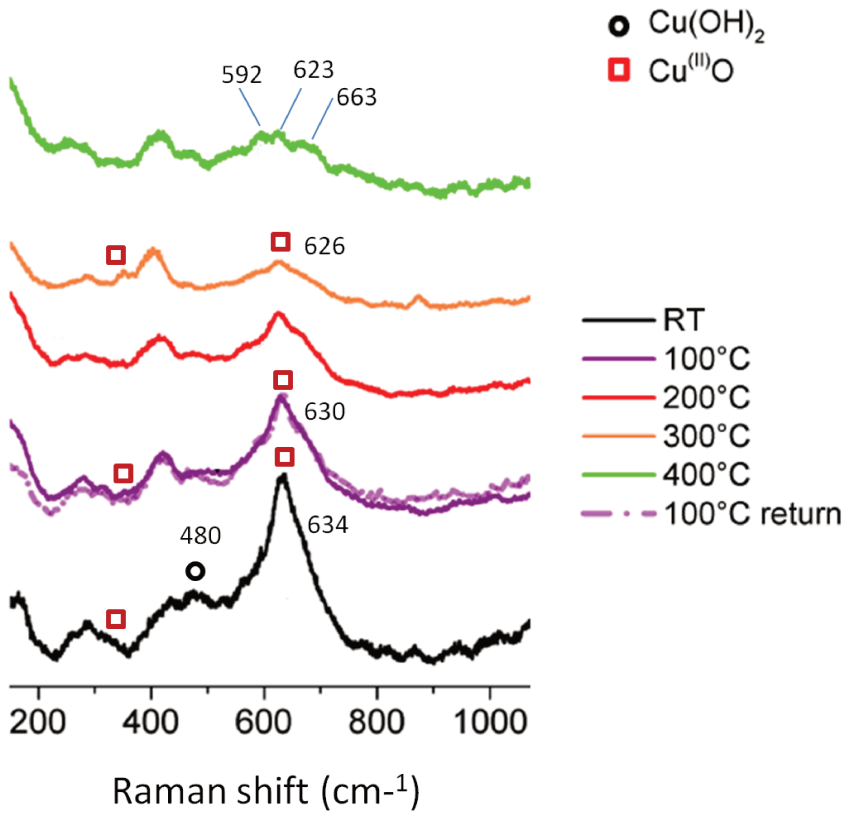

Figure 5.4: *In situ* Raman spectra of $La_{0.7}Fe_{0.8}Cu_{0.2}O_3$ during activation treatment under 20% O_2/He.

decreases and a weak line at 350 cm^{-1} becomes visible. Basically, at 300 and 400°C, the spectra is very similar to the one obtained under O_2/He under the same temperature. Finally, the return spectrum is once again similar to 100°C spectrum at the beginning. Only copper(II) oxide and the substituted perovskite $La_{0.7}Fe_{0.8}Cu_{0.2}O_3$ will likely participate in a reaction over 200°C. No evidence of hematite phase expected at 212 cm^{-1} is evidenced under the presence of moisture, unlike $La_{0.7}FeO_3$, which showed an intense formation of new peaks of hematite (α-Fe_2O_3) under similar conditions [9].

In situ reduction under hydrogen

The Raman spectra under hydrogen with increasing temperature have been shown in Fig.5.6. The spectra at 100 and 200°C do not undergo any changes as compared to the features observed under O_2 and during hydration treatment previously. Even at higher temperature the Raman spectra is quite similar to the preceding steps with no evident changes, irrespective of the reducing atmosphere. Only the stretching mode ~650 cm^{-1} undergoes less distortion in contrast to the oxidative environment. However, any reduc-

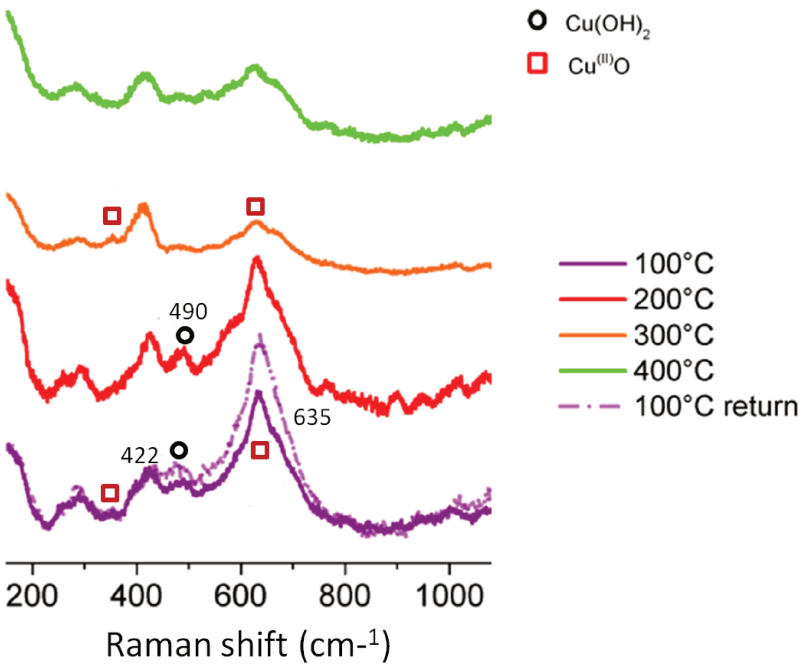

Figure 5.5: *In situ* Raman spectra of $La_{0.7}Fe_{0.8}Cu_{0.2}O_3$ during heating under hydrating atmosphere.

tion related changes are not obvious. Exposure of the sample under full hydrogen flow for longer duration (dotted green line) lead to the loss of spectral definition.

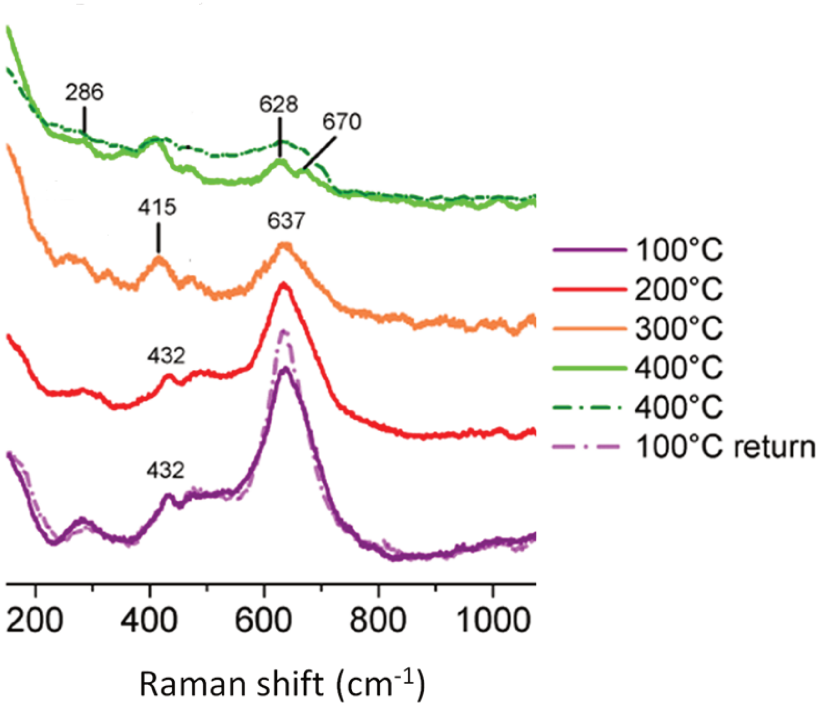

Figure 5.6: *In situ* Raman spectra of $La_{0.7}Fe_{0.8}Cu_{0.2}O_3$ under 20% H_2 in He; dotted green line represents exposure to full H_2 flow.

CuO particles are known to reduce to metallic copper under hydrogen below 400°C [11]. Due to the complexity of the spectra at higher temperature, the $La_{0.7}Fe_{0.8}Cu_{0.2}O_3$ perovskite will be also studied under reducing environment by quasi-*in situ* XPS to investigate the chemical environment in section 5.1.3.

Re-oxidation under O_2 in He

The $La_{0.7}Fe_{0.8}Cu_{0.2}O_3$ perovskite catalyst was re-exposed under O_2/He until 400°C to regain the initial state of the material by oxidizing any reduced species. The Raman spectra obtained from this treatment is identical to the ones during the activation step in section 5.2.1.

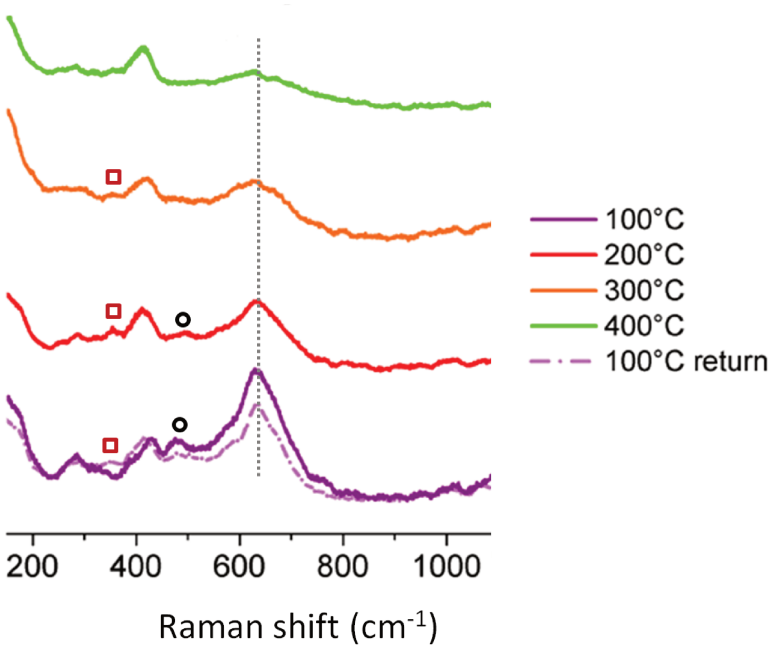

Figure 5.7: *In situ* Raman spectra of $La_{0.7}Fe_{0.8}Cu_{0.2}O_3$ during re-oxidation treatment under 20% O_2/He.

Temperature-programmed reaction under CO in He

The Raman spectra recorded under a flow of CO have been shown in Fig.5.8 in high and low resolutions using gratings of 1800 and 600 grooves, respectively. The spectra were additionally analyzed with the 600 grating to include the higher frequency region with the same experimental time frame. As the sample is heated, the relative intensities of the lines at 488 and 290 cm^{-1} decrease and they become broader. The spectrum under CO at 400°C is similar to the Raman fingerprint of $LaFeO_3$. No Raman signature of copper(I)

oxide is evidenced during the CO exposure and the $LaFeO_3$-related lines remained consistent under the reducing environment. In Fig.5.8(b), as the temperature rises the intensity of the lines at ~1300 and ~1600 cm^{-1} keeps increasing. These are attributed to the poly-aromatic hydrocarbons (PAHs), which cover the catalysts surface as the CO reacts with the surface [12]. The intensity of the line at ~1600 cm^{-1} continues to increase up to the second spectrum at 400°C (400-2, orange) and then starts to decrease as they get thermally decomposed after prolonged exposure at this temperature. In general, adsorbed surface oxygen species or the α-O help to drive the CO oxidation reaction especially at lower temperatures while bulk oxygen are involved at very high temperature above 600°C [1].

As evident from the series of the above spectra of $La_{0.7}Fe_{0.8}Cu_{0.2}O_3$, Cu species although present are quite difficult to be clearly detected at different experimental steps by Raman analysis due to the inherent spectral quality. Thereby, yielding concrete information regarding the Cu species becomes quite difficult owing to the complex nature of these spectra and is mainly used as a means to study temperature related changes and for comparison with other compositions.

The corresponding online CO to CO_2 conversion acquired during this experiment has been shown in Fig.5.9. Here, the conversion sharply increases at each temperature ramp as Cu^{2+} species are expected to reduce to Cu^{+}/Cu^{0}. Besides some Fe^{2+} species may also take part, although not evidenced here. However, the conversion falls as no regenerative process can occur to restore the active oxygen species that assists the CO oxidation reaction with only CO in the gas feed. As the temperature increases in the next temperature ramp, higher mobility of oxygen is favored and some surface O-species are formed again thereby increasing the activity. The conversion reaches close to the maximum already above 200°C as the Cu-species are expected to reduce around this temperature [6]. The maximum conversion is maintained around 5% achieved after each temperature ramp.

The Raman spectra during the applied redox cycles mainly highlighted the signature of stoichiometric $LaFeO_3$ without significant alteration of the frequency of the Γ-point modes of $LaFeO_3$. The most prominent changes came to be induced by temperature and are mostly reversible by nature. As far as Cu-related species are concerned, CuO (and $Cu(OH)_2$), although possibly observed under specific conditions (*ie.* upon hydration and at room temperature), their Raman signature could not be attested at higher temperature, owing to the loss of intensity from thermal effects, low amount of Cu-species and/or

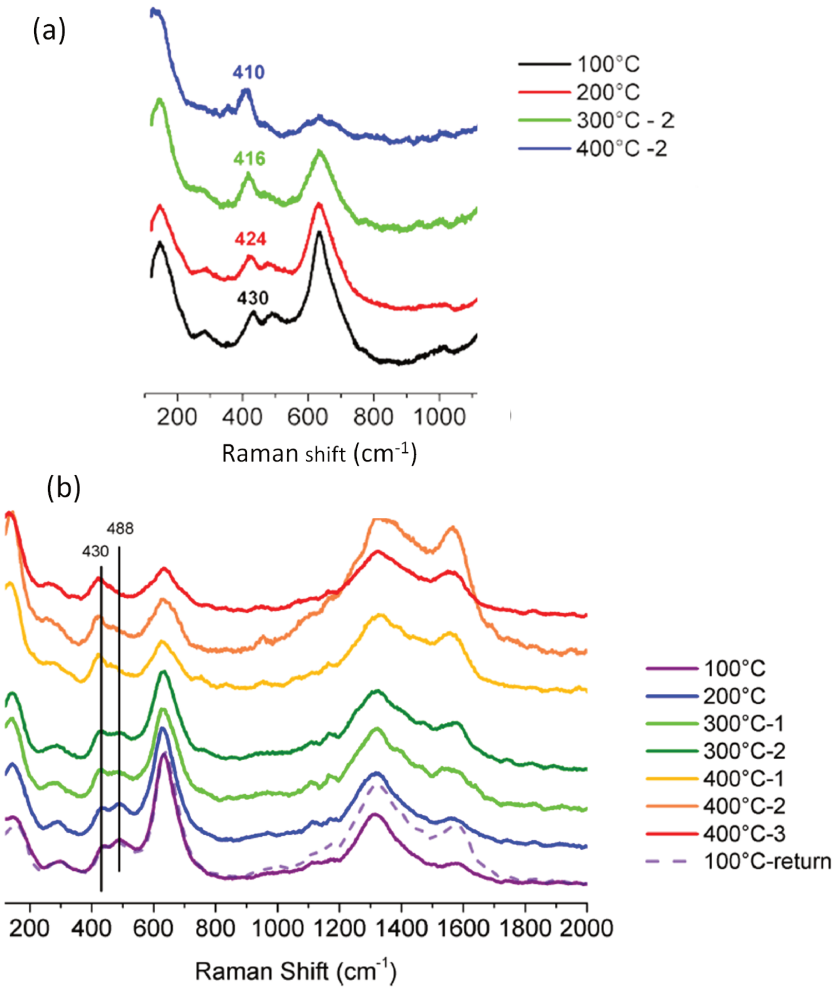

Figure 5.8: *In situ* Raman analysis of $La_{0.7}Fe_{0.8}Cu_{0.2}O_3$ under 5% CO/He: (a) 1800 grooves grating and (b) 600 grooves grating.

possible spectral overlapping of different components. Interestingly, these observations indicate that in $La_{0.7}Fe_{0.8}Cu_{0.2}O_3$, on substitution by copper, the $LaFeO_3$ fingerprint do not undergo drastic changes.

5.1.3 Quasi-*In situ* XPS analysis of $La_{0.7}Fe_{0.8}Cu_{0.2}O_3$

The $La_{0.7}Fe_{0.8}Cu_{0.2}O_3$ perovskite was treated under oxygen as the activation step in the treatment cell coupled to the XPS analysis chamber. Similarly, this was followed by exposure to CO. The material surface was then subjected to an oxidant like NO to investigate the reactivity of the perovskite surface. The La 3d, Fe 2p and Cu 2p photopeaks after each treatment step have been shown in Fig.5.10.

Catalyst activation under 20% O_2/He: The $La_{0.7}Fe_{0.8}Cu_{0.2}O_3$ perovskite was heated

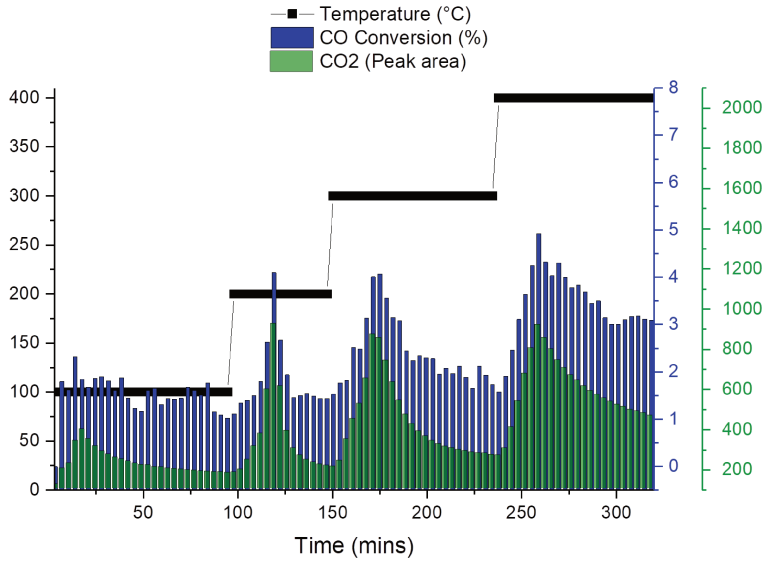

Figure 5.9: CO conversion to CO_2 during *in situ* Raman analysis of $La_{0.7}Fe_{0.8}Cu_{0.2}O_3$ under 5% CO/He.

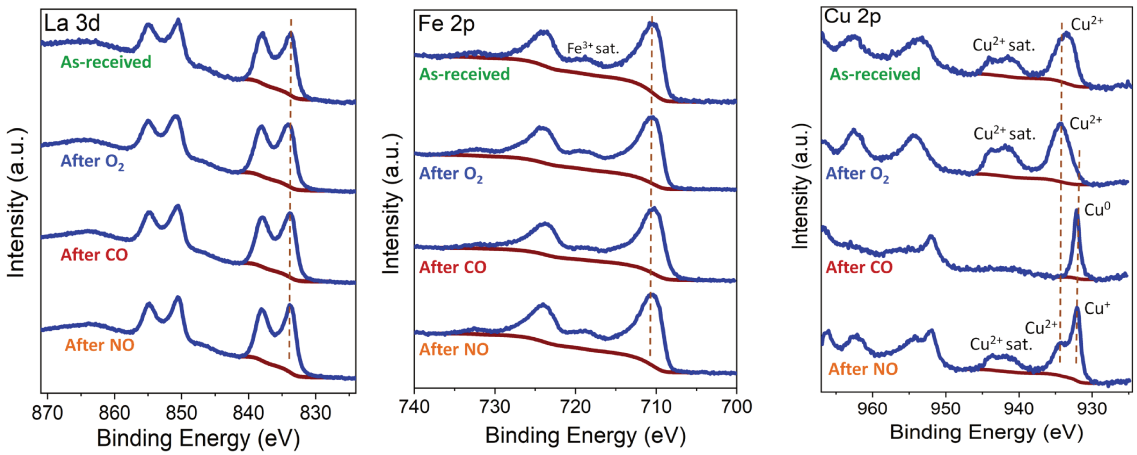

Figure 5.10: Quasi-*In situ* XPS spectra of $La_{0.7}Fe_{0.8}Cu_{0.2}O_3$ powder under 20% O_2/N_2, 5% CO/He and 2% NO/He.

under oxidative conditions at 500°C for 1 hour, and the La 3d, Fe 2p and the Cu 2p photopeaks have been shown in Fig.5.10. The binding energy of La 3d is 833.9 eV while that of the Fe 2p is 710.4 eV, similar to the as-received state, both remaining in +3 valence states. In case of the Cu 2p, the binding energy is shifted to 934.2 eV still retaining an intense satellite feature. This satellite structure indicates the presence of Cu^{2+} species. The La/(Fe+Cu) and Cu/Fe atomic ratios remain unchanged at 0.64 and 0.34, respectively.

Catalyst reduction under 5% CO in He: The perovskite was then subjected to CO flux at 500°C, the XPS spectra after this treatment step were shown in Fig.5.10. No change

in the Fe 2p was evident after CO treatment. The binding energy, intensity of the Fe^{3+} satellite as well as the FWHM values remained similar after the CO exposure. In contrast, copper undergoes drastic changes under CO. The Cu 2p spectrum shows a complete disappearance of the Cu^{2+} satellite feature besides a shift of the binding energy value to 932.1 eV possessing quite a narrow peak width. Such a narrow peak at lower binding energy is indicative of reduced copper species such as Cu^0 or Cu^+. Since the binding energy for both are experimentally expected at the same value, the modified Auger parameter (α) is used for the assignment of the Cu-species. This can be evaluated from the binding energy values and calculating the modified Auger parameter (α), which is defined by

$$\alpha = E_{k(\mathrm{LMM})} + E_{b(Cu)} \tag{5.1}$$

where, $E_{k(\mathrm{LMM})}$ is the kinetic energy of the LMM Auger peak of copper and $E_{b(Cu)}$ is the binding energy of the Cu $2p_{3/2}$ orbital [13]. The α is estimated to be 1851.2 eV, corresponding to the metallic copper (Cu^0) state. This reduction of copper is in line with literature, where CuO is shown to be completely reduced to metallic copper at around 400°C according to H_2-TPR studies. After CO exposure, La/(Fe+Cu) and Cu/Fe atomic ratios change remarkably to 1.14 and 0.11, respectively. This can be explained by the reduction of the CuO particles to the metallic state accompanied by change in dispersion of the metallic species on surface and/or their diffusion into the bulk such that the amount of copper in the extreme surface becomes limited.

Catalyst re-oxidation under 2% NO in He: Finally, the partially reduced $La_{0.7}Fe_{0.8}Cu_{0.2}O_3$ was subjected to a flow of NO gas. Under this oxidizing atmosphere, the Cu 2p signal evolves as the Cu^{2+} satellite appears again along with a clear shoulder of the Cu $2p_{3/2}$ at 933.9 eV. At this point the copper is present in 2 oxidation states, evident from the presence of the additional peak at 932.1 eV. The α was calculated to be 1848.8 eV. This value is close to the one expected from Cu^+. Thereby, the Cu^0 formed under CO step have re-oxidized to a mixture of CuO and Cu_2O after re-oxidation under NO. The La/(Fe+Cu) and Cu/Fe atomic ratios were further changed to 0.82 and 0.17, respectively, as the metallic copper transforms to the oxidized phases. These observations highlight that the important redox behavior in $La_{0.7}Fe_{0.8}Cu_{0.2}O_3$ is mainly enhanced by the presence of the segregated copper oxide phases that seems to play a major role in CO or NO reaction for TWCs

application.

5.2 B-site substituted $LaFeO_3$ by Mn ($La_{0.7}Fe_{0.8}Mn_{0.2}O_3$)

5.2.1 Physicochemical characterization of $La_{0.7}Fe_{0.8}Mn_{0.2}O_3$

XRD analysis

The diffraction pattern of $La_{0.7}Fe_{0.8}Mn_{0.2}O_3$ powder has been shown in Fig. 5.11. It displays intense diffraction peaks at 32.2°, 40.0°, 46.1° and 57.4° corresponding to the reflection planes (121), (220), (202) and (240), respectively, characteristic of the orthorhombic phase. The lattice constants are a=5.547Å, b=7.815Å and c=5.536Å with pnma space group (JCPDS PDF 37-1493). No other reflections arising from additional phases such as Fe_2O_3, La_2O_3 or Mn_2O_3 were observed.

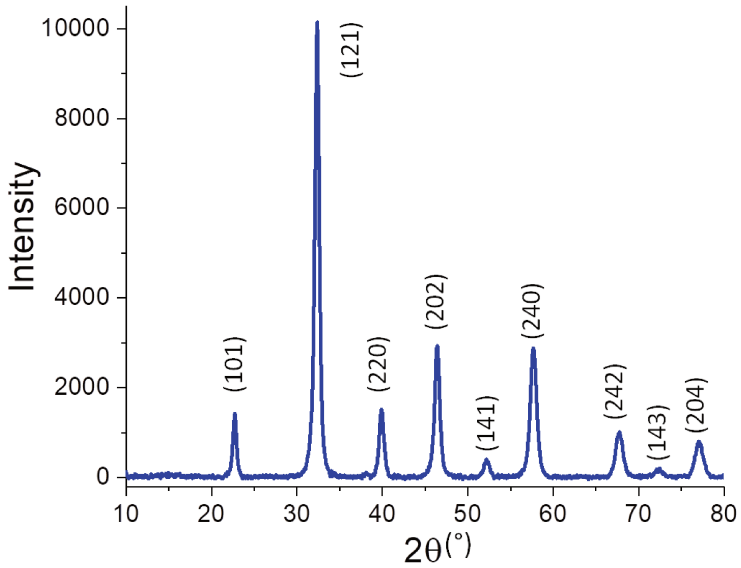

Figure 5.11: X-ray diffraction pattern of Mn-substituted perovskite powder, $La_{0.7}Fe_{0.8}Mn_{0.2}O_3$ (PDF 37-1493).

XPS analysis

The XPS spectra of $La_{0.7}Fe_{0.8}Mn_{0.2}O_3$ perovskite, namely, La 3d, Fe 2p, Mn 2p, C 1s and O 1s photopeaks, are presented in Fig. 5.12. The O 1s signal at 529.6 eV is attributed to the lattice oxygen of metal oxides, while the one at 531.7 eV arises from the surface adsorbate species and defects in oxides [4, 14]. The C 1s photopeak presents well known characteristics of adventitious carbon, contributing to 27% of the atomic concentration. The La

3d peak is located at 833.9 eV with a multiplet splitting component separated by 4.1 eV signifying the presence of La^{3+}, as was observed for the $LaFeO_3$ perovskites in previous chapters. The Fe 2p signal is present at a binding energy of 710.4 eV with the characteristic Fe^{3+} satellite feature at 719 eV. The Mn 2p photopeak at a binding energy of 641.8 eV is characteristic of oxidized Mn. The determination of the oxidation state using Mn 2p orbital alone is not straightforward. One possibility is the use of Mn 3s splitting level from which an average oxidation state (AOS) of Mn can be estimated [15]. Due to low amount of surface Mn species, it was preferred to decompose the Mn 2p spectrum spectrum with the multiplet splitting parameters given by Biesinger et al to determine the oxidation state of Mn ion [5]. According to these authors, reference spectra of manganese oxides such as MnO_2, Mn_2O_3 and MnO representing the 4+, 3+ and 2+ valence states respectively, is fitted with 5 to 6 components each with constant FWHM values, binding energy differences and component distribution with respect to each other. The decomposition of the Mn 2p photopeak has been shown in Fig. 5.12 exhibiting predominantly Mn^{3+}. Thereby, the as-received $La_{0.7}Fe_{0.8}Mn_{0.2}O_3$ perovskite contains both the B-site ions in +3 oxidation state. The La/(Fe+Mn) atomic ratio is equal to 0.76, close to the bulk composition of $La_{0.7}Fe_{0.8}Mn_{0.2}O_3$. The B-site ionic ratio, Mn/Fe, is 0.26, close to that of the empirical formula. The surface and bulk compositions are often varying in bulk catalysts like perovskites, however in this case, the XPS atomic ratios are well representative of the bulk composition.

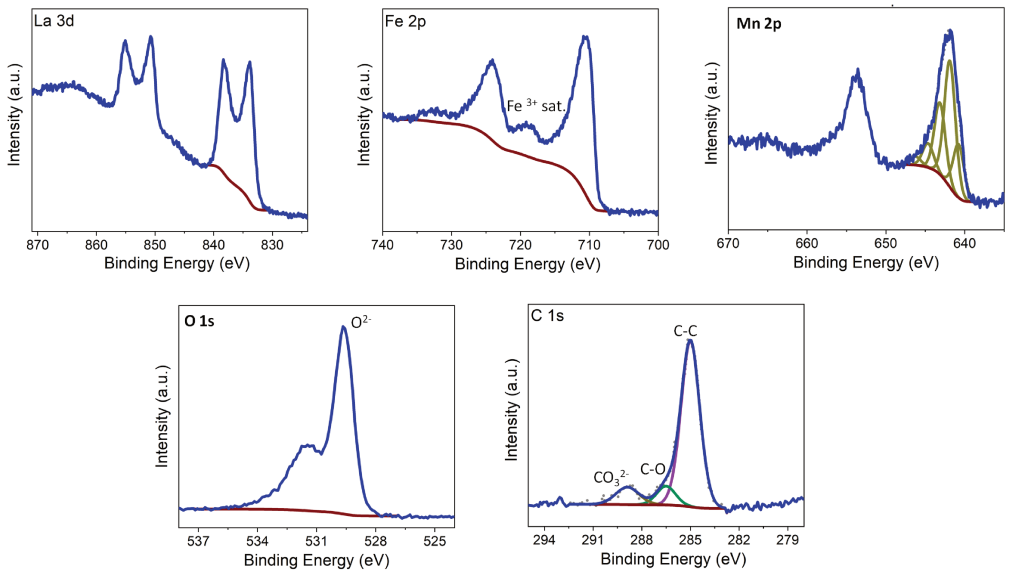

Figure 5.12: XPS La 3d, Fe 2p, Mn 2p, C 1s and O 1s spectra of Mn-substituted perovskite powder, $La_{0.7}Fe_{0.8}Mn_{0.2}O_3$.

Raman analysis

The Raman spectrum of $La_{0.7}Fe_{0.8}Mn_{0.2}O_3$ has been shown in Fig. 5.13. On the first look, the Raman spectrum appears completely different from the parent perovskite structure of $LaFeO_3$. It shows two intense lines at 506 and 657 cm^{-1} with a weak band at around 300 cm^{-1}, corresponding to the O-bending, O-stretching and MnO_6 rotation modes, respectively [16]. Such a spectral fingerprint corresponds to $LaMnO_3$-like perovskite structure. This means that even a small amount of substitution of Mn within the perovskite structure leads to a complete change in the Raman spectrum [17]. The same tendency was also shown by Mn-substitution at a lower extent such as La-deficient $La_{0.7}Fe_{0.9}Mn_{0.1}O_3$ as presented in Fig.5.14. In fact, $LaFe_{0.9}Mn_{0.1}O_3$ and $LaFe_{0.8}Mn_{0.2}O_3$ with a stoichiometric composition also show identical spectral features. The perovskite with higher amount of Mn at B-site show slight shift of 650 cm^{-1} band towards higher wavenumbers (blue shift) without any effect of the La-content. This kind of shift was also observed by Sultan et al on $PrFe_{1-x}Mn_xO$-based perovskites caused by an increased compressive stress in the parent perovskite structure as the Mn-content increases [18].

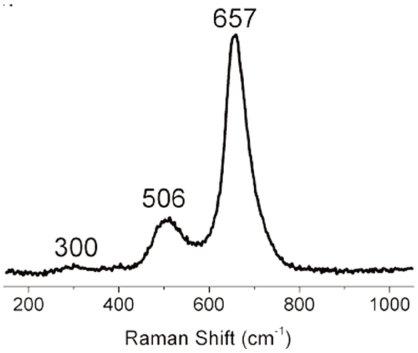

Figure 5.13: Raman spectrum of Mn-substituted perovskite powder, $La_{0.7}Fe_{0.8}Mn_{0.2}O_3$ ($\lambda_{exc.}$=488 nm).

Mn^{3+} is a Jahn Teller active ion, the presence of which can cause structural distortion within the perovskite lattice. According to the Jahn Teller (JT) theorem, if any non-linear molecule is in an electronically degenerate state, it attempts to lower the symmetry and energy to remove the existing degeneracy by undergoing structural distortions by for example, change of the Mn-O distance in the MnO_6 octahedra within the perovskite. Hence, besides the already distorted structure of a perovskite by octahedral tilting as is the case in $LaFeO_3$ (tolerance factor $\neq 1$), the perovskite can undergo further distortions caused by the Jahn-Teller effect of the B-site cation, such as the Mn^{3+} here. The electronic configura-

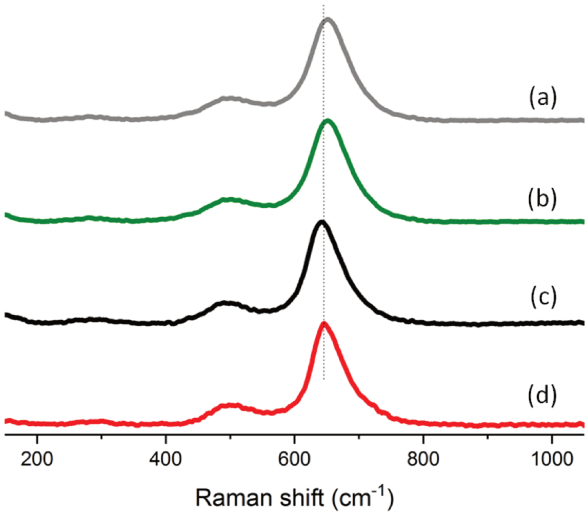

Figure 5.14: Raman spectra of (a) $La_{0.7}Fe_{0.8}Mn_{0.2}O_3$, (b) $LaFe_{0.8}M_{0.2}O_3$, (c) $LaFe_{0.9}Mn_{0.1}O_3$ and (d) $La_{0.7}Fe_{0.9}Mn_{0.1}O_3$ ($\lambda_{exc.}$=488 nm).

tion of Mn^{3+} and Fe^{3+} are given in Fig.5.15 in high spin state [19]. The JT effect causes the Raman fingerprint to change completely from that of the $LaFeO_3$ to the one of $LaMnO_3$ like perovskite. The orthorhombic $La_{0.7}Fe_{0.8}Mn_{0.2}O_3$ shows only 3 lines at room temperature at 300, 506 and 657 cm^{-1}. More Raman bands of lower frequency range exist and are observed at much lower temperatures or at fixed scattering configurations around 140, 170, 198, 257, 284 and 308 cm−1 with very low intensities, completely hidden in the noise under the current configuration [16, 20, 21]. In general, manganite based perovskites are sensitive to temperature or laser power of the Raman source resulting in broader peaks and increased shift in line position with temperature (red shift). The two most intense bands at 506 and 657 cm^{-1} correspond to the A_g and B_{2g} modes representing the bending and stretching vibrations of MnO_6 octhedra. In the orthorhombic manganite, JT distortions are static and coherent, or in other words, they are compatible with the perovskite structure leading to a strong enhancement of some Raman signals.

It is likely that the Raman spectrum of $La_{0.7}Fe_{0.8}Mn_{0.2}O_3$ is the sum of the contribution from $LaFeO_3$-like and $LaMnO_3$-like spectra. However, due to the much higher Raman cross-section of the manganite perovskite, only its fingerprint is predominantly visible.

5.2.2 *In situ/operando* Raman analysis of $La_{0.7}Fe_{0.8}Mn_{0.2}O_3$

In this section, the $La_{0.7}Fe_{0.8}Mn_{0.2}O_3$ powder was also subjected under relevant reaction conditions to observe its behavior during model reaction steps.

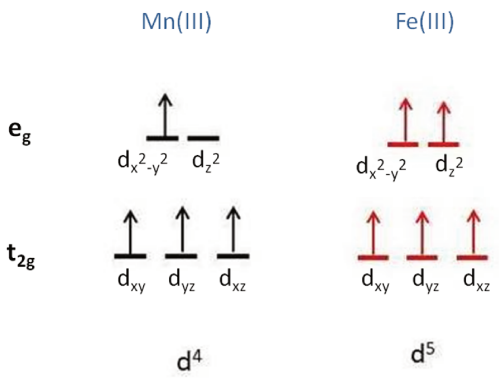

Figure 5.15: Electronic configuration diagram of Mn(III) and Fe(III) in high spin state.

Thermal treatment under He

The Raman spectra of $La_{0.7}Fe_{0.8}Mn_{0.2}O_3$ perovskite during heating under He in inert atmosphere is shown in Fig.5.16. The spectra do not show any significant temperature-induced changes. The Raman line positions and the shapes remain intact, only small decrease in the intensity of the band at 650 cm^{-1} with temperature is observed, similar to the $La_{0.7}Fe_{0.8}Cu_{0.2}O_3$ in the previous section. On reducing the temperature back to 100°C, i.e. the return spectrum remains identical to the one during the initial run at 100°C indicating that the relative changes in the line intensities are fully reversible and are caused only due to thermal effect as the lattice expands with temperature.

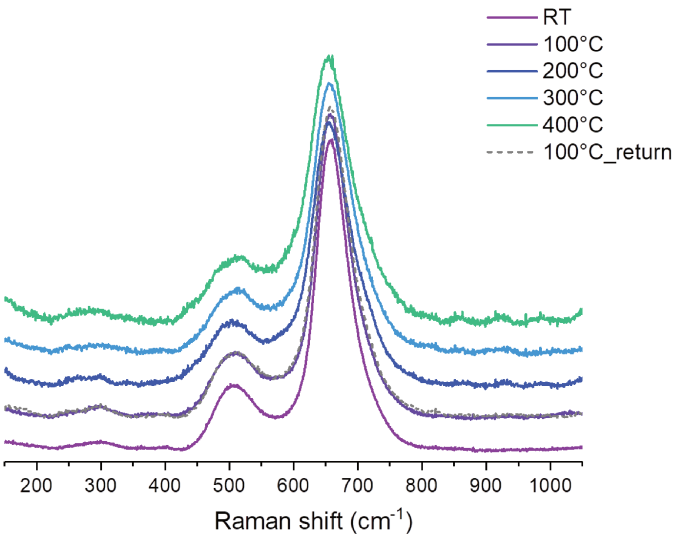

Figure 5.16: *In situ* Raman spectra of $La_{0.7}Fe_{0.8}Mn_{0.2}O_3$ during thermal treatment under He.

Thermal treatment under partial pressure of water

The mixed oxide was then heated in presence of vapour pressure of water (~940 Pa) up to 300°C, presented in Fig. 5.17. As it was previously shown by our research group, the presence of moisture (and O_2) allows to evidence the presence of segregated hematite phase on La-deficient $La_{0.7}FeO_3$. However, similar to the previous step, no change in the Raman spectra was evident in case of $La_{0.7}Fe_{0.8}Mn_{0.2}O_3$ [9]. Here the Raman bands of hematite usually located at 212, 276 and 412 cm^{-1} could be hidden in the noise and difficult to be seen due the relatively high Raman cross-section of manganite-based perovskites.

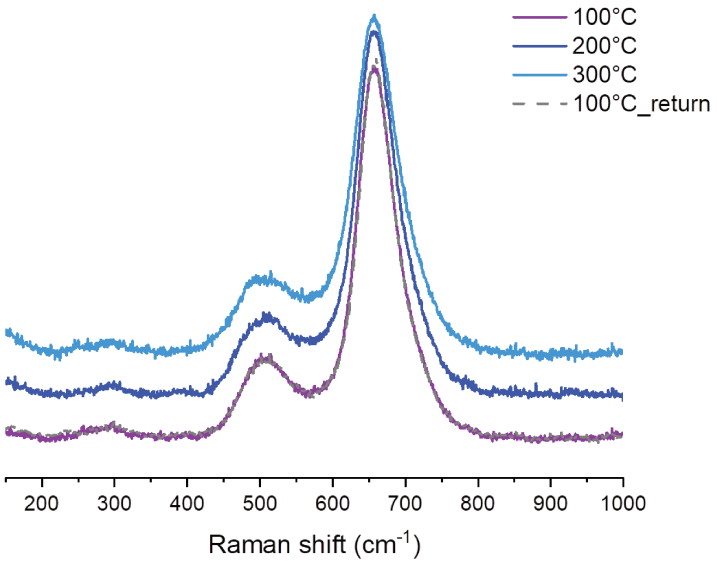

Figure 5.17: *In situ* Raman spectra of $La_{0.7}Fe_{0.8}Mn_{0.2}O_3$ under partial pressure of water (~940 Pa).

In situ treatment under hydrogen

The Raman spectra during hydrogen treatment of $La_{0.7}Fe_{0.8}Mn_{0.2}O_3$ have been shown in Fig.5.18. The spectrum evolves above 300°C with formation of new lines at 260, 295 and 425 cm^{-1} with an increasing contribution at 150 cm^{-1}. Also, the band at 650 cm^{-1} shifts to 644 cm^{-1} with an asymmetric shape. These lines correspond to the appearance of Raman fingerprint of $LaFeO_3$ perovskite. Under hydrogen, the existing JT active Mn^{3+} species reduces to JT inactive Mn^{2+}. As this reduction process occurs, the initial spectrum of $La_{0.7}Fe_{0.8}Mn_{0.2}O_3$ caused by the JT distortions now disappears and the Raman fingerprint of $LaFeO_3$, which is the parent structure begins to become visible. The return spectrum at 100°C also indicates some significant variations compared to the starting point at 100°C, especially near the region of 150, 420 and 650 cm^{-1} with less intense $LaFeO_3$

lines. The appearance of the Raman bands is confirmed by peak decomposition as shown in Fig.5.19. At 100°C, the $La_{0.7}Fe_{0.8}Mn_{0.2}O_3$ spectrum is decomposed with 3 peaks at 290, 505 and 650 cm^{-1} (manganite perovskite), while at 450°C new lines at 260, 295 and 425 cm^{-1} ($LaFeO_3$) can be fitted to represent the experimental spectrum [9, 20]. As the temperature is reduced back to 100°C under hydrogen (Fig.5.18), these *in situ* generated spectral features decrease but do not completely disappear indicating the presence of some residual JT inactive Mn^{2+} species. These observations under reducing atmosphere highlight the direct experimental evidence of the JT effect occurring in this $La_{0.7}Fe_{0.8}Mn_{0.2}O_3$ perovskite-based catalyst.

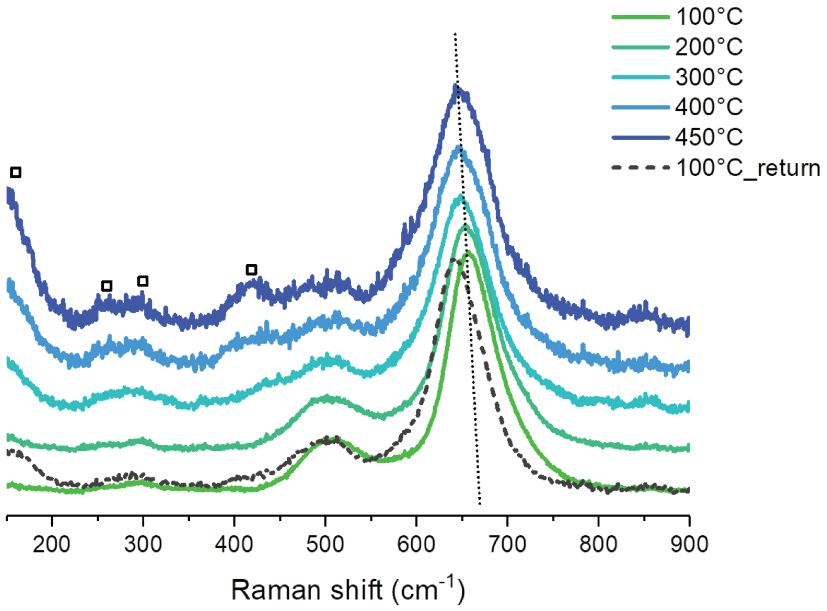

Figure 5.18: *In situ* Raman spectra of $La_{0.7}Fe_{0.8}Mn_{0.2}O_3$ under H_2.

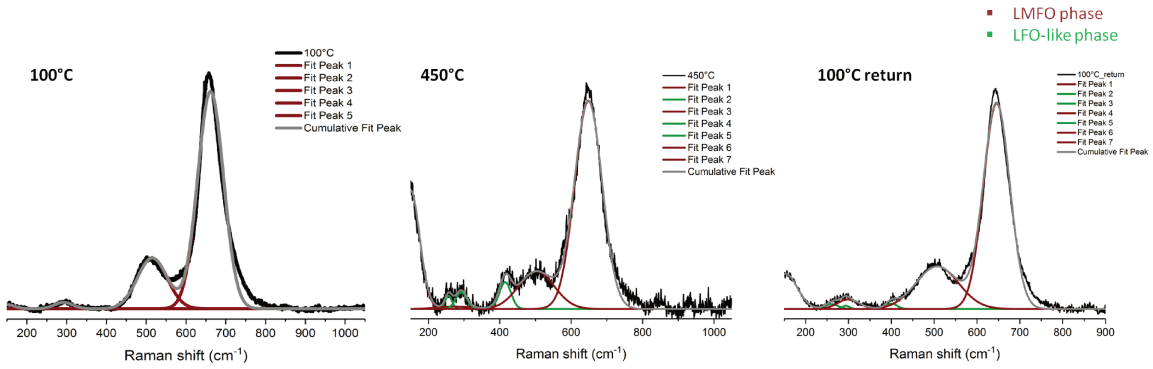

Figure 5.19: Spectral decomposition of *in situ* Raman spectra of $La_{0.7}Fe_{0.8}Mn_{0.2}O_3$ under H_2 at 100°C, 450°C and return at 100°C (left to right) using $La_{0.7}Fe_{0.8}Mn_{0.2}O_3$ (LFMO) and $LaFeO_3$ (LFO) contributions.

In situ treatment under 20% O_2/He

After the reduction step under hydrogen, the material was kept under helium overnight before exposing it under oxygen to restore its initial oxidized state. The perovskite surface already regenerates to its initial state at 100°C under oxygen with re-appearance of the Raman fingerprint of the manganite-based perovskite phase as shown in Fig.5.20. This could be supported by the low activation energy of oxygen diffusion that can readily occur to at least partially oxidize the reduced Mn species into Mn^{3+} [22]. No changes in the spectra are observed as the sample is heated up to 400°C and finally cooled down to 100°C.

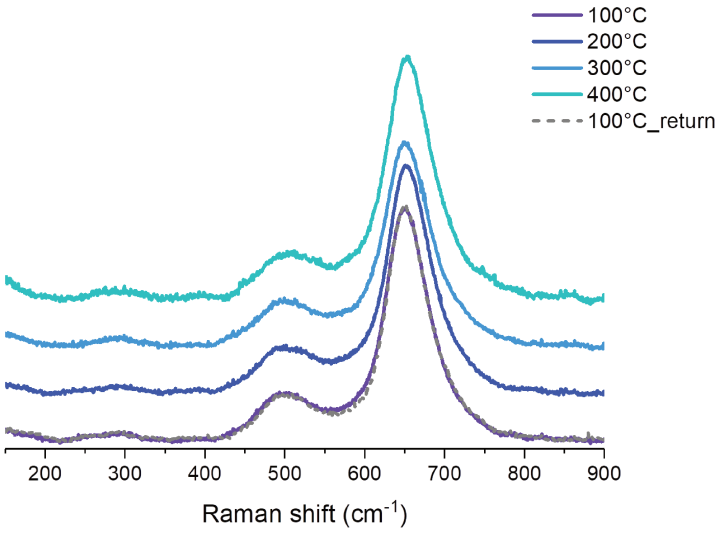

Figure 5.20: *In situ* Raman spectra of $La_{0.7}Fe_{0.8}Mn_{0.2}O_3$ during treatment under 20% O_2/He.

Temperature-programmed reaction under CO in He

The evolution of the Raman spectra during heating under CO has been shown in Fig. 5.21. The spectra undergo no change below 300°C, beyond that new lines are formed at 260, 290 and 430 cm^{-1} besides the bands at 650 and 500 cm^{-1} already present. Similar changes have also been observed at around the same temperature under hydrogen in the previous step. The new lines correspond to the Raman fingerprint of $LaFeO_3$ structure, which is formed as the Mn species in $La_{0.7}Fe_{0.8}Mn_{0.2}O_3$ transform from 3+ to 2+ state and the JT effect inherent in the structure is diminished [23, 24]. As the Mn^{2+} is formed, JT distortions are reduced such that the structure takes the form of $LaFeO_3$. This observation is demonstrating the occurrence of such JT distortions in the perovskite structure exper-

imentally during CO oxidation reaction. CO exposure causes the reduction of the B-site ions of the perovskite with structural changes. This means the catalytic performance in any manganite-based perovskite is not only driven by the B-site ion itself but also by the structural changes it can cause. In addition, new lines appeared at about 1300 and 1600 cm^{-1} after exposure to CO above 300°C. The occurrence of these two lines is attributed to surface covering poly-cyclic aromatic hydrocarbon (PAHs) species [12]. The PAHs deposits have been observed to form only in case of the La-deficient perovskite ($La_{0.7}FeO_3$) as is the case here and not in case of the stoichiometric one ($LaFeO_3$) under similar conditions according to Blanck *et al* [9].

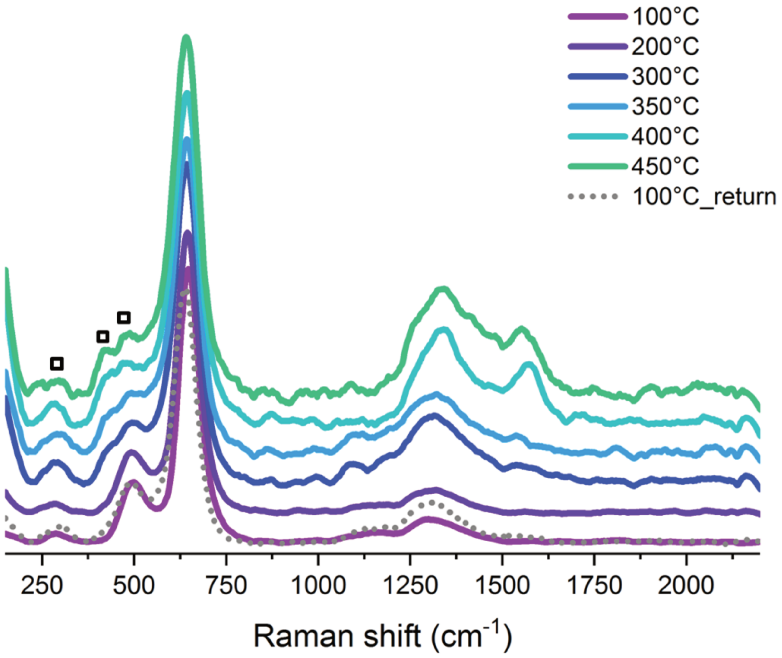

Figure 5.21: *In situ* Raman spectra of $La_{0.7}Fe_{0.8}Mn_{0.2}O_3$ under 5% CO/He.

The corresponding conversion of CO to CO_2 during the CO oxidation reaction has been presented in Fig. 5.22. Here, similar to the Cu-substituted perovskite, the conversion sharply increases at each temperature ramp as more Mn^{3+} reduces to Mn^{2+} and oxygen vacancies are created in order to maintain the electrical neutrality. However, the conversion falls sharply as no regenerative process can occur to restore the active oxygen species that can assist the CO oxidation. The best conversion (8%) is achieved at 350°C, where the reduction of Mn^{3+} begins to occur and the perovskite takes the structure similar to $LaFeO_3$. The presence of more reducible Mn^{3+} species besides Fe^{3+} in the perovskite helps in enhancing the catalytic activity by helping to generate more O-vacancies that eventually help to improve the oxygen mobility and availability of surface oxygen species

for CO reaction.

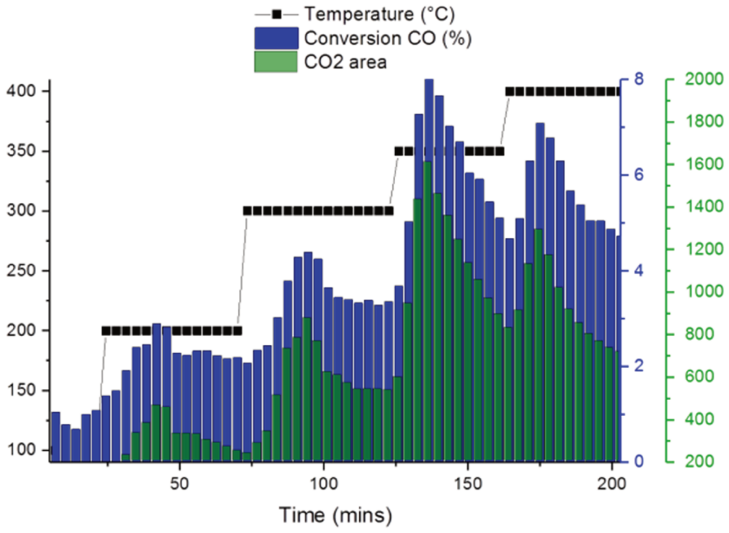

Figure 5.22: CO conversion to CO_2 during *in situ* Raman analysis of $La_{0.7}Fe_{0.8}Mn_{0.2}O_3$ under 5% CO/He.

5.2.3 Quasi-*in situ* XPS analysis of $La_{0.7}Fe_{0.8}Mn_{0.2}O_3$

The $La_{0.7}Fe_{0.8}Mn_{0.2}O_3$ was subjected to oxygen, CO and NO successively in the treatment cell and transferred to the XPS analysis chamber under UHV without exposure to air. The quasi-*in situ* La 3d, Fe 2p and Mn 2p photopeaks after each treatment have been shown in Fig. 5.23.

Catalyst activation under oxygen: The $La_{0.7}Fe_{0.8}Mn_{0.2}O_3$ powder was treated under 20% O_2/He to remove most of the surface carbonaceous contaminants. After the activation step, more than 90% of the adventitious carbon contamination was removed revealing a cleaner surface. The surface chemistry did not change for La, Fe or Mn present in the sample compared to the as-received state. All the Mn, Fe and La are present in the +3 valence state. Thus, this step only ensures a surface activation treatment for succeeding *in situ* treatments.

Reaction under 5% CO in He: When $La_{0.7}Fe_{0.8}Mn_{0.2}O_3$ was analyzed after exposure under CO, it showed some distinct spectral changes. The Fe 2p signal clearly exhibited the presence of metallic iron at 706.8 eV. The presence of Fe^{2+} from its satellite structure is not so obvious by simple observation due to its overlapping with the predominant Fe^{3+}

fingerprint. The spectral decomposition reveals less than 5-10% of Fe^{2+} component. The atomic concentration of the metallic Fe stands at 6% and the rest remains as Fe^{3+} [5]. The quantitative amount of Fe^{2+} is in the same range of uncertainty of the spectral decomposition. But the presence of Fe^{2+} is mostly suggested qualitatively by the small shift to lower binding energy of the $2p_{3/2}$ signal and by the variation of the assymmetric lineshape of the multiplet structure of the Fe $2p_{3/2}$. The Mn 2p orbital has been decomposed according to Biesinger et al, as mentioned in section 2.1.2 (Fig.5.24). The fitting results shows the presence of 67% Mn^{2+} and 33% Mn^{3+} (average oxidation state=2.3). The Mn^{3+} species shows more extensive reduction than the Fe^{3+} species, when reacting under CO. This is in line with the catalytic performances where manganite-based perovskites perform better as a CO oxidation catalysts owing to better reducibility [25].

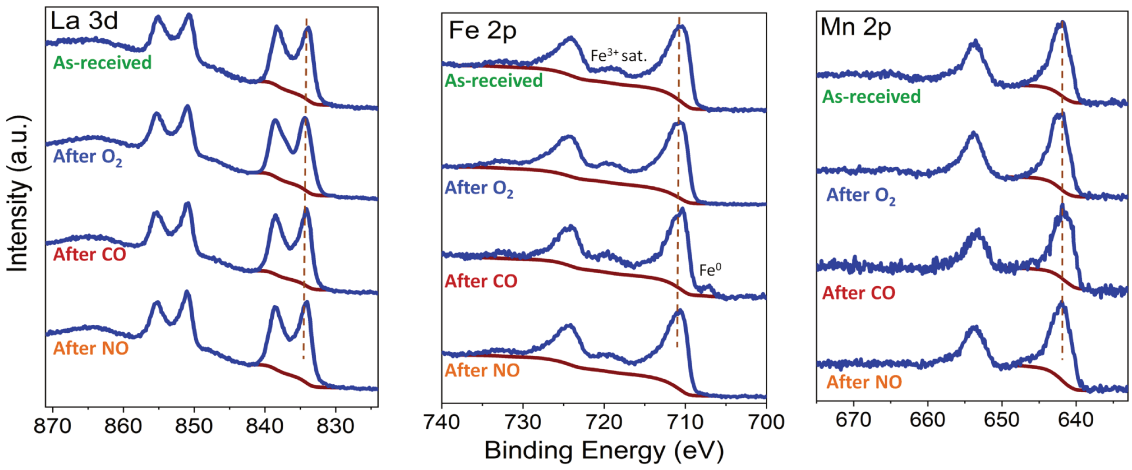

Figure 5.23: Quasi-*in situ* XPS spectra of $La_{0.7}Fe_{0.8}Mn_{0.2}O_3$ under 20% O_2/N_2, 5% CO/He and 2% NO/He.

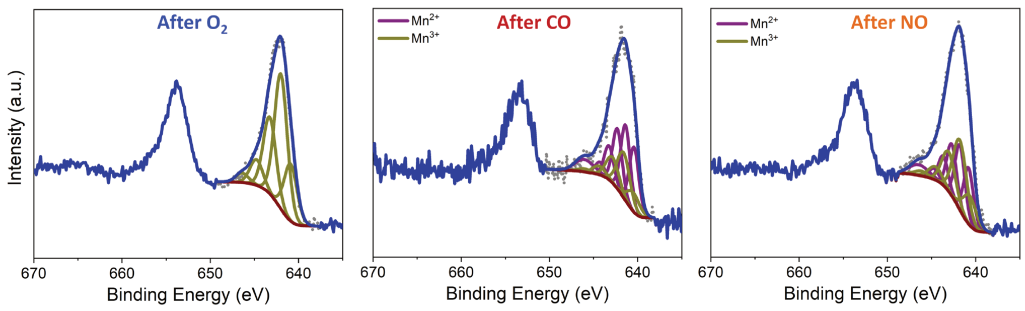

Figure 5.24: Mn 2p peak fitting of quasi-*in situ* XPS spectra of $La_{0.7}Fe_{0.8}Mn_{0.2}O_3$ under 20% O_2/N_2, 5% CO/He and 2% NO/He.

Reaction under 2% NO in He: Finally, the $La_{0.7}Fe_{0.8}Mn_{0.2}O_3$ was subjected to NO gas

exposure to study the reactivity and stability of the reduced Mn and Fe species. In case of the Fe 2p photopeak, it re-oxidizes back to the initial state and the metallic Fe contribution is completely removed. The reduced species of iron present in the preceding step have re-oxidized. The Mn 2p signal, however, still remains partially reduced with 47% Mn^{2+} and 53% Mn^{3+} (average oxidation state=2.7). This means 30% of the Mn^{2+} re-oxidizes back to Mn^{3+} when reacting with NO. This indicates that the Fe^{3+} species are more easily oxidized compared to the Mn^{3+} ions under NO.

5.3 Comparison of $La_{0.7}Fe_{0.8}Cu_{0.2}O_3$ and $La_{0.7}Fe_{0.8}Mn_{0.2}O_3$ with respect to their catalytic operating modes

The extensive study by Raman spectroscopy highlighted some major differences between the two kinds of B-site substituted perovskites, namely $La_{0.7}Fe_{0.8}Cu_{0.2}O_3$ and $La_{0.7}Fe_{0.8}Mn_{0.2}O_3$. The Cu-substituted perovskite showed the expected fingerprint of $LaFeO_3$-like phase in addition to the segregated phase of CuO, which was also confirmed by XPS and XRD analyses. XPS analysis further indicated an excess of Cu with respect to Fe in comparison to the bulk. This implies that only trace substitution by copper occurs at the B-site of the perovskite while rest remains as extra-lattice segregated phases located at the surface. Moreover, it is to be noted that Cu^{2+} ion is also JT active with a d^9 electronic configuration, similar to Mn^{3+}. From the Raman difference spectrum in Fig.5.3, it may be considered that the new lines at 475 and 635 cm^{-1} could also be attributed to a JT distorted structure similar to a manganite based-perovskite caused by the presence of some Cu^{2+} inside the perovskite structure. However, several arguments can be made against this assumption. Firstly, La-based mixed oxide with copper have a tendency to go to the Ruddlesden-Popper phase (La_2CuO_4) instead of the perovskite phase. Different synthesis methods under ambient pressure yield this type of structure including the citrate complexation route used in this study [26–30]. Secondly, the Cu-based perovskite phase ($LaCuO_3$) with Cu in +3 oxidation state is synthesized only under very high oxygen pressures of around ~200 bar [31–33]. In case of the $La_{0.7}Fe_{0.8}Cu_{0.2}O_3$ catalyst, no traces of either the Ruddlesden popper phase (characteristic Raman line expected at 220 cm^{-1} [34]) nor the occurrence of any Cu^{3+} were evidenced. Moreover, Cu-substitution has been widely carried out for several perovskite families in the literature. In most of the studies, Cu-substitution lead to the formation

of the segregated CuO phase for $AB_{0.8}Cu_{0.2}O_3$ perovskite compositions [35–37]. However, some authors have mentioned that this segregation is mostly favored at higher values of x (>0.4) [38–40]. Albaladejo-Fuentes *et al.* reported different synthesis routes for preparation of $BaTi_{0.8}Cu_{0.2}O_3$ perovskite, where CuO segregation has been evidenced for all cases [41]. Hence, the segregation of CuO can be considered structurally driven due to the nature of the Cu^{2+} ions. However, at this point it cannot be very precisely stated whether any copper ions are located at B-site of the perovskite while replacing some Fe^{3+}.

In contrast, in the case of $La_{0.7}Fe_{0.8}Mn_{0.2}O_3$ perovskite, there is no evidence of any additional phase besides the perovskite itself. XPS analysis indicated the expected ratio of Mn to Fe, similar to the bulk composition. The Mn^{3+} ion causes strong JT effect that results in a complete change in the Raman fingerprint as compared to the parent structure of $LaFeO_3$. Two possibilities can be considered for the Mn-substituted perovskite: (1) the Mn^{3+} is only substituted at the B-site of the perovskite yielding a single phase, *ie.* $La_{0.7}Fe_{0.8}Mn_{0.2}O_3$, or, (2) a solid solution of 20% $LaMnO_3$ and 80% $LaFeO_3$ is formed, which can also yield similar Raman spectrum with a manganite fingerprint owing to its high Raman cross-section.

Both questions related to $La_{0.7}Fe_{0.8}Cu_{0.2}O_3$ as well as $La_{0.7}Fe_{0.8}Mn_{0.2}O_3$ can be answered to some extent using the help of ToF-SIMS analysis. As discussed in chapter 3, the molecular fragmention involved is a direct evidence of the presence of the mixed oxide of perovskite. Some mixed oxide fragments detected on the secondary ion mass spectrum have been shown in Fig.5.25 for both $La_{0.7}Fe_{0.8}Cu_{0.2}O_3$ and $La_{0.7}Fe_{0.8}Mn_{0.2}O_3$, such as $La_2FeMO_5^+$, $LaFe_2MO_4^+$ and $La_3FeMO_6^+$ (M = Cu or Mn). In case of $La_{0.7}Fe_{0.8}Mn_{0.2}O_3$, the existence of these ionic fragments indicate the mixed oxide phase of perovskite substituted by Mn such that the Mn^{3+} is situated within the B-site of the parent $LaFeO_3$ structure. The detected mixed-fragments are verified with similar isotopic ionic fragments of ^{65}Cu and/or ^{54}Fe. Hence, it is indeed a single phase of $La_{0.7}Fe_{0.8}Mn_{0.2}O_3$ composition. In contrast, for the $La_{0.7}Fe_{0.8}Cu_{0.2}O_3$ perovskite, the presence of the mixed ionic fragments is negligible and the analogous isotopic ions with ^{65}Cu and/or ^{54}Fe are completely absent in the mass spectrum. This highlights the fact that very little or none of the Cu^{2+} ions have been substituted at the B-site of the perovskite. This is in agreement with many studies made on Cu-substituted perovskites where a preferential extra-lattice segregation of copper as CuO has been evidenced mostly by XRD analysis [36, 37, 41]. The segregated particles of copper species are also observed by SEM analysis as shown in Fig.5.26 on a ~70

nm thin film of $La_{0.7}Fe_{0.8}Cu_{0.2}O_3$ supported over SiO_2/Si(100) substrate, which acts as a relevant model as concluded in chapter 3 and [42]. The electron image contains some segregated particles over the flat and homogeneous film. EDX analysis confirms that these particles are Cu-rich species, mainly located densely at the top of the grain boundaries. No iron-rich zones or segregation can be determined by SEM here.

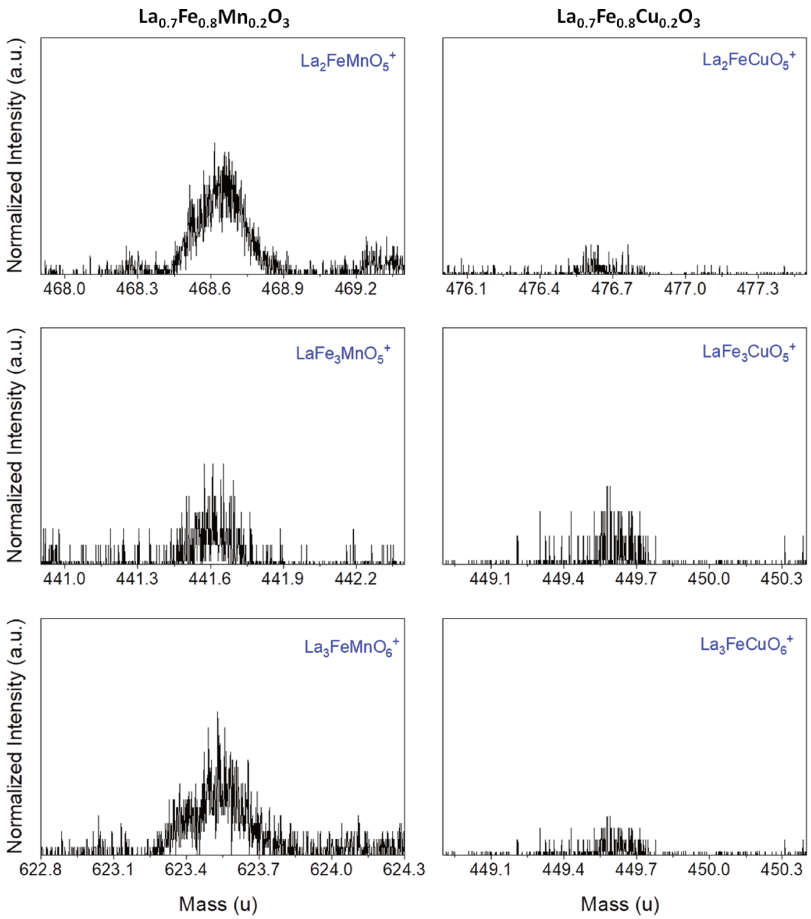

Figure 5.25: Mixed ionic fragments of $La_{0.7}Fe_{0.8}Mn_{0.2}O_3$ (left column) and $La_{0.7}Fe_{0.8}Cu_{0.2}O_3$ (right column) from ToF-SIMS mass spectra analyzed in positive mode.

Finally, the two perovskite powders were analyzed by XANES in the transmission mode at the Fe K-edge using the pellets of each. Their XANES spectra were compared to that of the parent perovskites: $LaFeO_3$ and $La_{0.7}FeO_3$. It is already known that $LaFeO_3$ consists of a single perovskite phase while $La_{0.7}FeO_3$ contains iron oxide (hematite) besides the perovskite phase. As shown in Fig.5.27, the $La_{0.7}Fe_{0.8}Mn_{0.2}O_3$ presents a XANES spectrum very close to that of the La-deficient $La_{0.7}FeO_3$, meaning it must also contain similar ratio of Fe_2O_3, while $La_{0.7}Fe_{0.8}Cu_{0.2}O_3$ is more close to the fingerprint of the stoichiometric $LaFeO_3$ structure except minor differences in the intensity of the white line, which suggests that the La deficiency retains the presence of Fe_2O_3 in lower amounts. This is further

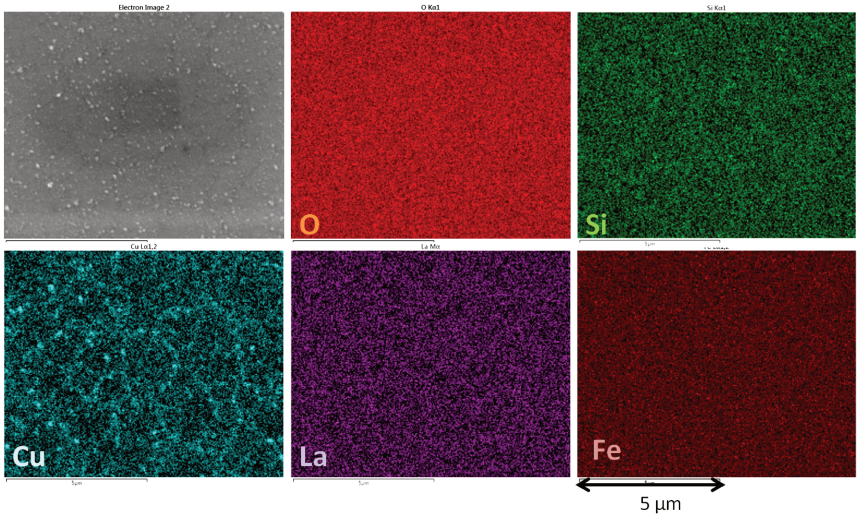

Figure 5.26: SEM images of $La_{0.7}Fe_{0.8}Cu_{0.2}O_3$/Si thin film with chemical mapping by EDX.

elucidated by the LCF fitting of each using reference spectra of iron oxides. The LCF results show that the $La_{0.7}Fe_{0.8}Mn_{0.2}O_3$ contains 33% of Fe_2O_3 and 67% of $LaFeO_3$, while the $La_{0.7}Fe_{0.8}Cu_{0.2}O_3$ consists of only 13% of hematite and 87% of $LaFeO_3$. This indicates that substitution with copper suppresses the formation of the segregated iron oxide by permitting more iron to remain at the B-site. This implies that copper substitution results into segregated CuO and Fe_2O_3 besides the perovskite, while in the case of $La_{0.7}Fe_{0.8}Mn_{0.2}O_3$ all the extra iron content settles as iron oxide resulting in a system consisting of stoichiometric Mn-substituted perovskite and the Fe_2O_3. Hence, both B-site substituted catalysts are quite different from their generic formula. In case of $La_{0.7}Fe_{0.8}Cu_{0.2}O_3$, it mimics more of CuO particles supported $LaFeO_3$ catalytic system, while the $La_{0.7}Fe_{0.8}Mn_{0.2}O_3$ catalyst is indeed a B-site substituted perovskite. Thus, this makes both catalysts very different with respect to their structural characteristics, which will drive a catalytic reaction by different operating modes.

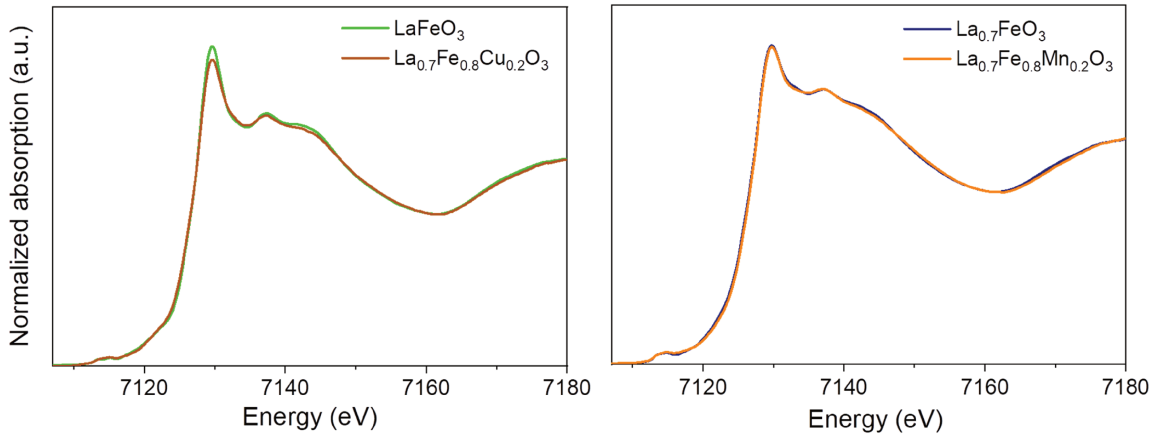

Figure 5.27: XANES spectra of $LaFeO_3$ (red), $La_{0.7}FeO_3$ (yellow), $La_{0.7}Fe_{0.8}Mn_{0.2}O_3$ (blue) and $La_{0.7}Fe_{0.8}Cu_{0.2}O_3$ (green) pellets at the Fe K-edge in transmission mode.

5.4 Conclusions

This chapter highlighted some major differences between two 20% B-site substituted perovskites, namely $La_{0.7}Fe_{0.8}Cu_{0.2}O_3$ and $La_{0.7}Fe_{0.8}Mn_{0.2}O_3$. Under dehydrated conditions, $La_{0.7}Fe_{0.8}Cu_{0.2}O_3$ consists of a $LaFeO_3$-supported CuO phase with almost no additional iron oxide. CuO was evidenced as being the only redox-active phase owing to no structural changes according to the Raman spectra under oxidizing/reducing cycles. In contrast, the $La_{0.7}Fe_{0.8}Mn_{0.2}O_3$ perovskite mostly consists of the perovskite phase together with Fe_2O_3 nano-phase as suggested by the XANES analysis. The Mn^{3+} ion causes strong Jahn Teller effect that results in a complete change in the Raman fingerprint as compared to the parent structure of $LaFeO_3$, while the reduction of Mn^{3+} to Mn^{2+} allows recovering the $LaFeO_3$ signature. The reduction of Mn^{3+} to Mn^{2+} under CO was confirmed by the evolution of the Mn 2p photopeak during the quasi-*in situ* procedure. Interestingly, the Fe_2O_3 phase was also found to undergo a redox behaviour, which could play a role in the enhanced activity of the $La_{0.7}Fe_{0.8}Mn_{0.2}O_3$ catalyst in TWC operating conditions.

5.5 References

[1] Sébastien Royer and Daniel Duprez and Fabien Can and Xavier Courtois and Catherine Batiot-Dupeyrat and Said Laassiri and Houshang Alamdari, *Chem. Rev.*, 2014, **114**(20), 10292–10368. 149, 158

[2] H. Tanaka and M. Misono, *Curr. Opin. Solid St. M.*, 2001, **5**(5), 381–387. 149

[3] D. Blanck *Modélisation de la structure et de la réactivité de la perovskite $LaFeO_3$ dopée* PhD thesis, Université de Lille, 2016. 149

[4] M. Sunding, K. Hadidi, S. Diplas, O. Løvvik, T. Norby, and A. Gunnæs, *J. Electron. Spectrosc.*, 2011, **184**(7), 399 – 409. 151, 162

[5] M. C. Biesinger, B. P. Payne, A. P. Grosvenor, L. W. Lau, A. R. Gerson, and R. S. Smart, *Appl. Surf. Sci.*, 2011, **257**(7), 2717 – 2730. 151, 163, 172

[6] J. Wu, J. P. Dacquin, C. Cordier, C. Dujardin, and P. Granger, *Top. Catal.*, 2019, **62**(1), 368–375. 151, 158

[7] Y. Deng, A. D. Handoko, Y. Du, S. Xi, and B. S. Yeo, *ACS Catalysis*, 2016, **6**(4), 2473–2481. 152

[8] H. Hagemann and H. Bill and W. Sadowski and E. Walker and M. François, *Solid State Commun.*, 1990, **73**(6), 447 – 451. 152

[9] D. Blanck, A. Schön, A.-S. Mamede, C. Dujardin, J.-P. Dacquin, P. Granger, J.-F. Paul, and E. Berrier, *Catal. Today*, 2016. 153, 154, 155, 167, 168, 170

[10] J. Andreasson, J. Holmlund, R. Rauer, M. Käll, L. Börjesson, C. S. Knee, A. K. Eriksson, S.-G. Eriksson, M. Rübhausen, and R. P. Chaudhury, *Phys. Rev. B*, 2008, **78**, 235103. 154

[11] S. A. Mock, E. T. Zell, S. T. Hossain, and R. Wang, *ChemCatChem*, 2018, **10**(1), 311–319. 157

[12] B. M. Vogelaar, A. D. van Langeveld, S. Eijsbouts, and J. A. Moulijn, *Fuel*, 2007, **86**(7), 1122 – 1129. 158, 170

[13] M. C. Biesinger, L. W. Lau, A. R. Gerson, and R. S. Smart, *Appl. Surf. Sci.*, 2010, **257**(3), 887 – 898. 161

[14] S. Thirumalairajan, K. Girija, V. R. Mastelaro, and N. Ponpandian, *ACS Appl. Mater. Inter.*, 2014, **6**(16), 13917–13927. 162

[15] E. Beyreuther, S. Grafström, L. M. Eng, C. Thiele, and K. Dörr, *Phys. Rev. B*, 2006, **73**, 155425. 163

[16] Iliev, M. N. and Abrashev, M. V. and Laverdière, J. and Jandl, S. and Gospodinov, M. M. and Wang, Y.-Q. and Sun, Y.-Y., *Phys. Rev. B*, 2006, **73**, 064302. 164, 165

[17] Y. Q. Jia, S. T. Liu, Y. Wu, M. Z. Jin, X. W. Liu, and M. L. Liu, *Phys. Status Solidi A*, 1994, **143**(1), 15–22. 164

[18] K. Sultan, M. Ikram, and K. Asokan, *Vacuum*, 2014, **99**, 251 – 258. 164

[19] P. Ravindran, A. Kjekshus, H. Fjellvåg, A. Delin, and O. Eriksson, *Phys. Rev. B*, 2002, **65**, 064445. 165

[20] M. N. Iliev and M. V. Abrashev, *J. Raman Spectrosc.*, 2001, **32**(10), 805–811. 165, 168

[21] M. N. Iliev, M. V. Abrashev, H.-G. Lee, V. N. Popov, Y. Y. Sun, C. Thomsen, R. L. Meng, and C. W. Chu, *Phys. Rev. B*, 1998, **57**, 2872–2877. 165

[22] T. Ishigaki, S. Yamauchi, J. Mizusaki, K. Fueki, H. Naito, and T. Adachi, *J. Solid St. Chem.*, 1984, **55**(1), 50 – 53. 169

[23] A. Schön, C. Dujardin, J.-P. Dacquin, and P. Granger, *Catal. Today*, 2015, **258**, 543 – 548. 169

[24] B. Levasseur and S. Kaliaguine, *Appl. Catal. A-general*, 2008, **343**, 29–38. 169

[25] S. Royer and D. Duprez, *ChemCatChem*, 2011, **3**(1), 24 – 65. 172

[26] A. Schön, J.-P. Dacquin, C. Dujardin, and P. Granger, *Top. Catal.*, 2017, **60**(3), 300–306. 173

[27] J. Longo and P. Raccah, *J. Solid St. Chem.*, 1973, **6**(4), 526 – 531.

[28] J. Liu, Z. Zhao, C. ming Xu, and A. jun Duan, *Appl. Catal. B - Environ.*, 2008, **78**(1), 61 – 72.

[29] M. Velasquez, A. Santamaria, and C. Batiot-Dupeyrat, *Appl. Catal. B - Environ.*, 2014, **160-161**, 606 – 613.

[30] S. Peter, E. Garbowski, N. Guilhaume, V. Perrichon, and M. Primet, *Catal. Lett.*, 1998, **54**(1), 79–84. 173

[31] G. Demazeau, C. Parent, M. Pouchard, and P. Hagenmuller, *Mater. Res. Bull.*, 1972, **7**(9), 913 – 920. 173

[32] H. Falcòn, M. Martinez-Lope, J. Alonso, and J. Fierro, *Appl. Catal. B - Environ.*, 2000, **26**(2), 131–142.

[33] J. F. Bringley, B. A. Scott, S. J. La Placa, T. R. McGuire, F. Mehran, M. W. McElfresh, and D. E. Cox, *Phys. Rev. B*, 1993, **47**, 15269–15275. 173

[34] G. Burns and F. H. Dacol, *Phys. Rev. B*, 1990, **41**, 4747–4748. 173

[35] N. Tien-Thao and H. Alamdari and M.H. Zahedi-Niaki and S. Kaliaguine, *Appl. Cata. A - General*, 2006, **311**, 204 – 212. 174

[36] V. Torregrosa-Rivero, V. Albaladejo-Fuentes, M.-S. Sánchez-Adsuar, and M.-J. Illán-Gómez, *RSC Adv.*, 2017, **7**, 35228–35238. 174

[37] V. Albaladejo-Fuentes, F. E. Lopez-Suarez, M. S. Sánchez-Adsuar, and M. J. Illán-Gómez, *Appl. Cata. A - General*, 2014, **488**, 189 – 199. 174

[38] F. Parrino, E. García-López, G. Marcì, L. Palmisano, V. Felice, I. N. Sora, and L. Armelao, *J. Alloy. Compd.*, 2016, **682**, 686 – 694. 174

[39] H. Yasuda, Y. Fujiwara, N. Mizuno, and M. Misono, *J. Chem. Soc. Faraday Trans.*, 1994, **90**, 1183–1189.

[40] P. Porta, S. D. Rossi, M. Faticanti, G. Minelli, I. Pettiti, L. Lisi, and M. Turco, *J. Solid St. Chem.*, 1999, **146**(2), 291 – 304. 174

[41] V. Albaladejo-Fuentes, F. E. López-Suárez, M. S. Sánchez-Adsuar, and M. J. Illán-Gómez, *Appl. Cata. A - General*, 2016, **519**, 7–15. 174

[42] S. Nandi, D. Blanck, T. Carlier, M.-H. Chambrier, A.-S. Mamede, M. Trentesaux, P. Simon, N. Nuns, P. Roussel, A. Ferri, J.-F. Paul, and E. Berrier, *Surf. Interf. Anal.*, 2018. 175

General Conclusions and Perspectives

$LaFeO_3$ based perovskites, considered as alternative materials for TWC application, were investigated in this thesis work. Such bulk materials often possess surface specificities that can directly affect the catalytic performance. The methodology used in this work involves both surface and bulk analytical techniques for investigating the structural and surface properties of the perovskites, involving, among others, the crystal phase, the presence of defects, the chemical composition and the oxidation state. To-date methods such as NAP-XPS or *operando* spectroscopies were appointed to investigate their surface reactivity under TWC-relevant environment, according to either the *in situ* or the *operando* approach. Discrete models of $LaFeO_3$-based materials, ranging from ultra-thin films towards the very same powders as those used for lab-scale evaluation of TWC performances. Therefore, overall this thesis aimed at the following:

- To prepare surface models of $LaFeO_3$-based catalysts by synthesizing model catalysts shaped as polycrystalline thin films for reliable surface analyses.
- To investigate the surface and structural properties of the model catalysts and evaluate their relevance as TWC models.
- To use the models to study the role of A-site La deficiency in the perovskite structure by *in situ* measurements.
- To compare B-site substitution in $LaFeO_3$ by two different elements (Cu or Mn) and investigate their catalytic operating modes.

To this end, discrete model materials of $LaFeO_3$ supported over SiO_2/Si(100) substrates were prepared by spin coating with thickness ranging from a few nm to µm. The thin films of 50-100 nm were chosen as suitable models for high temperature treatment (up to 650°C) and and those of <10 nm as surface models for highly element-sensitive techniques to be used for low temperature analyses (up to 300°C), respectively. $LaFeO_3$-SiO_2/Si(100)

featured similar chemical, structural and surface properties of an orthorhombic lanthanum ferrite oxide in both thickness ranges. The thin film also signified the presence of La-enrichment similar to conventional powder catalysts although with less surface contamination from adventitious carbon. Surface analysis further revealed that the La enrichment did not block all the active Fe sites on the outermost surface, indicating that some Fe sites still remain available for reaction. Finally, the model catalysts were compared to conventional powders at the surface as well as the bulk of the thin film, which allowed to validate these polycrystalline thin films as relevant models for further surface investigation of TWC reaction.

The perovskite based model catalysts were then utilized to successfully investigate the beneficial role of inducing a La-deficiency into the structure ($La_{0.7}FeO_3$) by comparison with the stoichiometric composition. $La_{0.7}FeO_3$ revealed the presence of ~40% of iron oxide and ~60% of perovskite phase with particles of Fe_2O_3 embedded on the perovskite, while the $LaFeO_3$ is solely composed of the perovskite phase. The non-stoichiometric perovskite showed higher reducibility to Fe^{2+} under CO exposure at high temperature compared to the stoichiometric composition by NAP-XPS. Some metallic iron formation occurred in $La_{0.7}FeO_3$ only, arising from the presence of the hematite phase since none was detected in case of $LaFeO_3$. Finally, to obtain more information regarding the phase compositions under CO environment GI-XANES was applied. The $LaFeO_3$ reduced to only the FeO phase (15%) while $La_{0.7}FeO_3$ reduced to majority of magnetite (69%) and some FeO (8%). Quantitative correlations highlighted the extensive formation of magnetite under CO atmosphere. This magnetite (Fe_3O_4) phase was never detected in stoichiometric $LaFeO_3$ under such conditions, supporting the key role of the interface between the perovskite and the hematite in $La_{0.7}FeO_3$ we propose here. The vicinity of both $LaFeO_3$ and hematite phases allows the FeO, resulting from the reaction of $LaFeO_3$ with CO, to immediately react with the iron oxide phase to form the magnetite. The synergistic role provided by the interface is in line with the previous catalytic performances of the respective perovskites. This study thereby highlights the driving force of the improved catalytic performance caused by inducing an A-site deficiency in the perovskite structure. In addition, it must be noted that the NAP-XPS and GI-XANES results cannot be directly quantitatively compared due to the unavoidable differences in the experimental conditions and experimental set-up.

Additionally, as a collaborative work within the PARTIAL-PGMs consortium, the effect of substitution at B-site by Cu or Mn were investigated for the $La_{0.7}Fe_{0.8}M_{0.2}O_3$ (M=Cu or Mn) powder catalysts. Substitution of Cu^{2+} leads to segregation of CuO while no additional phase segregation was detected after Mn-substitution. The *in situ* Raman analysis of $La_{0.7}Fe_{0.8}Cu_{0.2}O_3$ indicated likely presence of the CuO species that could impact the redox cycle, however, owing to the spectral complexity, conclusive remarks from Raman spectra alone could not be made. The presence of CuO species was thereby confirmed by XPS and XRD. In case of $La_{0.7}Fe_{0.8}Mn_{0.2}O_3$, a complete change in the Raman spectral signature was observed signifying the substitution of Mn^{3+} by replacement of Fe^{3+} sites at the B-site. The copper substitution in B-site remained negligible confirmed by ToF-SIMS. Hence, in case of $La_{0.7}Fe_{0.8}Cu_{0.2}O_3$, the copper exists as extra-lattice moieties in the form of CuO and can be definitively considered as a $LaFeO_3$-supported CuO catalyst. On the other hand, the $La_{0.7}Fe_{0.8}Mn_{0.2}O_3$ is indeed B-site substituted system. In conclusion, each perovskite will follow a different operating mode during a catalytic reaction. In this case particularly, $La_{0.7}Fe_{0.8}Cu_{0.2}O_3$ resulted in better catalytic performance during CO oxidation reaction.

Perspectives:

This work succesfully highlighted the adapted methodology to investigate fundamental aspects of perovskite-based bulk catalysts by shaping them as polycrystalline thin films for surface analysis by a multi-technique approach in *ex situ* as well as *in situ* modes. Of course future work is required in some areas for a more detailed understanding of the material and its reactivity.

As is the case for several other perovskite compositions, surface segregation of iron was observed in $LaFeO_3$ and $La_{0.7}FeO_3$. In stoichiometric $LaFeO_3$, it as driven by the A-site La-enrichment while for non-stoichiometric $La_{0.7}FeO_3$ it is mainly caused by the segregated Fe_2O_3 particles due to the induced La deficiency. Although, this surface enrichment or segregation phenomenon is clearly observed by depth profiling measurements, accurate depth scales could not be determined. This can be done in the future by coupling the ToF-SIMS measurements with AFM to determine the depth scales of the detected segregation zones.

Several authors use La-deficient ferrites as active catalysts but the driving force behind the improved catalytic performance is not completely understood so far. This study enabled to observe that any induced non-stoichiometry at the A-site resulted into segregation of the extra B-site ions as its oxide, since the perovskite prefers to maintain its stoichiometry. The presence of an interface was highlighted between the segregated Fe_2O_3 and the perovskite in $La_{0.7}FeO_3$, which helps to increase the reducibility during a reaction. It would be useful to analyze the cross-sectional FIB-lamella of the $La_{0.7}FeO_3$ thin film to observe the interface between perovskite and iron oxide at the atomic scale by HR-TEM to validate the interpreted observations.

Finally, the ultra-thin films <10nm range can be prepared by other techniques such as atomic layer deposition to have a homogeneous coverage of the perovskite layer and achieve better control of the thickness scale, which could be used as surface models for low temperature reactions below <300°C.

The thin film approach provides an unique possibility to analyze insulating bulk materials in a NAP-XPS lab, especially without any charge compensation. The following figure compares the Fe 2p spectra of $La_{0.7}FeO_3$ powder and thin film. The $La_{0.7}FeO_3$ particles adhering on to a Au foil face major charging problems which results in poor spectral quality as well as loss of the material during heating and transfer. Hence, shaping the samples as thin films will be an alternative way to record reliable signals in future.

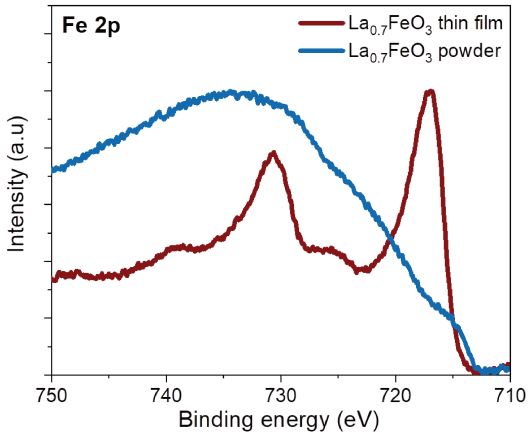

Figure 5.28: Comparison of the NAP-XPS Fe 2p spectra of $La_{0.7}FeO_3$ thin film (red) and powder (blue) recorded under similar conditions.

Further, the Cu or Mn substituted perovskites have been investigated by *in situ* Raman and quasi-*in situ* XPS. However, the redox behaviour of the CuO species was difficult to be interpreted with respect to the Raman spectra. This can be more precisely investigated in future by *in situ* XRD and/or XANES analyses to detect the change in phase compositions during a redox cycle. This would not only allow to determine the role of CuO species but also detect the presence of small traces of any other copper species such as Cu_3O_4, La_2CuO_4 and $FeCuO_2$, which were out of scope of the present work. Similarly, this will be also interesting for the Mn-substituted perovskites likewise.

In general, the undertaken approach of this work can be extended similarly to a large variety of oxides dedicated to redox applications, which will not only help to understand the surface characteristics more effectively but also propose better ideas for designing of active catalyst compositions.